E-398

HADRON PRODUCTION IN DEEP-INELASTIC MUON-PROTON SCATTERING AT 219 GeV

James Proudfoot

Worcester College

Thesis submitted for the degree of

Doctor of Philosophy in the University of Oxford.

October 1978

See Strength and Beauty hand in hand

Step forth into the golden land.

Gerald Massey

TO MY PARENTS

HADRON PRODUCTION IN DEEP-INELASTIC MUON-PROTON SCATTERING AT 219 GeV

J. Proudfoot,
Worcester College, Oxford.

Submitted for the degree of Doctor of Philosophy,
Michaelmas Term, 1978.

ABSTRACT

This thesis reports on an experiment using the Hadron Spectrometer Facility at Fermilab, Batavia, Illinois, in which high energy muons were scatterd from a proton target.

Results are presented on hadron production in the interaction

$$\mu + p \rightarrow \mu + \text{Anything}$$

Hadrons were identified in a large multicell Cerenkov counter positioned downstream of the spectrometer magnet. A discussion of the design and construction of this counter and the use of the information obtained from it is given.

A search for charmed D-meson production in the reaction

$$\mu + p \rightarrow \mu + D + X$$

through the invariant mass spectra of the hadronic D decay channels $K^{\pm}\pi^{\mp}$ and $K^{\pm}\pi^{\mp}\pi^{\mp}$ is presented. No enhancement in the invariant mass distributions in the vicinity of 1.87 GeV/c^2 is observed.

For $x_{Bj} < 0.1$, $Q^2 < 1.0$ (GeV/c^2)^2, no D-meson production is observed at a level of 6.9 nbarn with 90% confidence, and for $1 < Q^2 < 80$ (GeV/c^2)^2 at a level of 7.2 nbarn with 90% confidence. These results are in qualitative agreement with QCD predictions.

Particle flux ratios K^+/π^+, K^-/π^-, P/π^+, $\bar{P}/\pi^-$ are measured as a function of z and $P_\perp$. The particle fractions (f_π, f_K, f_p) of all charged hadrons are measured to be

$$f_\pi = 0.854 \pm 0.014$$
$$f_K = 0.12 \pm 0.027$$
$$f_p = 0.026 \pm 0.013$$

Proton production is compatible with background. A rise in the ratios K^+/π^+, K^-/π^- with $P_\perp^2$ is observed for $z < 0.3$ but not for $0.3 < z < 0.9$. As $z \rightarrow 0$, $K^+/\pi^+ \rightarrow 0.15 \pm 0.03$ and $K^-/\pi^- \rightarrow 0.11 \pm 0.03$. These limits are not well determined as $z \rightarrow 1$.

The results are in qualitative agreement with low energy data and with Q.C.D. and quark-parton model predictions.

ACKNOWLEDGEMENTS

High energy physics experiments are no longer possible without a large collaboration of people. It is a pleasure to thank those people whose help has contributed to the completion of this thesis. It is a long list ...

I am indebted to Professor Sir Denys Wilkinson and Professor D.H. Perkins for the use of the facilities of the Nuclear Physics Department.

Four institutions - Chicago, Harvard, Illinois and Oxford - were involved in the operation and analysis of this experiment. It is a pleasure to thank the members of the experimental team for their help and friendship. The experiment was carried out using the facilities of the Fermi National Accelerator Laboratory, Illinois, USA. I would like to thank the staff of that institution and, in particular, the Neutrino Section who not only provided excellent facilities but whose friendship made my stay in the USA so enjoyable. The computer staff at the Rutherford Laboratory deserve thanks for their services which allowed a speedy analysis of this experiment.

The following people are deserving of special mention:

Tom Quirk, my supervisor and the mastermind of the Oxford analysis, for his encouragement and excellent advice.

Andris Skuja for introducing me to high energy physics and to the USA.

Bill Williams and Norman Booth, the remaining members of the group at Oxford, for their readiness to give help when required.

My fellow graduate students on the experiment, Mervyn Staton, Bruce Gordon, Randy Hicks and Charling Tao who contributed so much to the success of this experiment.

John MacAllister and Lesley Jones who handlded my computing problems so efficiently.

Tricia Falconer Smith for her excellent typing of this thesis.

Elsa Mason and Avril Butler for their skilful drawing of the figures.

Brian Foster, a friend and fellow graduate student, whose encouragement was invaluable and for excellent comments on this thesis.

My brother Gary and his wife, Sue, for their love and forbearance.

Finally, to my mother and father, I offer my sincere thanks for their love and support these last twenty-five years.

CONTENTS

CHAPTER I

DEEP INELASTIC MUON SCATTERING AS A PROBE OF NUCLEON STRUCTURE

1.1 INTRODUCTION

Investigation of scattering processes has been the principal source of information on the nature of matter in recent years. The hope of the physicists carrying out these experiments is that by understanding the interactions between particles some insight into the nature of the particles themselves might be obtained. Experiments carried out by Rutherford and co-workers scattering a beam of alpha particles with an energy of a few MeV on a gold target revealed the charge distribution of the atom. From the results they concluded that the atom consisted of a positively charged central core containing most of the atomic mass, surrounded by a cloud of negatively charged particles - the first indication of internal structure in atoms. In the 50 or so years since these pioneering experiments were carried out, scattering experiments using beams with energies ranging from $1\text{-}10^{11}$ eV have revealed first the substructure of the nucleus as a bound state of charged and uncharged nucleons and are now revealing substructure in the nucleons themselves. The ultimate goal is an understanding of this structure and how it leads to the multitude of 'elementary particles' observed in these interactions.

The subject of this thesis is the hadrons produced in deep-inelastic scattering of muons from protons in the reaction

$$\mu^+ + P \rightarrow \mu^+ + X$$

Charged leptons interact with matter primarily via the electromagnetic current which is well understood by QED (their weak and gravitational interaction is negligible at our level of precision). It is therefore

possible to separate the effects due to the probe (the muon) from those due to the target proton and thereby obtain a clear picture of any structure in the proton. In order to justify this assumption it is essential to know how well QED predicts the electromagnetic interaction of the muon. A necessary requirement is to show that the muon is a true Dirac point particle. [It must be noted, however, that deviation from QED in the photon propogator cannot be distinguished from non-point-like behaviour at the muon vertex and will also be observed as a deviation from point-like behaviour.]

If the muon were not a point particle but had a charge distribution over a finite radius R, then its form factor must be modified to (1)

$$F(Q^2) = |f(Q^2)|^2 \; F(0) \qquad 1.1$$

where $F(0) = 1$ is the static form factor and Q^2 is the negative of the four-momentum transfer squared. The standard form taken for $f(Q^2)$ is

$$f(Q^2) = 1 \pm {}^{Q^2}/_{\Lambda^2} \qquad 1.2$$

where Λ is interpreted as the mass which determines the characteristic scale for the muon. Naively speaking, the magnitude of the four-momentum transfer is related via the Uncertainty Principal to the resolution attained in the interaction ($\delta x \sim \frac{h}{\sqrt{Q^2}}$). A glancing blow - low Q^2 can resolve only large distances whereas a 'hard' collision - high Q^2 can probe short distances. Eqn. 1.2 would therefore imply a characteristic 'radius' of the muon $R \sim {}^{h}/_{\Lambda}$. Clearly $\Lambda = \infty$ for a Dirac point particle. Limits on Λ can be obtained by comparing theoretical calculations with experimental results[2]. The best lower limit is obtained from the cross-section for the reaction $e^+e^- \rightarrow \mu^+\mu^-$ which gives $\Lambda \geq 27$ GeV/c^2 at 95% confidence. QED therefore predicts the behaviour of the muon down to distances of order 3×10^{-16} m.

Having established the validity of QED for the muon, relevant formulae will now be given. The differential cross-section for μ-p - elastic and inelastic scattering will be presented in Section 1.2 and a brief historical development of the subject in Section 1.3. The theoretical framework, within which hadron production in deep-inelastic scattering is described in this thesis, will be outlined in Section 1.4.

1.2 ELASTIC AND INELASTIC SCATTERING CROSS-SECTIONS

Elastic Scattering

The first order Feynman diagram for μ-p elastic scattering is shown in Fig. 1.1a (one-photon exchange). The electromagnetic coupling constant α is small and therefore higher order diagrams (e.g. Fig. 1.1b) can be neglected in the calculation of the cross-section. Moreover, since the interaction is elastic, it is described by a single independent variable (e.g. Q^2 or ν). The cross-section for scattering one Dirac particle of mass M_ℓ from a second, unlike Dirac particle of mass M can be calculated exactly from the first order Feynman diagram, Fig. 1.1a (by considering the proton a point particle):[1]

$$\frac{d^2\sigma_{point}}{dQ^2} = \frac{2\pi\alpha^2}{Q^4} \cdot \frac{Q^4 - 2sQ^2 + 2(s - M_\ell^2 - M^2)}{\lambda(s, M_\ell, M)} \qquad 1.3$$

Definitions of the variables are given in Fig. 1.1 and Table 1.1.

Neglecting the lepton mass terms, (which is justifiable in μ-p scattering since $M_\ell \gg M$), Eqn. 1.3 reduces to:

$$\frac{d\sigma_{point}}{dQ^2} = \frac{4\pi\alpha^2}{Q^4}\frac{E'}{E}\frac{\cos^2\theta/2}{1 + 2(E/M)\sin^2\theta/2}\left[1 + (Q^2/2M)\tan^2\theta/2)\right] \qquad 1.4$$

where the factor $(1 + 2(E/M)\sin^2\theta/2)$ is due to the nuclear recoil. However, the proton is not a point particle and Eqn. 1.4 must be modified to include effects of proton structure.

$$\frac{d\sigma_{elastic}}{dQ^2} = \frac{4\pi\alpha^2}{Q^4}\frac{E'}{E}\left[\frac{\cos^2\theta/2}{1 + 2(E/M)\sin^2\theta/2}\right] \times \left[\frac{G_E^2(Q^2) + G_M^2(Q^2)/4M^2}{1 + Q^2/4M^2} + \left(\frac{Q^2}{2M^2}\right)G_M^2(Q^2)\tan^2\theta/2\right] \qquad 1.5$$

This is the Rosenbluth formula. G_E and G_M are the electric and magnetic form factors, so called, since in the Breit frame of the nucleon they correspond exactly to the electric charge and magnetic dipole moment distribution of the nucleon.

Experimentally, the proton form factors are found to have the dependence[3]

$$G_E(Q^2) = \frac{G_M(Q^2)}{\mu_p} = \left(1 + \frac{Q^2}{0.71}\right)^{-2}$$

where μ_p is the magnetic moment of the proton. Elastic scattering is therefore strongly dependent on Q^2, for large Q^2:

$$\frac{d\sigma_{elastic}}{dQ^2} \sim \frac{1}{Q^4}\left[\left(\frac{1}{Q^2}\right)^2\right]^2 \sim \frac{1}{Q^{12}}$$

where a factor $1/Q^4$ is coming from the photon propogator and a factor $1/Q^8$ from the form factor dependence. It is therefore extremely unlikely that a proton will not break up when struck by a highly virtual photon.

Inelastic Scattering

Fig. 1.2 shows the first order Feynman diagram for the process $\mu^+ + p \rightarrow \mu^+ +$ Hadrons. In calculating the cross-section it is assumed that this is the dominant diagram (i.e. one-photon exchange). A comparison of ℓ^+N with ℓ^-N can be used to obtain an estimate of the two-photon exchange contribution - the sign of the interference term between the two amplitudes changing sign for the different beams. Experiments[4] have shown e^+p and e^-p to be equal to within 2%. Comparison of μ^+N and μ^-N[5] indicate a contribution from two-photon exchange of less than a few percent. It is therefore reasonable to calculate in the one-photon exchange approximation. The form of the inelastic differential cross-section is then[6]

$$\frac{d^2\sigma}{dQ^2 d\nu} = \frac{2\pi\alpha^2}{Q^4} \cdot \frac{1}{|\underline{P}|^2}\left[(2EE' - Q^2/2)W_2(Q_2(Q^2,\nu) + (Q^2 - 2M_\mu^2)W_1(Q^2,\nu)\right] \quad 1.6$$

averaged over initial lepton and proton spins and summed over final spin states.

Neglecting terms of order M_μ^2, and using the relation $Q^2 \approx 4EE'\sin^2\theta/2$, Eqn. 1.6 can be re-written as:

$$\frac{d^2\sigma}{dQ^2 d\nu} = \frac{4\pi\alpha^2}{Q^4}\frac{E'}{E}\left[\cos^2\theta/2\ W_2(Q^2,\nu) + 2\sin^2\theta/2\ W_1(Q^2,\nu)\right] \qquad 1.7$$

The functions W_1 and W_2 which describe the photon-nucleon vertex are called the deep-inelastic structure functions. In general they can be a function of the two independent invariants chosen to describe the interaction, e.g. (Q^2,ν) or (Q^2,x). Comparison with Eqn. 1.5 in the case of elastic scattering shows:

$$W_2 = \frac{G_E^2 + G_M^2 . Q^2/4M^2}{1 + Q^2 . 4M^2}\,\delta(\nu - \frac{Q^2}{2M}) \qquad 1.8$$

$$W_1 = \frac{Q^2}{4M^2}\,G_M^2\,\delta(\nu - \frac{Q^2}{2M})$$

Virtual Photon Cross-section

An equivalent formulation of the deep-inelastic cross-section, in terms of the absorption cross-section for transverse virtual photons $(\sigma_T(Q^2,\nu))$ and longitudinal virtual photons can also be made.[7] The scattering muon is considered a source for these virtual photons:

$$\frac{d^2\sigma}{dQ^2 d\nu} = \Gamma(E,E'\theta)\ [\sigma_T(Q^2,\nu) + (\varepsilon + \delta)\sigma_L(Q^2,\nu)] \qquad 1.9$$

Where

$$\Gamma(E, E', \theta) = \frac{\alpha}{2\pi} \cdot \frac{K}{Q^2} \cdot \frac{1}{E^2(1 - \varepsilon)}$$

is the flux of virtual photons.

$$\varepsilon = \frac{1}{1 + \dfrac{2(Q^2 + \nu^2)\tan^2\theta/2}{Q^2(1 - \dfrac{Q^2_{min}}{Q^2})^2}}$$

measures the longitudinal polarisation of the virtual photon.

$$\delta = \frac{2m_\mu^2(1 - \varepsilon)}{Q^2}$$

is a small kinematic factor which can be neglected at high Q^2.

$$K = \frac{W^2 - M^2}{2M}$$

is the 'equivalent photon energy', - it corresponds to the energy required by a real photon to produce the final mass state.

$$Q^2_{min} = 2EE' - 2|\underline{P}||\underline{P}'| - 2m_\mu^2$$

$$\approx \frac{m_\mu^2 \nu_\mu}{EE'} \quad + \text{ higher order terms}$$

is the minimum value of Q^2 allowed by the kinematics of the interaction.

It should be noted that K is a somewhat arbitrary factor, being constrained only by the condition that $K \to \nu$ as $Q^2 \to 0$, as is required for real photons. It then follows that the definitions of σ_L and σ_T are arbitrary to the extent that they depend on the definition of K.

The principal significance of this formulation is that a connection can be made between real and virtual photoproduction cross-sections. By gauge invariance, as $Q^2 \to 0$, $\sigma_L(\nu) \to 0$ and $\sigma_T(\nu) \to \sigma_{\gamma N}(\nu)$: i.e. σ_T becomes the total photoproduction cross-section for photons of energy ν.

Comparing Equations 1.6 and 1.9 yields the relationships between W_1, W_2, σ_T and σ_L:

$$W_1(Q^2,\nu) = \frac{K}{4\pi^2\alpha}\sigma_T(Q^2,\nu)$$

$$W_2(Q^2,\nu) = \frac{K}{4\pi^2\alpha}\frac{Q^2}{Q^2+\nu^2}\sigma_T(Q^2,\nu)[1 + R(Q^2,\nu)] \qquad 1.10$$

where by definition

$$R(Q^2,\nu) = \frac{\sigma_L(Q^2,\nu)}{\sigma_T(Q^2,\nu)}$$

is the ratio of longitudinal to transverse virtual photon cross-sections.

Frequently, the deep-inelastic cross-section is given in terms of νW_2 and R:

$$\frac{d^2\sigma}{dQ^2 d\nu} = \frac{2\pi\alpha^2}{Q^4} \cdot \frac{1}{|\underline{P}|^2} \cdot \frac{\nu W_2}{\nu} \left[(2EE' - Q^2/2) \right.$$

$$\left. + (Q^2 - 2m_\mu^2)(1 - \nu^2/Q^2) \frac{1}{1 + R} \right]$$

Separation of W_1 and W_2, or equivalently of W_2 and R. is difficult since at low scattering angles, the cross-section has only a weak dependence of W_1 (or R). However, the measurement of a single structure function can be made on the basis of an assumption about the other (or about the value of R). R has been measured in high statistics electron scattering experiments[8] which given an average value of $R = 0.25 \pm 0.10$, the large error being determined by systematics. However, in the experiment described in this thesis, data was taken at three incident beam energies and therefore allowed a measurement of R[9]. The average value of R obtained in the kinematic region where all three data sets overlapped was $R = 0.44 \pm 0.24$. This value of R was used to calculate νW_2. The effect of systematic errors in R was investigated by calculating νW_2 for the range $0.19 < R < 0.69$. Maximum differences of 10-20% were obtained, with average differences of a few percent.

1.3 Historical Review of Deep-Inelastic Scattering

Many reviews of the experimental and theoretical status of deep-inelastic scattering have been presented[8,10]. A brief summary of the main features will be given here.

Electron-nucleon scattering experiments have been carried out since 1955 and at that time were used to investigate nuclear resonances[11]. However, it was not until the prediction of 'scaling' by Bjorken[12] in 1969, and its rapid experimental discovery [13], that the process of deep-inelastic lepton scattering became one of the principal probes of nucleon structure. Using the methods of current algebra, Bjorken predicted that in the limit $Q^2 \to \infty$, $\nu \to \infty$, while the ratio $x = Q^2/2M\nu$ remained fininte, the structure functions νW_2 and $2MW_1$, normally functions of both Q^2 and ν, would become functions only of the dimensionless variable x. Introducing the scaling structure functions F_1 and F_2, this can be expressed as:

$$2MW_1(Q^2,\nu) \xrightarrow[\substack{\nu \to \infty \\ x \text{ finite}}]{\lim Q^2 \to \infty} F_1(x)$$

$$\nu W_2(Q^2,\nu) \xrightarrow[\substack{\nu \to \infty \\ x \text{ finite}}]{\lim Q^2 \to \infty} F_2(x)$$

This behaviour is termed Bjorken scaling and the variable $x = Q^2/2M\nu$ is usually denoted x_{Bj}.

In addition to the scaling behaviour, Bjorken also predicted that the inelastic cross-section would fall off more slowly than $1/Q^{12}$. The behaviour of the inelastic structure functions is therefore very different

from that of the elastic form factors. Recalling, that a point-like cross-section would fall off as $1/Q^4$, this behaviour could certainly be obtained from quasi-point-like scattering.

Closely following the discovery of scaling, Feynman[14] showed that in a constituent model of the nucleon, in which the virtual photon scatters incoherently from point-like particles, exact scaling would be obtained (the 'parton model'). This intuitively attractive model has become the standard framework within which deep-inelastic scattering is described and will be discussed in some detail in the following section.

The subject has progressed rapidly both experimentally and theoretically in the 10 years since the prediction of scaling. Following this prediction, high statistics experiments[15] using the electron beam at the Stanford Linear Accelerator verified scaling at surprisingly low values of Q^2 and ν. Nevertheless, physicists were quite happy with the situation, the parton model became firmly established and the partons became associated with Gell-Mann's quarks.[16]

Experiments were then designed to test the validity of scaling at shorter distances using a high energy muon beam available at the Fermilab accelerator which was then under construction. (The experiment described in this thesis is the third stage of one of these experiments - E98/E398, carried out by a Chicago-Harvard- Illinois-Oxford collaboration.) In 1975, deviations from scaling were observed in muon scattering on an iron target.[5] and were subsequently confirmed by the CHIO collaboration[17], which used hydrogen and deuterium targets. A first guess was that the scaling region of Q^2 and ν had not yet been attained. The scaling variable x' given by

$$x' = \frac{x}{1 + \frac{K^2 x}{Q^2}}$$

gave improved scaling for $W \gtrsim 2.6$ MeV in low energy data,[18] with $K^2 \sim 0.9$ GeV^2. x' asymptotically approaches x in the scaling limit and

appeared to restore scaling in the muon data for $K^2 \sim 1.5$ GeV^2.[19]

Moreover, the ψ meson had just been observed, indicating the existence of a fourth quark. This fourth quark could cause the observed rise of F_2 at low x. However, this violation of scaling could also be predicted in an asymptotically free gauge theory, (Quantum Chromodynamics). Further experiments at higher beam energies were planned and have now been reported[19,20]. Deviations from scaling of the order of 10-20% have been confirmed at low x. The theoretical picture is unclear as to how much of the deviation is due to the (now well-established) charmed quark and how much is due to intrinsic scaling violation in the theory.

To date, few very high energy experiments have identified the hadrons produced in the interaction. In the experiment described in this thesis, such identification was possible in a limited kinematic region. A direct search for charm production via the identification of D-meson decay was also carried out. The results obtained will be discussed in terms of the quark-parton model described in the following section and give information both on the deep-inelastic process and on the quark fragmentation description of hadron production.

1.4 Related Theoretical Topics

Parton Models

Constituent models of the nucleon of the type developed by Feynman and others[14, 21-24] are referred to by the generic name 'parton model'. The basic hypothesis of these models is that at large ν and Q^2, the virtual photon scatters incoherently off point-like, free constituents of the nucleon. These constituents are the 'partons' of the theory and correspond to the bare field particles of the state-function describing the nucleon. The justification that these constituents can be considered as free objects during the interaction (while in the environment of strong nuclear forces) is usually given in the infinite momentum frame of the nucleon. In this frame, the time between parton-parton interactions is slowed down by time dilation until they appear to be non-interacting particles (from the point of view of a non-infinite momentum virtual photon). Incoherent elastic scattering can then occur from a single parton (Fig. 1.3). Free partons however, are not observed among the final state hadrons. Various parton confinement theories[25] have been proposed to deal with this problem. The problem is usually avoided in the parton model by stating that the timescale of parton recombination to form the final state hadrons is much larger than the characteristic time for the interaction ($\sim 1/\sqrt{Q^2}$). Inelastic scattering is then given by the incoherent sum of elastic scattering from all the partons in the nucleon (an impulse approximation). Thus the naive partom model allows the calculation of the structure functions in terms of numbers, charges and momentum distributions of the partons.

An immediate development of the parton model was the association of partons with quarks. The standard framework for the study of deep-inelastic scattering is now the Kuti-Weiskopf[22] quark model where the quarks are treated as partons. In this model, baryons consist of:

3 valence quarks; a core of quark-antiquark pairs (the sea); and gluons (the exchange quanta of the force field between quarks). The three valence quarks are chosen from SU(3) predictions, $q\bar{q}$ pairs and gluons are chosen from a suitable distribution (e.g. using an asymptotically free gauge theory such as Quantum Chromodynamics and symmetry requirements). The development to include charmed quarks is straightforward.

This model provides good agreement with the experimentally observed behaviour of the cross-section.

Firstly, the point-like behaviour of the interaction results in a $1/Q^4$ dependence for the cross-section. Secondly, exact scaling can be derived in this model. Assuming the transverse momentum of partons to be small and finite (the observed $\langle P_\perp^2 \rangle \sim 0.4$ (GeV/c)^2 of the final state hadrons is the basis for this assumption), the momentum of the parton can be expressed as a fraction of the momentum of the nucleon ξP, (in the large but not necessarily infinite momentum frame). Similarly, neglecting the parton mass, the energy of the parton is approximately ξE. These results are clearly more justifiable at large momentum, where masses can be neglected. (The only problem exists when $\xi P \sim$ transverse momentum of the parton and is considered in Ref. 22). ξP scaling is therefore expected - i.e. the cross-section only depends on the scaling variable ξ. The cross-section can then be calculated, and the structure functions extracted,[22] giving for scattering off a single parton of type i:

$$\begin{aligned} \nu W_2(Q^2,\nu) &= e_i^2 \times f_i(x) && \text{for spin 0 and spin } \tfrac{1}{2} \text{ partons} \\ \nu MW_1(Q^2,\nu) &= e_i^2 f_i(x) && \text{for spin } \tfrac{1}{2} \text{ partons} \\ &= 0 && \text{for spin 0 partons} \end{aligned} \qquad 1.11$$

where

$x = Q^2/2M\nu$ is the Bjorken scaling variable

e_i = charge on parton i in units of electron charge

$f_i(x)dx$ = number of partons of type i with momentum between x and x + dx.

Summing over parton types (or flavours) in the proton gives the structure functions:

$$F_2^p(x) = \sum_{i=1}^{n} e_i^2 x f_i(x)$$

$$F_1^p(x) \sum_{i-1}^{n} e_i^2 f_i(x) \qquad 1.12$$

where the sum runs over both quark and anti-quark flavours. For an uncharmed SU(3) quark distribution n = 6 (i.e. u, d, s and antiquarks). Some interesting deductions can be obtained from this result:

Firstly, Equations 1.10 and 1.11 give in the scaling limit

$$R = \frac{\sigma_L}{\sigma_T} = \frac{F_2/x - F_1}{F_1}$$

$= \infty$ for spin 0 partons

$= 0$ for spin ½ partons.

The observed value of $R \sim 0.2$ suggests that the majority of partons are spin ½ (strictly, this conclusion refers to the charged partons).

Secondly, it is necessary to assume that part of the momentum is carried by neutrals. The total momentum carried by the quark flavour i is given by:

$$\eta_i = \int_0^1 x f_i(x)\,dx$$

Considering now the simple case of only the Gell-Mann quark assignment for the proton (uud) and no antiquarks, gives:

$$\int_0^1 f_u^p(x)\,dx = 2$$

$$\int_0^1 f_d^p(x)\,dx = 1$$

In addition to these integral relations, SU(3) symmetry requires $f_u^p(x) = 2f_d^p(x)$ for all $0 < x < 1$. Clearly, to go further, a model is required for $f_u^p(x)$ say - for simplicity take a uniform distribution. It is then straightforward to calculate

$$\int_0^1 F_2^p(x)dx = \tfrac{1}{2}(2e_u + e_d) = \tfrac{1}{2}$$

The measured value of this integral is[9] 0.167 ± 0.006 and this result would show that in this rather unphysical model, over half of the proton's momentum must be carried by neutrals, (the gluons?). An outline of a more reasonable derivation of this result will now be given as in addition it gives a useful introduction to the quark fragmentation scheme. Following the definitions of Feynman,[23] let

$u(x)$ = No. of up quarks with momentum x to x + dx in the proton

$d(x)$ = No. of down quarks with momentum x to x + dx in the proton

$s(x)$ = No. of strange quarks with momentum x to x + dx in the proton

Similarly $\bar{u}(x)$, $\bar{d}(x)$, $\bar{s}(x)$ the numbers of anti-quarks, and neglecting charmed quarks, then charge conservation gives

$$1 = \frac{2}{3}\int_0^1 [u(x) - \bar{u}(x)]dx - \frac{1}{3}\int_0^1 [d(x) - \bar{d}(x)]dx - \frac{1}{3}\int_0^1 [s(x) - \bar{s}(x)]dx$$

The isospin of the proton is $\frac{1}{2}$, giving

$$\frac{1}{2} = \frac{1}{2}\int_0^1 [u(x) - \bar{u}(x)]dx - \frac{1}{2}\int_0^1 [d(x) - \bar{d}(x)]dx$$

The strangeness of the proton is zero, giving:

$$\int_0^1 [s(x) - \bar{s}(x)]dx = 0$$

The solution to these equations is:

$$\int_0^1 [u(x) - \bar{u}(x)]dx = 2$$

$$\int_0^1 [d(x) - \bar{d}(x)]dx = 1$$

$$\int_0^1 [s(x) - \bar{s}(x)]dx = 0$$

i.e. the net number of quarks is given by the simple 3-quark model.

The structure function F_2 can be evaluated in terms of these quark distribution functions (Eqn. 1.12):

$$F_2^p(x) = x[\tfrac{4}{9}(u(x) + \bar{u}(x)) + \tfrac{1}{9}(d(x) + \bar{d}(x)) + \tfrac{1}{9}(s(x) + \bar{s}(x))]$$

giving

$$I^p = \int F_2^p(x)dx = \tfrac{4}{9}U + \tfrac{1}{9}D + \tfrac{1}{9}S \qquad 1.13$$

where

$$U = \int_0^1 x[u(x) + \bar{u}(x)]dx \quad \text{etc.}$$

F_2^n can be obtained in a similar fashion, noting that by isospin reflection, the number of u quarks in the proton is the same as the number of the d quarks in the neutron, giving

$$I^n = \tfrac{1}{9}U + \tfrac{4}{9}D + \tfrac{1}{9}S \qquad 1.14$$

If charmed particle production is important equations 1.13 and 1.14 must be modified by the addition of a term $\frac{4}{9}C$.

Calculation of these integrals in a reasonable model of the quark distribution functions leads to the prediction that some 49% of the momentum is carried by neutrals[26]. These neutrals are associated with the exchange quanta of the quark interaction field - the gluons. A Kuti-Weisskopf type model is thus seen to be a reasonable framework within which to describe deep-inelastic scattering with only one addition, the introduction of a further degree of freedom to maintain Fermi-Dirac statistics - colour.[27]

Quark Fragmentation in the Parton Model[26,28-31]

The general picture of final state hadron production in the parton model is a cascade process (Fig. 1.4): the initial baryon consists of

quarks xya; the struck quark, a, creates a colour field in which a quark-antiquark pair, $b\bar{b}$, are formed; $a\bar{b}$ combine to form a meson and the cascade continues via the quark b until one quark recombines with the remaining quarks from the initial state, completing the description of the interaction. [It should be noted that the fragmentation scheme does not include baryon production - experimentally found to be small.] The principal assumption of the model is that, defining the variable $z = p_z^{hadron}/p^{parton}$, the hadron distributions scale in z. This is referred to as "Feynman scaling'. Quark fragmentation functions can then be defined by $D_\alpha^K(z)dz$ as the number of mesons K in the range z to $z + dz$ produced in the final state from a quark of flavour α. The further assumption of minimal coupling via the charge of the quark allows the final state hadron distributions to be expressed in terms of the quark distribution functions and the fragmentation functions. Conservation of momentum requires that:

$$\sum_K \int_0^1 z D^K(z)\,dz = 1$$

the integral

$$\int_{z_{min}}^1 D_\alpha^h(z)\,dz$$

for this definition gives the mean multiplicity for particles of type h with $z > z_{min}$ resulting from an interaction with quark α.

In investigating hadron production therefore, assuming the quark distribution functions are known, or can be calculated in some model, the problem reduces to obtaining fragmentation functions such as

$$D_u^{\pi^+}(z),\ D_s^{K^+}(z),\ D_d^{\pi^-}(z) \text{ etc}$$

(restricting the discussion to SU(3)).

Charge-conjugation and isospin invariance reduces the number of independent D_q^{π} functions to

$$D_u^{\pi^+}(z) = D_{\bar{d}}^{\pi^-}(z) = D_{\bar{u}}^{\pi^-}(z) = D_d^{\pi^+}(z)$$

$$D_d^{\pi^+}(z) = D_{\bar{u}}^{\pi^-}(z) = D_{\bar{d}}^{\pi^-}(z) = D_u^{\pi^+}(z)$$

$$D_s^{\pi^+}(z) = D_{\bar{s}}^{\pi^-}(z) = D_{\bar{s}}^{\pi^+}(z) = D_s^{\pi^-}(z)$$

Six independent fragmentation functions are required to describe kaon production:

$$D_u^{K^+}(z) = D_{\bar{u}}^{K^-}(z) \quad ; \quad D_u^{K^-}(z) = D_{\bar{u}}^{K^+}(z)$$

$$D_s^{K^+}(z) = D_{\bar{s}}^{K^-}(z) \quad ; \quad D_s^{K^-}(z) = D_{\bar{s}}^{K^+}(z)$$

$$D_d^{K^+}(z) = D_{\bar{d}}^{K^-}(z) \quad ; \quad D_d^{K^-}(z) = D_{\bar{d}}^{K^+}(z)$$

At this stage it is necessary to build a model and calculate the hadron distributions either analytically or using Monte-Carlo methods, e.g. the number of positive pions produced in scattering from a proton target which is described by a a quark distribution.

$$P(x) = u(x) + \bar{u}(x) + d(x) + \bar{d}(x) + s(x) + \bar{s}(x)$$

is given by (omitting explicit x dependence)

$$\pi^{+ve}(x) = \int_{z_{min}}^{1} uD_u^{\pi^+}(z) + \bar{u}D_{\bar{u}}^{\pi^+}(z) + dD_d^{\pi^+}(z) + \bar{d}D_{\bar{d}}^{\pi^+}(z) + sD_s^{\pi^+}(z) + \bar{s}D_{\bar{s}}^{\pi^+}(z) \quad dz$$

These integrations have been carried out by several authors[26,28-31] using models to describe the fragmentation functions. The particle ratios $\frac{K^+(z)}{\pi^-(z)}$, $\frac{K^+(z)}{\pi^-(z)}$ etc. obtained from these calculations can then be compared with the experimental values.

Vector Meson Dominance

An alternative description of deep-inelastic scattering considers first that the virtual photon 'turns into' a neutral vector meson which then interacts via the strong interaction with the proton (Fig. 1.5). In its early stages of development the model only considered the well known vector mesons (ρ, ϕ, ω and more recently ψ, ψ'). However, to accommodate the observed scaling in deep-inelastic scattering required generalisation to a spectrum of vector meson states - G.V.M.D.[32] The model has some predictive success but the required spectrum of vector mesons has not been observed. In addition to this major disagreement with experimental evidence, the model also has the disadvantage that it replaces a known interaction, γp, with an unknown strong interaction, Vp.

Asymptotic Freedom

A discussion of the theory of deep-inelastic scattering would not be complete without at least a brief mention of asymptotically free gauge theories. These relate scaling to the behaviour of an underlying field theory through the techniques of the renormalisation group and the operator product expansion[33]. It was found that Yang-Mills gauge theories have the property of asymptotic freedom. This statement refers to the fact that in such theories the effective coupling constant is dependent on distance and goes to zero as momenta become large. The theory is called Quantum Chromodynamics[34] if the gauge group chosen is SU(3) (3 colours, and as many flavours as necessary up to the renormalisation limit of 16). Asymptotic freedom thus forms the basis for the parton model, justifying the impulse approximation at large momenta. Deviations from scaling behaviour can be calculated in this model.

This theory does not yet provide a complete description. Free quarks have never been observed - one unsolved problem is to devise a theory which accounts naturally for this confinement.[24]

TABLE 1.1

DEFINITION OF VARIABLES

m_μ	= mass of muon
M	= mass of proton
$P_1 = (E, \underline{P})$	four momentum of incident muon
$P_2 = (E', \underline{P}')$	four momentum of scattered muon
$q = P_1 - P_2$	four momentum transfer from
$= (\nu, \underline{q})$	muon to proton
$P_3 = (M, \underline{0})$	four momentum of incident proton
$Q^2 = -q^i q_i$	(invariant mass^2) of virtual photon
$= 2EE' - 2\lvert\underline{P}\rvert\lvert\underline{P}'\rvert\cos\theta - 2\, m_\mu^2 \approx 4\, EE'\sin^2\theta/2$	
$= 2M\nu$	for elastic scattering
$\nu = (P_2 \cdot q)/M$	laboratory energy of virtual photon
$\theta =$	muon scattering angle in laboratory
$\alpha =$	fine structure constant.
$s = 2ME + M^2 + m_\mu^2$	Total energy)
$W^2 = 2M\nu + M^2 - Q^2$	Invariant mass of final hadronic system
$\lambda(x, q, z) = x^2 + y^2 + z^2 - 2xy - 2xz - 2yz$	
$x_{Bj} = Q^2/2M\nu$	Bjorken Scaling Variable

First Order Elastic Scattering

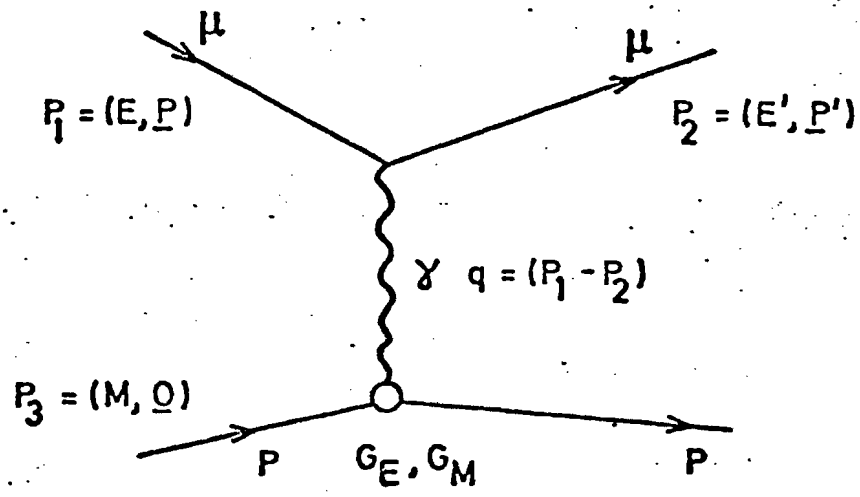

Fig. 1.1a

Possible Second Order Corrections to Elastic Scattering

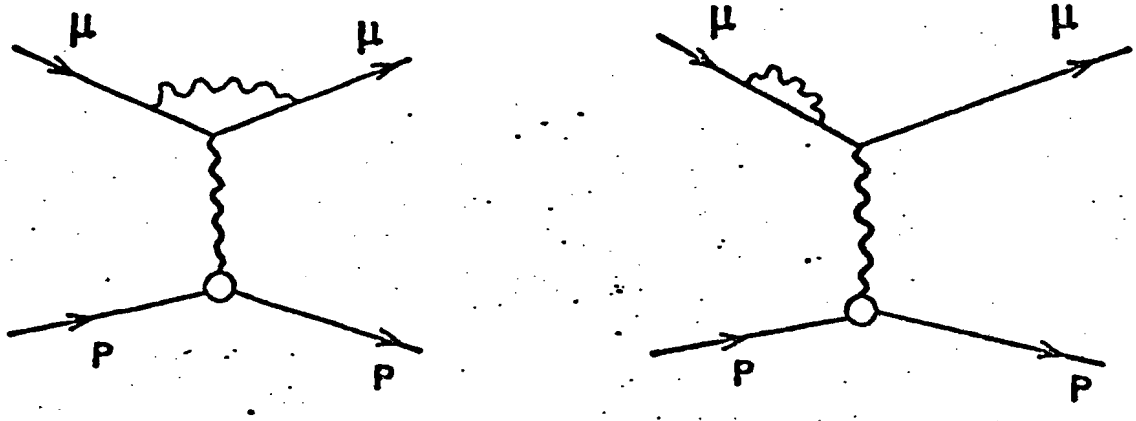

Fig. 1.1b

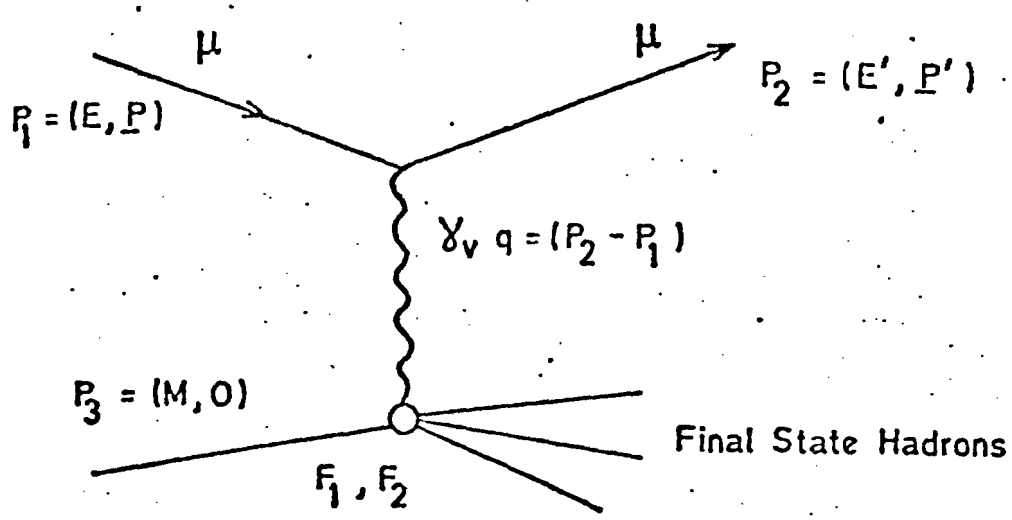

Fig. 1-2

Parton Model Description of Deep-Inelastic Scattering

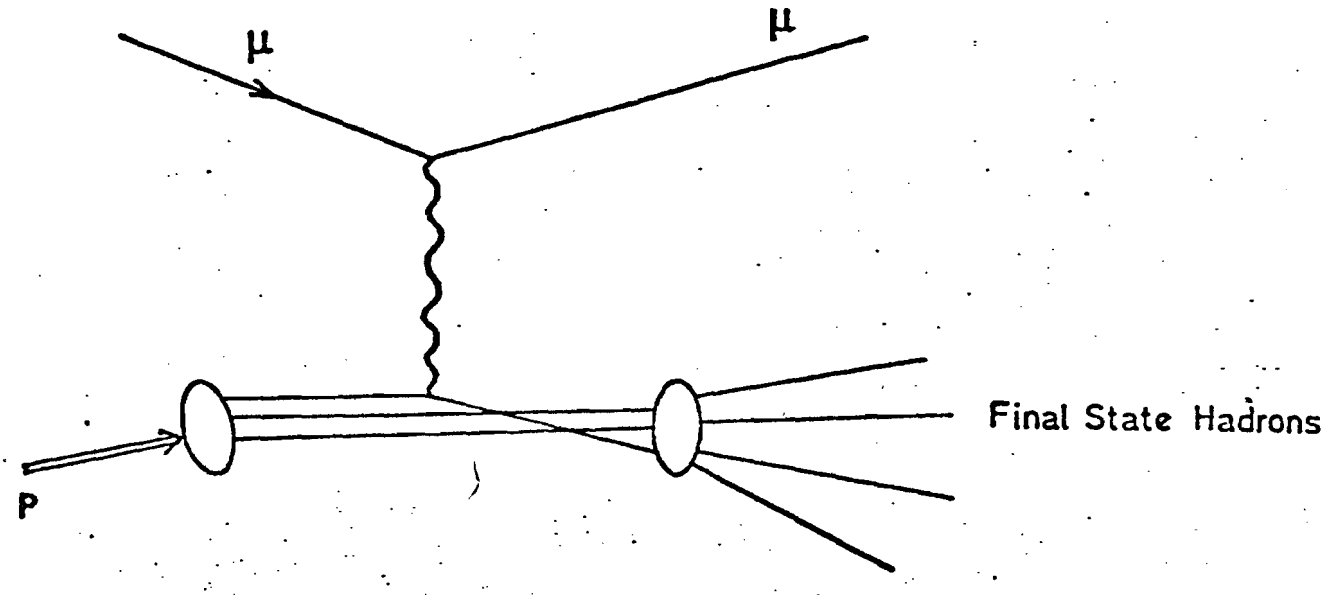

Fig. 1-3

Quark Fragmentation

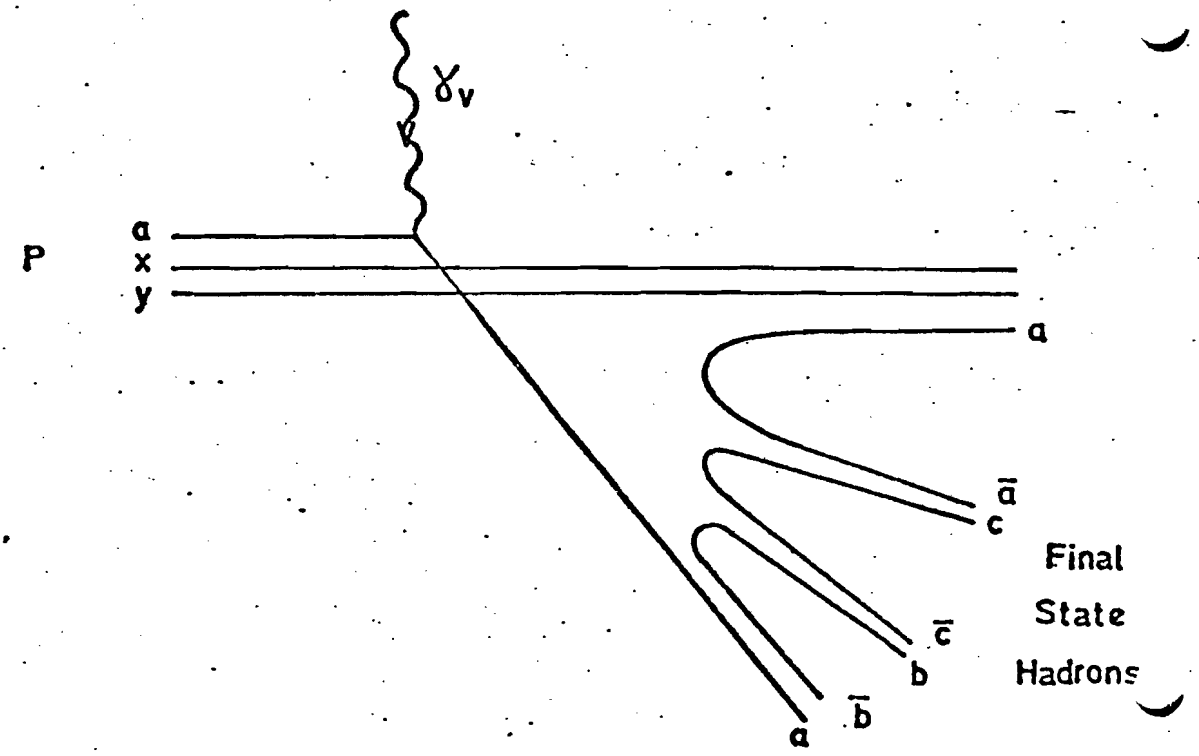

Fig. 1.4

Vector Meson Dominance

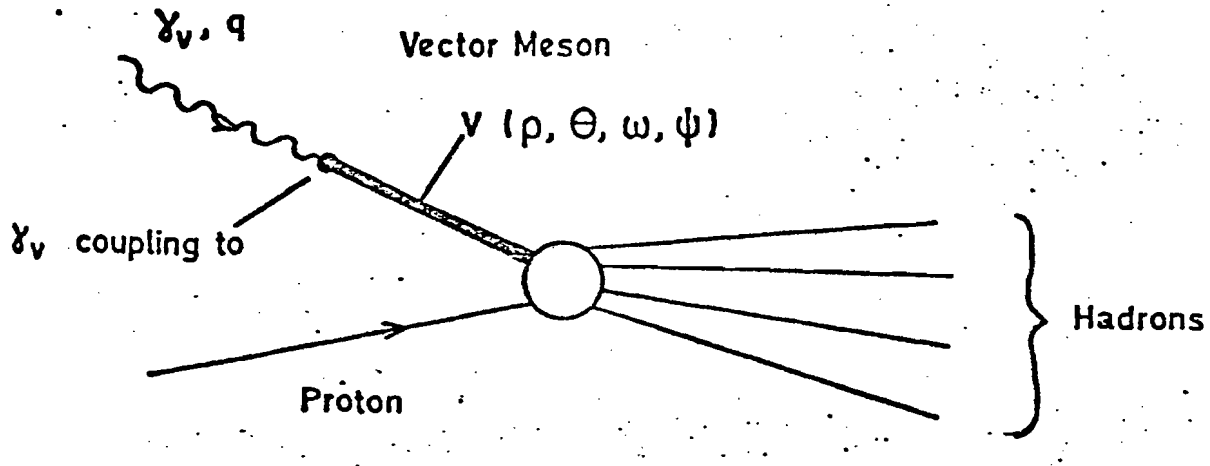

Fig. 1.5

CHAPTER 2

THE APPARATUS

2.1 INTRODUCTION

The data analysed in this thesis was taken in the third stage of an experiment on muon scattering which was carried out over several years by a Chicago-Harvard-Illinois-Oxford collaboration using the muon facility at Fermilab. The aim of this experiment was both to measure the differential cross-section $\frac{d^2\sigma}{d\nu dQ^2}$ at different beam energies (and thereby the proton structure functions F_1 and F_2) and also to study the hadrons produced in the interaction.

The beam energy used for this final run was 219 GeV/c^2, the highest available at the accelerator consistent with a reasonable muon flux. The same basic equipment was used as for the previous runs at 98 and 149 GeV/c^2. However, the addition of a large multicell Cerenkov counter and additional proportional chambers downstream of the target greatly improved the ability to study the hadrons produced in the interaction with which this thesis is concerned. The apparatus can be split logically into three elements: the beam transport system; the beam defining elements; the analysing spectrometer. These will be discussed in some detail in the following sections.

2.2 MUON BEAM TRANSPORT

The Beam Line

The muon beam is produced by the decay in flight of secondary pions and kaons produced in high energy proton nucleon collisions. Therefore, the aim of the beam transport system is to collect these secondaries, allow as many to decay as possible, remove all unwanted particles (hadrons and muons with the wrong momentum or charge) and then transport the final muon beam to the experimental area.

A schematic of the Fermilab muon line is shown in Fig. 2.1. A 400 GeV proton beam extracted from the main ring is transported over a kilometre to a production target of 30 cm of aluminium (one interaction length). Secondary pions and kaons produced at small angles ($\sim$2 mrad) are strongly focussed by a quadrupole triplet onto a 500 m evacuated decay pipe. There are no further elements to contain the beam until the end of the decay pipe. Then follow two bending stations separated by a quadrupole focussing station to deflect the charged beam from the neutrino beam and focus it onto the hadron absorber, allowing a further 400 m of decay path. These elements also provide momentum selection, the momentum band of the beam being reduced to $\sim$1%. Of the secondaries, 95% of the pions and 90% of the kaons do not decay, and these plus any other hadrons are removed by an absorber packed into the third stage of bending magnets (D3). The absorber consisted of 21.3 m of high densith polyethylene which reduced the contamination, giving a π/μ ratio of 2×10^{-6}. The final set of Q quadrupoles (Q4) then focusses the muon beam onto the experimental target. Momentum selection is made at the last bending station (D4). The muon beam had a momentum spread of $\pm$3% and an angular divergence of $\sim$1 mrad. The cross-sectional area was approximately 100 cm^2.

Intensity

$\pi \rightarrow \mu\nu$ decay produces muons with a uniform laboratory energy spectrum from $\sim E_\pi$ to $0.57\ E_\pi$. A maximum muon flux is obtained by selecting a pion momentum slightly higher than the muon momentum required as this allows pions to decay right up to the absorber. A maximum flux of secondary pions and kaons of approximately the required momentum is therefore required. This is obtained by selecting a pion/kaon momentum which is roughly half the primary proton momentum.

In this experiment the primary proton momentum was 400 GeV/c and the muon beam-line magnets were set to pass 220 GeV/c particles within a band of 1%. A μ/p ratio of approximately 10^{-7} was obtained resulting in 10^6 muons per beam pulse.

This procedure produces a polarised muon beam, its spin being oppositely aligned to its momentum vector. As yet, this polarisation has not been used in deep-inelastic scattering at the highest energies.

Halo

A major problem in the design of a muon beam is that unlike hadron or electron beams, particles which leave the beam can travel large distances before being absorbed. These particles are called 'halo'.

The beam-line optics are not completely matched and therefore despite earth shielding along the length of the beam-line, muons leaving the beam in the upstream elements result in halo over a large area of the experimental hall. In addition, muons scraping the beam-line magnets but not quite leaving the system give rise to close-in halo around the beam. For this data, the ratio of halo to beam varied from 2-5 with most of this halo within 50 cm of the beam.

The trigger requirements necessary to minimise the effects of halo are discussed in Chapter 3. However, the halo was extremely useful in the setup stage of the experiment when it was used to plateau all counter hodoscopes in situ.

Pion Contamination

A measurement of the pion contamination was not carried out at this energy. However, this can be estimated from data obtained with a 150 GeV/c beam[35]. The absorption length at 220 GeV/c is estimated to be 1.6 m. 21.3 m of absorber were used giving a π/μ ratio of 2.3×10^{-6}.

R.F. Structure

In a proton synchro-cyclotron, the radio-frequency cavities used to accelerate the beam tend to bunch protons around the accelerator ring. At Fermilab, bunches are 2 nsec long and are separated by 18 nsec. The structure of the tertiary muon beam reflects this frequency with muons arriving in 2 nsec 'buckets' and separated by a minimum of 18 nsec. As a 2 sec. spill-length was used, there is only a small probability of more than one muon in any r.f. bucket ($\sim$1%). Uneven and spiky beam spill can increase this however.

2.3 BEAM DEFINITION AND MOMENTUM MEASUREMENT

Beam Definition

The beam defined for the experiment is selected at the final dipoles in the beam-line D4 (Fig. 2.1). These dipoles provide the momentum measurement of the incident beam and the purpose of the defining elements is to restrict the beam to those particles which pass cleanly through them. This definition is carried out by a sequence of counters in coincidence and anti-coincidence to form an electronic collimator (Fig. 2.2).

Counters V1, V2, V3 match the apertures of the last two bending magnets (10 cm x 9 cm) and are used to veto scraping beam. BH1-BH6 are each 8 element scintillation counter hodoscopes. BH1 consists of 1.2 cm scintillator covering an area 20 cm x 20 cm. The remaining five hodoscopes are 15 cm x 15 cm in area and use 0.6 cm scintillator. BH1, 2, 3, 5 are arranged in vertical strips to provide x readout. BH4 and 6 provide y readout (Fig. 2.3). The beam is defined by a coincidence between one element in BH1 and BH2, one element in either BH3 or BH4 and one in either BH5 or BH6. Counters V1-3 are required in anticoincidence with this signal to veto scraping beam, and the halo veto wall is also required in anticoincidence to remove halo. The beam hodoscopes were also latched for use in beam reconstruction.

Beam Momentum Measurement

A measurement of accurate knowledge of the beam particle's trajectory through the bending plane of the analysing magnet system. This is carried out using the beam hodoscopes BH1-6 used in the beam definition and 6 multiwire proportional chambers. The MWPCs are 20 cm x 20 cm in area, with a wire spacing of 2.0 mm. Those with

vertical readout wires are described as X chambers and those with horizontal wires as Y chambers. The beam hodoscope information corresponds to the beam chamber information at each beam station. Stations 1 and 2 have an X hodoscope and chamber pair, stations 3 and 4 have both X and Y hodoscope and chamber pairs. As the bending takes place in the X-Z plane, all four stations can be used to reconstruct the momentum of the beam particle, with the xy points at stations 3 and 4 providing the momentum vector of the incident beam into the laboratory. The beam hodoscopes were all positioned downstream of their corresponding chambers to prevent the chambers from seeing any knock-on electrons which might cause track confusion.

2.4 THE SPECTROMETER

This section briefly discusses the various components of the spectrometer. In part they have been described in much greater detail elsewhere and the appropriate references are given. A diagram of the spectrometer apparatus used in this analysis is shown in Fig. 2.4.

Coordinate System

This is an appropriate place to define the experimental coordinate system. The centre of the momentum analysing magnet (the Chicago Cyclotron Magnet) is taken as the origin. The nominal beam direction defines the positive z-axis, the horizontal beam left direction the x-axis, and the vertical direction in a right-handed sense the y-axis.

Target

The target flask is positioned approximately 6 m upstream of the Chicago Cyclotron Magnet. It is 18 cm in diameter and 120 cm long. Filled with liquid hydrogen this corresponds to an approximate target thickness of 8.3 gm/cm^2, with the target flask material representing only 0.4 gm/cm^2. The flask was designed so that it could be emptied and filled quickly to enable target-full and target-empty running to be evenly distributed through the data set.

Halo Veto Wall

The halo veto wall stands immediately upstream of the target, covering the entire area of the halo veto which is mounted on its upstream side. Consisting of 1 m thick concrete blocks with a hole to allow the beam through, its function is to prevent any backscattered particles from a real event hitting the halo veto and thus vetoing

1m x 1m Multiwire Proportional Chambers

A bank of 8 1m x 1m MWPCs[36] with 1.5 mm wire spacing are arranged with alternately X and Y readout immediately downstream of the target flask. An additional pair with X and Y readout are positioned near the centre of the Chicago Cyclotron Magnet. Their wire spacing provides a spatial resolution of 0.5 mm r.m.s. and their gate pulse of typically 120 nsec sets their timing resolution. They detect all forward going charged particles from an interaction in the target. In this respect their time resolution is important as there is a large flux of beam and close-in halo through the central region which might otherwise cause serious confusion.

The Chicago Cyclotron Magnet

The momentum analysing magnet for the spectrometer is the former Chicago Cyclotron Magnet. It is a large volume magnet with a pole tip radius of 2.2 m and an aperture of 1.25 m. The magnet can produce a maximum field of 1.5 Tesla, drawing a current of 5000 Amp at 400 volts. However, for this data the field used was 1.4 Tesla corresponding to a current of 4200 Amps (Fig. 2.5). The magnetic field has cyclindrical symmetry and has been mapped to determine its uniformith and fringe field.[37] The field map was accurate to ±4 Gauss. and the field is stable over periods of running to within 0.2%. The field polarity was set to bend positive particles towards negative x. Acceptance of charged hadrons by the downstream spectrometer is determined by the momentum cut-off of the C.C.M. At 1.4 Tesla this is 6 GeV/c.

Illinois MWPCs

For this run, five additional proportional chambers were positioned between the last two 1 m chambers to improve the low momentum particle acceptance. Each chamber had two readout planes and had an area 80 cm x 80 cm. The wire spacing was 3.2 mm. The planes were arranged in an XYXYUVU'V'XY pattern. The tilted planes were XY planes tilted at an angle $\theta(= \tan^{-1}\frac{1}{8})$ and $-\theta$ between the x-u and x-u' axes respectively, and were required to resolve xy ambiguities in trackfinding. These planes were used primarily for a low momentum analysis of strange particle production.[38]

The Downstream Spark Chambers

Immediately downstream of the C.C.M. is a bank of twelve 2m x 4m spark chambers with 1 mm wire spacing.[36,39] As they were required to operate in a large fringe field (~0.5 Kgauss) these planes used shift register readout. At approximately 9 m downstream of the magnet and downstream of the Cerenkov counter there is a further bank of eight 2m x 6m spark chambers.[35] These planes also had 1 mm wire spacing and used capacitive readout. The downstream trackfinding was carried out in these 20 planes to obtain the space tracks of particles passing through the C.C.M. However, the y track projection could not be obtained directly as the extent of these chambers prohibited the stringing of horizontal wires with this spacing. In both banks there are UX, VX and UV planes with wires strung at $\theta = \tan^{-1}\frac{1}{8}$ and $-\theta$ to the vertical and these are used to obtain the y projection. The 2m x 4m planes had a live time of 1 μsec and the 2m x 6m planes a live time of 3 μsec. This results in them 'seeing' many stale halo and beam tracks which then add to the trackfinding confusion. The 2m x 6m planes had a mylar deadener in the beam region to overcome this problem.

The Cerenkov Counter

There is an 18 cell nitrogen filled Cerenkov counter between the 4 m and 6 m chambers. Each cell mirror is 60 cm x 100 cm and they are mounted in two banks of 9 mirrors above and below the median plane of the apparatus. The overall size of the counter is 2.6 m deep by 2.5 m high by 6 m broad. The counter plays an essential part in this analysis and is discussed in detail in Chapter 5.

Muon Identification

Muon identification in the spectrometer is provided by a hadron absorber consisting of an iron wall approximately 3m x 6m by 2.5 m deep. This is positioned roughly 20 m downstream of the spectrometer magnet. Immediately behind the absorber is an array of hodoscopes and veto counters used in the trigger. Beyond this array there is a bank of four 2m x 4m spark chambers,[35] each with two readout planes. These planes use magnetostrictive-wand readout and are constructed in a similar fashion to the 6m chambers to obtain space reconstruction of tracks.

Muons are identified by their ability to penetrate the hadron absorber and set the counters behind. The pion punch-through probability is extremely low (10^{-5}/pion). Multiple coulomb scattering causes the only identification problem as it can deflect the muon by up to 40 cm at low momentum.

Additional Particle Identification

Between the final six metre plane and the hadron absorber there is a system of filters and chambers designed to obtain some identification of e, γ, π^0 and neutral hadrons. This consists of initially a 4 cm (3 r.l.) steel plate followed by a bank of spark

chambers. Through spark counting in these planes one would observe electron cascades from electron bremsstrahlung and γ conversion in the steel plate. Immediately downstream of this bank of chambers is a 0.3 m thick lead wall to stop the electromagnetic element in the shower. Development of neutron induced hadronic cascades can then be observed in a second bank of spark chambers. In practise, this system failed as the spark chambers were inefficient and unreliable - no attempt has been made to obtain any information from them in this analysis.

The Trigger Hodoscopes

The apparatus is triggered and read out when a particle is seen to leave the beam and is observed downstream of the hadron absorber. The downstream signal for this is obtained by 4 banks of scintillation counter hodoscopes, and one array of beam veto counters. Figures 2.6-2.11 show the counter arrangement in these banks, labelled: G, H and H', M and N, M', and K (the veto).

The arrays G, H and H' form a crossed counter array immediately downstream of the final 6m plane and before the steel wall. Four of the G counters are displaced to form a hole in the beam region and two of the H counters have a section of scintillator in this region replaced by lucite. The H' array surrounds this hole and can be moved laterally or vertically to change its size.

The arrays M, N, M' form a second crossed array of counters downstream of the hadron absorber. Again counters in the beam region in banks M and M' are displaced. The N counter is on a trolley which can be moved laterally to cover this hole. By moving the N and by removing appropriate elements of it from the trigger, the composite M hole can be made to match the beam veto.

The beam veto is the K hodoscope, which is also on a trolley to enable it to be moved laterally. This freedom is necessary as it was necessary to determine its final position experimentally (Chapter 3). Air light guides were used on this hodoscope as Cerenkov radiation in the lucite of the alternative would give rise to unwanted vetos. The phototubes used were RCA 8575 which give a fast rise time. The pulse was shaped to minimise deadtime.

Further details of the operation of these hodoscopes and their use in the experimental trigger are given in Chapter 3.

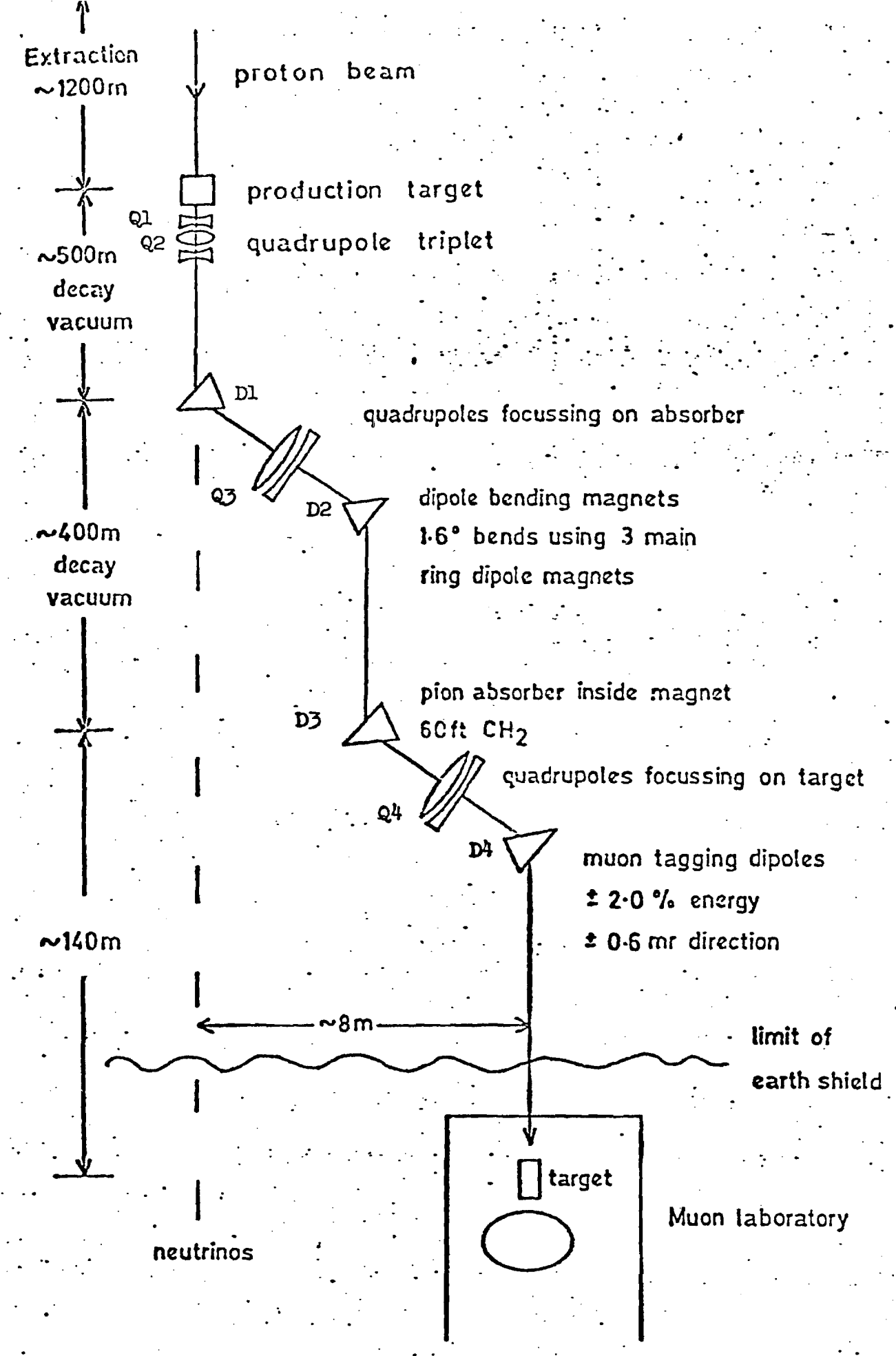

BEAM TRANSPORT.

Not to scale

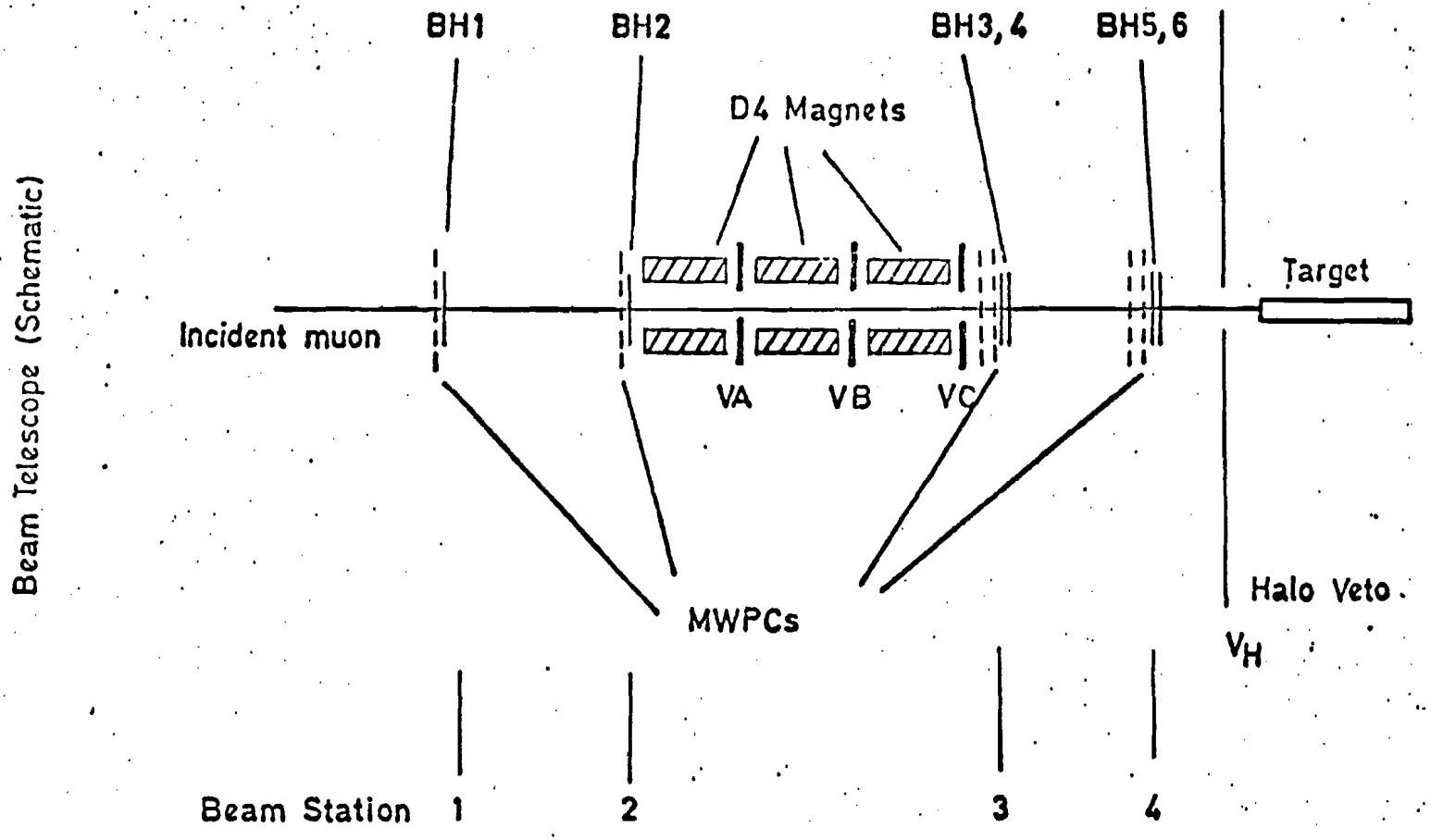
Beam Telescope (Schematic)
BH1
BH2
BH3,4
BH5,6
D4 Magnets
Target
Incident muon
VA
VB
VC
MWPCs
Halo Veto
V_H
Beam Station
1
2
3
4

Fig. 2.2

Hodoscope Readout

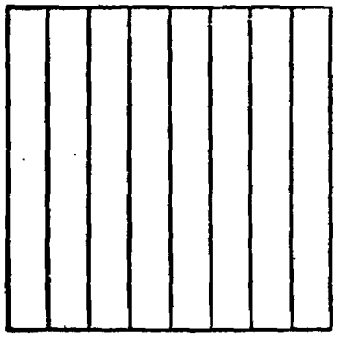

BH1, 2, 3, 5

Vertical Elements

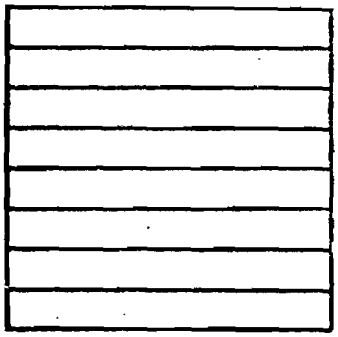

BH4, 6

Horizontal Elements

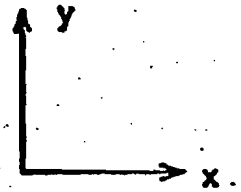

Fig. 2-3

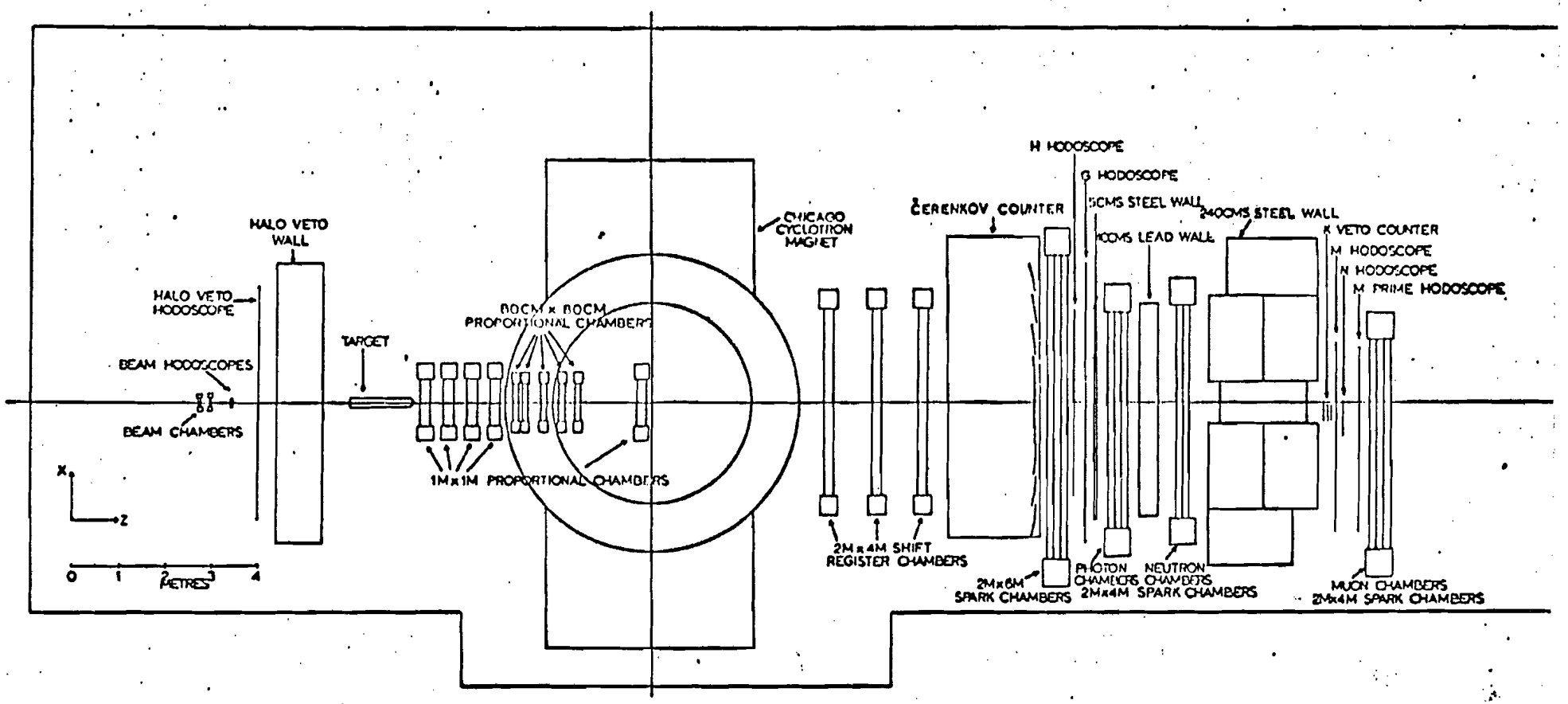

The Spectrometer

Fig. 2.4

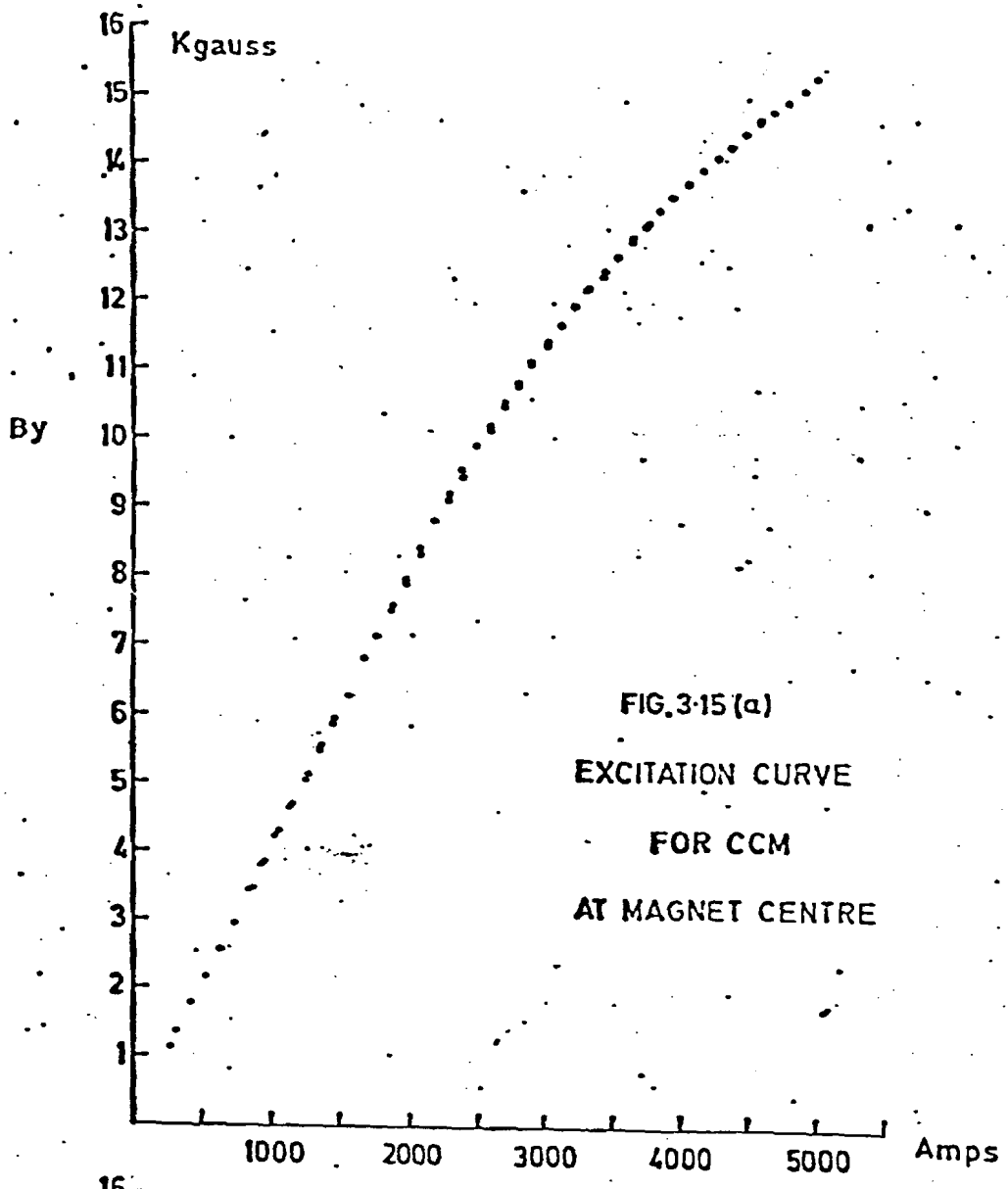

FIG. 3·15 (a)

EXCITATION CURVE

FOR CCM

AT MAGNET CENTRE

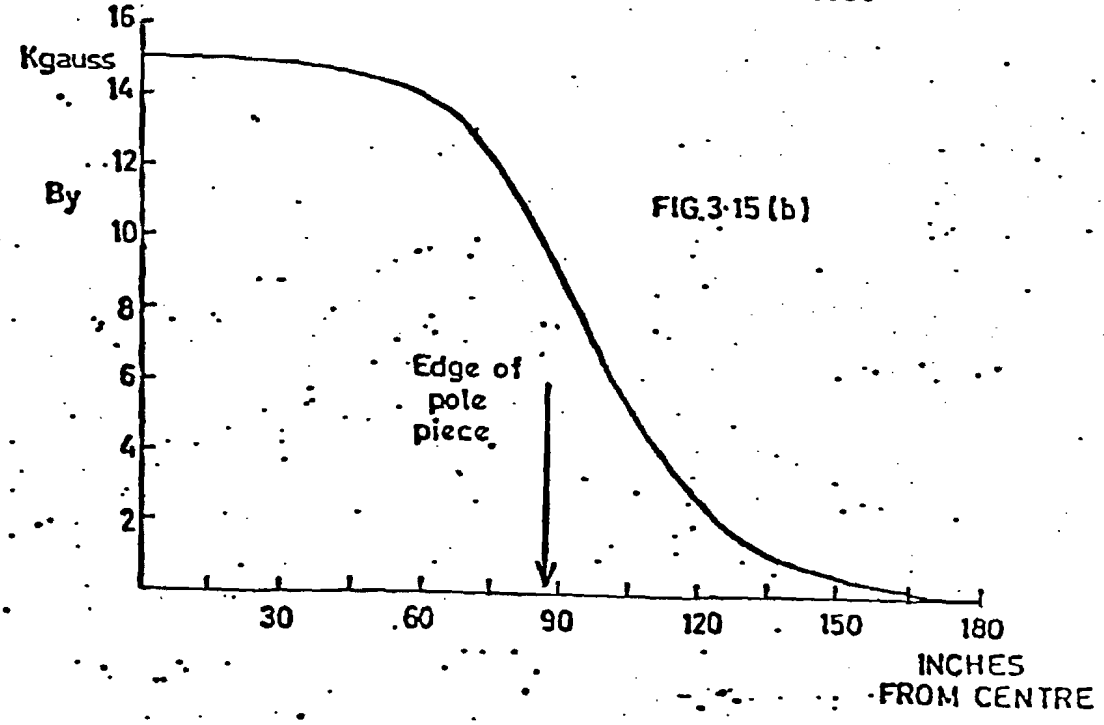

FIG. 3·15 (b)

By ALONG CENTRAL PLANE.

Fig. 2.5

Fig. 2.6

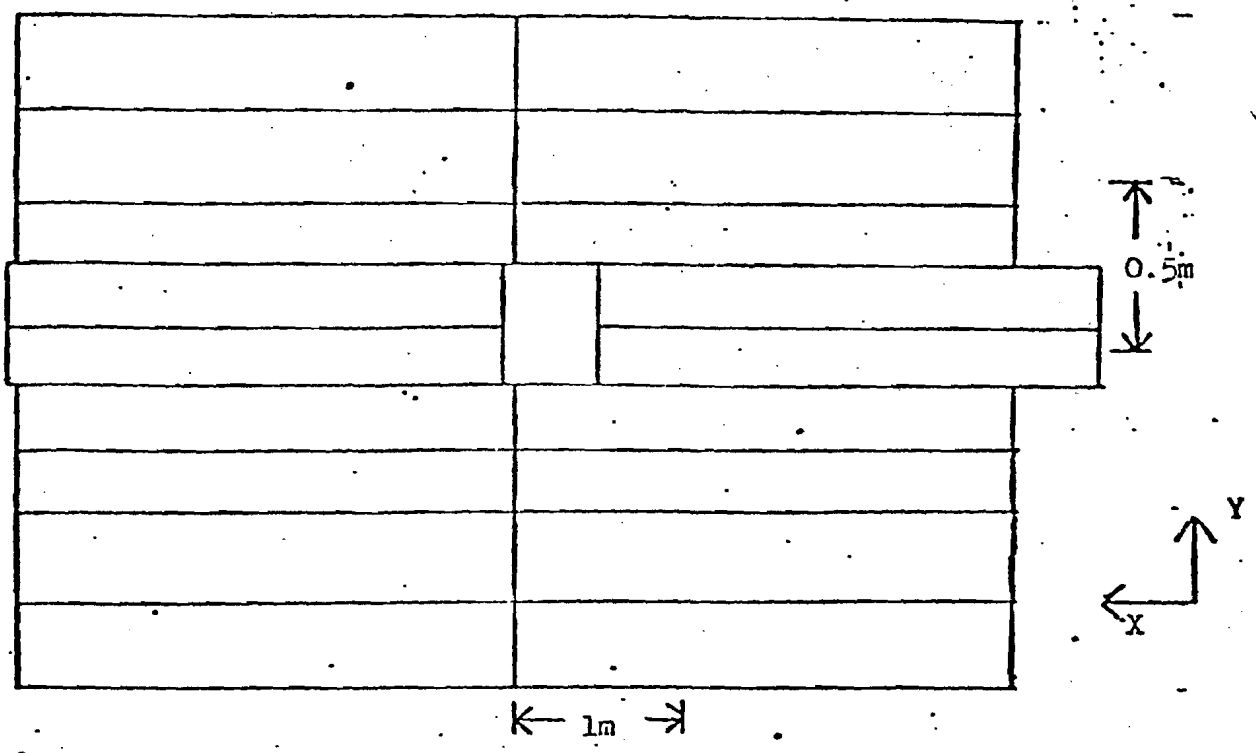

The G hodoscope

Fig. 2.7

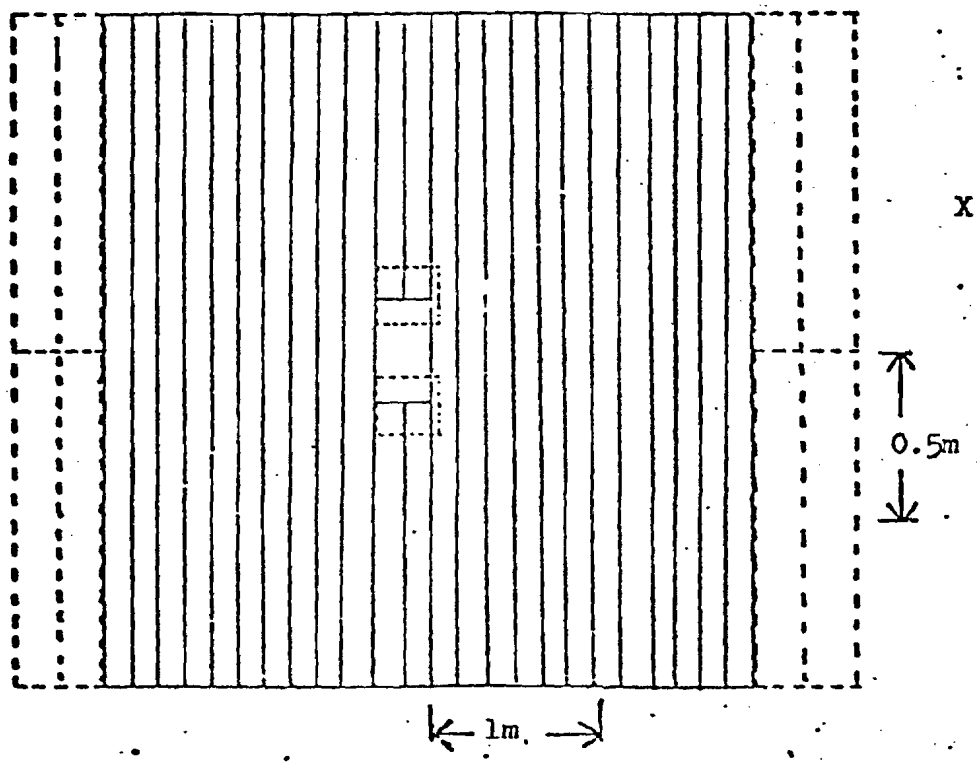

The H (solid lines) and H' (dotted lines) hodoscopes.

Fig. 2.8

The M hodoscope

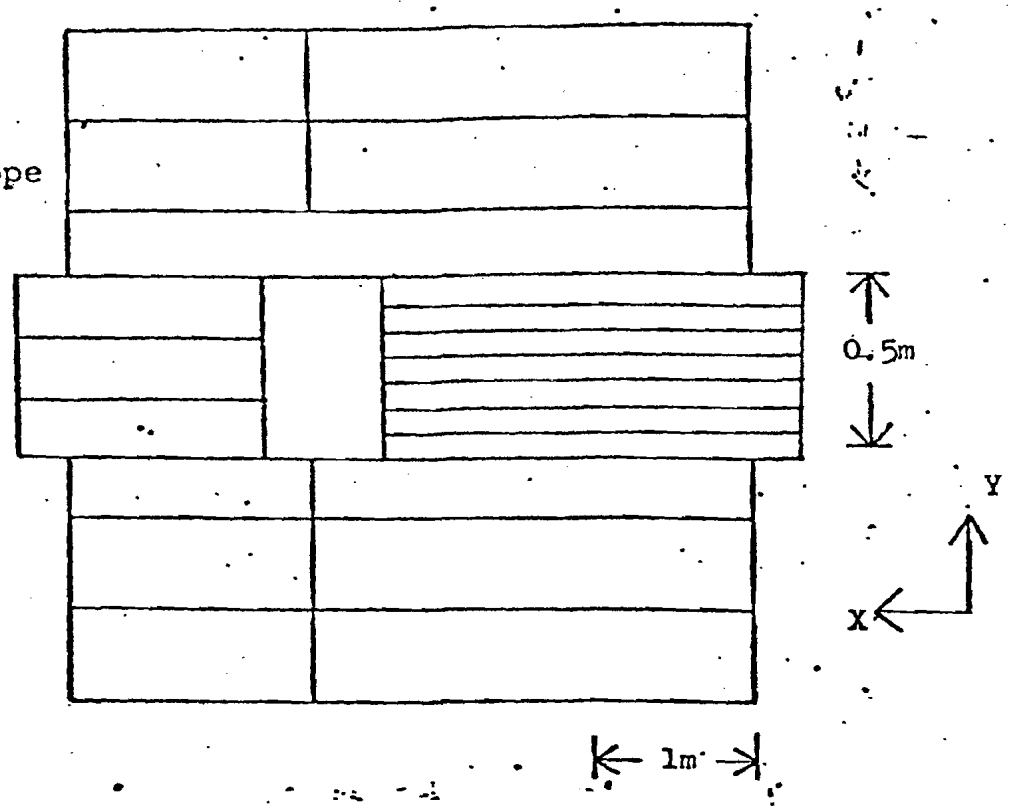

Fig. 2.9

The M' hodoscope

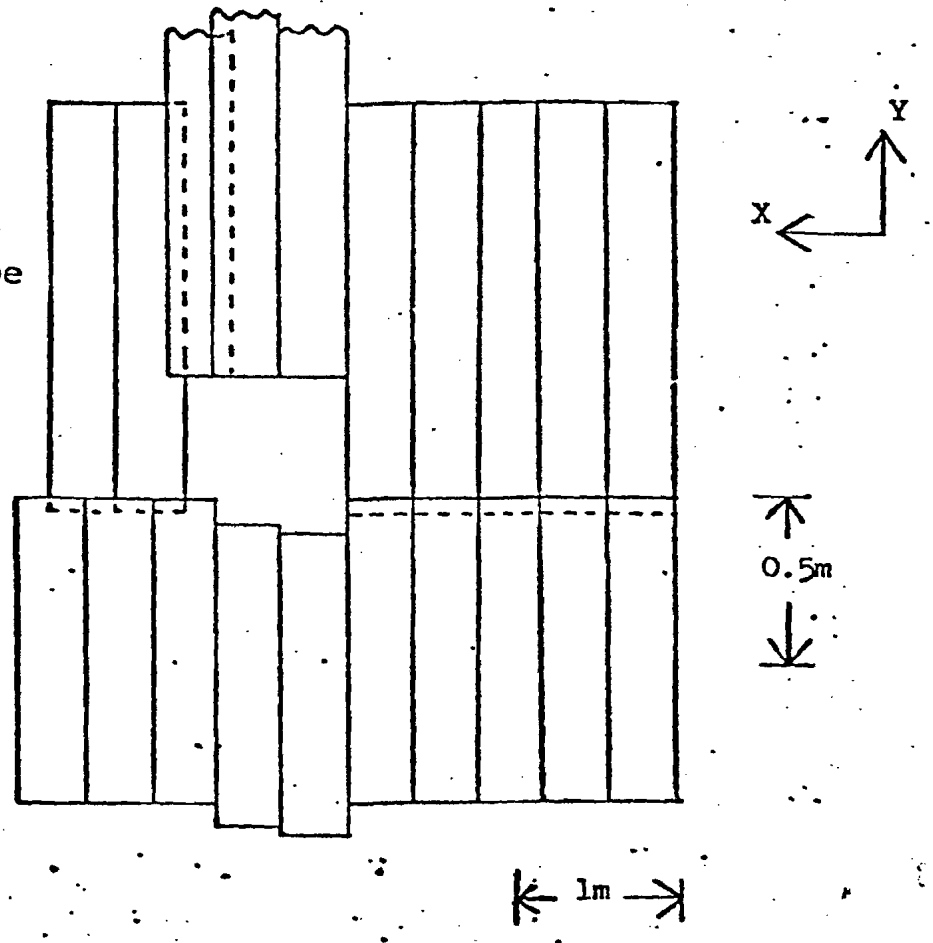

Fig. 2.10

The N Hodoscope

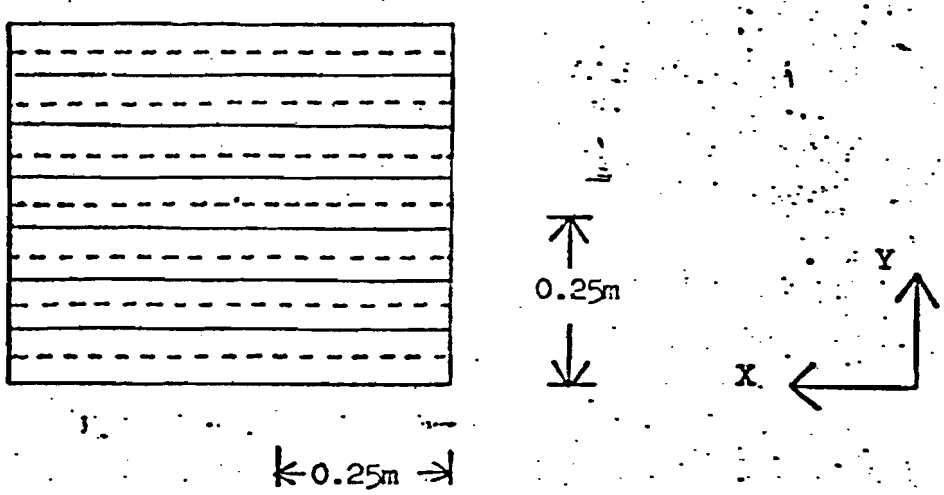

Fig. 2.11

The K Hodoscope

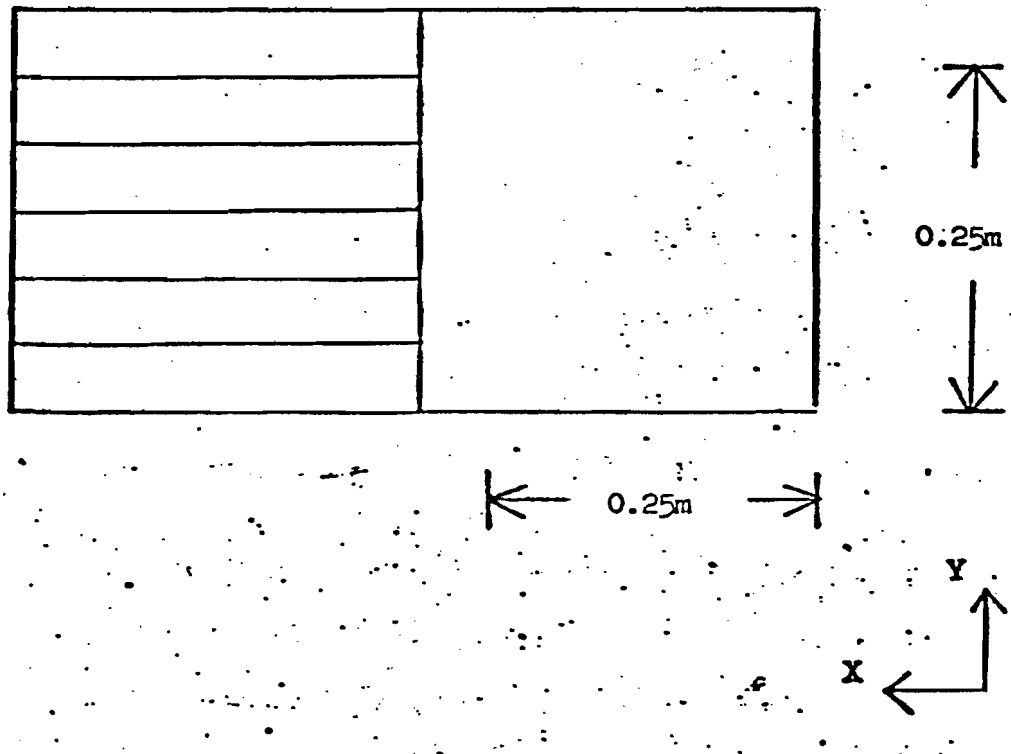

CHAPTER 3

DATA TAKING

3.1 INTRODUCTION

The principal advantage of an electronic particle-detection system is that one can trigger the system only when an event of interest has occurred, thereby greatly reducing experimental dead-time and the amount of data processing required. The signal that an event has occurred is usually obtained from some scintillation counter system which produces fast light pulses following the passage of charged particles through it. These pulses can be detected by photomultipliers which then provide output pulses which can be detected electronically. Fast electronic logics circuits can then be used to trigger the rest of the apparatus: chamber firing, latching and data-readout etc.

The experiment described in this thesis was designed to investigate inclusive and semi-inclusive muon scattering and the trigger used was quite straightforward. The only requirement was to detect a beam muon which scattered in the target. Muons were identified by their ability to pass through 2.4 m of iron absorber (Fig. 2.4). Details of the trigger hodoscopes, their function and the logic used is described in Sections 3.2 and 3.3. The data readout sequence is briefly described in Section 3.4 and details of on-line checks and equipment checks carried out during data taking are described in Section 3.5.

3.2 THE TRIGGER

The positions of the downstream elements of the trigger are shown in Fig. 2.4. A schematic of the complete trigger system is shown in Fig. 3.1. The timing resolution of the system is determined by the lengths of the various hodoscope elements. Thus the incident beam resolution is ~5 ns and the scattered muon resolution 20-30 ns. The minimum resolving time is therefore approximately 30 ns. The detailed discussion of the trigger is given in terms of its two logical sections: the definition of a good incident muon; the detection of a scattered muon.

Beam Signal

A provisional beam signal is defined by the logic:

$$T = BH1.BH2.(BH3 \text{ or } 4).(BH5 \text{ or } 6)$$

where BH1 represents any element in the hodoscope BH1 being set etc. Four sets of vetos were applied to this coincidence signal to provide the 'good beam' signal:

(a) $\overline{VA}.\overline{VB}.\overline{VC}$

(b) $\overline{V}_H$

(c) $\overline{BH2 > 1}.\overline{BH3 > 1}.\overline{BH4 > 1}.\overline{BH5 > 1}.\overline{BH6 > 1}$

$$\equiv \overline{BH > 1}$$

(d) $\bar{B}_{\Delta t}$

(a) VA, VB, VC - These are three pairs of counters which match the entrance and exit apertures of the three dipole magnets comprising D4 (the beam momentum analysing magnet) (Fig. 3.1, 3.2). Used in veto they ensure that all beam particles pass cleanly through this magnet and therefore allow an accurate determination of their momenta

(b) V_H - Mounted upstream of the experimental target there was a hodoscope consisting of an 18 element hodoscope array covering 3m x 5m with a large hole in the beam region and 4 small counters which accurately defined the beam hole (Fig. 3.3). The hodoscope matches the muon hodoscopes in the trigger and was used to veto halo. Wide angle halo is removed by the main hodoscope area. Close-in halo and marginal beam is removed by the four small counters (the veto 'jaws'). These also restricted the beam spot to an area completeley within the target. A halo muon will satisfy the downstream requirements of the trigger and only requires to be in coincidence with a beam particle which fails to set the K-veto in order to trigger the apparatus. This coincidence can occur most likely either as a result of inefficiency in the K-veto or of a real scatter in the iron absorber, (coincidence with a real event trigger is improbable). The rate $\frac{B.\bar{K}}{B}$ was typically 2×10^{-4}. The ratio of beam to halo was large, being about 1 to 3. Therefore, even assuming 99% efficiency in the halo veto, a trigger rate of 3×10^{-6} is obtained from 'halo' triggers. Clearly, a highly efficient veto was essential.

(c) BH > 1 - This signal was used to detect and veto events in which two muons passed through the apparatus within the 5 ns resolution of the beam counters. In such an event, if one of these muons were to interact in the target the second would still veto a trigger by setting the K-veto. Assuming a uniform spill structure, the probability of two muons arriving in the same r.f. bucket was approximately 1%. However, spikes in extraction (as was the case for sections of the data) would increase this probability.

Muon scatters in material in the beam line (especially μ-e scatters) can also give rise to two particles in the beam. If the scatter occurred upstream of the beam analysing magnet, these particles

would be swept out of the beam. However, if this did not occur (e.g. following an interaction in BH3 or 4) the muon would definitely trigger the apparatus since having much lower energy would cause it to be bent out of the beam veto by the C.C.M.

The effect of this veto was a 3-5% reduction in useable beam.

(d) $B_{\Delta t}$ - Muons can generate large electromagnetic showers on passing through the hadron absorber. The large pulses induced by such showers in the K-veto counters could disable their phototubes. A muon passing through the apparatus while these were inactive could then trigger the apparatus simply as a result of a random coincidence between a G and an M counter. Therefore, each beam muon vetoed the r.f. bucket following it (18 ns later).

The Scattered Muon

The definition of the scattered muon was simply a coincidence between an element in the G or H hodoscopes with one in any of the M, M' or N hodoscopes and in anti-coincidence with the K-veto. The logic is

$$S = (G + H).(M + M' + N).\bar{K}$$

where the symbol '+' represents a logical 'OR'.

In the $\bar{K}$ we have the signal that the assumed incident muon has left the beam, (M + M' + N) that a muon (presumed to be the scattered muon) has been detected elsewhere in the apparatus downstream of the iron absorber. The coincidence with (G + H) was required both to cut down random coincidences due to noise, and because a wide angle scatter in the hadron absorber could also provide an $Mu.\bar{K}$ signal ($Mu \equiv (M + M' + N)$).

One may note that as G and H, and M, M' and N are in logical 'OR', the efficiency of these counters can be measured directly from the experimental data in the regions where the hodoscopes overlap.

Combining the beam and scattered muon signals provides the event trigger.

$$\text{Trig} = B.\bar{K}.(H + G).(M + M' + N)$$

where

$$B = T.\overline{BH > 1}.\bar{B}_{\Delta t}.\bar{V}_{ABC}.\bar{V}_{H}$$

3.3 THE FAST ELECTRONICS

The description 'fast electronics' refers to the electronic logic used to form a trigger signal following an interaction and the various subsidiary circuits used for normalisation and for monitoring the experiment (Fig. 3.4). The setting-up and efficiency of this system was crucial to the successful operation of the experiment. The efficiency was mainly determined by the detection efficiency of the hodoscopes forming the trigger. However, electronic and timing inefficiency in the logic circuits also required careful consideration. The procedures used in the setting-up of the fast electronics will be described here in some detail. The setting-up was largely carried out several months prior to data-taking using parasitic beam, although the electronics was completely checked again in the first few days of data-taking.

Plateauing Hodoscopes

To ensure optimum efficiency, the best operating voltage for each phototube must be determined. This procedure is called 'plateauing'. The scheme used to plateau a counter (i.e. the phototube viewing a scintillation counter) is shown in Fig. 3.5. Counters C_1 and C_2 in coincidence (S_1) define particles which are passing roughly through C_3 (the counter to be plateaued). The signal at C_3 is set to be in-time with S_1 at the coincidence unit S_2. Therefore, the rate S_{2/S_1} gives a measure of the efficiency of counter C_3. Variation of the voltage on the phototube of C_3 gives the 'plateau curve' for C_3. A typical curve is shown in Fig. 3.6. At low voltages, the gain of the tube is low and therefore the efficiency is low (Region 1). The efficiency then rises to a plateau region as the voltage is increased (Region 2) followed by a sharp increase in rate as the voltage is increased further (Region 3). Region 3 is the noise region in which electrons emitted from the photocathode

and dynodes due to thermal noise are being amplified and swamp S_2 with accidental coincidences. The operational voltage is chosen to be below the noise region, to reduce accidentals, but sufficiently far onto the plateau to obtain a stable high efficiency. Typically this is chosen to be 100-150 v onto the plateau.

There are two further points to note concerning this procedure. Firstly, the transit time for electrons in a phototube changes with voltage at approximately 1 ns/100 v. Therefore, if the plateauing is carried out over a large voltage range, care must be taken to ensure that C_3 is in-time with S, over the full range. In practice, this can be achieved by making the signals S_1 and C_3 sufficiently wide to cover this variation.

The second point is directly concerned with the size of the downstream hodoscope elements. The aim of plateauing is to make these counters (which are two to three metres long) efficient over their full length. To do this one must plateau for light collection from the end of the counter furthest from the phototube. This could be done for all hodoscopes as they were arranged in two sets of crossed arrays. Appropriate elements could be selected to give the required trajectory, and wide angle halo used to provide the 'beam'.

Every counter in the apparatus was plateaued using this general procedure - some 200 elements.

Timing

The trigger electronics is required to detect the pulse produced by the same particle in different hodoscopes and then to correctly associate these pulses using a coincidence method. The difference in arrival times between any two pulses determines whether they are considered to be in-time or not. In this experiment a coincidence was defined by

any overlap of the two pulses and therefore the determining factor is the width of the pulses. If the timing criteria are too loose (i.e. wide pulses) spurious events may be taken as a result of random coincidences. If, however, they are too tight (i.e. narrow pulse widths) real triggers will be lost due to fluctuations in signal propagation times. Therefore, in addition to ensuring that all counters in the trigger produce a pulse at the same time at the event trigger coincidence unit, one must also ensure that pulse widths take proper account of the intrinsic resolution of the counters.

All counters in the same hodoscope were connected to the fast electronics by equal lengths of cable. This allowed the entire hodoscope to be timed in by timing in a single element. The beam and halo veto counters had the problem that their signals must travel up to 200 m to the fast electronics (which was situated behind the hadron absorber) (Fig. 2.1). The counters in these hodoscopes were OR-ed together in the enclosure and the resultant signals transmitted via fast air-cored coaxial cable to the fast electronics. Signals for V_{ABC}, V_H and BH > 1 were formed and transmitted in a similar fashion.

The construction of the BH > 1 signal for each hodoscope was quite straightforward. The output singals from the discriminator on each counter were summed via a linear fan-in. This summed output was then attenuated by a factor of ten and passed through a second discriminator with a threshold of 110 mV. A double Nim-level signal attenuated by a factor of 10 is 150 mV and therefore this second discriminator would only fire if at least two counters in the bank were set.

The remaining hodoscopes were sufficiently close to the fast electronics to allow their individual signal cables to be brought there directly from the phototube output. An OR-ed output was then formed for each hodoscope.

The fast electronics therefore used the discriminated ouputs from the counters rather than their direct signals to detect an event. The thresholds for these discriminators were set below the level for minimum ionising particles but above noise levels (50-100 mV). All phototube outputs were clipped to reduce dead-time (Fig. 3.7a).

The timing resolution of the trigger is determined by the width of the OR signal for each hodoscope. These in turn are principally dependent on the length of the counters in the array. The typical jitter in a phototube is 1-2 ns. However, the transit time of light in scintillator is 7ns/m and this causes the variation between hodoscopes. The widths are therefore: 5 ns (BH5, 6); 10 ns (all other beam hodoscopes, BH > 1, and $B_{\Delta t}$); 15 ns (V_{ABC}, N, K); 20 ns (M'); 25 ns (H, H_V, M); 30 ns (G). These widths were set up at the 'equal-time' fanouts indicated in Fig. 3.4. Apart from BH5-6, the output widths for the equal-time fanouts were produced using a clipped output pulse from a discriminator (Fig. 3.7b). Thus for example, the 30 ns G pulse was produced with a discriminator output width of 15 ns tied to a shorted 7½ ns clip cable. As the discriminator cannot accept a second pulse until after the trailing edge of the first, this reduced the electronic dead-time from 30 ns to 15 ns in this case. The signal BH5, 6 determined the relative timing of the apparatus. It was therefore made as short as possible using an E.G. and G. fast discriminator which had a rise time of ∿2 ns, and could produce a narrow pulse.

The use of equal-time fanouts enabled the easy formation of the many scalars which were required for setting-up, monitoring, and normalisation of the experiment. A second bank of fanouts whose outputs were delayed by 54 ns relative to the first (not shown in Fig. 3.4) were used to measure random rates.

The usual procedure was followed to time the beam telescope. Firstly, signals were timed visually on a cathode ray oscilloscope by comparing the arrival times of pulses from the various counters with that from B115, 6. (Beam vetos V_{ABC} and veto jaws were moved into the beam to make this easier.) Although this could be done quite accurately (±1 ns) a delay curve was also obtained about the visual value to confirm the result (Fig. 3.8). Timing of the downstream counters with respect to the beam was complicated both by the length of the counters and their positions. In this case the timing was only done visually using the counter most accessible to the beam in each hodoscope. Allowance was then made for transit time in the scintillator. Thus: G, M and M' were timed at their furthest edges from their phototubes and therefore the pulses corresponded to the latest pulse possible from these counters; the H counter was timed with particles passing its centre. The relative timing of these hodoscopes is shown in Fig. 3.9.

Latching

All counters other than the K counters were latched and read out for each event. The same problems occur with the latch gate timing as with the trigger timing for the downstream hodoscopes. A similar procedure was used to ensure 100% latching efficiency. Latch gates were 20 ns wider than the pulse they were latching.

The fast electronics had built into it a system to provide a fake pulse input in coincidence for all counters in the trigger. This could be used to check out both the discriminators and logic units in the trigger, and the counter latching.

Scalars

The equal-time fanouts were used principally to form the many coincidences which required to be scaled for monitoring and normalising the experiment. 54 ns was chosen for the delayed equal-time fanouts used to measure random rates as this corresponds to a delay of 3 r.f. buckets. The electronics provided both 'gated' and 'ungated' scalars for visual and CAMAC readout. A discussion of the gating signals is given in section 3.4.

The K-Veto

The K-veto is the most important hodoscope in the apparatus as its function is to veto the unscattered beam. A failure to veto will allow a random coincidence between say the G and M hodoscopes to trigger the apparatus. The K-veto must therefore have high efficiency. The efficiency of this counter was measured by temporarily fixing a small counter (C) immediately downstream of the K and measuring the rate $\frac{B.C.\bar{K}}{B.C}$. A value of 2×10^{-6} was obtained.

The vertical and horizontal positions of the K-veto were fixed prior to data-taking. A vertical scan of the rate $\frac{B.\bar{K}}{B}$ was made on a counter by counter basis (Fig. 3.10). This scan was used to position the central veto counter (6-7) on beam centre. The positioning however was fairly rough. The horizontal position of the K-veto could be readily changed as the hodoscope was mounted on a trolley. The spectrometer acceptance is determined by the inner edges of the combined M hole in the beam region. Clearly, the K-veto must be positioned to match this hole. A minimum in the rate $\frac{B.\bar{K}}{B}$ for a horizontal scan was chosen to fix this position. (Fig. 3.11).

3.4 DATA READOUT

The computer used in this experiment for data readout and on-line data monitoring was a Xerox Σ3 with the following peripherals: a card reader, a teletype, a lineprinter, two 9-track tape drives, a 750K word drum and a Tektronix 611 storage display scope. The computer was interfaced via CAMAC to the fast electronics and the chamber scanners. Details of the scanners used to read out the spark and proportional chamber information can be found in references 35, 36, 40. Standard Lecroy CAMAC latch and scalar modules were used for the counter and scalar readout. Readout of the Cerenkov counter pulse heights were by two LRS2249A twelve channel analogue to digital converters.

A description of the data acquisition program and interrupt-servicing routines can be found in ref. 41. A brief general description will be given below (Fig. 3.12).

The Σ3 has a hardwire interrupt structure reasonably suited to its operation as an on-line computer. Each interrupt has two status controls: armed/disarmed; enabled/disabled. The highest priority interrupt which is both armed and enabled is serviced first and automatically suspends operation on any lower level interrupt. While a particular interrupt is being serviced, that interrupt is disabled and no further interrupts can be accepted at that level until the task has been completed. Having completed the task corresponding to the highest priority interrupt, control passes to any which have been suspended in order of priority.

Data readout and tape writing were assigned the two highest priority interrupts (13 and 12 respectively). However, tape was normally only written at the end of each spill, events being written to disk during the spill and copied to tape following it.

Although no major analysis was carried out on-line, various sampling routines and a crude track-finder were used to monitor the operation of the apparatus and to display selected events. These operations were handled by lower priority interrupts. The particular mode required was selected by one of 32 toggle switches which were periodically tested and up-dated by the on-line program.

The Run Box

Overall program control was carried out from a panel containing only four buttons termed the run-box.

Switch 1 (Begin Run)

This armed all interrupts and sent a request to the teletype for operators comments (run number, target status etc.). Following this input at the teletype, all scalars and latches were cleared and a 'Begin-Run' record written to tape.

Switch 2 (Run)

This was a simple switch which completed the electrical circuit for the priority 13 interrupt and then allowed data to be taken.

Switch 3 (Stop)

This was a switch which could disable the priority 13 interrupt at any time during the run to suspend data taking.

Switch 4 (End-Run)

This disabled all interrupts at the end of a run. An 'end-run' record was then written on tape and a summary of performance of the spectrometer during the run printed (a 'SAGA').

The switches had to be pressed in the correct sequence to initiate data taking - Begin Run; Run; Stop; End-Run. Stop and End-Run could be used as often as desired during a run to suspend and restart data taking.

Trigger and Interrupt Sequence

The pulse sequence required to issue an interrupt to the computer, latch counters, fire chambers and then initiate data-readout was generated by electronics known as the 'event-box' (Fig. 3.13). The timing diagram for this electronics is shown in Fig. 3.14.

Immediately following a trigger, the event-box issued a 'prompt-out' signal which prepared the computer to accept the interrupt, latched the counters and then fired the spark chambers. The computer was deadened for 3 msec while the chambers were fired and then when all electrical noise had died away, the interrupt was sent to the computer to initiate data readout. On completion of data readout, the computer issued a reset to the master flip-flop in the event box. The event box, however, could not accept another trigger until a fixed 50 msec block was removed. This block was required to ensure in particular that the capacitors used to fire the 6m spark chambers were fully recharged before another trigger was received.

There were three other inhibits operating on the master event flip-flop. A signal obtained from the accelerator at the start of the beam spill was used to gate the trigger on only during the spill. The spill length used was either 1 sec or 2 sec depending on the accelerator mode in operation (principally dependent on cycle time and power consumption). In practice, the spill structure tended to be spiky at the beginning and the end of the spill, therefore the first and last 50 ms were gated off. An experiment in a neighbouring beam line which used

fast spill at intervals throughout the slow spill required the inclusion of the 'ping-circuit'. The arrival time of these pulses could be obtained from the accelerator clock and these were used to generate an inhibit on the master flip-flop for 1.5 msec covering the fast spill pulses. The final inhibit - RUNBAR - was produced from the run-box. This inhibited the master flip-flop when the STOP switch was used to suspend data-taking.

Gates

Three gates were generated by the event-box for use in the experiment. However, only two were used for gating scalars (Spill Gate and Event Gate) - the beam spill gate was simply used to monitor the start and finish of slow-spill. The Event Gate inhibited all scalars for the duration of a trigger. Thus the Event-Gated beam scalars determines the normalisation for the experiment. The Spill Gate only gated off scalars while the spark chambers were firing and was used to obtain total beam rates (e.g. for an estimate of dead-time).

3.5 THE RUN

The data analysed in this thesis was taken in a period of 9 weeks from October to December 1976. During this period, the accelerator operated quite smoothly on a schedule of 12 days running followed by two days of maintenance. There was only one major breakdown lasting several days in the middle section of the run. Two spill lengths were used depending on the cycle time of the accelerator. Slow spill $\sim$1 sec was used with a cycle time of 10-12 sec and $\sim$2 sec used with a cycle time of 18-24 sec. For most of the data the spill length was $\sim$2 sec.

The experiment was run with typically 10^{13} protons/pulse on target resulting in a muon flux of 10^6 μ's/pulse. An integrated flux of 7.5×10^{10} μ's was obtained giving 730 K triggers with target full and 175 K triggers with target empty.

Overall, the apparatus functioned well throughout the run. Major equipment failures occurred relatively infrequently (less than one a week) and usually only required 4-6 hrs. work to repair. However, minor problems such as electronics failures (mainly as a result of overheating or bad cables) occurred quite often and required continuous monitoring.

A comprehensive monitoring system complete with checklists was used to detect and rectify equipment failure as soon as possible. If the problems detected could not be rectified by the shift personnel, experts on the various parts of the apparatus could be called. As was mentioned in Section 3.4, the on-line program had access to various sampling routines. From these one could obtain beam chamber histograms, spark distributions for the downstream chambers on pulse-height distributions for the Cerenkov counter cells throughout a particular run. In addition one could obtain a current 'SAGA' output at any stage of a run to carry out a detailed check of the apparatus (Fig. 3.15). A final SAGA was obtained at the end of every run and checked for peculiar distributions.

As well as the computer based monitoring system, one also had to check the physical conditions of the apparatus. This included checking high voltage settings on phototubes and chambers against written values, gas flow rates and gas supplies. These checks were carried out once per shift (every 8 hours). Normally this would only result in changing a gas bottle once every few days.

In addition to these checks, for every run as a backup and a check of the computer readout, various important scalars for the run (beam and selected randoms) were written down on a 'run-sheet' and entered into the experimental log. The currents drawn by both the spectrometer magnet and the beam momentum analysing magnet (D4) were also noted. Fig. 3.16 shows a typical run-sheet and various rates occurring in the experiment.

The final stage in data taking was to copy the raw data tapes and ship the copies to Oxford for processing. The tape processing will be discussed in the following chapter.

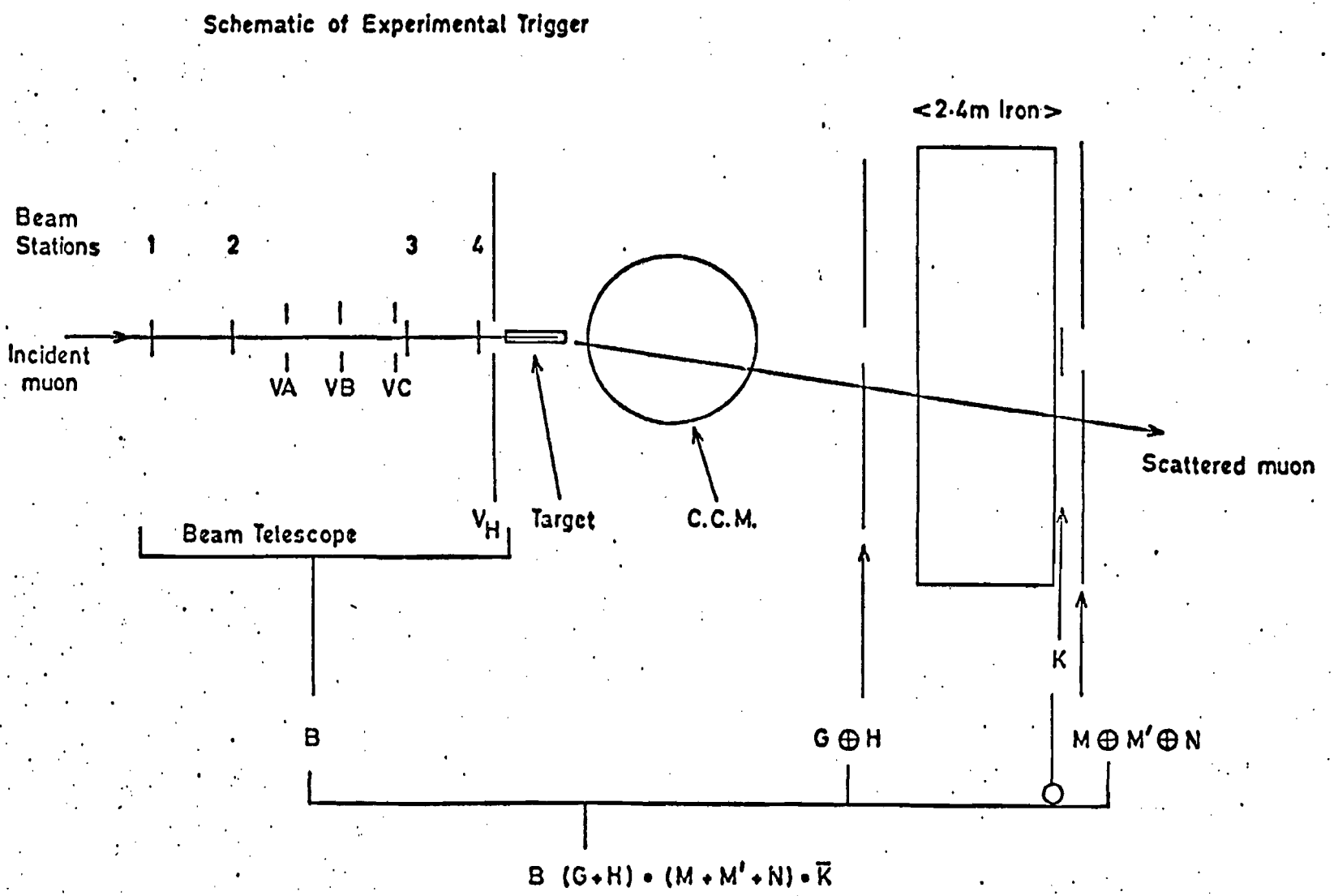
Schematic of Experimental Trigger
<2·4m Iron>
Beam
Stations
1
2
3
4
Incident
muon
VA
VB
VC
Scattered muon
Beam Telescope
V_H
Target
C.C.M.
K
B
G ⊕ H
M ⊕ M' ⊕ N
B (G+H) • (M+M'+N) • $\overline{K}$

Fig.

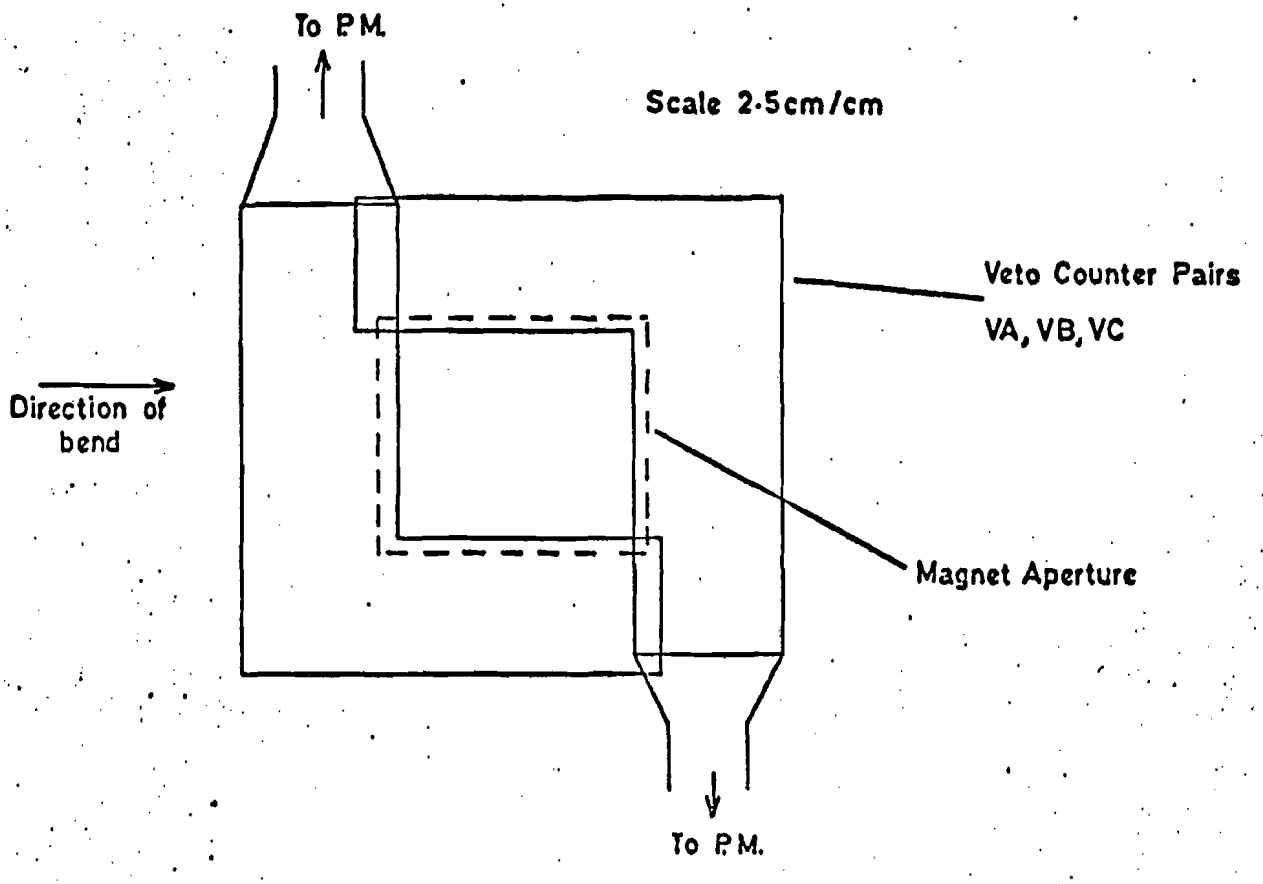

Position of Beam Vetos in Magnet D4

Fig. 3.2

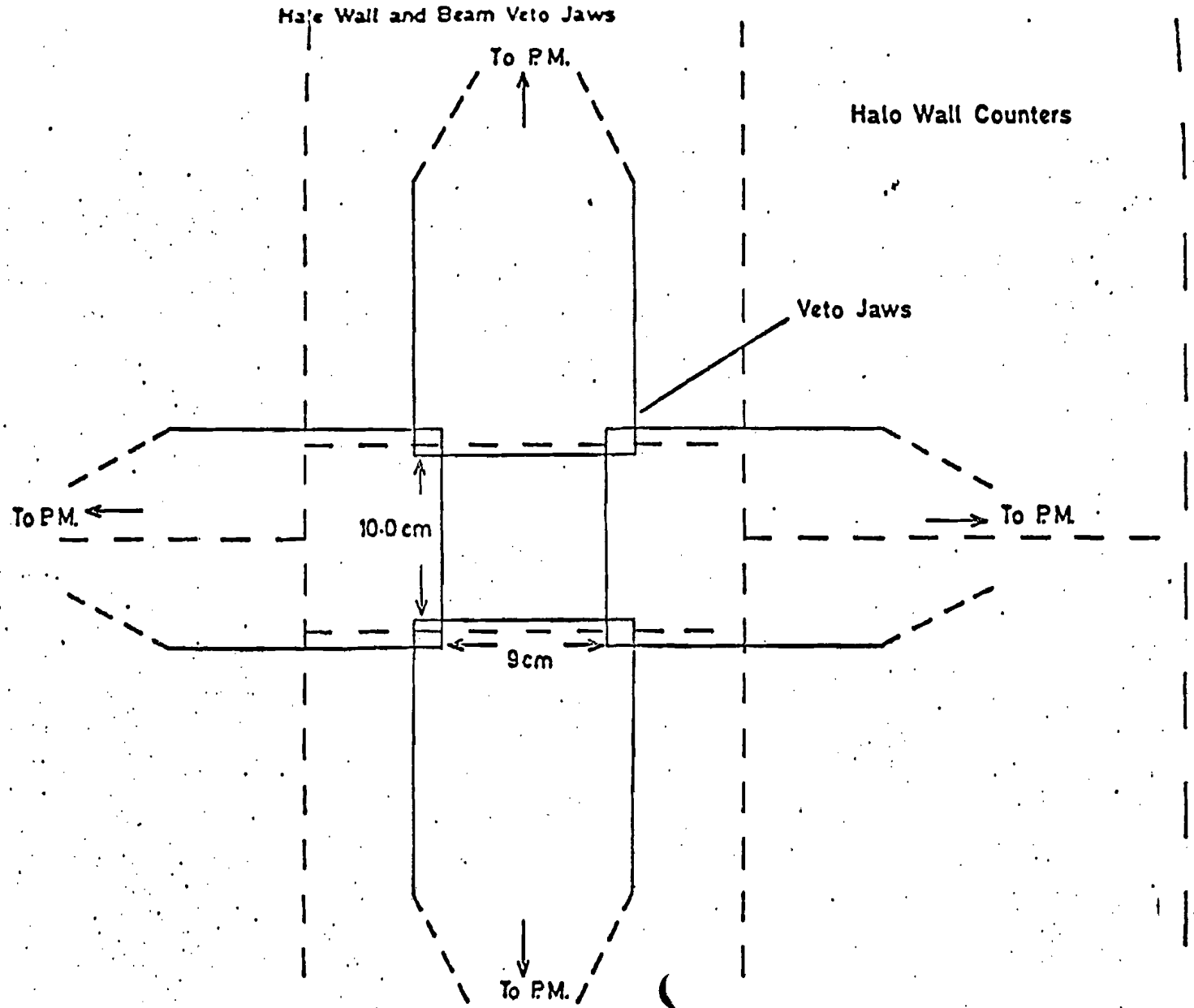
Halo Wall and Beam Veto Jaws
To P.M.
Halo Wall Counters
Veto Jaws
To P.M.
10.0 cm
To P.M.
9cm
To P.M.

Fig. 3.3

Trigger Electronics

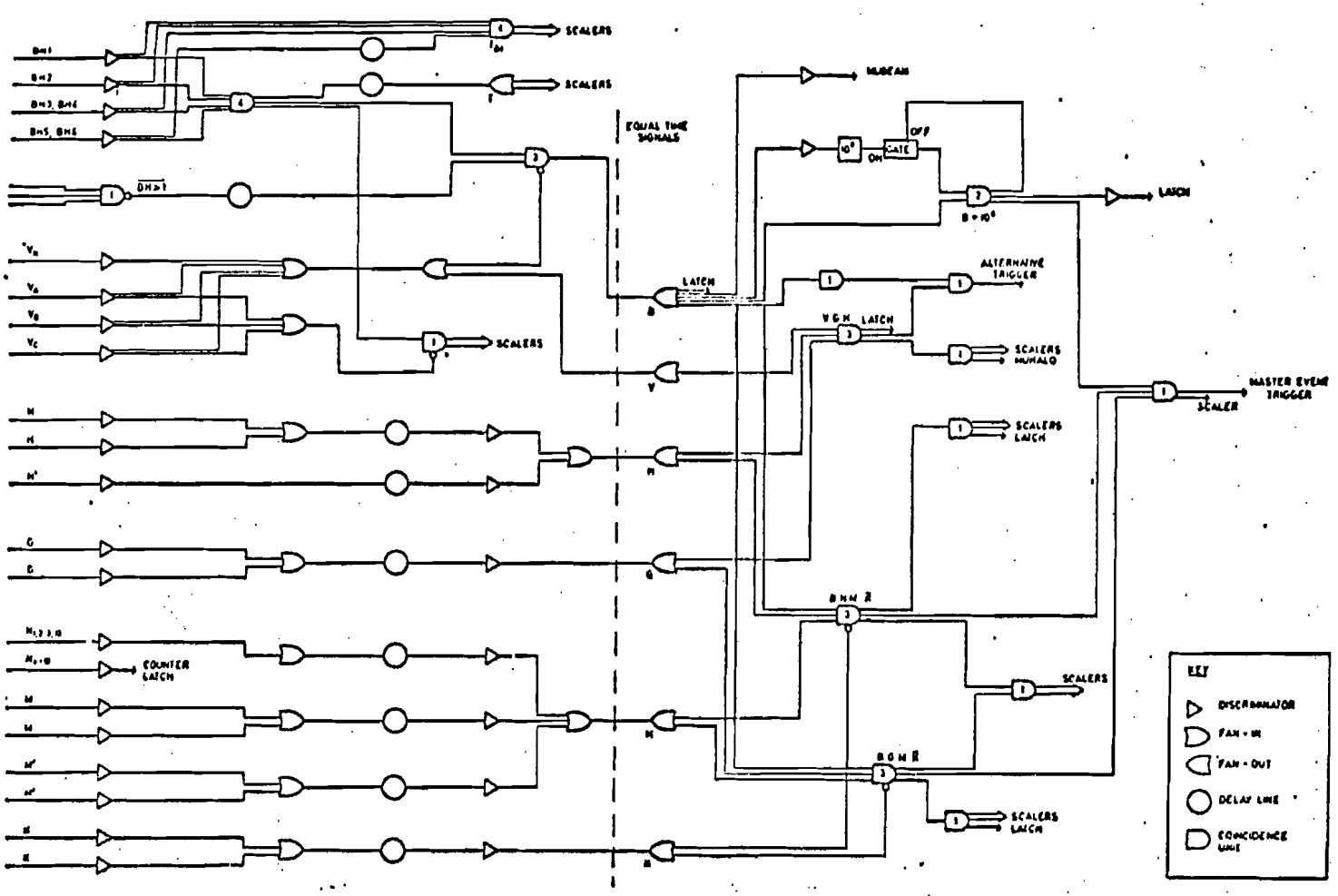

Fig. 3.4

Plateau Circuit

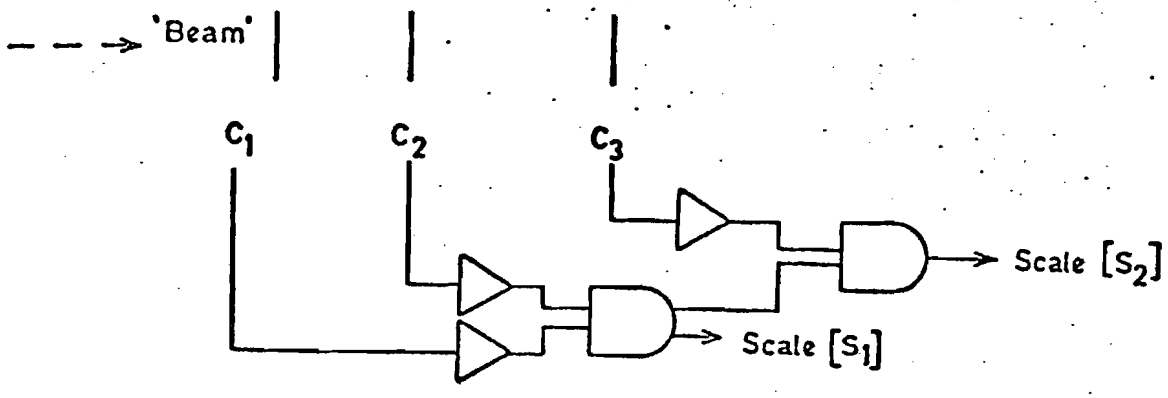

Fig. 3.5

Typical Plateau Curve

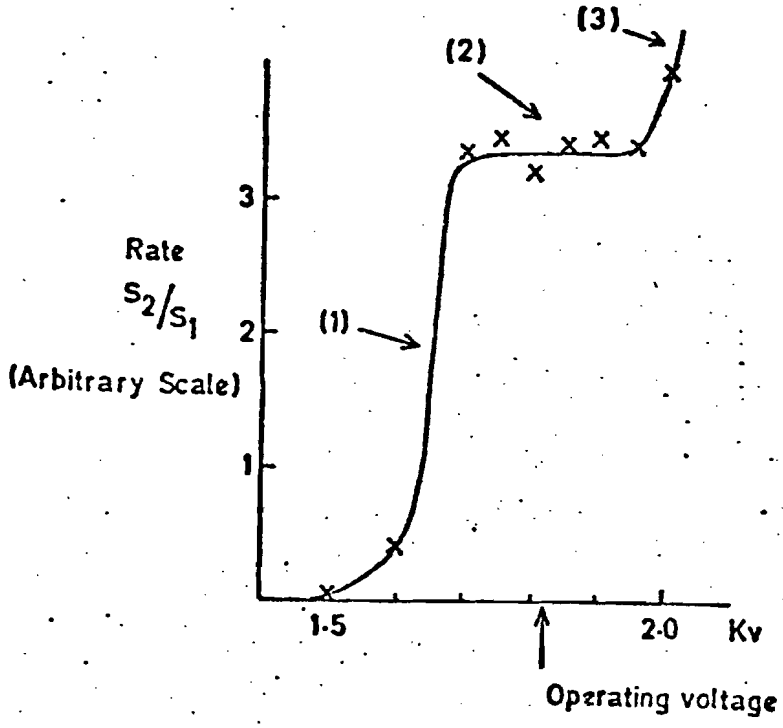

Fig. 3.6

Pulse Shaping (ie Clipping)

Phototube Pulse Shaping

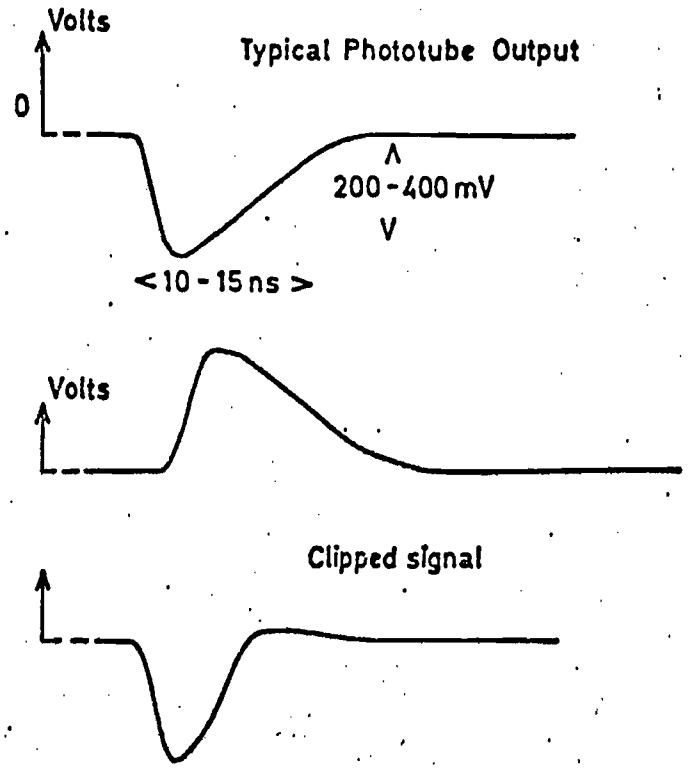

Fig. 3.7a

Discriminator Pulse Widening

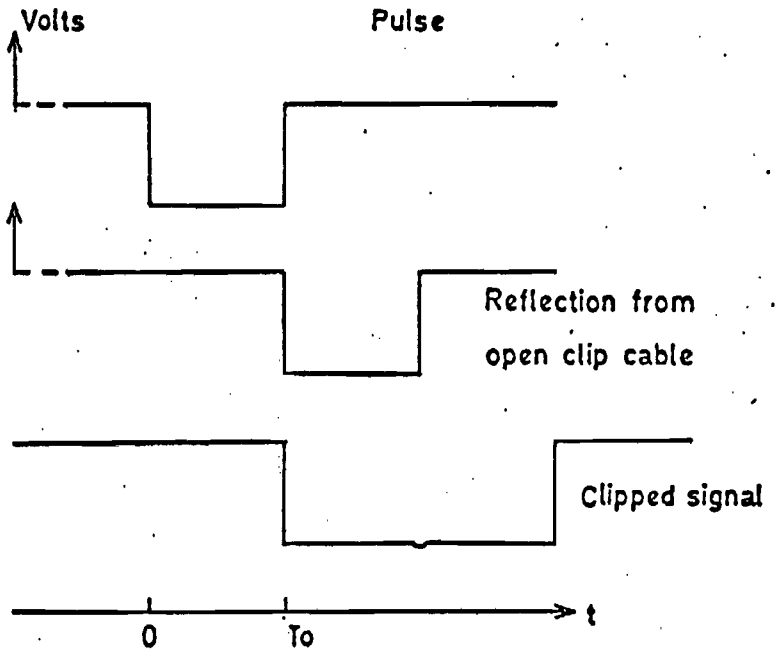

To = 2x (length of clip cable) x (velocity of light in cable)

Fig. 3.7b

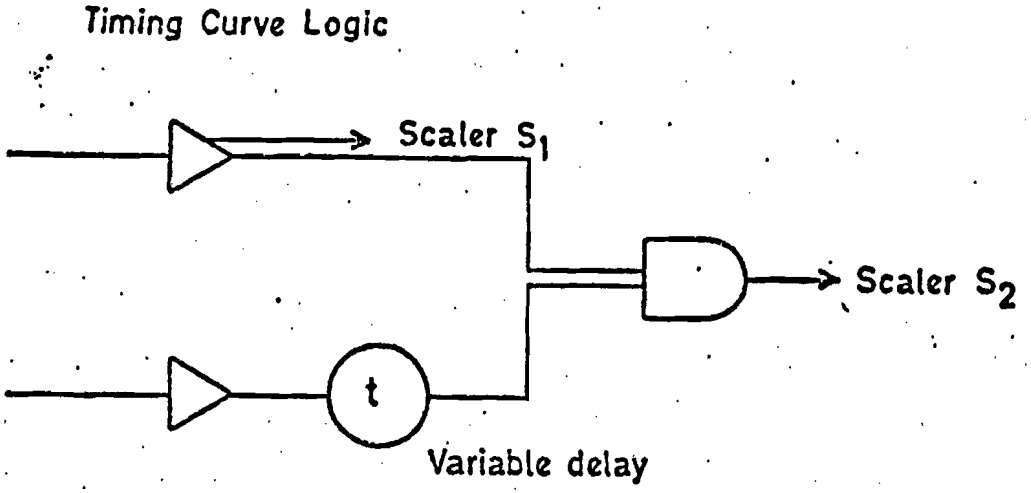
Timing Curve Logic
Scaler S_1
Scaler S_2
t
Variable delay

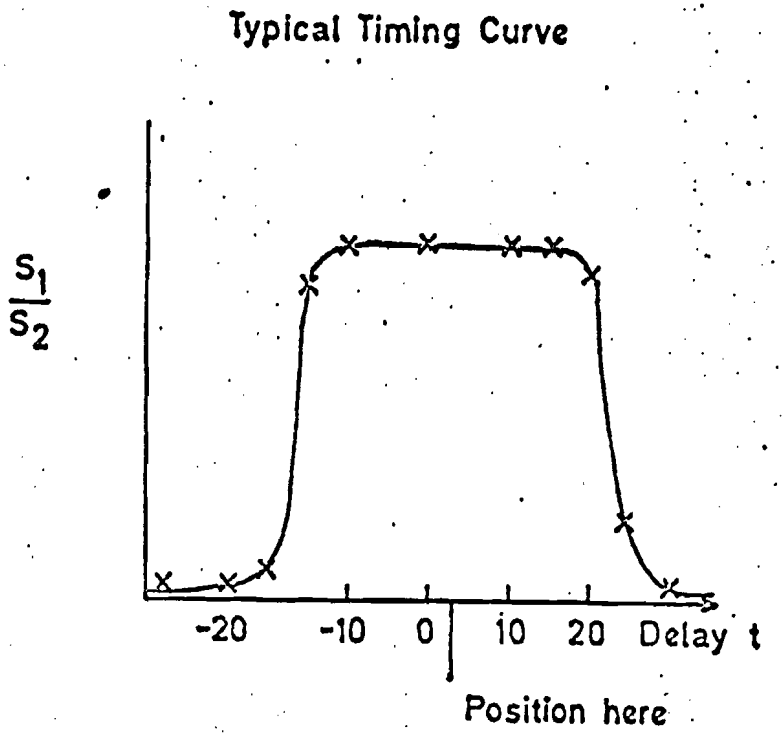
Typical Timing Curve
$\frac{S_1}{S_2}$
-20
-10
0
10
20
Delay t
Position here

Fig. 3.8

Trigger Timing Diagram

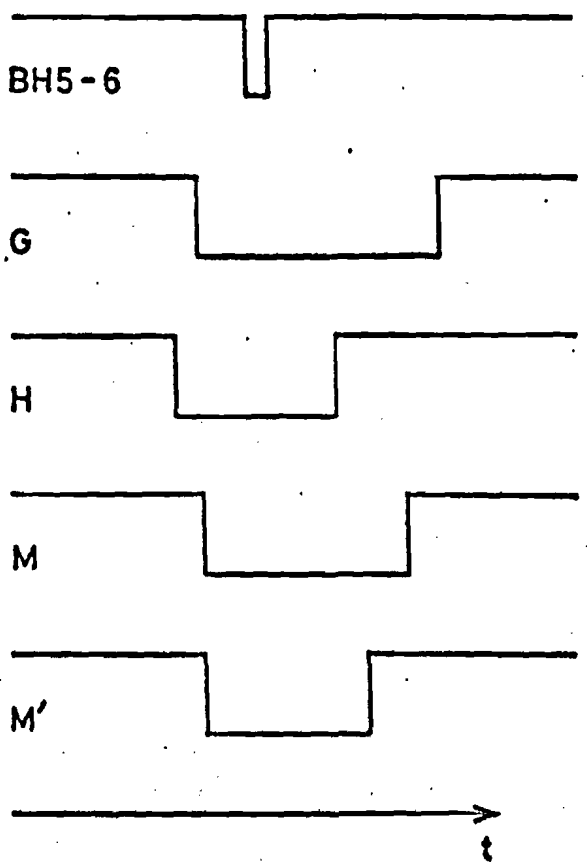

Fig. 3.9

Horizontal scan for K-veto

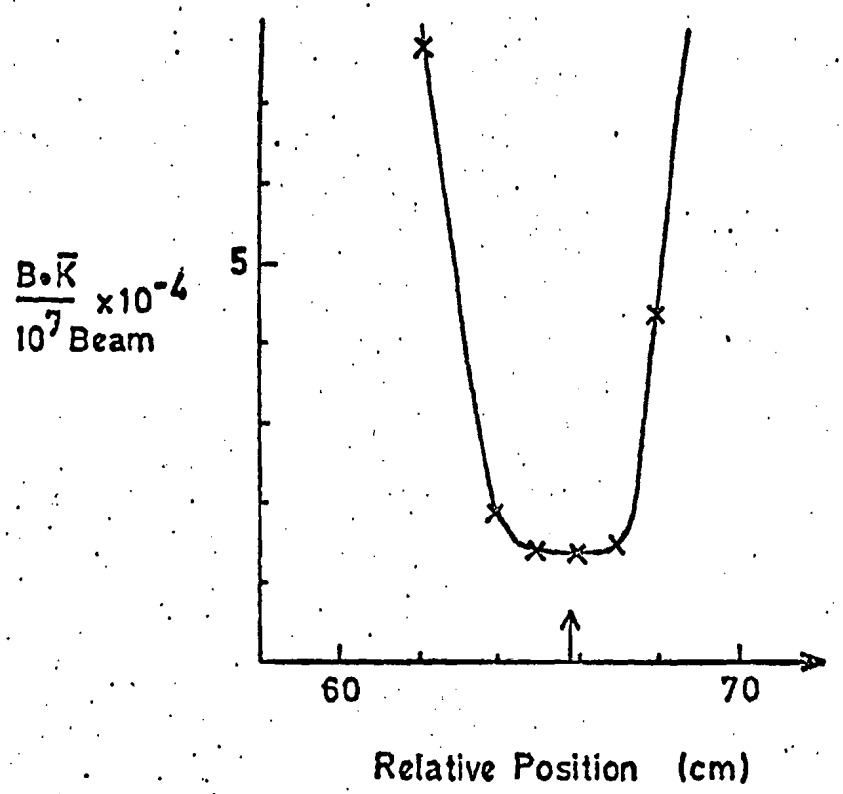

Fig. 3.11

Vertical scan for K-veto

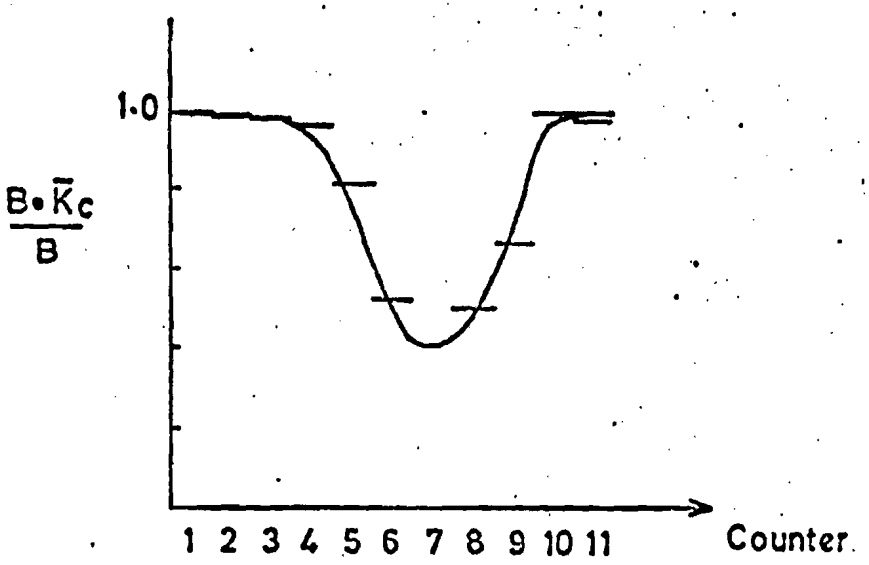

Fig. 3.10

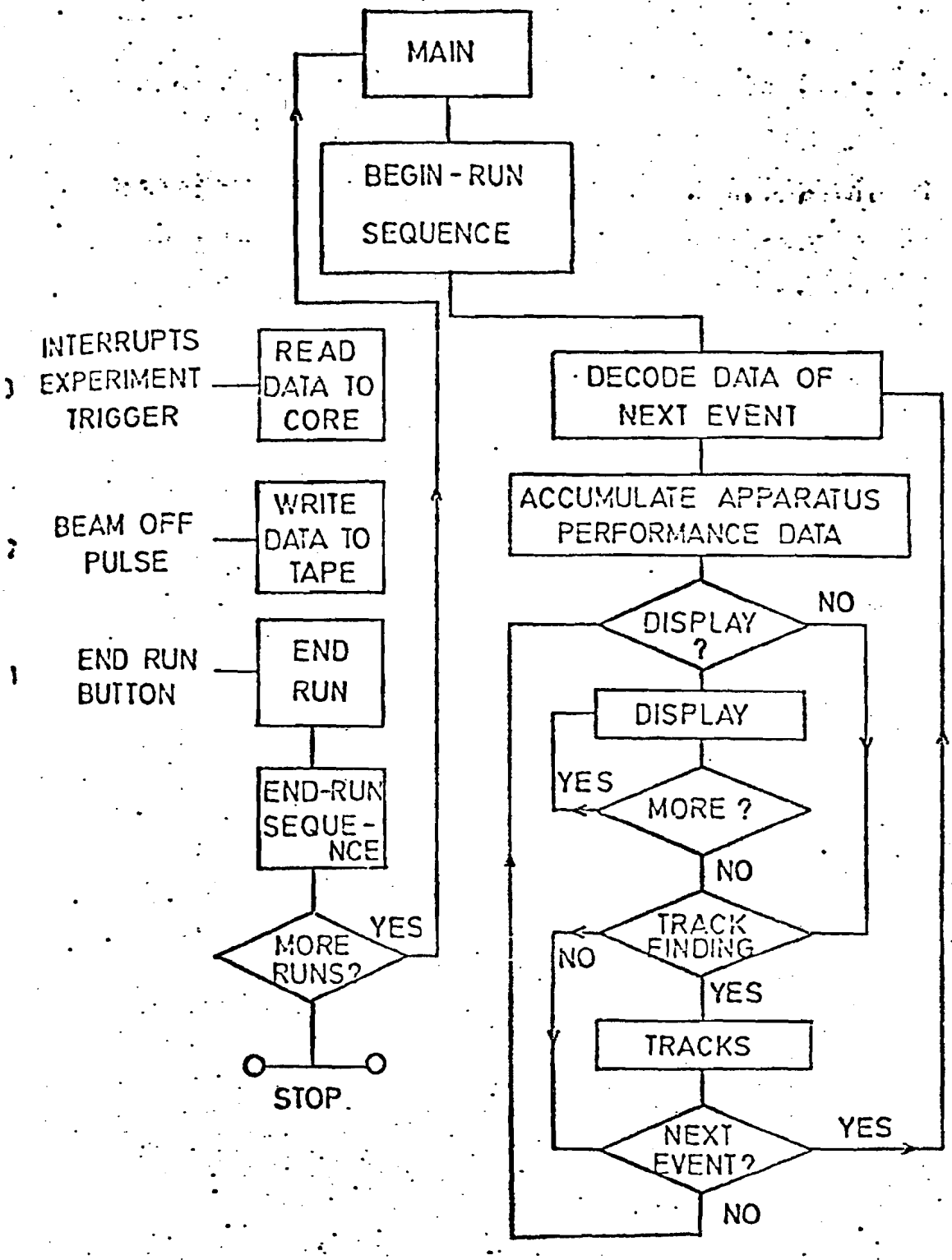

ON - LINE PROGRAM

Fig. 3.12

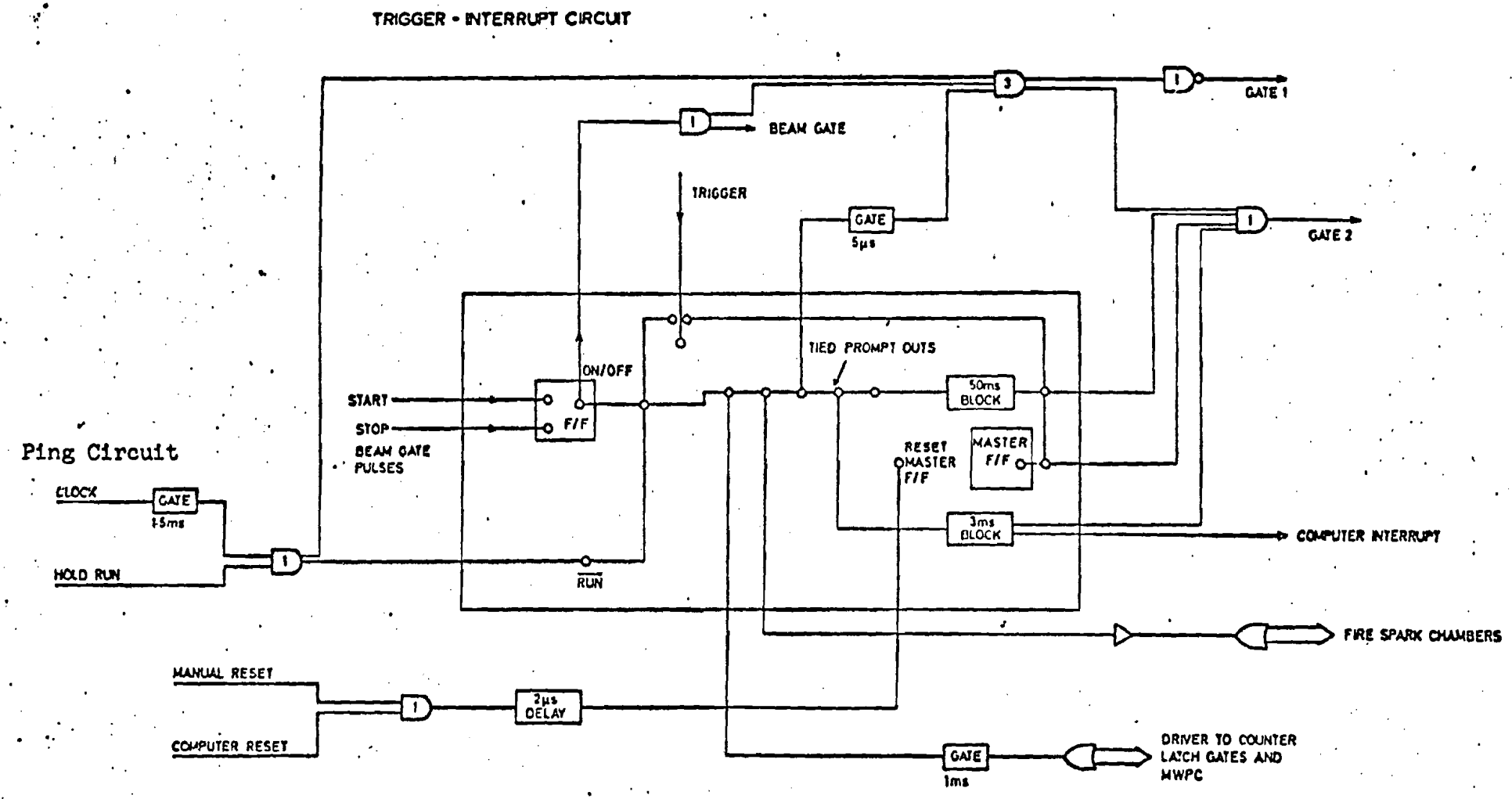
TRIGGER - INTERRUPT CIRCUIT
Ping Circuit
CLOCK
GATE
1.5ms
HOLD RUN
START
STOP
BEAM GATE PULSES
F/F
ON/OFF
BEAM GATE
TRIGGER
GATE
5μs
GATE 1
GATE 2
TIED PROMPT OUTS
50ms BLOCK
RESET MASTER F/F
MASTER F/F
3ms BLOCK
COMPUTER INTERRUPT
RUN
FIRE SPARK CHAMBERS
MANUAL RESET
COMPUTER RESET
2μs DELAY
GATE
1ms
DRIVER TO COUNTER LATCH GATES AND MWPC

Fig. 3.13

TRIGGER AND INTERRUPT SEQUENCE

Fig. 3.14

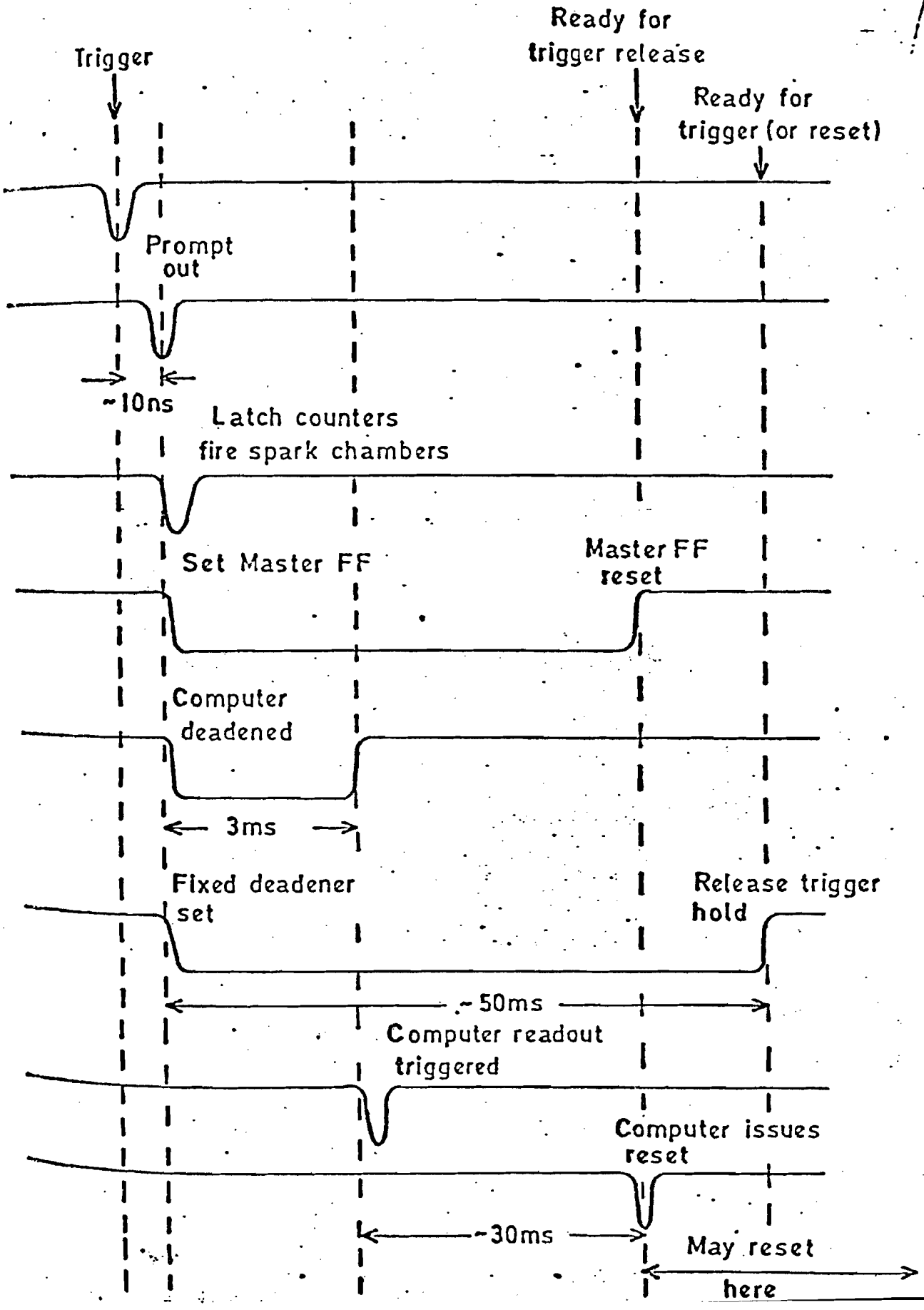

Typical 'SAGA'

RUN 1910 TAPE 494 DATE 23/04/76 0125 AT 0 GEV/C

808 EVENTS PROCESSED

SCALERS	COUNTS		RATES		RATES
T NG	16022268	B/T	0.574E+00	/	0.0
B NG	14000878	VGH/B	0.270E+01	/	0.0
VGH NG	3492085?9	B(D)/T	0.390E-01	/	0.0
HK NG	10717	TV/T	0.807E+00	/	0.0
KKH NG	2845	BKG/T	0.196E-04	/	0.0
KKHH NG	995	H/BKG	0.295E+05	/	0.0
BOK NG	134174956	BK/B	0.781E-04	/	0.0
BKDHHVNG	137	BKP/B	0.200E-04	/	0.0
T	16646?902	BKGH/B	0.701E-05	/	0.0
TV	13429064A	BKHH/B	0.70HE-05	/	0.0
BKG	3232	BKGHH/B	0.577E-05	/	0.0
B	955000?4	HGK/B	0.966E+00	/	0.0
BH	19498200	BKCPV/B	0.32HE-05	/	0.0
BH	795?8341	BKCPHV/B	0.85VE-06	/	0.0
BK	7287	H/B NG	0.6A2E+00	/	0.0
BKH	1910	BAHH/BKHH NG	0.679E+00	/	0.0
BKH	3347	/	0.0	/	0.0
BKHH	676	/	0.0	/	0.0
BKGH	671	/	0.0	/	0.0
BKGHH	551	/	0.0	/	0.0
VGH	257676940	/	0.0	/	0.0
TRIGGER	787	/	0.0	/	0.0
H(D)	6493928	/	0.0	/	0.0
BOK	92068653	/	0.0	/	0.0
BKHDHV	206	/	0.0	/	0.0
BKHDHV	119	/	0.0	/	0.0
BKDHHV	82	/	0.0	/	0.0
HKDB	66	/	0.0	/	0.0
BKHHDB	8	/	0.0	/	0.0
BKDHV	313	/	0.0	/	0.0
BKCHGV	425	/	0.0	/	0.0
EDHV	4218007	/	0.0	/	0.0

HODOSCOPES															MULTIPLICITIES	0	1	2	3	4	5	6	7	8	9	>9
BH1 1- A	6	5	24	222	437	272	66	11								0	959	40	1	0	0	0	0	0	0	0
BH2 1- A	7	4	157	245	252	280	62	9								38	924	34	1	0	0	0	0	0	0	0
BH3 1- A	6	15	205	257	225	200	44	6								42	954	4	0	0	0	0	0	0	0	0
BH4 1- A	0	1	2	136	565	243	10	0								41	958	1	0	0	0	0	0	0	0	0
BH5 1- A	46	142	215	191	163	147	72	20								5	994	1	0	0	0	0	0	0	0	0
BH6 1- A	0	10	166	269	282	202	69	11								14	972	14	0	0	0	0	0	0	0	0
G 1- 9	53	90	63	72	113	85	187	103	904							116	332	235	135	75	45	24	14	6	5	10
10-18	914	136	141	75	15	82	56	61	57																	
19-20	0	0																								
H 1-12	24	31	45	57	41	74	103	157	188	283	110	87				209	328	183	92	39	47	26	7	9	6	14
13-24	270	136	100	66	45	41	36	37	30	26	27	24														
H' 1-12	30	25	35	28	0	228	347	103	6	20	16	16				546	312	99	31	11	1	0	0	0	0	0
M 1-12	24	7	74	11	36	28	37	33	36	14	28	17				230	636	104	31	10	2	1	1	0	0	0
13-19	16	36	79	162	321	57	15																			
20-22	32	90	35																							
M' 1-10	48	17	14	17	26	22	47	54	36	28						390	448	131	20	12	0	0	0	0	1	0
11-20	48	43	33	74	106	30	52	41	74	15																
N 1-19	26	28	77	51	46	64	153	151	87	77	32	54	51			631	52	217	45	27	9	18	4	1	1	1
P 1-16	31	17	19	14	10	22	19	33	64	83	15	20	186	38	21	22	150	474	239	85	30	11	9	1	1	0	0
17-32	14	15	4	4	7	11	6	12	12	22	17	12	15	22	28	13										
33-48	5	27	47	52	68	12	33	202	61	26	25	14	9	6	9	5										
49-54	11	5	10	1	11	8																				

CERENKOV DISTRIBUTIONS

	1	2	3	4	5	6	7	8	9	10	11	12	13	14	15	16	17	18
1- 20	0	0	0	14	87	72	47	23	0	12	217	245	259	241	71	36	37	42
21- 70	808	804	799	779	707	728	756	785	807	796	564	499	509	504	734	772	770	764
71-120	0	4	9	12	14	6	5	0	1	0	4	6	12	10	1	0	1	2
121-170	0	0	0	3	1	2	0	0	0	0	8	8	15	4	0	0	0	0
171-220	0	0	0	0	0	0	0	0	0	0	4	5	8	6	0	0	0	0
>220	0	0	0	0	0	0	0	0	0	0	4	5	7	3	0	0	0	0

Fig. 3.15

E398 Runsheet.

E-398

Chicago
Harvard
Illinois
Oxford

Shift Personnel: WHL / FMP

Underline Scribe

Run Number	11159	Proton Mom.	GeV	400		DATE	TIME
Tape Number	426	Muon Mom.	GeV	225	Begin		0310
Run Log Book Number	10	IW2	AMP	3649 / 4189 / 4189	End		0645
Run Log Book Page	269	IE41	AMP	4757.	Target		LH2
		Cyclotron	AMP	4200	Trigger		P157

SCALERS		SCALERS			
		T/16	64.049M	Total Muons Begin 4096	6886148
		T(ΣV̄)/16	37.74M	End	6380721
		B/16	33.134M	B̄KH(G+H)/B	10.69×10^{-6}
E·H(G + H)	5666	$B_{ungated}$/16	45.72M		
Triggers	6286	B̄K	48268	Calculated Quantities	
E·B$_{\Delta t}$	386	VGH/16	120.391M	$T_{\Delta t}/T$	0.0289
Beam Pulses	929	B̄KM	13732	TV_{ABC}/T	0.825
SEM	8075712	B̄KMH	4740	B/TV_{ABC}	0.627
B̄·HB$_{\Delta t}$	53	B̄K$_{\Delta t}$/16	32.62M	B̄K/B	91.0×10^{-6}
B̄·H(HV)$_{\Delta t}$	1108	T($\bar{V}_{ABC}$)/16	52.83M	B̄KMG/B	9.21×10^{-6}
B̄·H(H̄V)$_{\Delta t}$	1640	$T_{\Delta t}$/16	1.85M	Triggers/B	11.8×10^{-6}
B̄·H(HV)$_{\Delta t}$	784	B̄KMG	4881	B/VGH	0.275
				$B_{ungated}$/SEM * 10^9	0.906×10^{-7}
				$B/B_{ungated}$	0.725

MACHINE SAGA ✓
CHECK LISTS ✓ + TICK

EQUIPMENT FAILURES 84,44; large COC

COMMENTS:

Fig. 3.16

CHAPTER 4

DATA PROCESSING AND EVENT RECONSTRUCTION

4.1 INTRODUCTION

Processing of the raw data was carried out in two stages. In the first stage, the spark data was unpacked from the set-wire addresses written on the raw tapes and re-written in terms of the experimental coordinates (x, y, u, v) onto a second set of data tapes, ('secondary' or 'scaled' data tapes). In addition, at this stage the counter latches and scalar information were unpacked and the raw data checked for bad records. In the second stage, the scaled data tapes were used as input to the trackfinding routines for the production of a third set of tapes written with reconstructed events ('tertiary' tapes). These tapes were then used as the basis for physics analysis. Some 200 data tapes were written during the experiment. This was reduced to roughly 60 secondary tapes and finally 10 tertiary tapes - a reduction partially due to a higher tape density (6250 BPI for secondary and tertiary c.f. 800 BPI for raw data).

Much of the procedures used for event reconstruction are similar to those used in earlier runs of this experiment and a more detailed discussion of some of them can be found in ref. 35, 37 and 42.

3.2 SECONDARY TAPE PRODUCTION

As can be imagined, the major effort in secondary tape production is in obtaining the space coordinates of sparks from their set-bit addresses - the scalars and latches being virtually a straight copy. In fact the major problem is in ensuring the correct relative alignment of the many components in the apparatus.

The initial alignment was carried out using beam triggers taken with the C.C.M. off. The resulting muon trajectories are therefore straight lines through the apparatus. Beam stations 3 and 4 had been accurately surveyed by Fermilab (Fig 2.2) - their separation of some 31 m together with their high resolution serves to define the position of the muon track to within $\pm\frac{1}{2}$ mm at any plane in the apparatus. The deviation of the observed spark position from the projected one can be used to obtain a correction for each plane which minimises such deviations over a section of data from each run. Non-linearities in the magnetostrictive wands of the Harvard spark chambers (due to irregularities in the wands) could result in up to a 2 mm variation and required run-by-run consideration. A three pass iteration was used to correct for these variations. From the first 400 events of a run, a simple trackfinder seeded from any three out of the four 6m spark-chamber gaps was used to obtain the corrections for all 2 x 4m and 2 x 6m planes. These corrections were then used for a second 400 events and the process repeated to obtain better values. The process was repeated a third time and the tape was then rewound and the whole run reprocessed using the corrections. The 'scaled' spark data, scalars, unpacked counters and Cerenkov ADC information were written to tape.

In addition, at this stage, each run was scanned for major failures such as high inefficiencies or missing fiducials in the chambers, or bad counter distributions. Any run which had such a major equipment failure was removed from the data sample.

4.3 TRACKFINDING AND TERTIARY TAPE PRODUCTION

The scaled data tapes were used as input to trackfinding routines for the production of a third set of data tapes - the tertiary tapes. The track trajectories, momentum and timing information on tracks as well as the vertex and scattered muon pointers determined by the trackfinding routines were recorded for each event written. As such, the tertiary tapes contained all necessary information for physics analysis. In addition, sufficient information was written on them to allow all major sections of processing except for the downstream track finding to be repeated (timing, linking, vertex fitting, selection of the scattered muon, and trackfinding in the proportional chambers).

Trackfinding was carried out separately in four regions of the spectrometer: the beam telescope; the upstream proportional chambers; the downstream hadron chambers, and the muon chambers. The separate Tracks were then linked to form particle trajectories through the spectrometer. The counter information was applied to remove stale (out-of-time) or spurious tracks. Linking between in-time hadron chamber tracks and muon chamber tracks was used to determine the scattered muon track in the hadron chambers. The upstream links to this track and the beam muon track were then used to determine the interaction vertex. All momenta were then calculated using the vertex and downstream tracks assuming a hard core model for the C.C.M. field.

A brief description of the event reconstruction procedure will be given in the following sections.

Beam Reconstruction

Good beam reconstruction was required on all events processed. If the incident beam muon could not be determined or had a badly defined

track the event was rejected. Both the counter elements set and the hit wires in the beam proportional chambers at each beam station were used to define a good incident muon. The following criteria were used (in order of decreasing preference), the precise ones applied at each beam station depending on the resolution required:

(1) A single set wire masked by a single lit beam counter.

(2) A single set wire and no lit counter.

(3) A single set counter and no set wires.

(4) A single set counter and a number of set wires.

The incident muon trajectory is important both for determining its momentum and for determining the position of the muon at the target (and thus the interaction vertex). Therefore, the most stringent conditions were placed on the closest beam stations which define the trajectory of the muon after the beam momentum analysing magnet. A successfully reconstructed beam track was required to pass all of the following cuts:

(a) Beam stations 1 and 2 satisfy any of 1-4 above.

(b) Beam Station 3 satisfies any of 1-3 above in both x and y views.

(c) Beam Station 4 satisfied any of 1 or 2 above in both x and y views.

(d) The x-track upstream of the bending magnets (as defined by beam stations 1 and 2) is required to link within 8.75 mm with the x-track downstream of the bending magnets (as defined by beam stations 3 and 4).

(e) The trajectory is required to be inside the entrance, centre and exit apertures of all the bending magnets.

Proportional Chamber Tracks

Trackfinding was carried out separately in the x and y views of the $1m^2$ proportional chambers. A simple trackfinder using two sets of

seed planes fitted any three and four point tracks which pointed to within 25 cm of the target. The chisquared for the tracks was calculated using the measured chamber resolutions and tracks with less than 2% probability rejected. Chamber resolutions were measured from the imbedded beam triggers interspersed with event triggers (the apparatus was triggered for every 2 million muons to provide this sample). These triggers clearly have only one track in the spectrometer and deviations from the fitted track give the chamber resolution; typically $\sigma_{rms} \sim 0.4$ mm.

Finally, following the downstream trackfinding (discussed later in this section), a routine using downstream tracks with no link to one of these upstream tracks was used to recover some tracks lost through proportional chamber inefficiency. A road defined by the impact parameter of the downstream track and the vertex was searched for hits. The track was fitted if two or more hits were found (the vertex and impact parameter were not included in the fit). A chisquared for two-point tracks was defined by the deviation in impact parameter from the seed value. A maximum chisquared of 2 was allowed for these tracks.

Tracks with two or more sparks in common were considered the same. The track with the best chisquared was taken, with preference being given towards three and four-point tracks.

Muon Chamber Tracks

Trackfinding in the muon chambers made use of the fact that these planes are closely spaced compared with their distance from the C.C.M. The algorithm used (FINDIT) considered all the planes simultaneously. Firstly, correlated xy pairs were formed from the xuv sparks in the read-out. A straight line fit was made through sparks which grouped together in x. If the track passed a simple chisquared cut (corresponding to a deviation of 1.25 mm per x point on the track) the corresponding y

values were searched for a track. The y resolution was much poorer as it is derived from uv information and a chisquared cut corresponding to a deviation of 15 mm per y point on the track was used to reject tracks.

Track Finding in the 6m and 4m Spark Chambers

As with the muon chambers, the 6m planes are closely spaced and the same algorithm used in the muon chambers was used to provide 'seed' hadron tracks. These tracks were projected through the twelve 4m planes and a search made for further sparks within a road of 3 cm. The whole track was then refitted using any extra sparks. If no sparks were found in the 4m planes, the road was allowed to swing by up to 2.5 cm in an attempt to pick up additional sparks. In typically 80-90% of the 6m plane seed tracks, additional sparks were found in the 4m chambers with the resultant track passing chisquared cuts ($\chi^2 < 50$). In 10% of the tracks a swing was required to pick up extra sparks.[43] To be effective, this procedure clearly requires a high efficiency in the 6m chambers since if the seed track is not identified, then the whole track is lost. Thus this algorithm was inefficient particularly in the beam region where the beam deadener in the 6m chambers removed all sparks and outside this area, halo often produced many extra sparks which led to confusion.[43]

A second independent trackfinding algorithm (SWEEP) also operated on the hadron planes. This used the impact parameter of an unlinked upstream proportional chamber track together with an xy spark in one of the last two 4m chambers to define a road of 0.5 cm in which to search for further sparks. Although a minimum of 7 sparks were required to define a track, no 6m chamber sparks were required in this algorithm. As with FINDIT, the SWEEP road was allowed to swing by up to 2 cm in an

algorithm to pick up the required tracks. A simple chisquared cut was used again to reject poor tracks and then the corresponding y points searched to obtain a y track. Throughout the downstream spectrometer the chisquared cuts for y correspond to position deviations which are 8 times more than for x - reflecting the poorer y resolution given by the UV wire angles $\pm\tan^{-1}\frac{1}{8}$ to the vertical.

A Monte Carlo program was used to estimate the efficiency of these algorithms. This inserted sparks along a 'fake track' according to the measured chamber efficiencies and resolutions (Fig. 4.1). Inefficiency in the beam region is apparent but even there the reconstruction efficiency of the two algorithms is better than 80%. Outside the beam region the inefficincy is consistent with that resulting from chamber inefficiency and the minimum spark cut.

Timing

The $1m^2$ proportional chambers have a live time of ~100 ns and therefore give reasonable timing resolution on the upstream tracks with little contamination from halo. The downstream spark chambers however have a live time varying from 1-10 μsec and therefore contain many sparks due to stale beam (coming before and after the trigger) and halo in addition to the event associated tracks. The good timing resolution of the downstream trigger hodoscopes (20-30 ns) was used to sort out event associated tracks from accidentals.

To compensate for poor resolution, the edges of all counters were enlarged by 3cm. The counters through which each track passed were tested to see if the counter had fired. The track was then given a timing status depending on the number of counters pointed at and lit. Timing status was given separately to tracks found in the muon and hadron chambers. The timing status given was as follows:-

(a) Class 1 timing:-

three counters lit out of three counters pointed at;

two counters lit out of three counters pointed at;

two counters lit out of two counters pointed at;

one counter lit out of one counter pointed at.

(b) Class 2 timing:-

one counter lit out of three counters pointed at;

one counter lit out of two counters pointed at.

Class 2 timing is clearly of poorer quality than Class 1. Tracks with no counters lit were deemed out-of-time. Neglecting the small counter inefficiencies, these are either spurious or stale tracks.

At this point, one might consider the problems involved in obtaining the counter positions. The scheme described in Chapter 5 which was used to determine the edges of the Cerenkov counter mirrors is a variation of that used to determine counter positions. Details of the scheme used to determine counter positions are given in reference 42.

Linking

The linking of tracks found in the muon chambers with those found in the hadron planes, and the tracks found in the hadron planes with those in the 1m proportional chambers was carried out independently of the timing. Two different procedures were used since the two regions pose quite different problems.

The 1m proportional chambers do not provide sufficient information to allow stereo construction of tracks. Linking must therefore be carried out separately in the x and y views, but was simplified by the cylindrical symmetry of the C.C.M. field. As a result of this symmetry, both upstream and downstream tracks should have the same slope and intercept in v

(neglecting helix corrections). In x, the impact parameter of the downstream track should be the same as that of the upstream track (Fig. 4.2). This led to simple linking criteria for upstream and downstream tracks. A downstream track was labelled as linking to an upstream x track if their x-intercepts differed by less than 0.9 cm. (Cylindrical symmetry implies that u/s and d/s intercepts at z = 0 are equal.) (Fig. 4.3). The matching of slope and intercept was considered simultaneously in y. A downstream track was labelled as linking to an upstream y-track if:

$$\frac{(\delta_{\text{intercept}})^2}{(2\text{ cm})^2} + \frac{(\delta_{\text{slope}})^2}{(6\text{ mrad})^2} < 1 \qquad \text{(Fig. 4.4)}$$

Linking of muon chamber tracks with hadron chamber tracks required consideration of multiple scattering in the hadron absorber. This effect depends on both the energy of the muon and its trajectory through the hadron absorber (as this determines the length of iron traversed). Due to the poor y resolution, the main criteria were based on the x slopes and intercepts (taken in this case at the centre of the iron absorber). High energy muons were required to have slopes matched to within 12.5 mrad and x-intercepts matched to within 3.7 cm. These cuts were increased by up to a factor of 9 to allow for multiple scattering by low energy muons ($\sim$20 GeV/c^2). The y slope and intercept comparisons were only used to discriminate between similar x candidates.

Muon Selection

Hadron tracks were labelled as muons if they either linked to an in-time track in the muon chambers or pointed at a lit muon counter. The minimum track requirements were: at least one G or H counter set on the hadron track, at least one upstream link on the hadron track, at

least one M or M' counter lit along the muon track. Selection of the scattered muon gave preference to hadron tracks linking to in-time muon chamber tracks and which had the best timing and upstream linking.

Vertex Fitting

The interaction vertex was determined using an iterative procedure which, given a set of x and y tracks with their error matrices returned thebest estimate for the vertex[35]. Initially the incident beam track and the upstream links to the scattered muon track were used. At least an x link was required as this improves the momentum resolution. If the y-link was missing, the downstream y slope and intercept were used instead. If a good vertex was found, any additional upstream tracks which linked to downstream tracks were added and the vertex refitted incorporating them, and thus improving resolution (Fig. 4.5).

Momentum Measurement

The incident beam momentum was calculated from its trajectory through the magnets D4. The magnetic field was known for these magnets. The currents drawn by them were continuously monitored and the field used to calculate momenta was itself calculated from the measured current in any particular event.

A calculation of the momentum was only made for in-time hadron chamber tracks (Class 1 and 2) which had at least one upstream link to a proportional chamber track. The interaction vertex and the slope and impact parameter of the downstream track were used to calculate its momentum (Fig. 4.6). An x-link was not required since the downstream impact parameter had higher resolution (1 mm compared with 3 mm for proportional chamber tracks). Use of the interaction vertex also results in improved resolution as it contains the high resolution of the incoming

beam coupled with any proportional chamber tracks which could be included in the fit. A hard edged model for the C.C.M. field was used with an effective field of 1.4 Tesla and a radius of 2.47 m. These values were calculated from a fit to a full set of field measurements. The current drawn by the C.C.M. was also monitored continuously and the value measured for each event used to calculate momenta.

Calculation of track momenta was the final stage in event reconstruction prior to writing the event to tape. However, two further procedures were run following this on these tapes to produce a slightly modified version of the tertiary tapes with re-calibrated momenta and additional track-sorting information. These will be discussed in Sections 4.4 and 4.5.

4.4 MOMENTUM CALIBRATION

Calculation of a particle's momentum requires a knowledge of the magnetic field and of the bending angle in the field. Particle momenta are measured by the beam magnet and the spectrometer magnet, and clearly internal consistency between them is necessary. The magnetic field of both magnets were very well known through careful field mapping. However, measurement of the bending angle assumed that the axes on which the chambers had been aligned were the same on both sides of the field. Relative miscalibration can occur in part as a result of a rotation of beam stations 1 and 2 in the alignment procedure. As a result, different momenta would be obtained by the C.C.M. and by D4 for the same particle. A second source of miscalibration is a relative rotation of the axes used in the downstream chambers with respect to the upstream chambers, again during the alignment procedure. An overall normalisation is also necessary. Fortunately, these effects can be separated using the large number of μ-e scatters in the data as they affect positive and negative particles differently.

For the C.C.M., the particle momentum P is given by:-

$$P\theta = K \qquad 4.1$$

where θ is the magnitude of the bend imparted by the field, and K is the transverse momentum imparted by the field. For this data the value of K was 2.08 GeV/c.

Fig. 4.7 shows the effect of an angular misalignment of the downstream chamber axis β with respect to the upstream chamber axis α by an amount ε. α and β are assumed to be same by the analysis which measures θ^+ and θ^- for positive and negative particles respectively giving by Eqn. 4.1

$$P^{+}_{seen} = \frac{K}{\theta^{+}} \quad , \quad P^{-}_{seen} = \frac{K}{\theta^{-}}$$

and therefore

$$P^{+}_{t} = \frac{K}{(\theta^{+} - E_{\varepsilon})} \quad , \quad P^{-}_{t} = \frac{K}{(\theta^{-} + \varepsilon)} \qquad 4.2$$

If the miscalibration of the C.C.M. relative to D4 is δ then Eqns. 4.1 and 4.2 give

$$P^{+}_{seen} = (1 + \delta)\,\frac{(\theta^{+} - \varepsilon)}{\theta^{+}}\,P^{+}_{t}$$

$$P^{-}_{seen} = (1 + \delta)\,\frac{(\theta^{-} + \varepsilon)}{\theta^{-}}\,P^{-}_{t} \qquad 4.3$$

Muon electron scatters are elastic events with one particle of each sign downstream and 4.3 therefore gives:

$$P^{total}_{seen} = P^{+}_{seen} + P^{-}_{seen} = (1 + \delta)\,\frac{\theta^{\mu} - \varepsilon}{\theta^{\mu}}\,P^{\mu}_{t} + \frac{\theta^{e} + \varepsilon}{\theta^{e}}\,P^{e}_{t}$$

since δ and ε are assumed small terms in $\delta\varepsilon$ are neglected and this reduces to:

$$P^{total}_{seen} = (1 + \delta)P_{beam}\,(1 - \frac{\varepsilon}{K}(P^{\mu}_{t} - P^{e}_{t})) \qquad 4.5$$

or

$$\Delta E = P_{beam} - P^{total}_{seen} = -\delta P_{beam} + \frac{\varepsilon}{K}(P_{\mu} - P_{e})P_{beam} \qquad 4.6$$

Where, since P_{μ}, P_{e} are large (40-160 GeV/c) and the differences from the true values are small, the measured momenta can be used.

δ and ε can therefore be obtained from a plot of $P_{\mu} - P_{e}$ against ΔE (Fig. 4.8). Imbedded beam events can also be used with $P_{e} \equiv 0$ and give the point at large positive $(P_{\mu} - P_{e})$ in the plot.

Having determined the relative momentum calibration as described above, the overall momentum normalisation was calculated. Again this procedure used μ - e scatters. For these

$$Q^2 = 2\, m_e \nu = 4EE' \sin^2\frac{\theta}{2} + Q^2_{min} \qquad 4.7$$

where

$$Q^2_{min} = \frac{m_\mu^2 \nu^2}{EE'}$$

giving

$$\theta_{calc} = 2\sin^{-1} \frac{(2m_e \nu - Q^2_{min})^{\frac{1}{2}}}{EE'} \qquad 4.8$$

The measured scattering angle was compared with the calculated value for various normalisation factors β defined by $P_{new} = \beta P_{old}$.

The known angular resolution ($\sim$0.6 mrad, obtained from the spatial resolution of the proportional chambers and their lever arm of $\sim$1m) was used to calculate a chisquared distribution over a sample of events for each value of β. The value of β at the minimum was used as the normalisation factor (Fig. 4.9).

4.5 TRACKSORTING

The philosophy used in trackfinding was that any track with a reasonable number of sparks (7) and a reasonable chisquared could be written on the tertiary tape. Timing and linking cuts could then be applied in further analysis to reduce the number of spurious tracks. However, the poor y resolution led to groups of tracks with essentially the same x parameters but with varying y parameters and these could not be removed on the above cuts alone. A further source of spurious tracks was the region of high halo intensity close to the beam. Here again the above cuts were not wholly successful in removing the stale tracks as invariably the counters close to the beam would be set. (Fig. 3.15).

A scheme was used whereby tracks were awarded points on the following criteria:

1. 30 points for duplicates (i.e. same x slope as another track but with a different y slope).
2. 20 points for unphysical behaviour ($P_\perp > P_{max}$, momentum greater than 1.1 x P_{beam}).
3. 10 points for making the total momentum downstream greater than 1.2 P_{beam} after all high quality tracks had been counted.
4. 1-5 points for various minor 'misdemeanours' (few sparks, shared timing).

This information was written to tape but not implemented. The user could then consider it when tracksorting if desired. This information was used in the analysis described in this thesis (allowing some poor behaviour but nothing major). Multiparticle events are necessarily fairly messy. Fig. 4.10 shows one such event before and after tracksorting.

Use of the Cerenkov counter information relies on identifying particles which fail to light the Cerenkov counter cell they pass through.

spurious tracks will certainly not light the Cerenkov cell and must be removed or they would provide an unacceptable background to the kaon and proton signals.

For comparison, Figs. 4.11-4.14 show other typical event triggers. Fig. 4.11 shows a mu-electron scatter which is easily recognisable from the observed small angle of scatter in the upstream view and with only the scattered muon and one negatively charged particle seen downstream. Fig. 4.12 shows what is probably a radiative tail event where the muon has radiated a high energy photon in the target. However, the signature is not unique as there is no efficient photon identification in the apparatus. Fig. 4.13 is an example of the most frequent (and unwanted) trigger in the experiment - a halo trigger. Finally Fig. 4.14 shows a high multiplicity deep-inelastic scattering event.

4.6 TRIGGER AND EVENT RECONSTRUCTION EFFICIENCY

To obtain a correct measurement of the inclusive and semi-inclusive cross-sections for deep-inelastic scattering, corrections must be applied to the normalisation to account for inefficiency in the trigger and in the reconstruction programs. The effect of these inefficiencies can be considered as a reduction in the observed muon flux by an amount:

$$\varepsilon = (1 - \varepsilon_1)(1 - \varepsilon_2)\cdot\varepsilon_3\cdot\varepsilon_4\cdot\varepsilon_5\cdot\varepsilon_6$$

where

ε_1 = trigger inefficiency

ε_2 = beam self veto probability

ε_3 = beam reconstruction efficiency

ε_4 = proportional chamber efficiency with the required linking.

ε_5 = hadron chamber trackfinding efficiency

ε_6 = muon detection efficiency.

Fortunately all these correction factors can be estimated from the data.

$\underline{\varepsilon_1}$:

An obvious inefficiency inherent in the apparatus is the probability that the trigger hodoscope system would not detect the scattered muon. Inefficiency in the beam telescope is clearly irrelevant to the beam normalisation - one is simply rejecting some fraction of good beam. The efficiency of the downstream hodoscopes can be estimated by measuring the efficiency of their individual counters. Except for a few odd counters, these efficiencies are better than 98% and rarely less than 90%[43]. The 'OR' logic used for both sets of hodoscope planes in

the trigger therefore gives an efficiency better than 99.98% for detecting the scattered muon. The trigger inefficiency is therefore small enough to be neglected ($\varepsilon_1 = 0$).

ε_2:

A further inefficiency in the trigger system is in the beam self-veto rate whereby an event is vetoed if two beam muons arrive within the resolving time of the trigger counters. The fraction of beam which would thus be lost could be measured by the rate $B.B_{\Delta t}/B$. ($B_{\Delta t}$ corresponds to a beam signal from 3r.f buckets earlier than B), where one assumes a uniform probability distribution for the beam. This rate was not scaled, but can be estimated from the rates $\frac{T.T_{\Delta t}}{T}$ and B/T where B and T are as defined in Chapter 3 and $T_{\Delta t}$ is the random T signal defined by

$$T_{\Delta t} \doteq BH1.BH2.(BH3 \text{ or } 4).(BH5 \text{ or } 6)_{\Delta t}$$

where Δt corresponds to a delay of 3 r.f. buckets. The measured rates were:

$$\frac{T.T_{\Delta t}}{T} = 0.054 \pm 0.015$$

$$\frac{B}{T} = 0.51 \pm 0.15$$

The values have been averaged over the data and the errors are an estimate of run to run variations (statistical errors on any single measurement are very small).

However, the effect of the BH > 1 veto must be considered in making this calculation. This will only fail to veto if both muons pass through the same counters in the beam telescope. The probability that this will occur can be measured by comparing the beam counter

signature of one beam event with that from the following one. This probability is measured to be

$$\alpha = 7.04 \pm 0.63 \times 10^{-3}.$$

The beam self veto probability is then given by:

$$\varepsilon_2 = \alpha . \frac{T . T_{\Delta t}}{T} / \frac{B}{T}$$

$$= 1.93 \pm 0.80 \times 10^{-4}.$$

ε_3:

The beam reconstruction programs had stricter cuts on good beam than that defined by the beam telescope. As failure to reconstruct the beam caused the event to be removed from the data, this is effectively a reduction in the incident flux. The beam reconstruction efficiency was measured from the imbedded beam triggers taken throughout the data (taken for every 10^6 beam particles initially and decreased to 2×10^6 for later runs). The reconstruction efficiency was between 55% and 75% for most runs, its average for the data gave:

$$\varepsilon_3 = 0.616 \pm 0.05$$

ε_4: 1 m Proportional Chamber Efficiency

The analysis described in this thesis required both the scattered muon track and all hadron tracks to link to both an x and a y proportional chamber track. The linking efficiency was measured directly using the

scattered muon. First of all, muon tracks which were 'perfect' in all respects downstream were tested for an x or y link. This efficiency was found to be

$$\varepsilon_a = 0.964 \pm 0.003$$

The sample of tracks with an x or y link was tested to obtain the proportion with an x link and those with an y link to obtain

x linking efficiency $\varepsilon_b = 0.972 \pm 0.003$

y linking efficiency $\varepsilon_c = 0.952 \pm 0.009$

giving $\varepsilon_4 = 0.892 \pm 0.01$

ε_5: Hadron Chamber Efficiency

The downstream trackfinding algorithms FINDIT and SWEEP required few sparks in the road to operate. FINDIT required 3 sparks in the 4m planes plus the seed track and SWEEP required a minimum of 7 sparks with at least three 4m plane sparks. The gap efficiencies were measured using the data [43]. The efficiency is the probability that there will be sufficient sparks on the track and can be estimated from the gap inefficiencies to be

$$\varepsilon_5 = 0.995 \pm 0.005$$

ε_6: Muon Chamber Efficiency

Muon identification was principally made on the muon hodoscopes and the programs only looked for clusters of sparks in the rough vicinity of the projected track. Muon chamber inefficiency therefore had no effect on the data. However, muons were required to have perfect timing which is estimated to give an inefficiency of less than 0.1% (ref. 43)

i.e. $\varepsilon_6 > 0.999$

The inefficiency in the experiment for detecting on analysis an event therefore corresponds to a reduction in the observed muon flux by an amount

$$\epsilon = 0.549 \pm 0.01$$

This gives a corrected flux for the full data sample

$$N_\mu \epsilon = 0.35 \times 10^{10} \text{ muons.}$$

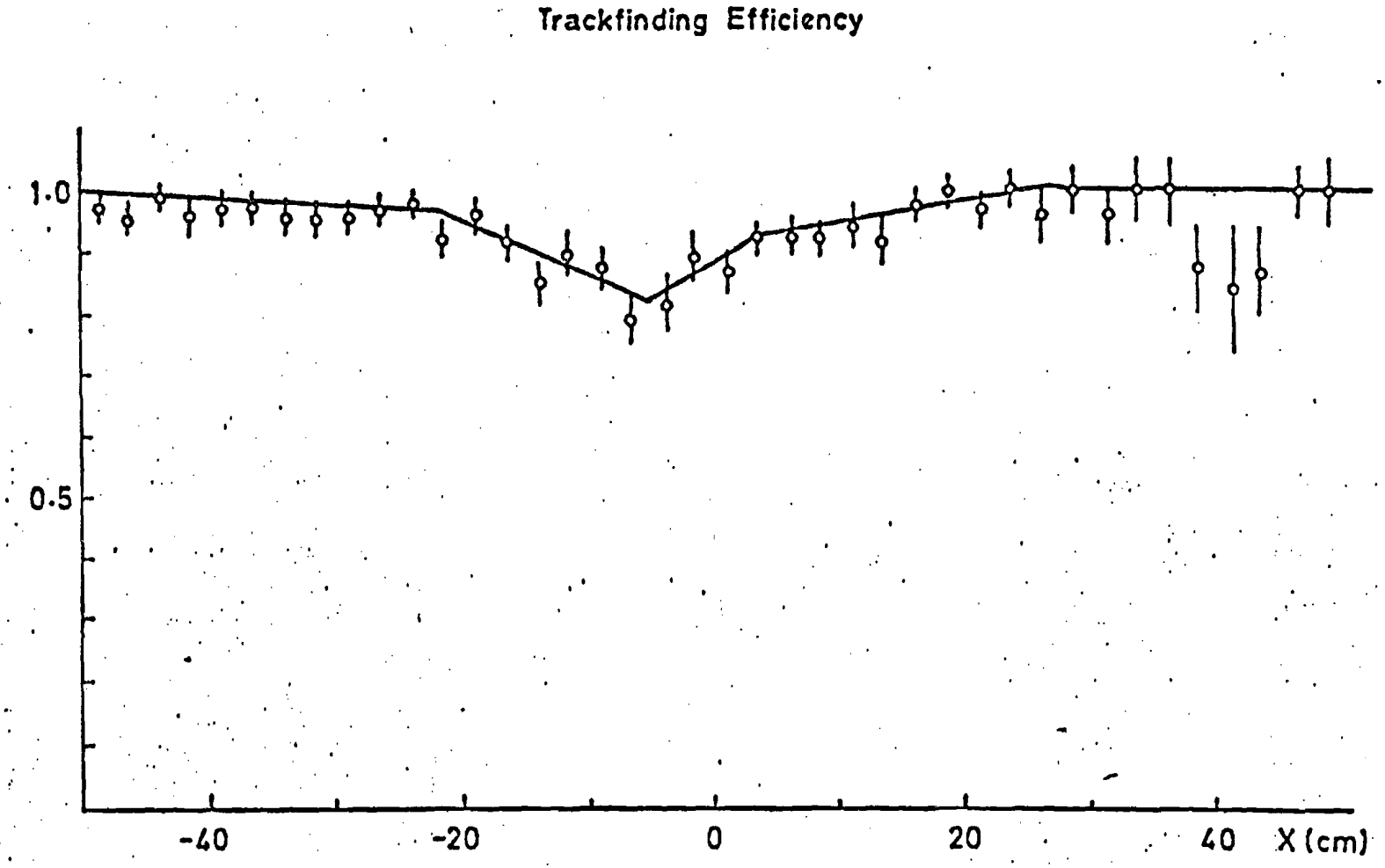

Fig. 4.1

Track Linking Through Magnet

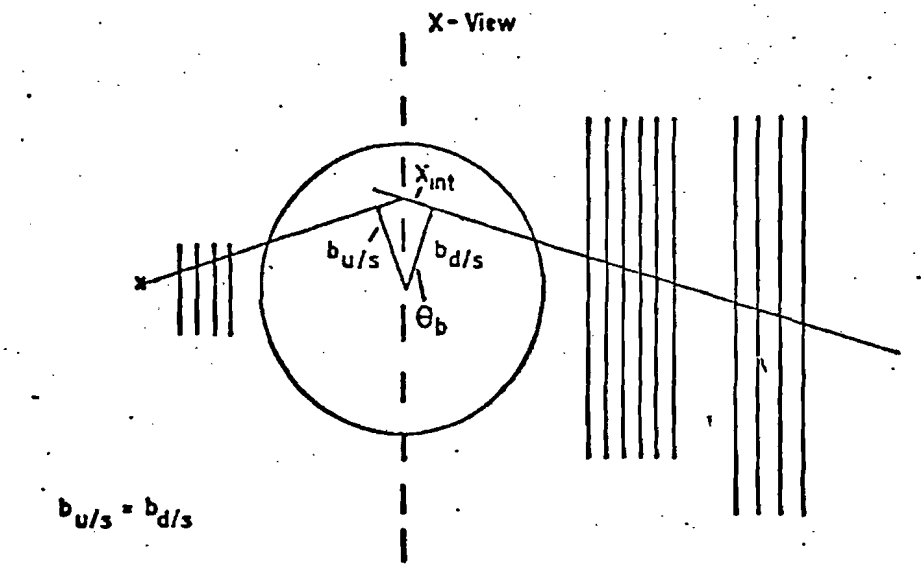

For Cylindrical Symmetry X_{int} u/s = X_{int} d/s

Fig. 4·2

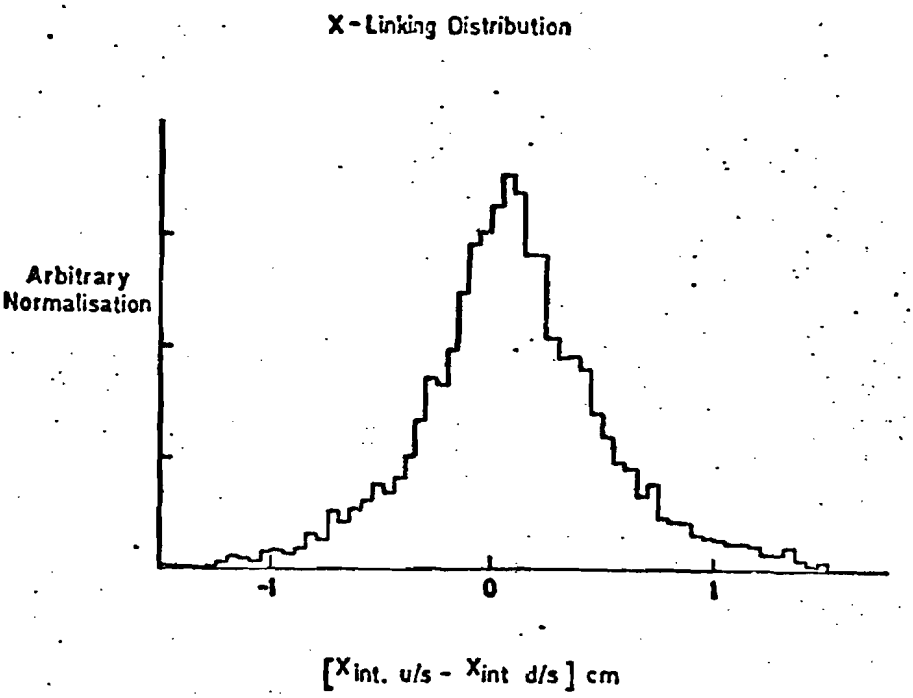

Fig. 4·3

Projected Y - Linking Distributions

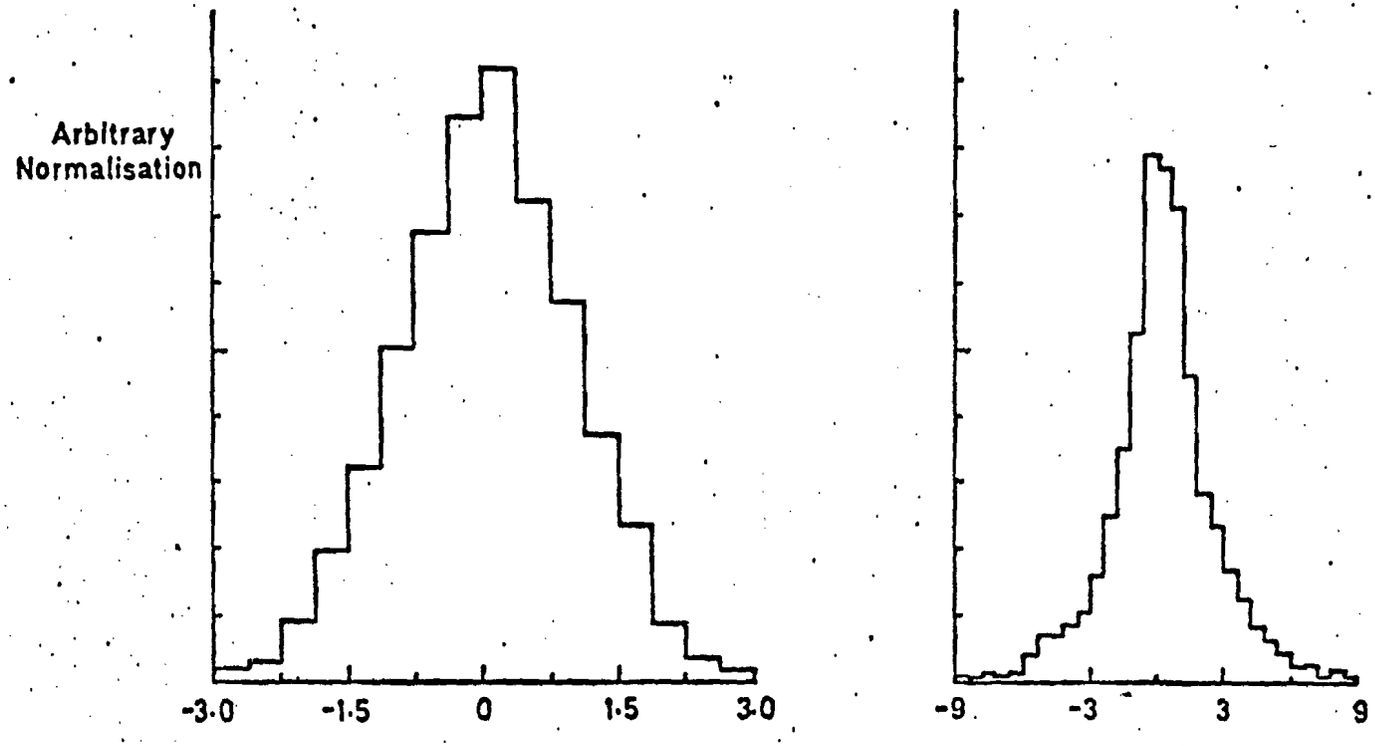

Fig. 4.4

Vertex Distributions

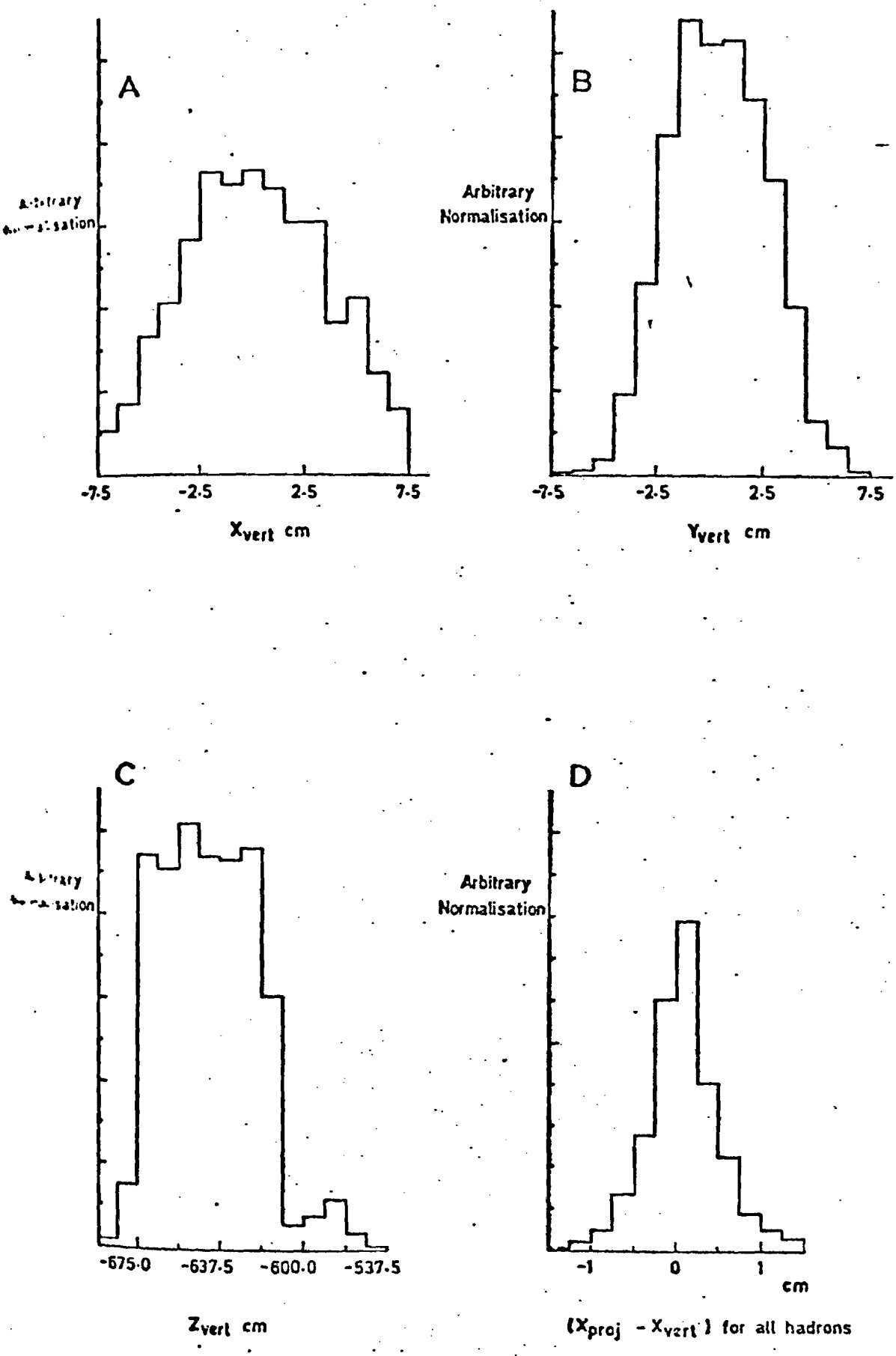

Fig. 4.5

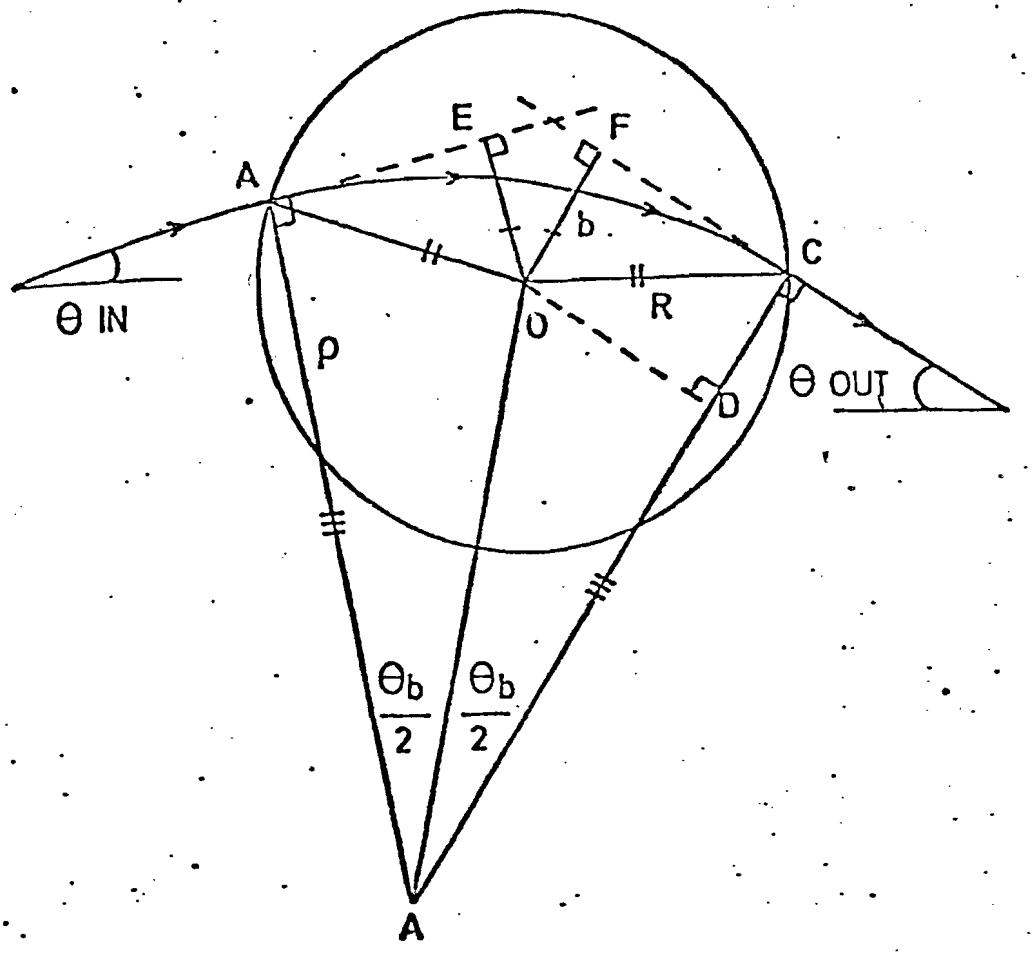

O is the centre of the magnetic field

A is the centre of the path taken by the particle

θ_b is the total bend in the field

b is the impact parameter

ρ is the radius of curvature of the particle track

FOR A HARD EDGE FIELD IN WHICH

B_o is the effective field in kilogauss

R is the effective field radius in metres

$$\rho = AD + DC = (R^2 - b^2)^{1/2} \cot\left(\frac{\theta b}{2}\right) + b$$

$$P = \frac{cB_o\rho}{10^{10}} \simeq 0.03\, B_o\rho$$ where P = momentum in GeV/c

c = velocity of light in metres/sec

Fig. 4.6

Effect of Appartus Rotation on Momentum Normalisation.

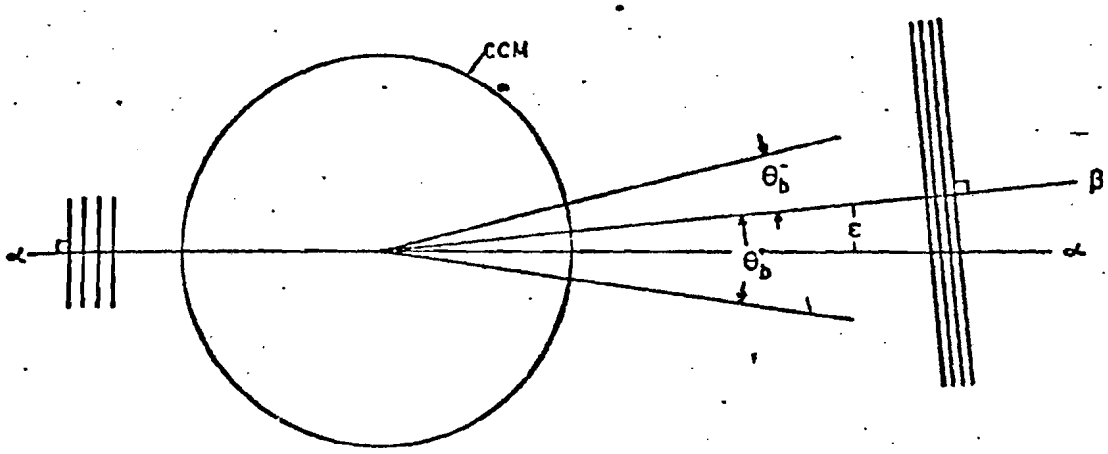

Fig. 4-7

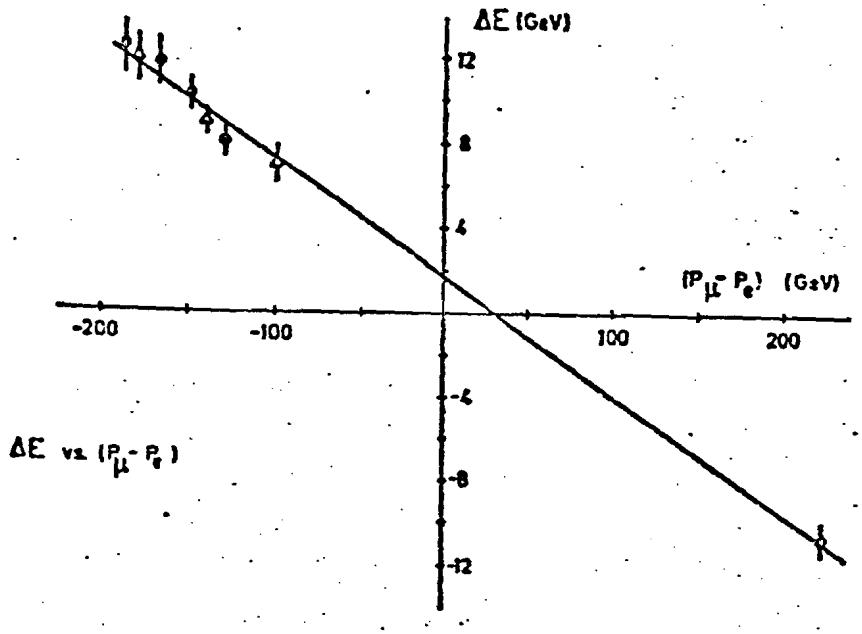

Fig. 4-8

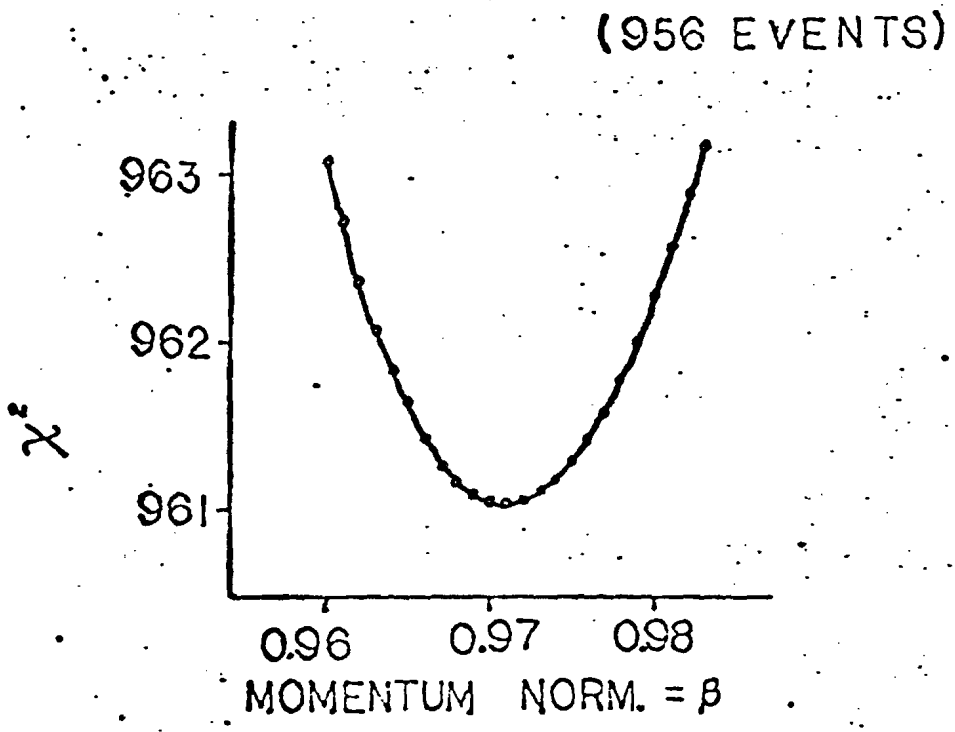

Momentum Normalisation Curve.

Fig. 4.9

High Multiplicity Event

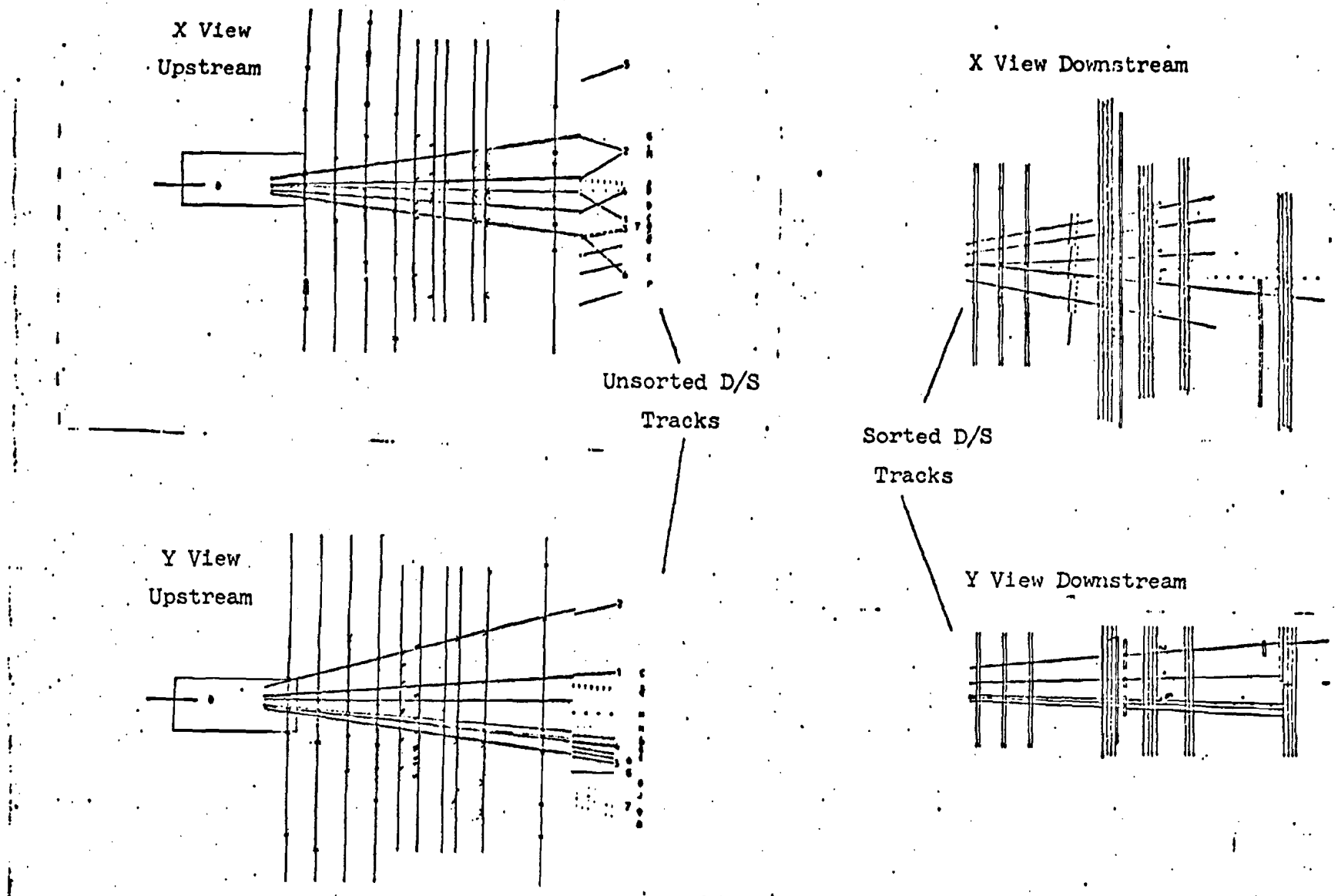

Fig. 4.10

Muon Electron Scatter

Y View.
Upstream

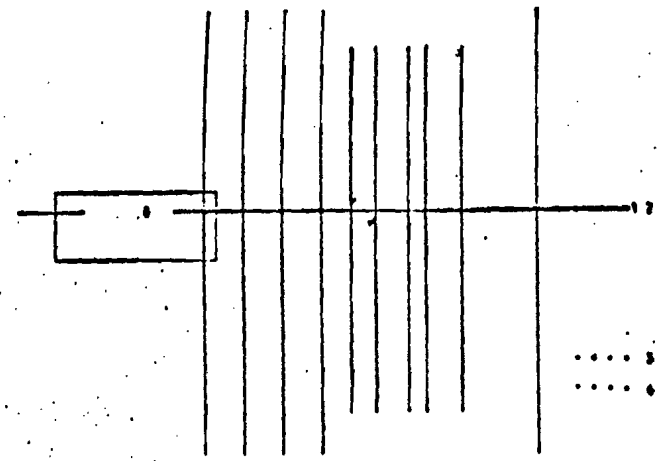

X View Downstream

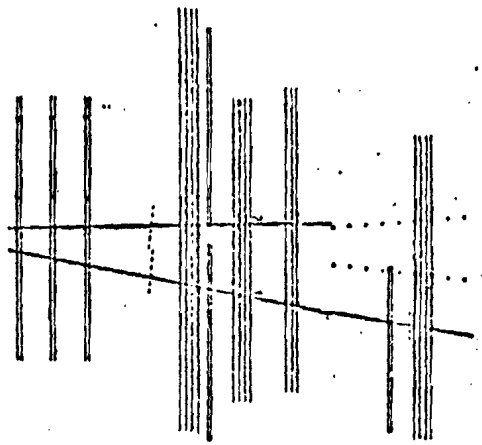

X View.
Upstream

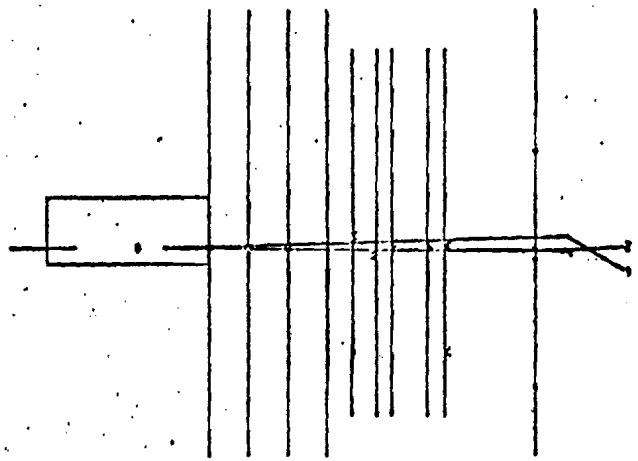

Y View Downstream

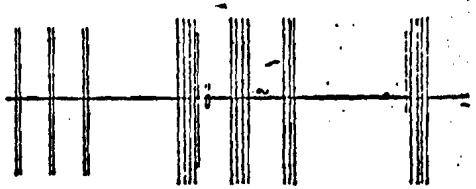

Fig. 1

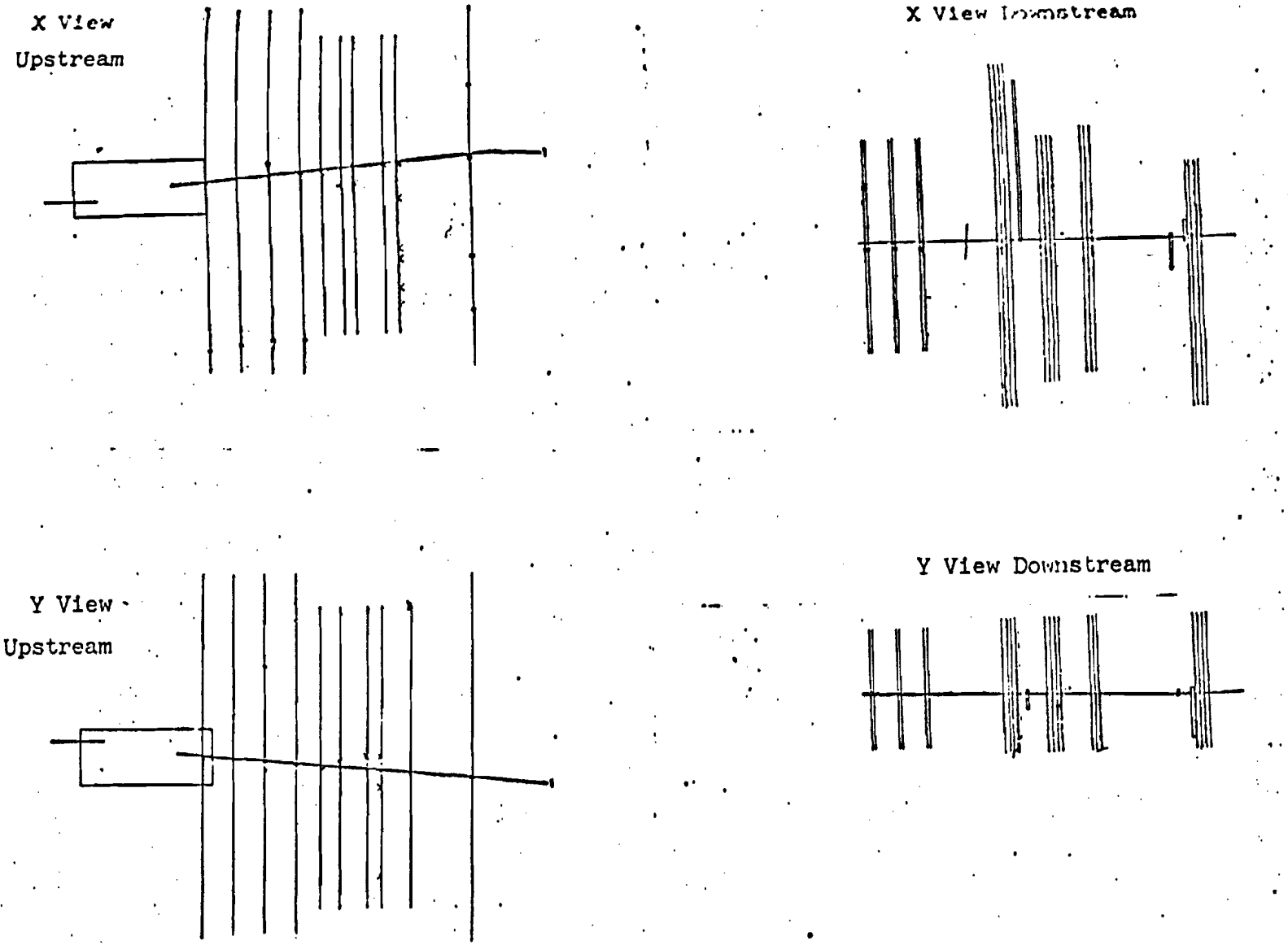
X View
Upstream
X View Downstream
Y View
Upstream
Y View Downstream

Fig. 4.12

Halo Trigger.

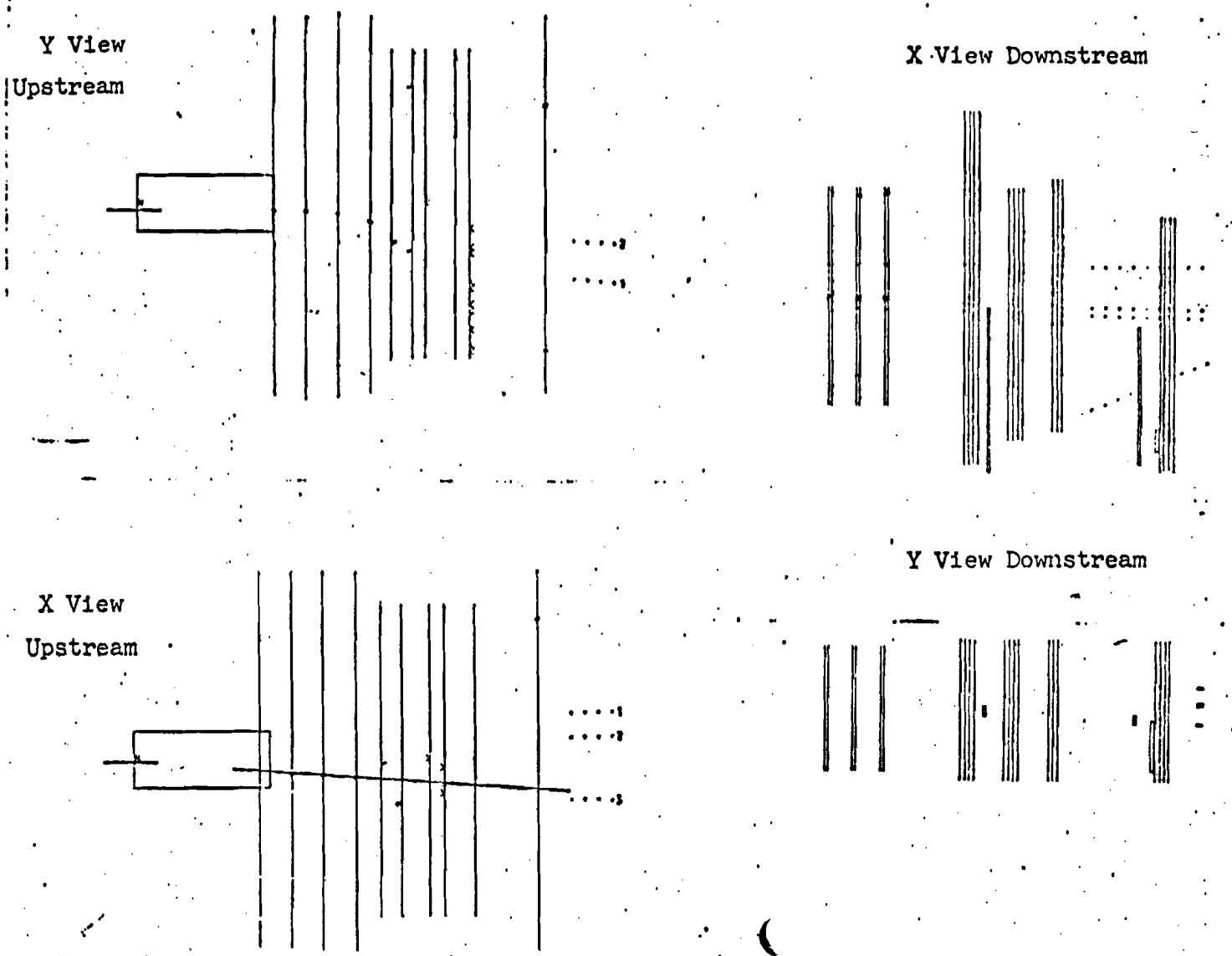

Fig. 4.13

Typical Deep Inelastic Event

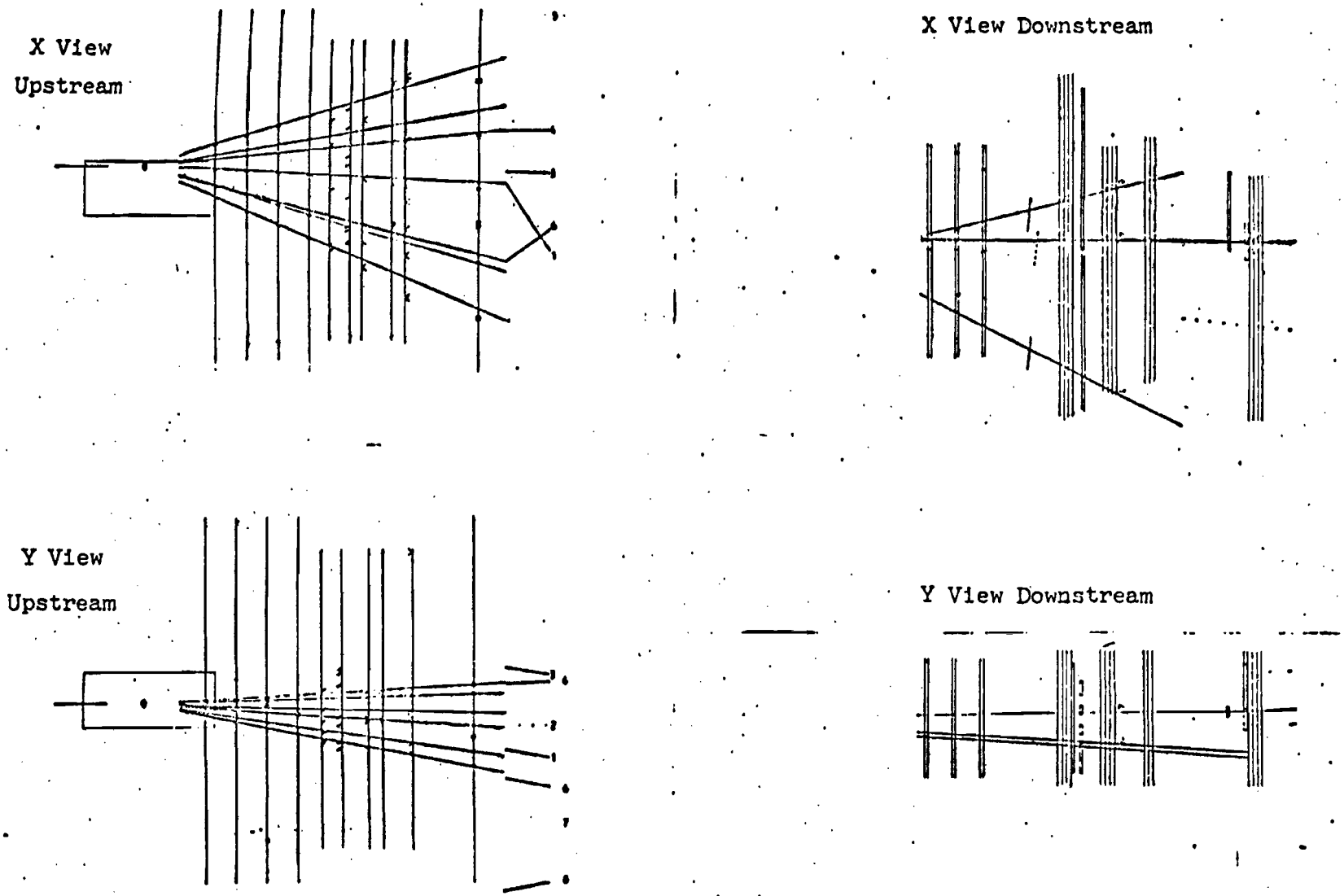

Fig. 4.14

CHAPTER 5

THE CERENKOV COUNTER

5.1 INTRODUCTION

A particle moving in an isotropic medium emits electromagnetic radiation if the velocity of the particle is greater than the velocity of light in that medium. This is known as the Cerenkov effect and was first observed by Cerenkov in 1934[44]. Subsequent experiments were carried out by Cerenkov and Vavilov to determine the source, intensity and spectral distribution of this radiation. These resulted in a classical interpretation of the effect by Tamm and Frank[45]. This theory gives the following important results:

(a) A particle moving in an isotropic medium with dielectric constant ϵ, and magnetic permeability $\mu = 1$ emits radiation of frequency ν at an angle θ to its direction of motion given by

$$\cos\theta = \frac{1}{\beta n(\nu)} \quad \text{for } \beta n(\nu) > 1 \tag{5.1}$$

where $\beta = \frac{v}{c}$ and $n(\nu) = \frac{1}{\sqrt{\epsilon(\nu)}}$ is the refractive index of the medium.

(b) For a particle of unit charge, the radiation energy per unit path length is given by

$$\frac{dW}{d\ell} = Z^2\frac{e^2}{c^2}\int_{\beta n>1}\left(1 - \frac{1}{\beta^2 n^2}\right)\omega d\omega \tag{5.2}$$

where $\omega = \frac{1}{\nu}$ and Z is the charge on the particle. Equations 5.1 and 5.2 do not depend on the mass of the particle. Therefore particles of different mass emit Cerenkov light in a given medium at the same β and therefore at different momenta. One can then use either the angular dependence of the radiation or its threshold behaviour to differentiate between particles of unequal mass.

A quantum mechanical treatment of Cerenkov radiation reproduces the results of the Tamm and Frank Theory. Detailed discussion of both the classical and quantum mechanical treatments of Cerenkov radiation and the experimental verification of the results obtained can be found in reference 46.

The remainder of this chapter describes the Cerenkov counter used in the spectrometer and discusses the information which can be obtained from it. The various off-line data checks carried out to obtain an estimate of the particle identification efficiency are also discussed.

5.2 THE CERENKOV COUNTER

A Cerenkov counter is a system designed to detect the Cerenkov radiation emitted from a charged particle traversing some medium and correctly associate the radiation with that particle. In practice, the precise design depends on whether one wants to be sensitive to the Cerenkov angle θ or simply detect the radiation. Typically, a closed box is used containing the radiator and an optical system consisting of a mirror or lens which focusses the radiation onto the photocathode of a photomultiplier and thereby detect it. In this experiment, the counter was required to provide particle identification over a large area for events with high multiplicity. To minimise confusion between different particles, a multicell design using an array of mirrors reflecting onto a corresponding array of photomultipliers was used. This design was also necessary from a constructional viewpoint as the counter was required to cover an area approximately 6m by 2m normal to the beam.

The containing box had dimensions 6 m by 2.5 m by 2.6m deep. It consisted of a steel frame covered with 3mm aluminium sheet on the four sides parallel to the beam and with an opaque mylar window 0.5 mm thick on the upstream and downstream faces (Fig. 5.1a). All joints were sealed with epoxy resin to make the assembly light-tight.

The light collection system consisted of 18 mirrors mounted in two banks of nine near the downstream window. These focussed onto corresponding photomultipliers mounted above and below the active area of the counter (Fig. 5.1b). The mirrors were 6 mm sheets of perspex formed with a radius of curvature of 2m and dimensions 0.6 x 1m. A film of aluminium evaporated onto the convex surface provided the reflective coating. The photomultipliers used were RCA 4522[47] which have 5 inch diameter photocathodes. They were mounted in Winston cones[48] to improve light collection efficiency.

Mirror Alignment

The target is seen downstream as a point source in the Y-Z plane and as an extended source in the X-Z plane due to the deflection of particles by the C.C.M. (Fig. 5.2). The mirrors were aligned so that light from a track hitting half way up a mirror was reflected into the centre of the photomultiplier. In the Z-X plane all mirrors pointed at the centre of the C.C.M. since the transverse momentum kick of the magnet (~2 GeV/c) was greater than the average transverse momentum of hadrons in the interaction (~500 MeV/c).

Shielding

The fringe field of the spectrometer magnet was approximately 30 gauss in the vicinity of the photo-tubes and these required substantial shielding to operate in this field (Fig. 5.3).

A 1000 turn bucking coil covering the length of the dynodes was fitted between the photomultiplier and its mu-metal mounting. A second section of mu-metal 6 mm thick surrounding the entire photomultiplier and Winston cone completed the mounting assembly. An additional layer of shielding surrounding this was required to completely absorb the fringe field. Cylinders of conetic shielding material[49] (which has a high field saturation level) could be obtained conveniently and this was used to complete the shielding. This level of shielding was sufficient to enable the photomultipliers to operate in the fringe field of the C.C.M. resulting from a full field strength of 1.4 Tesla. The currents required in the bucking coils were typically 1 amp.

Operation and Readout

The base circuit and resistor chain for the photomultipliers is shown in Fig. 5.4. This was set up to provide maximum gain as the yield

of photo-electrons from the first dynode was small. Typical operating voltages were in the range 2-2.5 kV.

Readout was via a 12 bit analogue-to-digital converter (LRS2249A) coupled to the anode of the phototube. The ADC's had a full range from 0-256 pc covering the readout range 0-1024 counts. The pedestals on the ADC's were set at 10-20 counts, corresponding to 2.5-5 pc. A cell was considered 'lit' when the pulse height recorded in the ADC was greater than the pedestal. Typical pulse distributions obtained with tracks going through cells 4 and 13 are shown in Fig. 5.5.

In tests at the start of data-taking, a high inefficiency was observed in cells in the beam region (cells 5 and 14). This inefficiency was due to the flux of particles in the beam and near-beam region causing saturation in the phototube bases. To enable these cells to work efficiently outside the beam region, a deadener 35 cm x 25 cm was inserted to prevent light from particles in this region from reaching the mirrors.

5.3 THE CERENKOV MEDIUM AND EFFICIENCY

A single Cerenkov counter does not permit a complete identification or pions, kaons and protons at the same momentum. If one can only detect the presence or absence of Cerenkov radiation (as in this counter), then the threshold behaviour of the radiation completely determines the level of separation possible. Therefore, from Eqn. 5.1, in any given medium

$$p_{\pi}^{th} < p_{K}^{th} < p_{p}^{th}$$

where $P_{\pi,K,p}^{th}$ is the threshold momentum for π, K, p to emit Cerenkov radiation. For a particle with momentum p, the following separation can be obtained:

(a) $P < p_{\pi}^{th}$: No identification possible since no hadrons will emit radiation.

(b) $p_{\pi}^{th} < P < p_{K}^{th}$: Particles which emit radiation are definitely pions. Those which do not may be kaons or protons.

(c) $p_{K}^{th} < P < p_{p}^{th}$: Particles which emit radiation may be pions or kaons. Those which do not are protons.

(d) $P > p_{p}^{th}$: No identification possible since all hadrons will emit radiation.

The above classification clearly assumes perfect efficiency. Inefficiency (e.g. as results from quantum inefficiency near threshold) introduces ambiguity into those classifications which depend on no Cerenkov radiation being observed. However, no ambiguity exists in pion classification (b) which although possibly inefficient is the sole

positive identification available in this counter, whereas classification (d) is useful in measuring inefficiencies.

Choice of Medium

An important factor in the choice of medium is to maximise the range of momentum over which the above separation is possible. A second important consideration is to have as many photons as possible emitted by the particle when radiating in order to obtain good detection efficiency.

Particles observed downstream in the spectrometer have momenta greater than 6 GeV/c and therefore a corresponding β very close to 1. This then requires $n(\nu)$ close to 1 to obtain the required ranges in threshold momenta for π's, K's and p's. However, as can be seen from Eqn. 5.2, as $\beta \to 1$ and $n \to 1$, $\frac{dW}{d\ell}$, the radiated energy per unit path length decreases. Therefore, the detection efficiency becomes important, particularly as the length of radiator had been constrained by other equipment in the spectrometer to be a maximum of 2m.

For Cerenkov radiation incident on the photocathode of a photomultiplier, the number of secondary electrons arriving at the first dynode is given by[46]

$$N(\beta) = 2\pi\alpha\eta\xi \int_{\lambda_{min},\ \beta n > 1}^{\lambda_{max}} \left(1 - \frac{1}{\beta^2 n^2}\right) \frac{S(\lambda)}{\lambda^2} d\lambda \qquad (5.3)$$

where η = collection efficiency of the first dynode

ξ = collection efficiency of the optical system

α = fine structure constant.

λ_{min}-λ_{max} = transparent region of the phototube window.

$S(\lambda)$ = quantum efficiency of the photocathode as a function of wavelength.

A graph of the quantum efficiency for an R.C.A. 4522 phototube is shown in Fig. 5.6. A fourth order polynomial fit through 12 points taken from this graph was used to obtain $S(\lambda)$ (Fig. 5.7). The transparent range of the quartz window used was 2200-5900 Å.

By neglecting any light collection inefficiency in the optical system, the maximum number of photo-electrons arriving at the first dynode can be calculated from Eqn. 5.3. Graphs of N as a function of momentum for π's, K's and P's in Nitrogen, Neon and Freon 13 (refractive index 1.00029, 1.00007 and 1.00072 respectively) are shown in Fig 5.8. was assumed to be $\sim$0.5. The calculation gives the maximum numbers of photo-electrons to be roughly 12, 2.5 and 32 for Nitrogen, Neon and Freon 13 respectively. Nitrogen was chosen as the radiator: it gives better separation than Freon 13, much better quantum efficiency than Neon and is the least expensive. These calculations, however, do not agree with the measured inefficiency of the counter cells. This will be discussed further in Section 5.5.

During the initial part of the run, the counter was filled with air to allow easy access. However, the main section of the data was obtained with a filling of dry nitrogen at atmospheric pressure - no difference could be observed between the two data sets.

Variation of Refractive Index with Temperature and Pressure

The dependence of the refractive index of a gas on density is given by the well-known Clausius-Mossotti formula

$$\frac{n - 1}{n + 2} \propto \rho \qquad 5.4$$

where n is the refractive index of the gas and ρ its density.

Variations of temperature and pressure of a gas, which affect its density therefore alter its refractive index also. This variation is approximately given by[50]

$$n_{T,P} = (n_s - 1) \times \frac{P[1 + P(61.3 - T) \times 10^{-10}]}{96095.4 \times (1 + 0.003661T)} \qquad 5.5$$

assuming $\rho_{air} \tilde{\propto} P_{N_2}$ at S.T.P.

where

n_s is the refractive index of nitrogen at S.T.P.

P is the pressure in N/m^2

T is the temperature in °C.

Pressure and temperature monitors were installed in the Cerenkov counter to measure these variations at two heights. These never worked in a reliable fashion and there was insufficient time to repair or replace them before data-taking began. To access the counter once it had been filled with nitrogen would have taken one day of pumping air as a minimum and two days to refill. At that stage in the experiment, the monitors were abandoned. It is now apparent that this was not a major loss of information.

Table 5.1 shows the refractive index at three pressures and four temperatures as calculated from Eqn. 5.5 The values chosen correspond to reasonable variations which might be expected during the autumn at Fermilab. The average value of the refractive index for the 12 points in the table is 1.000291 with a standard deviation of 9.8×10^{-5}. The maximum variations from the mean are -15.6×10^{-5} and $+15.8 \times 10^{-5}$. Fig. 5.9 shows the variation in the Cerenkov thresholds for π's, K's and P's as a function of refractive index. Clearly this variation is more important for K's and P's but the threshold momenta change by $\sim$1 GeV/c

in the range $1.000280 < n < 1.00030$. This variation is not quite negligible and had a minor effect on the final particle classification scheme described in Section 6.

Frequency Dependence on Cerenkov Thresholds

As the refractive index of nitrogen depends on frequency, the Cerenkov momentum thresholds also depend on the frequency of the radiation emitted. Fig. 5.10 shows this dependence assuming $n_{air}(\lambda) \tilde{\approx} n_{N_2}(\lambda)$ [51]. Two other frequency dependent effects must also be considered simultaneously with this:

(a) The Cerenkov radiation spectrum has a $\frac{1}{\lambda}$ distribution.

(b) The transparent region of the quartz window is 2200-5900 Å.

Together, these effects restrict the principal variations to the range 2200-4000 Å. Since the refractive index in this region is roughly 1.000280-1.000310 the effect of frequency variation can be dealt with using the same criteria as that of temperature and pressure variation. A shift in threshold momenta from their mean values was made to obtain some little contamination just below threshold from extreme variations as will be seen in Section 6.

5.4 PARTICLE CLASSIFICATION

As was observed in Section 5.3, Cerenkov thresholds in nitrogen are smeared by frequency variations in refractive index. This variation will be disregarded in this description of the rough particle classification and the standard value of refractive index for nitrogen at atmospheric pressure and 20°C used[51], (1.000290). β_{th} is therefore 0.99971 and the momentum thresholds for Cerenkov radiation can be determined from equation 2.1:-

(a)	Pions	:	5.8 GeV/c
(b)	Kaons	:	20.5 GeV/c
(c)	Protons	:	38.9 GeV/c

Hadrons can then be classified according to their momentum and the status of the Cerenkov cell they pass through.

(a) Hadrons with a momentum in the range 6-20.5 GeV/c which light the cell they pass through are definitely pions. (Class 1).

(b) Hadrons with a momentum in the range 20.5-39 GeV/c which light the cell they pass through are either pions or kaons. (Class 2).

(c) Hadrons with a momentum in the range 6-20.5 GeV/c which fail to light the cell they pass through are either protons or kaons. (Class 3).

(d) Hadrons with a momentum in the range 20.5-39 GeV/c which fail to light the cell they pass through are definitely protons. (Class 4).

(e) All particles with a momentum greater than 39 GeV/c should light the cell they pass through.

The above classification assumes 100% efficiency in the Cerenkov cells. These efficiencies are therefore critical to any statement made above particle classification and should be understood completely. Near threshold, quantum inefficiency in the phototube requires detailed

consideration. In particular, a high inefficiency will cause major backgrounds in classes 3 and 4 from pions which fail to light the cell they pass through. The remaining sections are devoted to various off-line estimates of this inefficiency and techniques for minimising it.

5.5 ESTIMATES OF CELL INEFFICIENCIES

Mirror Positions

A reliable estimate of the cell inefficiencies requires an accurate knowledge of the mirror positions in the experimental coordinate system. However, the use of these positions was complicated by the smearing effect of the Cerenkov light cone (for $\beta = 1$, $\cos\theta_c = \frac{1}{n}$ which corresponds to a radius in nitrogen of 4.7 cm over 2 metres) and also by the possibility of light collection inefficiency at the mirror edges.

Experimentally, the edges were determined in the following manner (in an identical fashion to the determination of counter edges[42]). Good downstream tracks were picked in the vicinity of the edge to be determined (20 cm) - these positions were roughly known from survey measurements. Tracks which fall definitely within the x limits(horizontal) of the cell were used to determine the y edge (vertical) and vice versa for the x edge. Then in bins of 1.25 cm vertically (horizontally) across this strip the ratio

$$N_{Lit}/_{N}$$

was measured, where N is the number of tracks in each bin and N_{Lit} is the number which lit the cell in question (Fig. 5.11).

The following cuts were made on tracks to reduce background:-

(a) Class 1 timing.

(b) Downstream track linked in x or y to an upstream track.

(c) No other track in the central region of the cell.

Muon and hadron tracks were both used for this analysis. Typical distributions for neighbouring cells are shown in Fig. 5.12. Statistics limited the accuracy with which the edges of the outer cells could be determined to ±1 cm. The edges of the inner cells could be determined to ±0.5 cm. The position of the beam deadener was determined in a similar fashion. (Fig. 5.13)

Determination of Cell Inefficiencies Using the Scattered Muon

The momentum threshold for muons to emit Cerenkov radiation in nitrogen is 4.2 GeV/c. The acceptance of the spectrometer required that all scattered muons had a momentum greater than 10 GeV/c and therefore all muons should have lit the Cerenkov cell they passed through. Therefore, particles that had been identified as muons by the track-finding programs (i.e. have passed through the hadron absorber) could be used to determine cell efficiencies. There was, however, the disadvantage that only half of the Cerenkov cells could be analysed by this method - only those through which positive particles pass. In fact only six cells were illuminated by muons with sufficient statistics to allow a determination of their inefficiency.

As a first step in removing spurious tracks, the standard cuts on duplicates, timing, linking and vertex pointing were made on the muon tracks (Chapter 4). In addition, the muon tracks which passed the above cuts were required to point outside the K-veto and within the outer limits of the M hodoscope. These cuts were sufficient to define good muon tracks. Two standard geometric cuts were used to restrict particles to high efficiency regions of the counter:

Tracks were required to point at least 2.5 cm inside the boundary of the cell. This allowed for the Cerenkov cone, any edge inefficiency and any p track pointing uncertainty.

The track must point outside the deadener.

A final requirement, which was only used in this part of the analysis was that there be only one track in the cell.

Having made these requirements, the number of tracks passing through the cell and the number which fail to light it throughout the data set were used to find the inefficiency. Table 5.2 shows the average inefficiency for cells 3-5 and 12-15 using this method for the entire

data set (integrated flux of 3.8×10^{10} μ's). The errors given are statistical. The average inefficiency is dominated by cells 3, 4, 12 and 13 and is 1.7 ± 0.2%. To investigate any variation of efficiency with position, the cells were divided into three horizontal and vertical bands and the same analysis carried out (Fig. 5.14). The results are shown in Tables 5.3 and 5.4. The data are primarily in the central band of the cells (Region 1_V) and statistics are clearly limited. However, no significant variation with position was observed

Determination of Cell Inefficiencies from the Observed Pulse Height Distribution

The photo-cathode/dynode system of a photomultiplier gives rise to an inefficiency due to quantum fluctuations in the number of photo-electrons collected by the first dynode. If the mean number of photo-electrons collected is n the number collected for any pulse (m) follows a Poisson distribution with mean n and variance n. Therefore, the probability e^{-n} is the probability that m = 0 and is an estimate of the quantum inefficiency of the phototube.

For an observed pulse height distribution with mean μ and variance σ^2, $\frac{\mu^2}{\sigma^2}$ gives an unbiased estimate of n - the mean number of photo-electrons collected. This can then be used to calculate the corresponding quantum inefficiency ε. If there are N entries in the pulse height distribution then the relative error on n is $\frac{1}{\sqrt{N}}$ and this can be used to calculate upper and lower errors on ε, (δ^+, δ^-). A great advantage of this technique was that relatively little data (~50 events) allowed a reasonable estimate of the inefficiency and more important, all cells could be analysed.

The standard cuts described in this chapter were used to define hadrons and the pulse height for those which lit the cell they passed

distributions was then calculated and the corresponding cell inefficiency deduced. A variation of pulse distribution with momentum is predicted by Eqn. 5.3 and therefore this pulse analysis was carried out for three momentum bands for hadrons, and for muons:-

(a) Hadrons with momenta in the range 6-18 GeV/c.

(b) Hadrons with momenta in the range 22-40 GeV/c.

(c) Hadrons with momenta greater than 45 GeV/c.

(d) Muons only.

The average inefficiencies for these classes of particles are given in Tables 5.5-5.8. To investigate any variation of inefficiency with position, vertical and horizontal scans were carried out where there were sufficient data to obtain meaningful results (Tables 5.9-5.15). All particles with a momentum greater than 45 GeV/c should have lit the Cerenkov cell they passed through. Therefore, the failure rate of this class also gave a direct measure of the inefficiency. The average inefficiency for the cells illuminated by these tracks is given in Table 5.16. A horizontal scan was also possible (Table 5.17).

This analysis produced a large amount of data on cell inefficiencies. The results are consistent with:-

(a) No large variation of inefficiency among the cells.

(b) No observable variation with position in the cell.

(c) No observable variation with momentum.

Elastic ρ Mesons

The $\rho \rightarrow \pi^+\pi^-$ decay could also be used as a source of particles to use in a measurement of the Cerenkov cell inefficiencies. Moreover, one might hope to obtain a reasonable direct estimate of inefficiencies in the

Elastic ρ mesons were selected using the following simple cuts (Fig. 5.15):-

(a) A single muon observed downstream.

(b) Only two hadrons downstream with one positive and one negative.

(c) Each hadron track links to both x and y proportional chamber tracks.

(d) Missing energy in the event was required to be less than 20 GeV/c^2.

(e) Laboratory opening angle greater than 5.5 mrad.

(e) $|M_{\pi^+\pi^-} - M_\rho| < 0.4$ where $M_{\pi^+\pi^-}$ is the invariant mass of the dipion system.

The standard Cerenkov geometrical cuts were then applied to the hadron tracks and the failure rates measured for the various cells illuminated (Table 5.18). Statistics are poor, particularly in the region of most interest (the outer cells). Clearly this only provides a consistency check on the previous estimates of the cell inefficiencies.

5.6 REMARKS AND CONCLUSIONS

Three methods of estimating cell inefficiencies and one consistency estimate have been made. A comparison of the experimental measurements of cell inefficiencies of Section 5.5 shows:-

(a) The direct measurement of cell inefficiency and the indirect method of estimating the efficiency from the pulse distribution are consistent within experimental errors. The direct measurements using pions from ρ decay are also consistent with these results though with large errors.

(b) Vertical and horizontal scans across the mirrors show no statistically significant variation of efficiency.

(c) The average inefficiency of the counter cells as a whole was $2.0 \pm 0.1\%$ corresponding to a mean effective number of photo-electrons collected at the first dynode of 3.95.

From these results it is clear that the theoretical estimate of the number of photo-electrons collected at the first dynode was incomplete. The two most obvious sources of errors are the estimate of the light-collection efficiency of the phototube-mirror system and of the quantum efficiency of the photocathode. No more reliable estimates of these can be obtained in the experimental operating conditions than those already given. Assuming the measured efficiency, however, one can use the estimate of the quantum inefficiency to obtain another set of curves of the mean number of photo-electrons collected as a function of momentum (Fig. 5.16). This then introduces the fact that the quantum inefficincy has a significant effect on particle identification. Moreover, the effect of threshold smearing must also be included.

It was decided to obtain as large a kaon identification range as possible consistent with high detection efficiency. The following momenta were therefore used for the selection criteria:

(a) 12.4 GeV/c - the momentum at which 95% of all pions should light the Cerenkov counter.

(b) 21.2 GeV/c - the maximum value for P_K^{th} possible in the transparent region (the minimum is 20 GeV/c).

(c) 31.4 GeV/c - the momentum at which 90% of all kaons should light the Cerenkov counter.

(d) 38.2 GeV/c - the minimum momentum at which protons should light the Cerenkov counter.

The 95% confidence level for pions is necessary since these compose approximately 90% of all hadrons and would therefore produce an unacceptable background below this level. Even a 5% failure rate results in a background of 20% in the kaon signal. The 90% level for kaons was chosen to provide a reasonable range over which to search for protons. Kaon inefficiency would then result in a total background of 1% failures for all hadrons. Clearly any proton signal would be required to be significantly greater than this.

Smearing in the Cerenkov threshold due to variations in refractive index will only result in a maximum of 10% of kaons in momentum range 20.0-21.2 GeV/c lighting the Cerenkov counter. This would only cause an insignificant background to the pion signal while significantly increase the range over which kaon identification should be possible. The choice of 38.2 GeV/c, the minimum momentum at which protons emit Cerenkov radiation, ensures an unambiguous interpretation of failures below that momentum as protons if inefficiency is negligible.

With these reservations, the following particle selection criteria were determined:-

1.	Momentum < 12.4 GeV/c:	Lit:	Definitely pions
		Unlit:	Kaons, protons and a large pion background.
2.	12.4 < Momentum < 21.2 GeV/c:	Lit:	Pions with a very minor kaon background.
		Unlit:	Kaons, protons and a maximum pion background of 5%.
3.	21.4 < Momentum < 31.4 GeV/c:	Lit:	Pions and kaons up to 90%.
		Unlit:	Protons, kaons below 90%, and pion background of ∿3%.
4.	31.4 < Momentum < 38.2 GeV/c:	Lit:	Pions and kaons.
		Unlit:	Protons, a 2% pion background and a 1% kaon background, (maximum).
5.	Momentum ≥ 38.2 GeV/c:	Lit:	All hadrons
		Unlit:	Inefficiency of ∿2%.

These criteria were used to determine the classification of hadrons into pions, kaons and protons in the analysis discussed in the following chapters.

TABLE 5.1

VARIATION OF REFRACTIVE INDEX WITH TEMPERATURE AND PRESSURE

δ T°C	15	21	27	32
P (in Hg)				
29	288.1	281.1	275.4	270.9
30	296.9	290.8	285.0	280.0
31	306.8	300.5	294.5	289.7

δ = $(N_{T,P} - 1) \times 10^6$ where $N_{T,P}$ is the refractive index at T°, P in.

$\langle\delta\rangle$ = 291 for $15 < T < 32$°C

σ = 9.8 for $29 < P < 31$ in. Hg.

TABLE 5.2

AVERAGE CELL INEFFICIENCY FROM MUON FAILURE RATE

Cell	Inefficiency (%)	+/-
3	3.8	1.2
4	1.2	0.3
5	5.9	5.7
12	5.8	1.6
13	1.3	0.3
14	0.0	5.6

Average overall is 1.7 ± 0.2%.

TABLE 5.3

HORIZONTAL INEFFICIENCY SCAN FROM MUON FAILURE RATE

Cell	Region 1_H Inefficiency (%)	+/-	Region 2_H Inefficiency (%)	+/-	Region 3_H Inefficiency (%)	+/-
3	0.0	11.0	2.7	1.9	4.6	1.9
4	1.0	0.7	1.0	0.3	0.6	0.2
5	2.9	0.8	5.5	1.5	2.9	2.0
12	8.3	8.3	4.3	3.1	7.8	2.5
13	2.7	1.2	0.9	0.3	1.3	0.3
14	2.2	0.8	1.9	1.8	0.0	19.0

TABLE 5.4

VERTICAL INEFFICIENCY SCAN FROM MUON FAILURES

Cell	Region 1_V Inefficiency (%)	+/-	Region 2_V Inefficiency (%)	+/-
3	3.6	1.3	6.7	6.7
4	1.2	0.3	4.8	4.8
5	12.5	12.5	0.0	8.3
12	5.2	1.7	14.3	10.1
13	1.3	0.3	0.0	3.0
14	0.0	3.5	0.0	16.7

TABLE 5.5

AVERAGE INEFFICIENCY FROM PULSE HEIGHT DISTRIBUTION FOR $6 < P_{Had} < 18$ GeV/c

Cell	$\langle N_{pe} \rangle$	+/-	Inefficiency (%)	δ^+	δ^-
2	3.6	0.6	2.7	2.1	1.2
3	4.7	0.4	0.9	0.5	0.3
4	4.0	0.7	1.8	2.0	0.9
5	2.6	1.1	7.6	15.8	5.1
6	2.7	0.5	6.6	4.0	2.5
7	4.8	0.5	0.8	0.6	0.3
8	3.2	0.5	4.2	2.8	1.7
9	14.1	10.0	0.0	1.6	0.0
11	3.3	0.6	3.6	3.2	1.7
12	3.2	0.3	4.3	1.6	1.2
13	3.5	0.6	3.1	1.5	1.4
14	4.8	2.0	0.8	5.5	0.7
15	3.3	0.6	3.7	3.1	1.7
16	2.5	0.3	7.9	2.4	1.9
17	3.2	0.6	4.0	3.3	1.8
18	2.9	2.6	5.3	68.1	4.9

TABLE 5.6

AVERAGE INEFFICIENCY FROM PULSE HEIGHT DISTRIBUTION FOR $22 < P_{Had} < 40$ GeV/c

Cell	$\langle N_{pe} \rangle$	+/-	Inefficiency (%)	δ^+	δ^-
3	8.0	3.5	0.0	1.1	0.0
4	3.5	0.4	3.0	1.3	0.9
5	3.7	1.0	2.5	4.2	1.6
6	3.9	0.4	2.0	1.0	0.6
7	4.7	2.8	0.9	14.8	0.8
12	5.3	2.4	0.5	4.9	0.5
13	3.4	0.3	3.2	1.2	0.9
14	3.4	0.8	3.2	3.7	1.7
15	4.4	0.4	1.3	0.7	0.5
16	3.0	1.5	4.7	17.1	3.7

TABLE 5.7

AVERAGE INEFFICIENCY FROM PULSE HEIGHT DISTRIBUTIONS FOR $P_{Had} \geq 45$ GeV/c

Cell	$\langle N_{pe} \rangle$	$^{+}/_{-}$	Inefficiency (%)	δ^{+}	δ^{-}
4	5.1	0.8	0.6	0.7	0.3
5	4.8	0.4	0.8	0.4	0.3
6	4.6	0.9	1.0	1.5	0.6
13	3.4	0.6	3.2	2.6	1.5
14	5.2	0.4	0.6	0.3	0.2
15	5.8	1.2	0.3	0.7	0.2

TABLE 5.8

AVERAGE INEFFICIENCY FROM PULSE HEIGHT DISTRIBUTION FOR MUONS ONLY

Cell	$\langle N_{pe} \rangle$	$^{+}/_{-}$	Inefficiency (%)	δ^{+}	δ^{-}
3	3.9	0.5	2.1	1.5	0.9
4	4.6	0.2	1.0	0.2	0.2
5	3.4	0.2	3.2	0.9	0.7
12	3.1	0.5	4.7	2.8	1.8
13	4.2	0.2	1.5	0.3	0.2
14	5.4	0.4	0.5	0.2	0.2

TABLE 5.9

CELL INEFFICIENCY FROM PULSE DISTRIBUTION FOR $6 < P_{Had} < 18$ GeV/c - HORIZONTAL SCAN

Cell	Region 1_H Inefficiency (%)	δ^+	δ^-	Region 2_H Inefficiency (%)	δ^+	δ^-	Region 3_H Inefficiency (%)	δ^+	δ^-
2	5.8	13.7	4.1	3.3	5.1	2.0	1.4	2.4	0.9
3	1.8	1.8	0.9	0.9	0.9	0.4	0.3	0.5	0.2
4	1.7	2.7	1.0	3.3	6.8	2.2	0.0	0.6	0.0
5	13.9	37.9	10.2		-		7.3	30.9	5.9
6	12.9	34.2	9.4	2.7	5.4	1.8	7.6	6.1	3.4
7	0.5	0.8	0.3	0.9	1.2	0.5	1.2	1.8	0.7
8	3.6	3.7	1.8	6.8	8.6	3.7	1.0	6.3	0.9
9	0.0	1.6	0.0		-		1.0	6.3	0.9
11	0.2	4.6	0.2	0.6	2.2	0.5	11.6	10.0	5.4
12	5.3	3.8	2.2	3.6	2.4	1.4	4.0	3.5	1.9
13	2.3	3.1	1.3	2.4	5.1	1.6	8.9	19.9	6.1
14	0.0	2.7	0.0	0.0	9.4	0.0	3.9	21.6	3.3
15	1.7	13.2	1.5	0.9	2.9	0.7	7.4	6.9	3.6
16	5.5	3.9	2.3	6.3	3.8	2.4	13.1	6.4	4.3
17	1.7	2.9	1.1	6.4	9.6	3.8	10.8	21.0	7.1
18	5.3	4.9			-			-	

TABLE 5.10

CELL INEFFICIENCY FROM PULSE HEIGHT DISTRIBUTION FOR $6 < P_{Had} < 18$ GeV/c - VERTICAL SCAN

Cell	Region 1_V			Region 2_V			Region 3_V		
	Inefficiency (%)	δ^+	δ^-	Inefficiency (%)	δ^+	δ^-	Inefficiency (%)	δ^+	δ^-
1	1.8	18.4	1.6	-	-	-	-	-	-
2	3.1	3.4	1.6	3.3	5.0	2.0	1.7	12.4	1.5
3	0.9	0.7	0.4	0.6	0.8	0.3	0.7	4.2	0.6
4	1.6	1.8	0.6	4.1	3.9	2.9	0.7	29.1	0.7
5	14.0	31.8	9.7	3.0	49.5	2.8	0.2	99.0	0.2
6	3.2	3.7	1.7	13.8	11.5	6.3	0.1	7.5	0.1
7	3.0	1.6	1.0	5.4	4.7	2.5	12.4	17.8	7.3
8	3.6	3.8	1.8	9.1	8.8	4.5	14.7	21.6	8.8
9	21.0	63.8	15.8	-	-	-	-	-	-
10	4,7	42.7	4.2						
11	8.0	8.1	4.0	0.9	2.6	0.7	3.3	20.4	2.8
12	6.7	2.7	1.9	7.8	4.8	2.9	9.8	16.6	6.1
13	12.9	7.0	4.6	2.2	4.4	1.5	7.4	31.0	6.0
14	0.1	17.4	0.1	0.0	19.2	0.0	0.3	9.8	0.3
15	8.0	5.7	3.4	3.3	9.3	2.4	13.5	27.5	9.0
16	6.9	2.9	2.0	12.6	6.5	4.3	8.5	14.3	5.3
17	8.2	6.4	3.6	2.7	5.5	1.8	18.4	42.5	12.8
18	6.1	53.8	5.5	-	-	-	-	-	-

TABLE 5.11

CELL INEFFICIENCY FROM PULSE HEIGHT DISTRIBUTION FOR $22 < P_{Had} < 40$ GeV/c - HORIZONTAL SCAN

Cell	Region 1_H			Region 2_H			Region 3_H		
	Inefficiency (%)	δ^+	δ^-	Inefficiency (%)	δ^+	δ^-	Inefficiency (%)	δ^+	δ^-
3	0.0	13.5	0.0	-	-	-	0.2	7.6	0.2
4	3.7	4.1	1.9	4.0	2.5	1.5	0.7	1.1	0.4
5	1.3	7.9	1.2	7.7	26.1	5.9	1.2	6.2	1.0
6	1.6	1.3	0.7	1.7	1.4	0.8	5.1	6.1	2.8
7	1.3	22.0	1.2	-	-	-	-	-	-
12	0.8	20.9	0.8	2.8	49.0	2.6	0.1	3.3	0.1
13	2.4	3.2	1.4	1.9	1.4	0.8	5.9	3.5	2.2
14	0.6	5.6	0.5	3.4	12.6	2.6	4.1	6.9	2.6
15	1.0	1.0	0.5	1.0	1.0	0.5	4.5	6.0	2.6
16	1.4	13.7	1.3	-	-	-	-	-	-

TABLE 5.12

CELL INEFFICINCY FROM PULSE HEIGHT DISTRIBUTION FOR $22 < P_{Had} < 40$ GeV/c -

VERTICAL SCAN

(Insufficient data in Region 3_V)

Cell	Region 1_V Inefficiency (%)	δ^+	δ^-	Region 2_V Inefficiency (%)	δ^+	δ^-
3	0.0	3.3	0.0	0.0	3.9	0.0
4	2.5	1.2	0.8	4.3	7.2	2.7
5	2.4	5.3	1.6	4.7	15.2	3.6
6	1.8	0.8	0.6	2.6	7.6	1.9
7	6.5	23.1	5.0	-	-	-
12	25.2	35.0	14.7	2.7	21.0	2.4
13	9.1	2.4	1.9	3.2	4.4	1.8
14	10.0	8.7	4.6	6.4	11.4	4.1
15	4.6	1.7	1.2	2.0	4.0	1.3
16	2.0	14.3	1.8	-	-	-

TABLE 5.13

CELL INEFFICIENCY FROM PULSE HEIGHT DISTRIBUTION FOR $P_{Had} \geq 45$ GeV/c - HORIZONTAL SCAN

Cell	Region 1_H			Region 2_H			Region 3_H		
	Inefficiency (%)	δ^+	δ^-	Inefficiency (%)	δ^+	δ^-	Inefficiency (%)	δ^+	δ^-
4	-	-	-	3.1	11.6	2.5	0.2	0.5	0.1
5	1.6	4.0	1.1	0.6	4.6	0.5	0.7	0.4	0.2
6	1.2	1.9	0.7	0.1	2.3	0.1	-	-	-
13	-	-	-	4.3	11.2	3.1	2.7	2.8	1.4
14	0.6	1.6	0.4	3.4	8.5	2.9	0.5	0.3	0.2
15	0.5	1.1	0.3	-	-	-	-	-	-

TABLE 5.14

CELL INEFFICIENCY FROM PULSE HEIGHT DISTRIBUTION FOR MUONS - HORIZONTAL SCAN

Cell	Region 1_H			Region 2_H			Region 3_H		
	Inefficiency (%)	δ^+	δ^-	Inefficiency (%)	δ^+	δ^-	Inefficiency (%)	δ^+	δ^-
3	0.0	0.6	0.0	2.2	3.2	1.3	2.2	2.2	1.1
4	3.2	2.1	1.3	0.7	0.2	0.2	1.0	0.3	0.2
5	2.2	1.0	0.7	6.0	2.8	1.9	0.3	0.9	0.2
6	0.2	16.0	0.2	-	-	-	-	-	-
12	0.2	7.8	0.2	4.4	7.0	2.7	5.7	4.0	2.4
13	0.9	0.9	0.4	1.5	0.5	0.4	1.5	0.4	0.3
14	0.4	0.3	0.2	0.9	1.0	0.4	0.2	0.6	0.2
15	0.0	43.0	0.0	-	-	-	-	-	-

TABLE 5.15

CELL INEFFICIENCY FROM PULSE HEIGHT DISTRIBUTION FOR MUONS - VERTICAL SCAN

(insufficient data in Region 3_V)

Cell	Region 1_V			Region 2_V		
	Inefficiency (%)	δ^+	δ^-	Inefficiency (%)	δ^+	δ^-
3	2.2	1.5	0.9	0.0	3.0	0.0
4	0.9	0.2	0.2	1.4	8.1	1.2
5	1.5	34.5	1.4	0.0	3.7	0.0
12	11.5	4.4	3.2	7.1	25.6	5.6
13	5.4	0.8	0.7	3.6	7.6	2.4
14	7.5	26.0	5.8	3.8	51.1	3.6

TABLE 5.16

AVERAGE INEFFICIENCY FROM FAILURE RATE FOR P_{Had} > 45 GeV/c

(errors are statistical)

Cell	Inefficiency (%)	+/-
4	0.6	0.6
5	3.9	0.8
6	2.8	1.6
13	4.2	1.7
14	2.7	0.7
15	1.9	1.3

TABLE 5.17

CELL INEFFICIENCY FROM FAILURE RATE FOR P_{Had} > 45 GeV/c - HORIZONTAL SCAN

(errors are statistical)

Cell	Region 1_H Inefficiency (%)	+/-	Region 2_H Inefficiency (%)	+/-	Region 3_H Inefficiency (%)	+/-
4	-	-	4.8	4.8	0.0	0.8
5	13.2	5.0	8.3	5.9	2.8	0.7
6	3.3	1.9	0.0	7.1	-	-
13	-	-	4.0	4.0	3.4	1.7
14	11.1	3.9	3.3	3.3	1.3	0.5
15	2.3	1.6	0.0	7.1	-	-

TABLE 5.18

CELL EFFICIENCY (1 - ε) USING ELEASTIC ρ-MESON EVENTS

Cell	No. of Pions Through Cell	No. of Times Cell Lit	Cell Efficiency (1 - ε)%	±
1	2	2	100	50
2	10	7	70	14
3	16	10	62	12
4	40	39	98	2
5	32	29	91	5
6	22	19	86	7
7	5	3	60	22
8	6	4	67	19
9	2	2	100	50
10	3	2	67	27
11	8	3	38	17
12	15	12	80	10
13	35	34	97	3
14	79	76	96	2
15	26	25	96	4
16	12	10	83	11
17	4	4	100	22
18	4	3	75	22

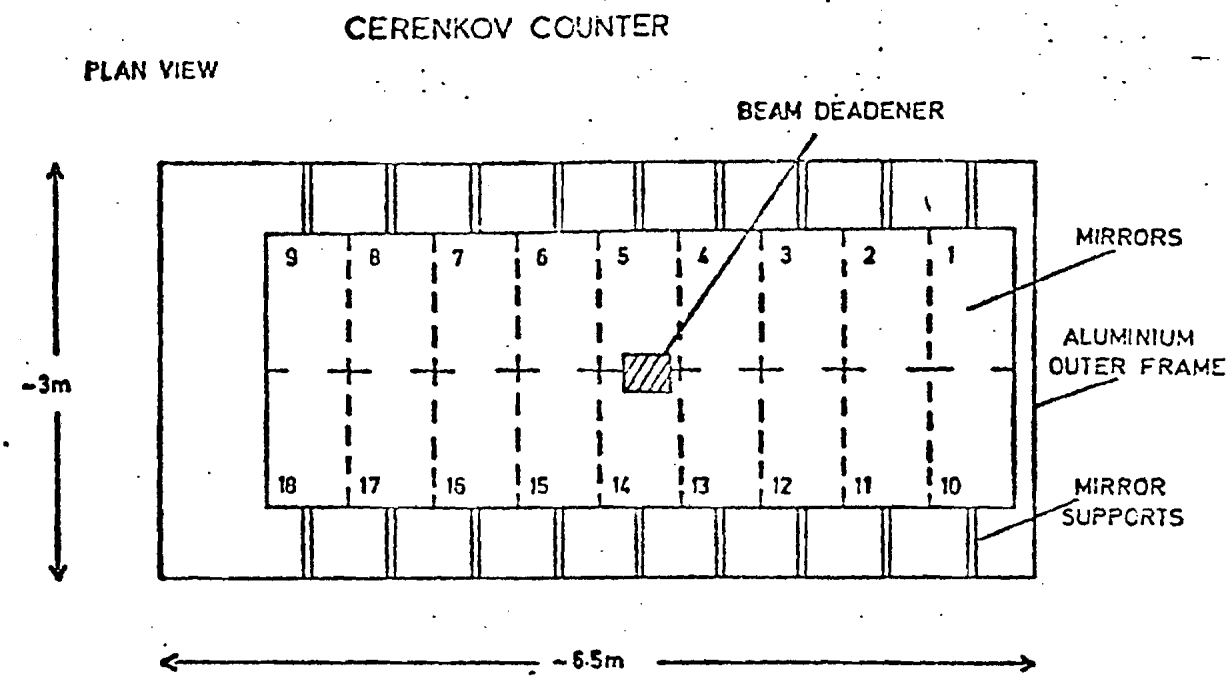

Fig. 5.1a

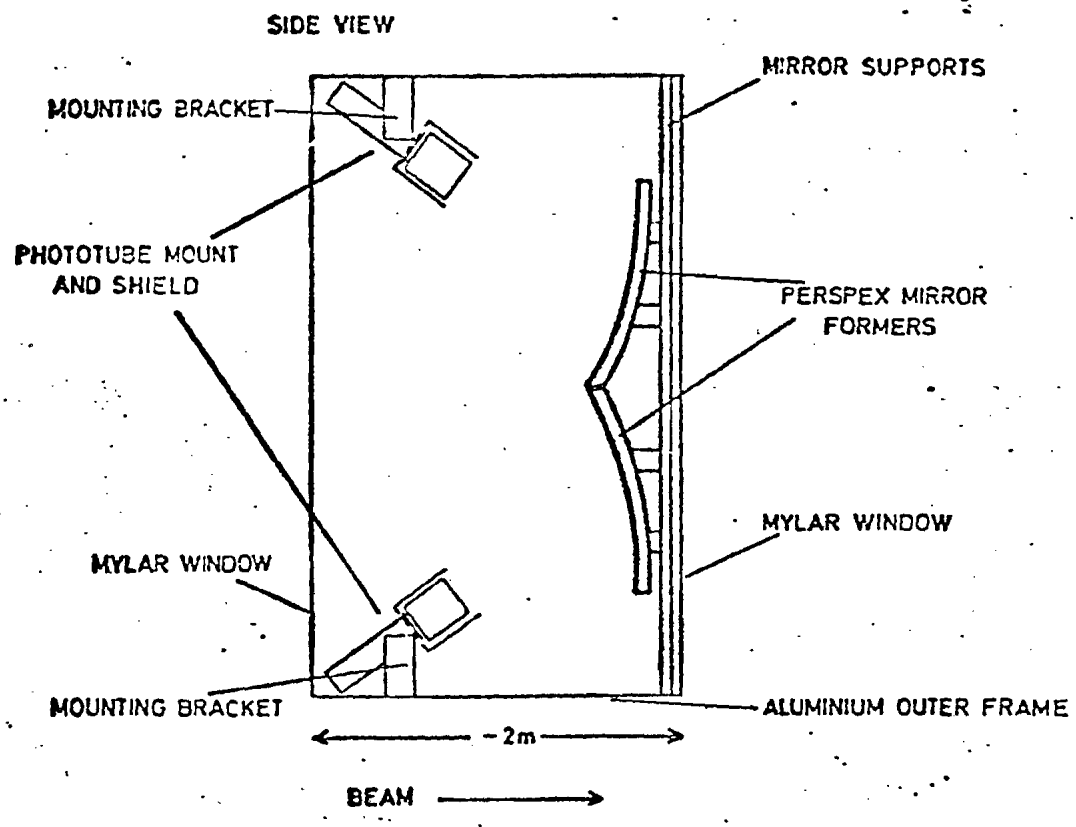

Fig. 5.1b

Cerenkov Counter Mirror Alignment (Schematic)

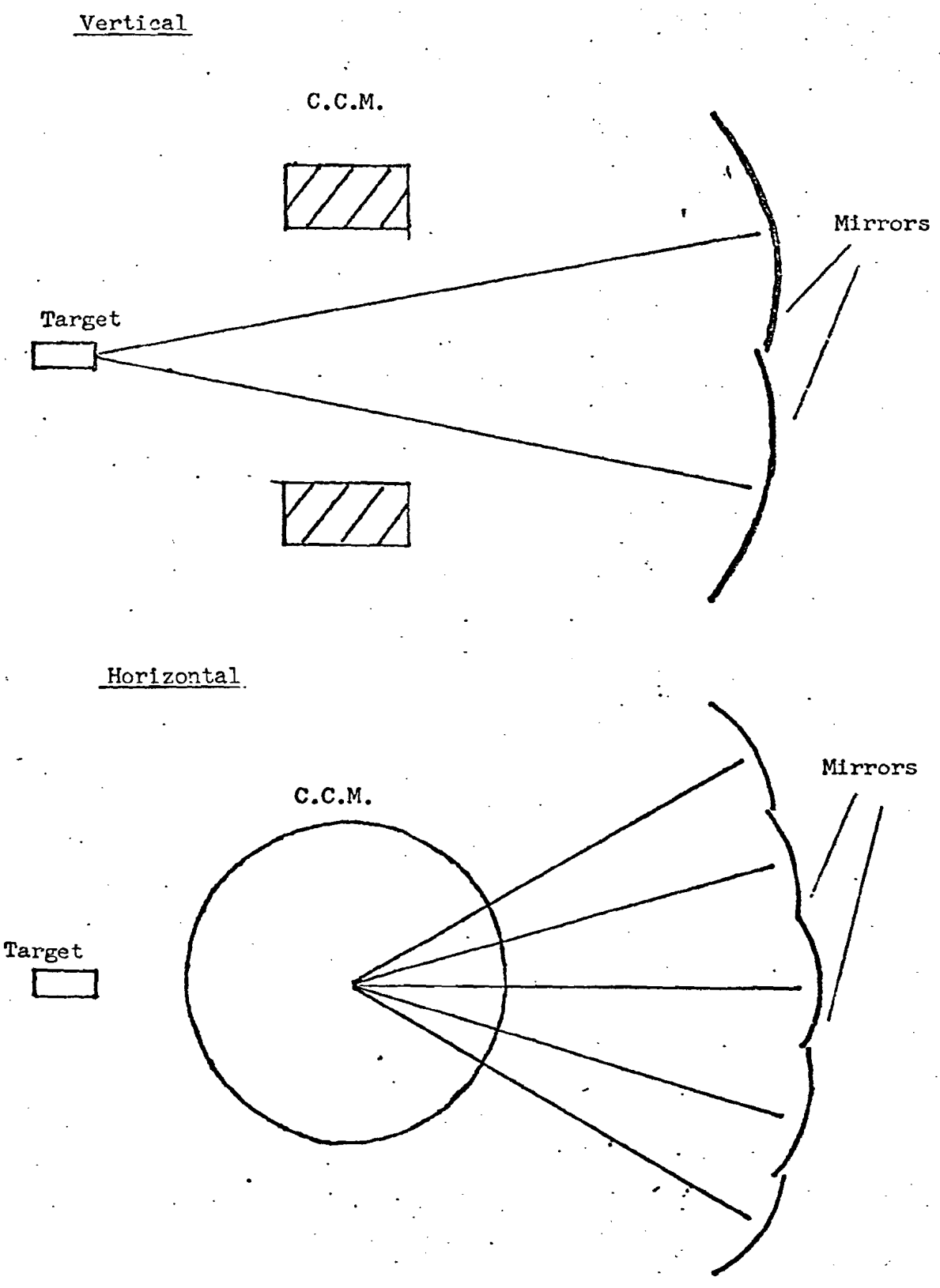

Fig. 5.2

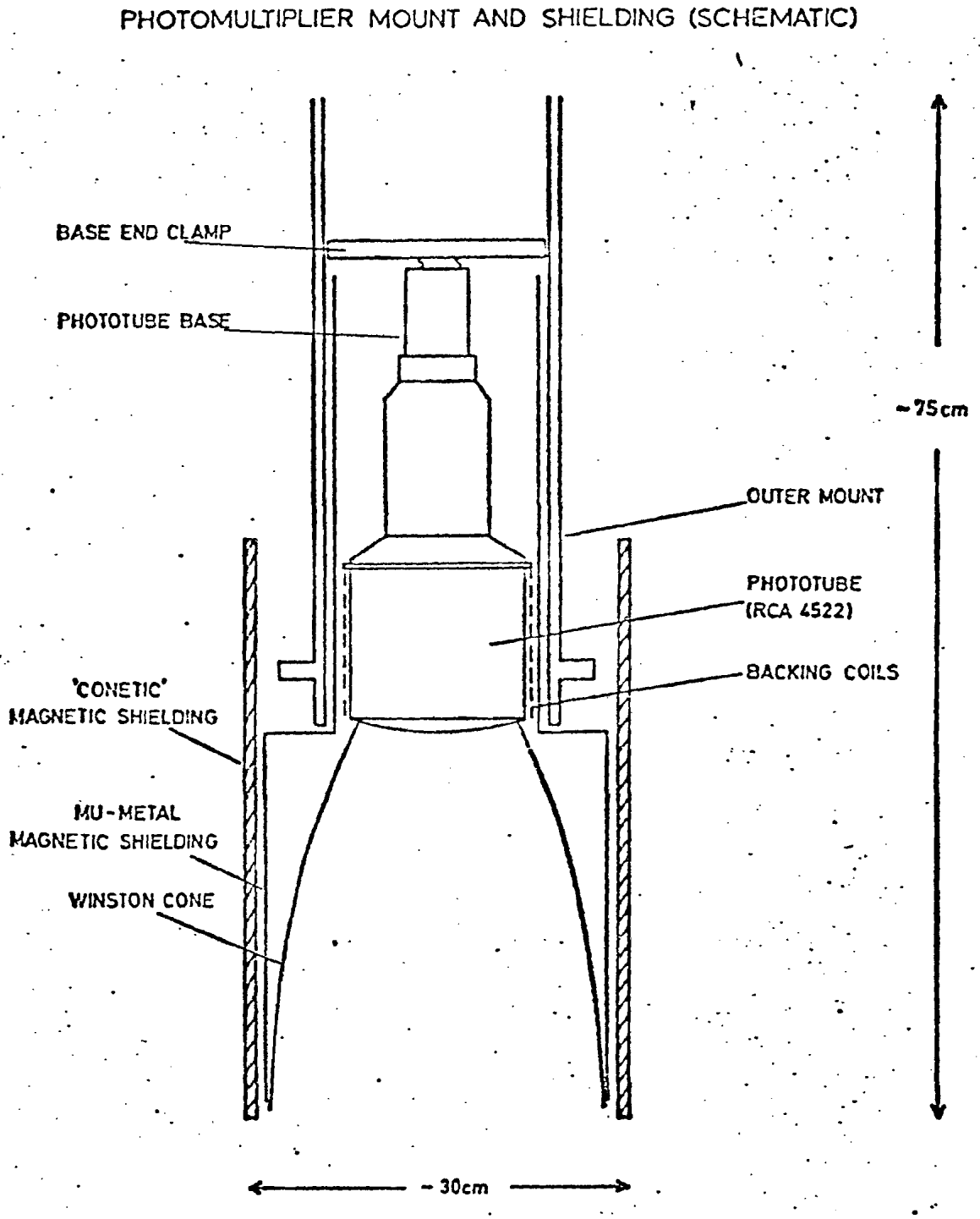
PHOTOMULTIPLIER MOUNT AND SHIELDING (SCHEMATIC)
BASE END CLAMP
PHOTOTUBE BASE
~75cm
OUTER MOUNT
PHOTOTUBE
(RCA 4522)
BACKING COILS
'CONETIC'
MAGNETIC SHIELDING
MU-METAL
MAGNETIC SHIELDING
WINSTON CONE
~30cm

Fig. 5.3

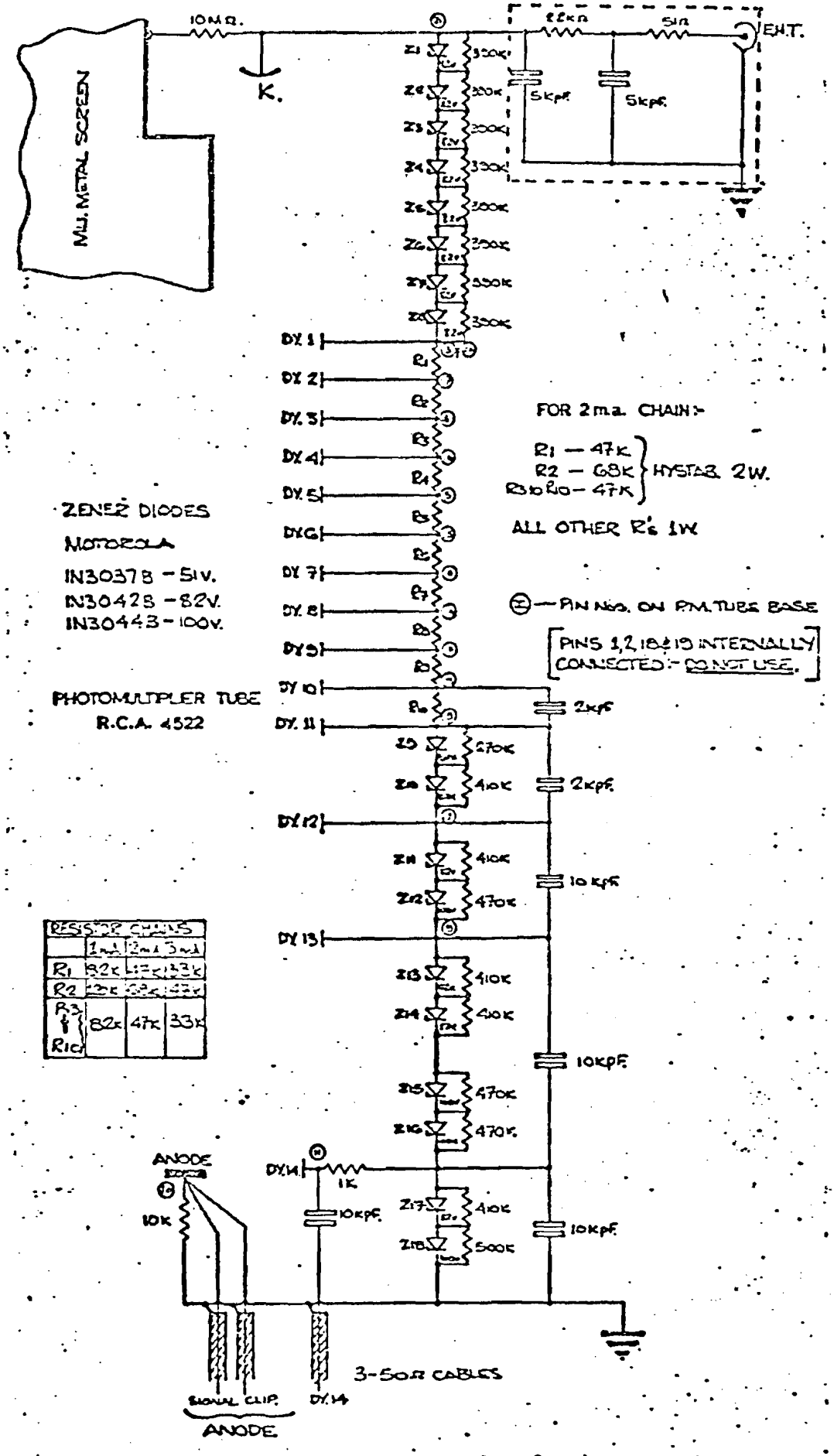
10MΩ.
K.
MU. METAL SCREEN
22kΩ
5MΩ
E.H.T.
5kpf
5kpf
Z1 320K
Z2 300K
Z3 300K
Z4 330K
Z5 300K
Z6 300K
Z7 330K
Z8 330K
DY 1
DY 2
DY 3
DY 4
DY 5
DY 6
DY 7
DY 8
DY 9
DY 10
DY. 11
DY 12
DY 13
DY 14
R1
R2
R3
R4
R5
R6
R7
R8
R9
R10
FOR 2 ma. CHAIN:-
R1 — 47K
R2 — 68K
R3 to R10 — 47K
HYSTAB 2W.
ALL OTHER R's 1W
ZENER DIODES
MOTOROLA
IN3037B - 51V.
IN3042B - 82V.
IN3044B - 100V.
PHOTOMULTIPLER TUBE
R.C.A. 4522
PIN Nos. ON P.M. TUBE BASE
PINS 1, 2, 18 & 19 INTERNALLY CONNECTED:- DO NOT USE.
2kpf
Z9 270K
Z10 410K
2kpf
Z11 410K
Z12 470K
10 kpf
Z13 410K
Z14 410K
10kpf
Z15 470K
Z16 470K
RESISTOR CHAINS
1mA 2mA 3mA
R1 82K 47K 33K
R2 82K 68K 47K
R3 to R10 82K 47K 33K
ANODE
10K
1K
10kpf
Z17 410K
Z18 500K
10kpf
3-50Ω CABLES
SIGNAL CLIP.
ANODE
DY.14

Fig. 5.4

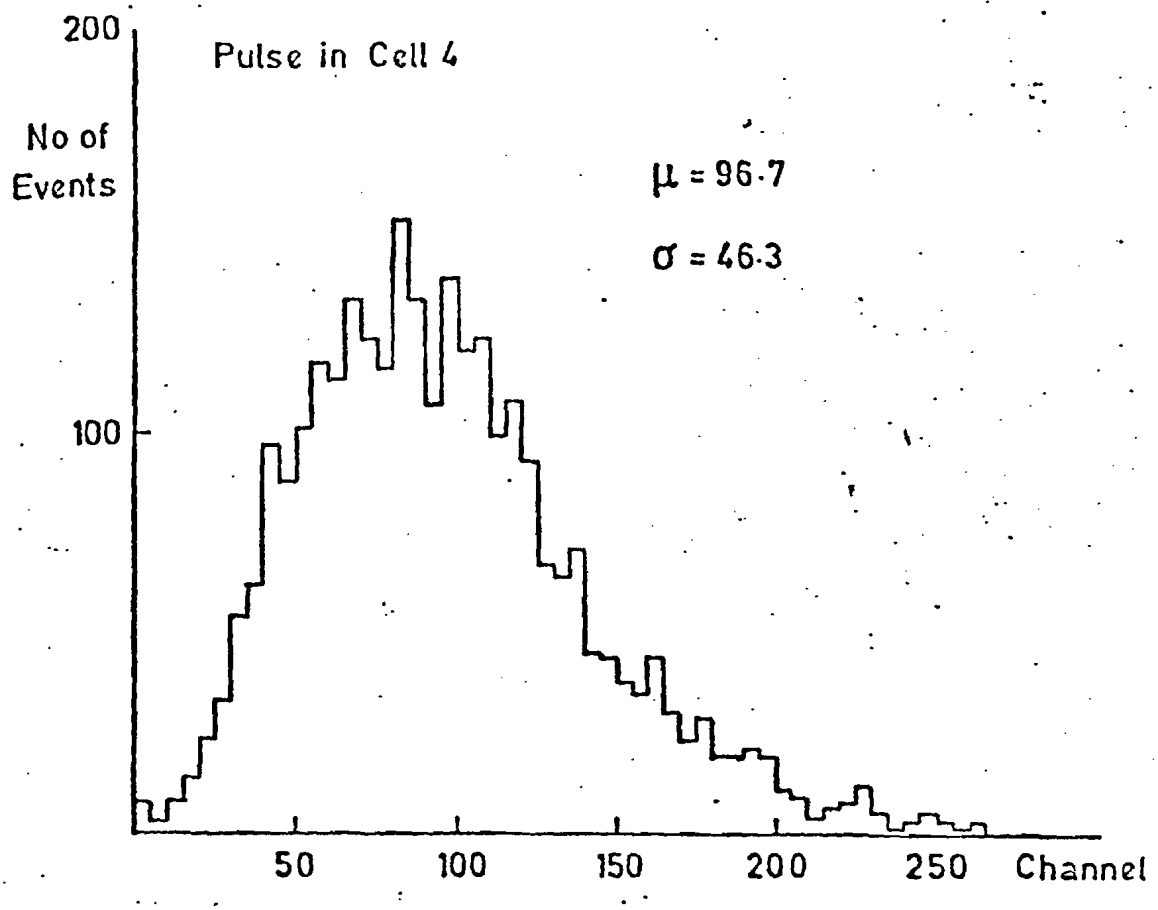
200
Pulse in Cell 4
No of Events
μ = 96·7
σ = 46·3
100
50
100
150
200
250
Channel

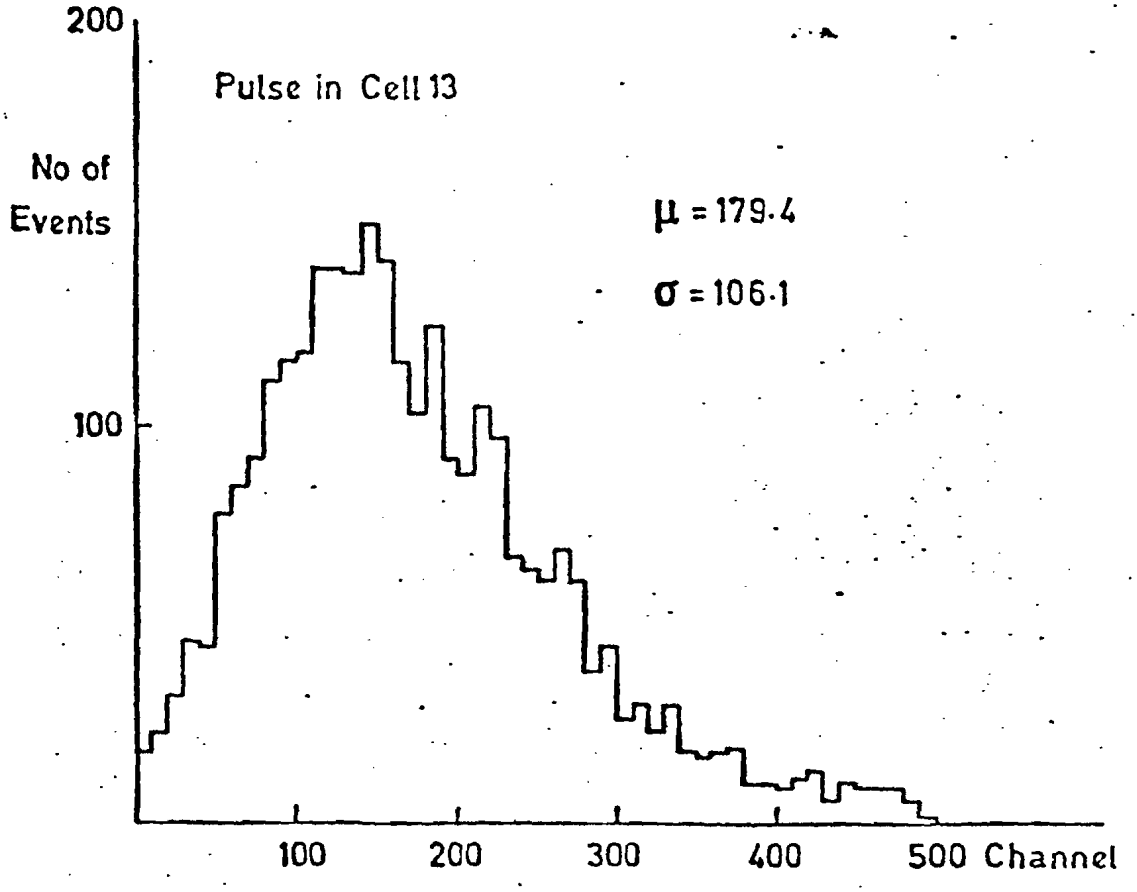
200
Pulse in Cell 13
No of Events
μ = 179·4
σ = 106·1
100
100
200
300
400
500 Channel

Fig 5.5

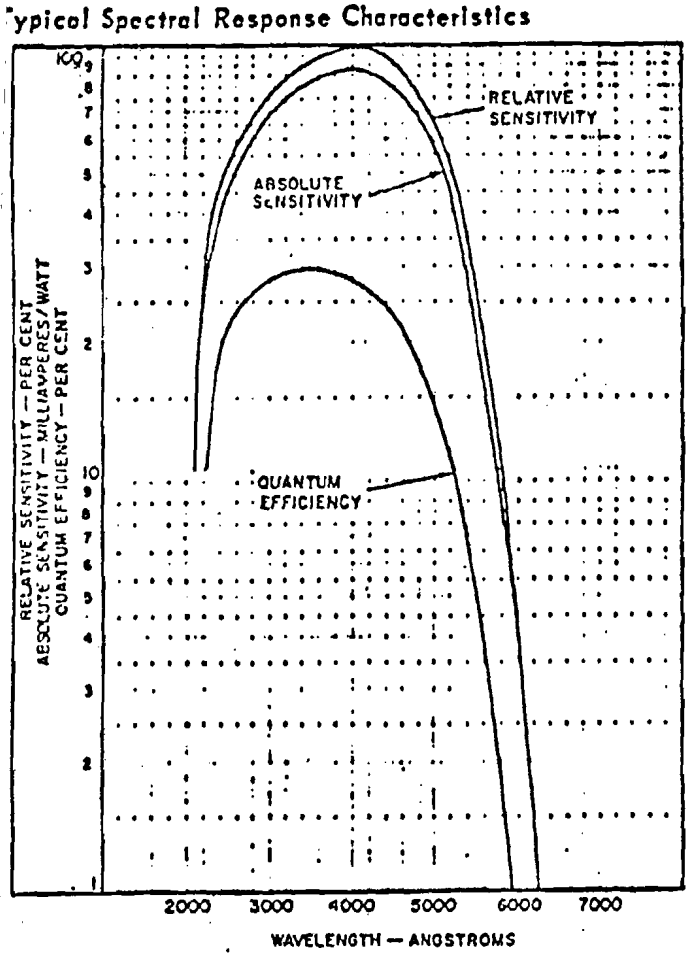
ypical Spectral Response Characteristics
RELATIVE SENSITIVITY — PER CENT
ABSOLUTE SENSITIVITY — MILLIAMPERES/WATT
QUANTUM EFFICIENCY — PER CENT
RELATIVE SENSITIVITY
ABSOLUTE SENSITIVITY
QUANTUM EFFICIENCY
2000
3000
4000
5000
6000
7000
WAVELENGTH — ANGSTROMS

Fig. 5.6

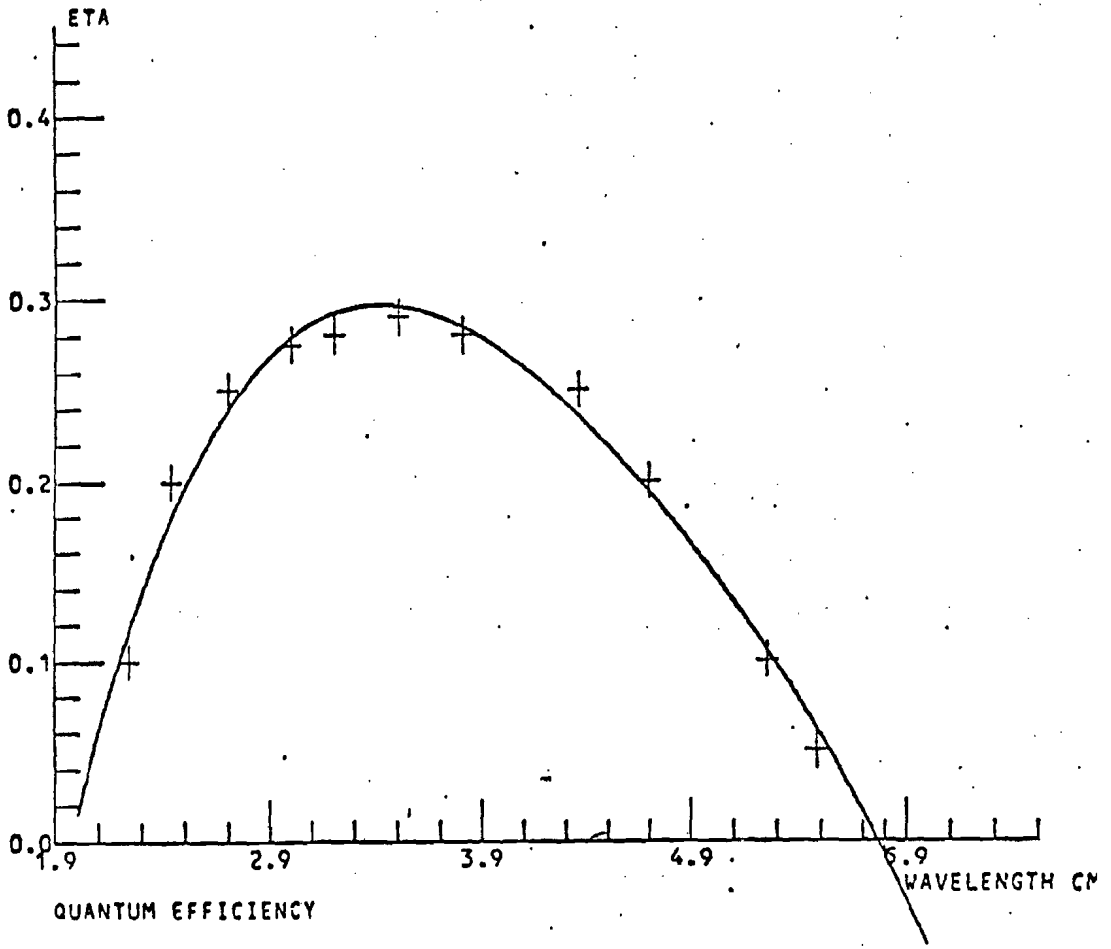
ETA
0.4
0.3
0.2
0.1
0.0
1.9
2.9
3.9
4.9
5.9
WAVELENGTH CM
QUANTUM EFFICIENCY

Fig. 5.7

Photo-electrons from Nitrogen at Atmospheric Pressure

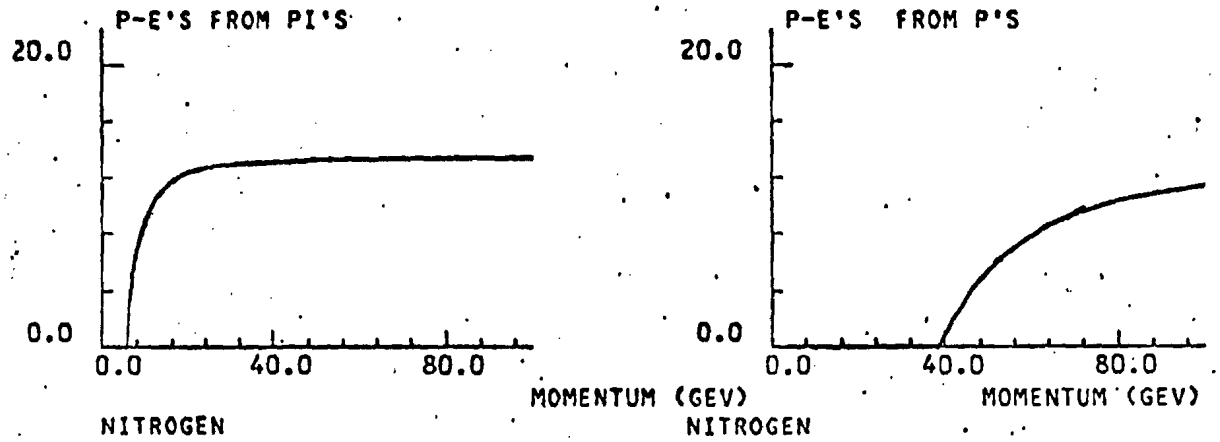

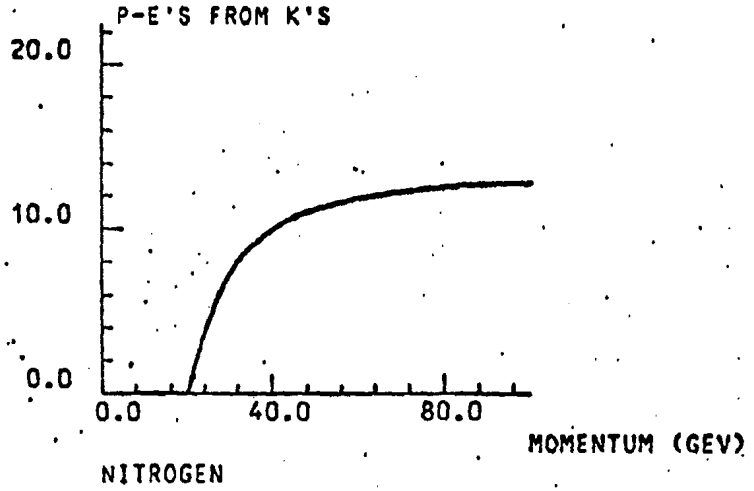

Fig. 5.8a

Photo-electrons from Neon at Atmospheric Pressure

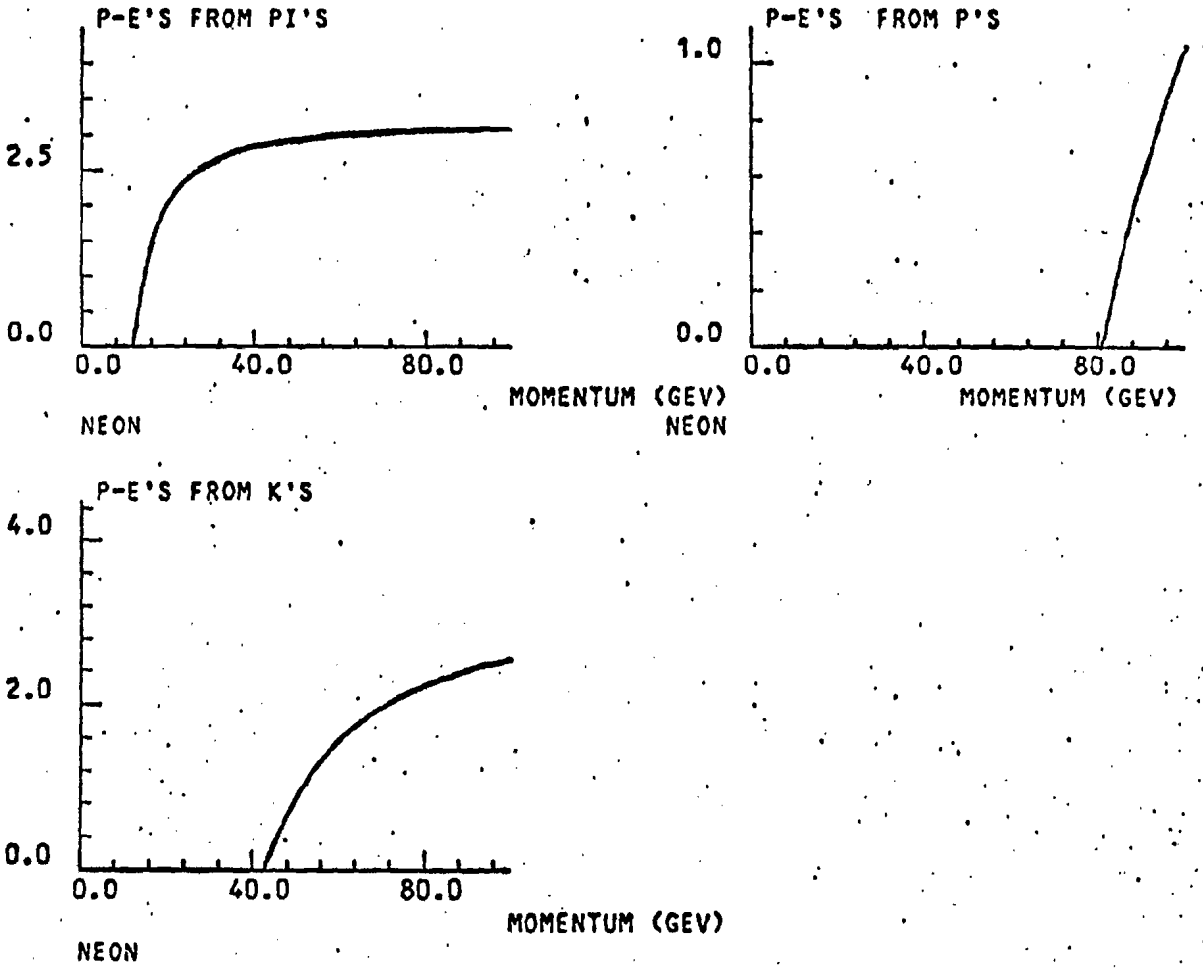

Fig. 5.8b

Photo-electrons from Freon 13 at Atmospheric Pressure

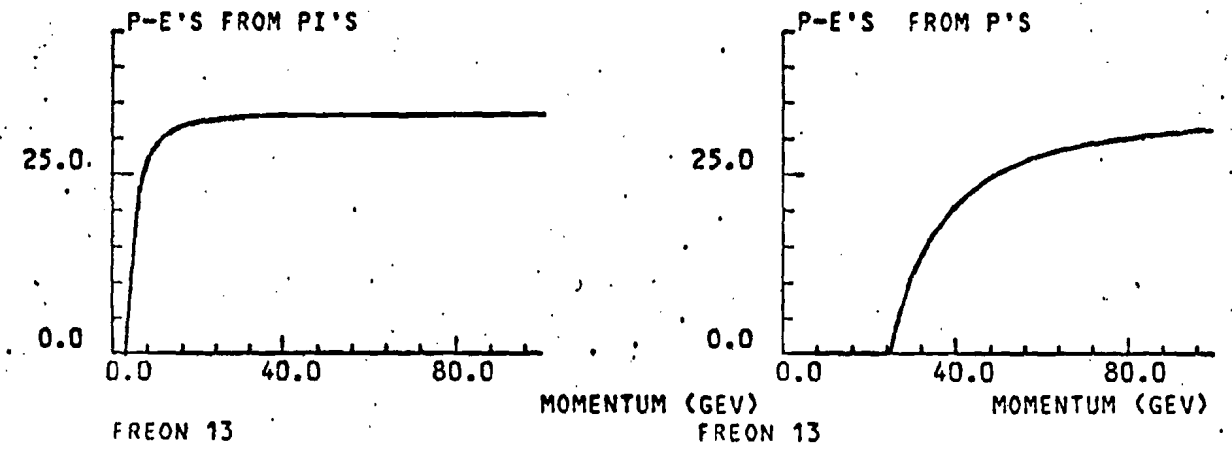

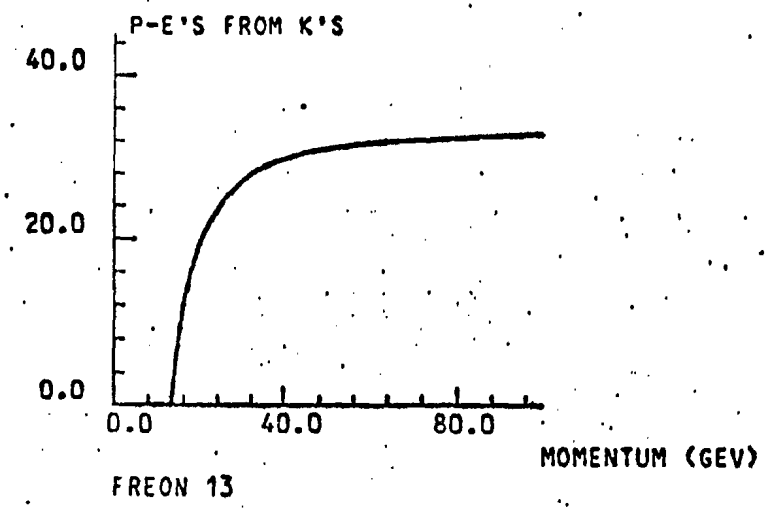

Fig. 5.8a

Variation of Cerenkov Threshold with Refractive Index

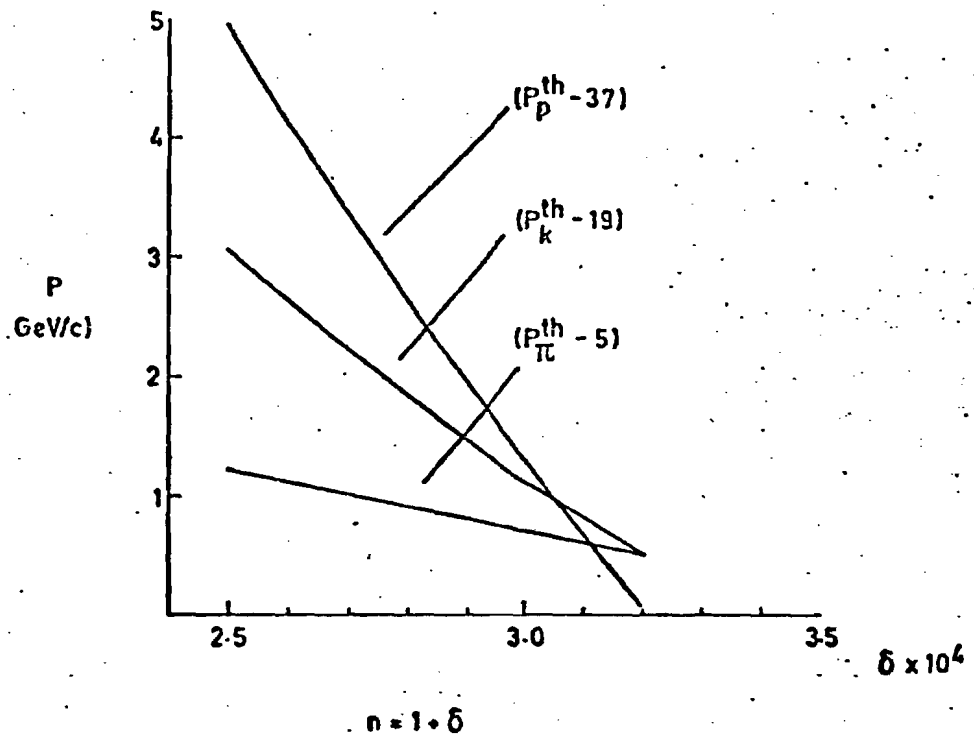

Fig. 5·9

Frequency Dependence of Cerenkov Threshold

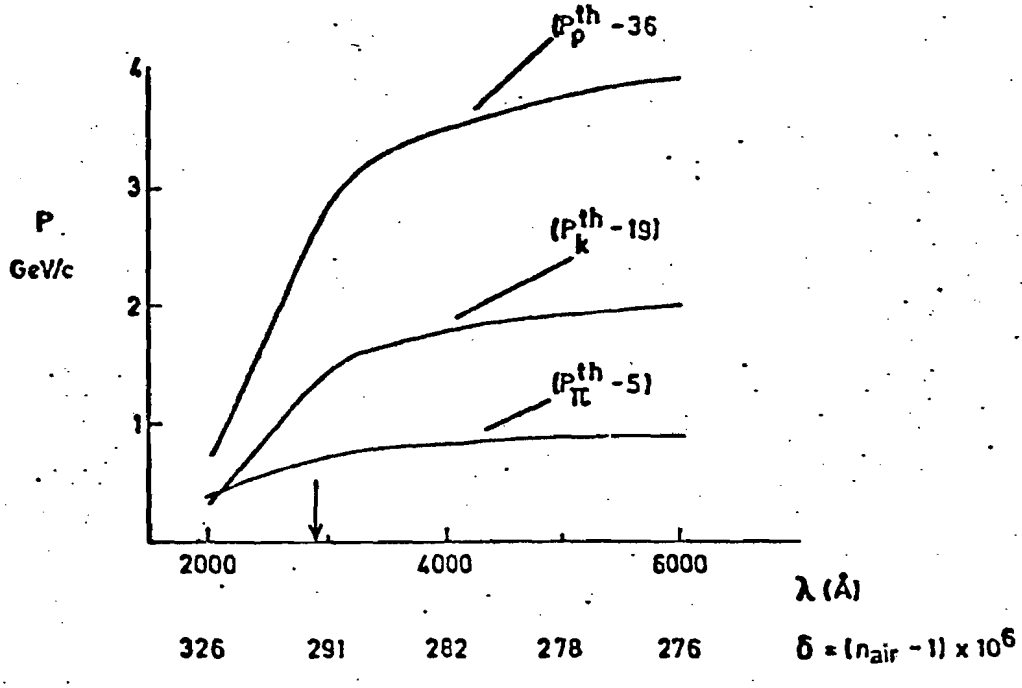

Fig. 5·10

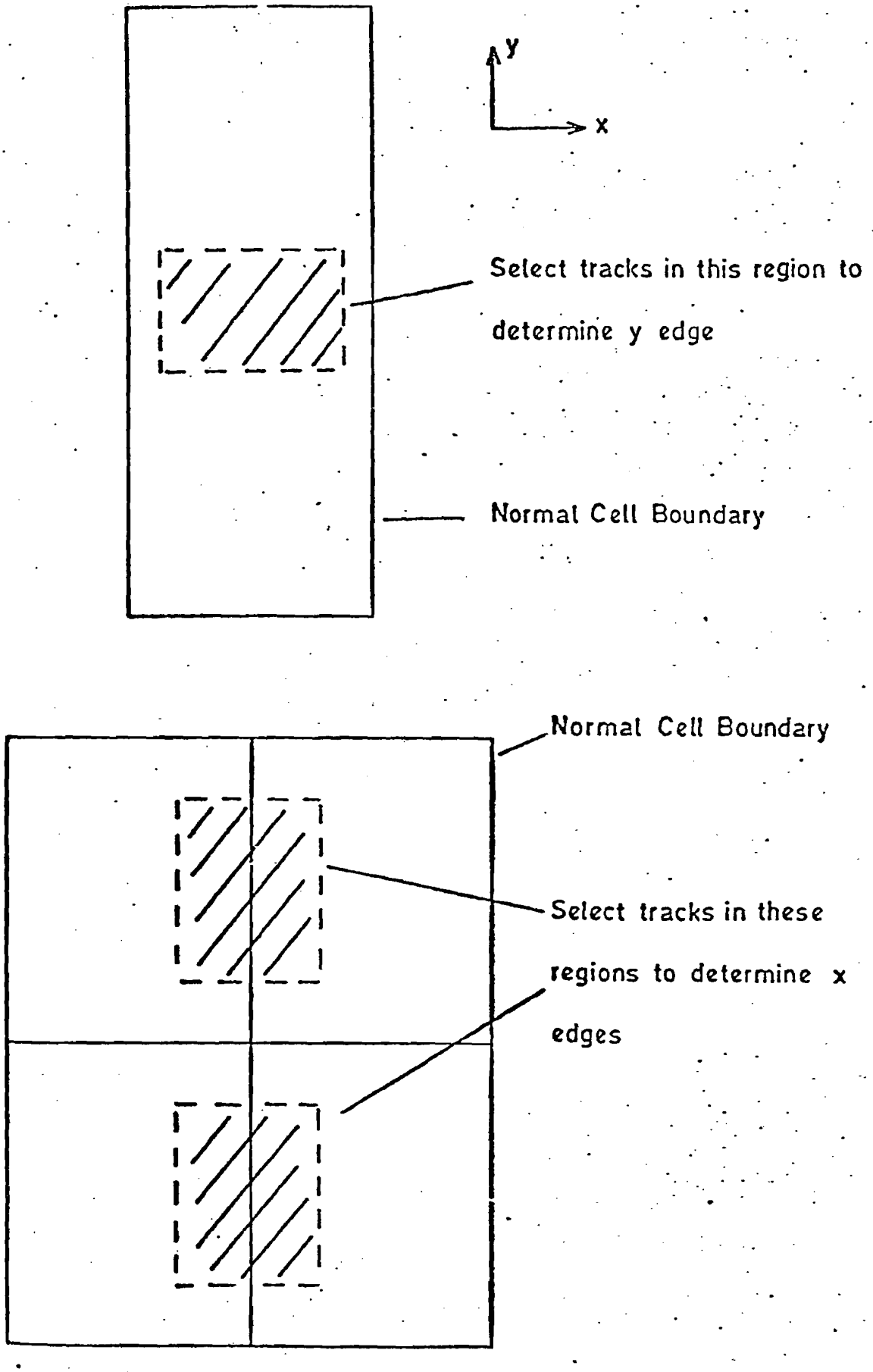
y
x
Select tracks in this region to determine y edge
Normal Cell Boundary
Normal Cell Boundary
Select tracks in these regions to determine x edges

Fig. 5·11

Typical y - edge Distribution

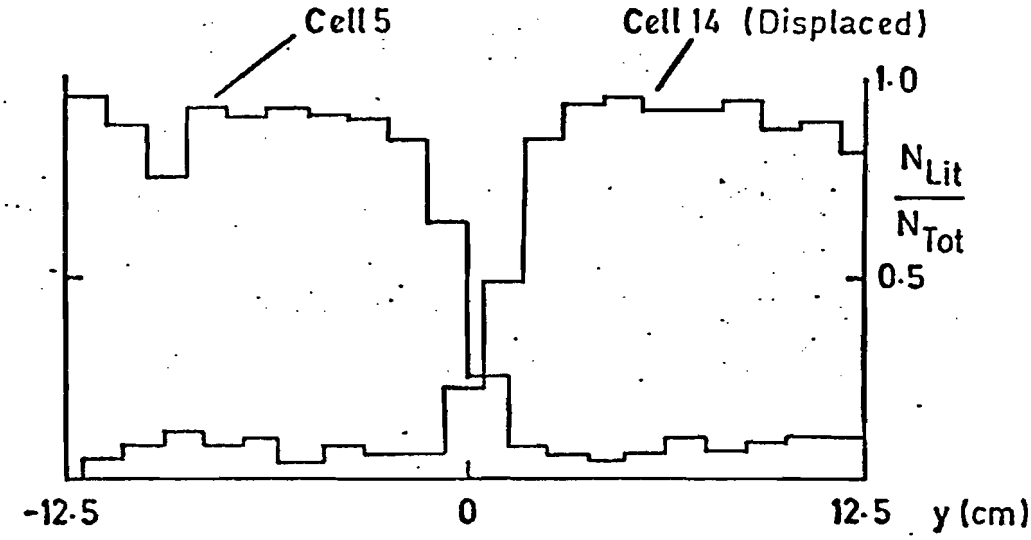

Boundary at y = 0

Typical x - edge Distribution

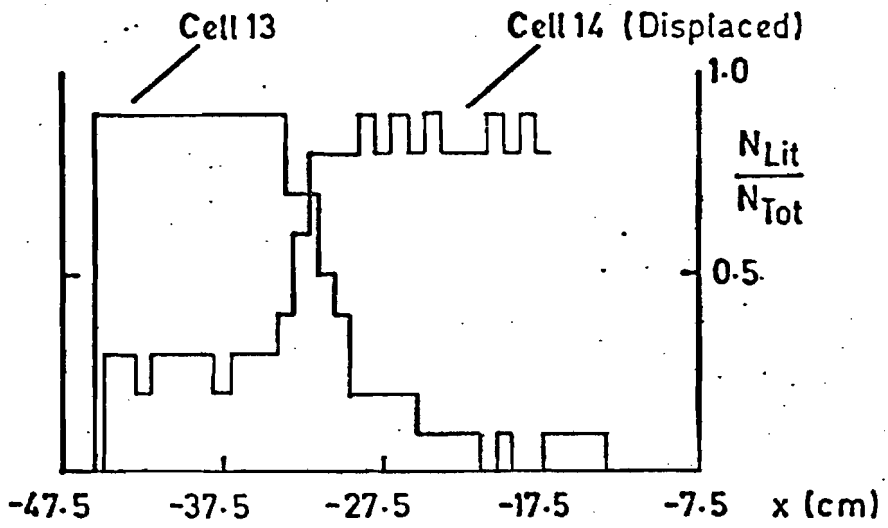

Boundary at x = 35·0 cm

Fig. 5·12

Cerenkov Counter Beam Deadener - y Distribution

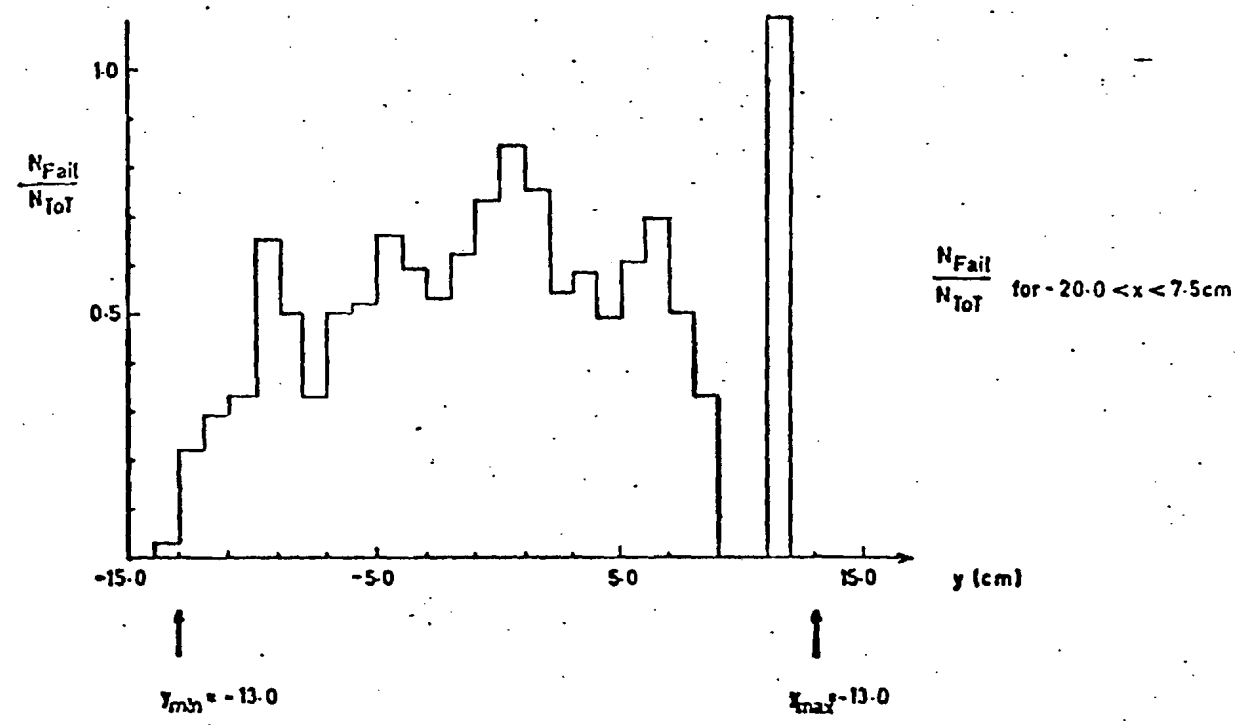

Cerenkov Counter Beam Deadener - x Distribution

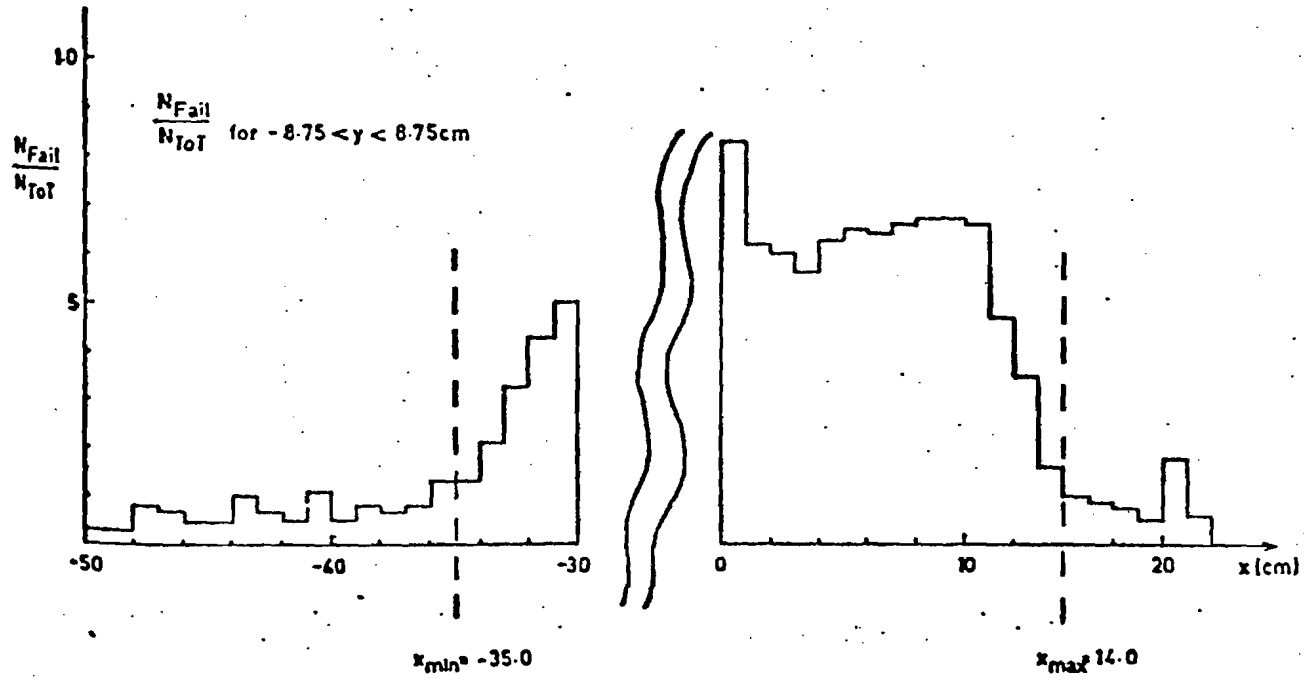

Fig. 5·13

Vertical Sections

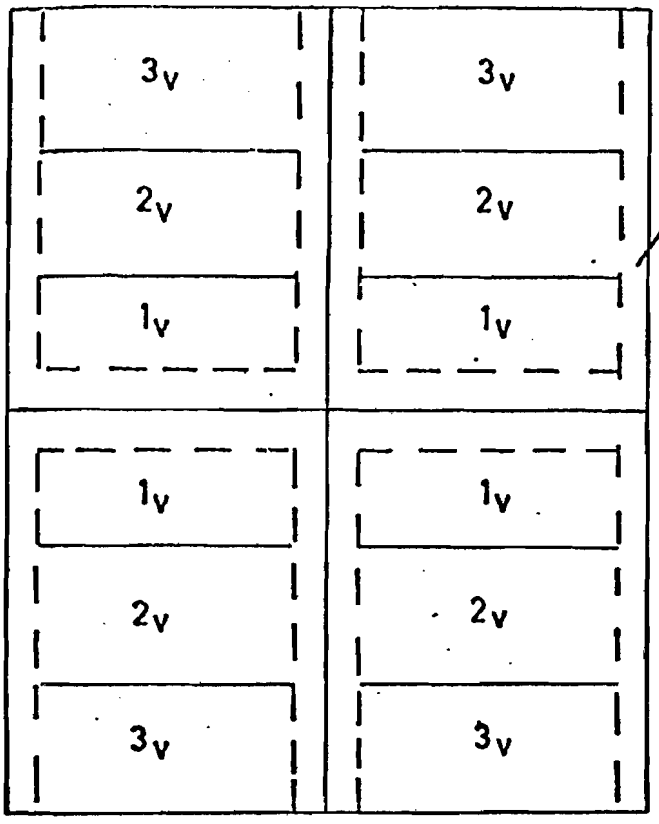

'Window Frame'

(Schematic)

y = 0 (Nominal centre edge)

Horizonal Sections

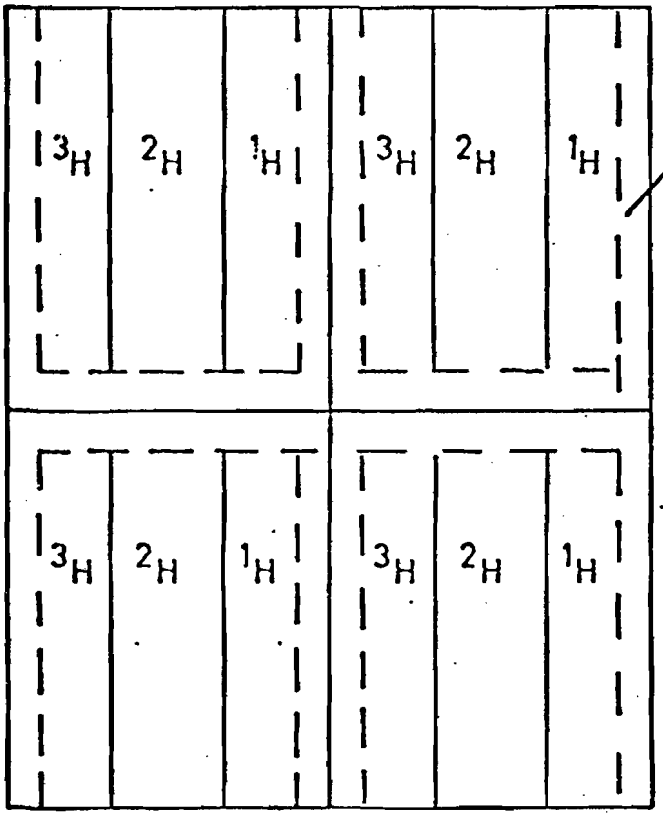

'Window Frame'

y = 0 (Nominal centre edge)

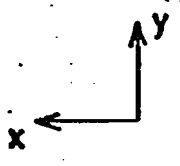

Fig. 5.14

Selected ρ - Meson Events

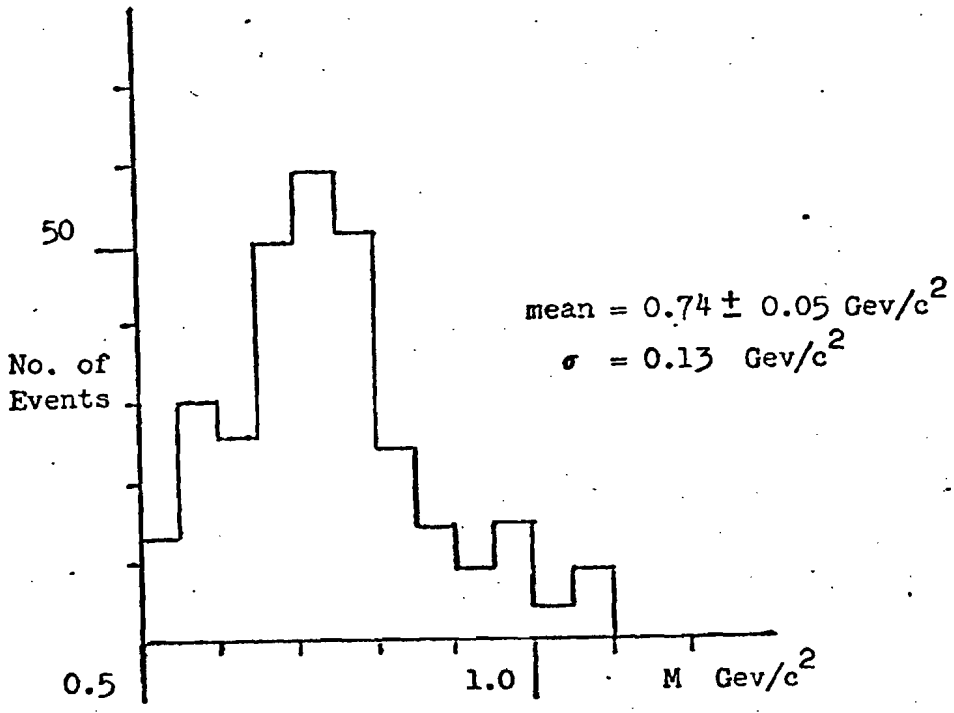

Fig. 5.15

Photo-electrons from Nitrogen at Atmospheric Pressure

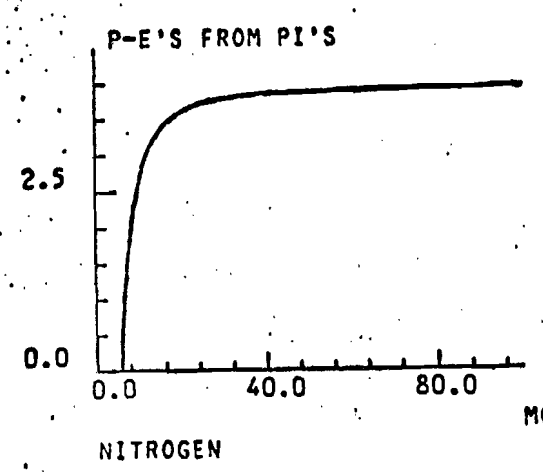

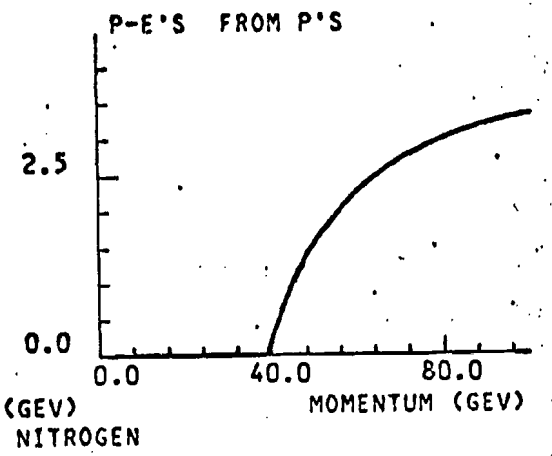

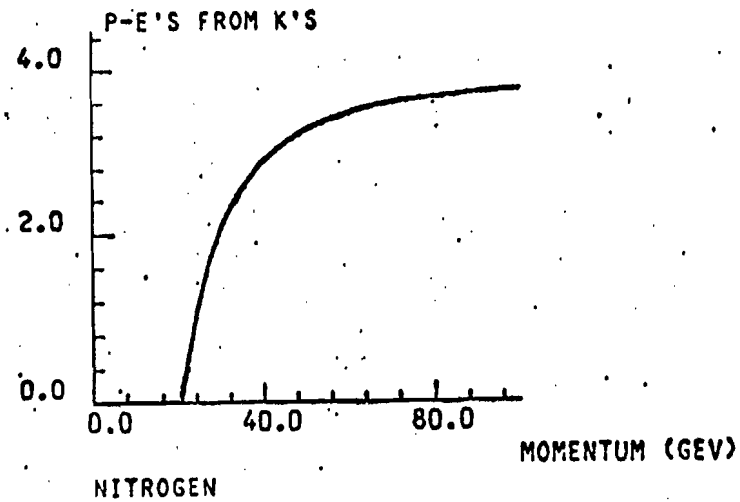

Fig. 5.16a

Photo-electrons from Neon at Atmospheric Pressure

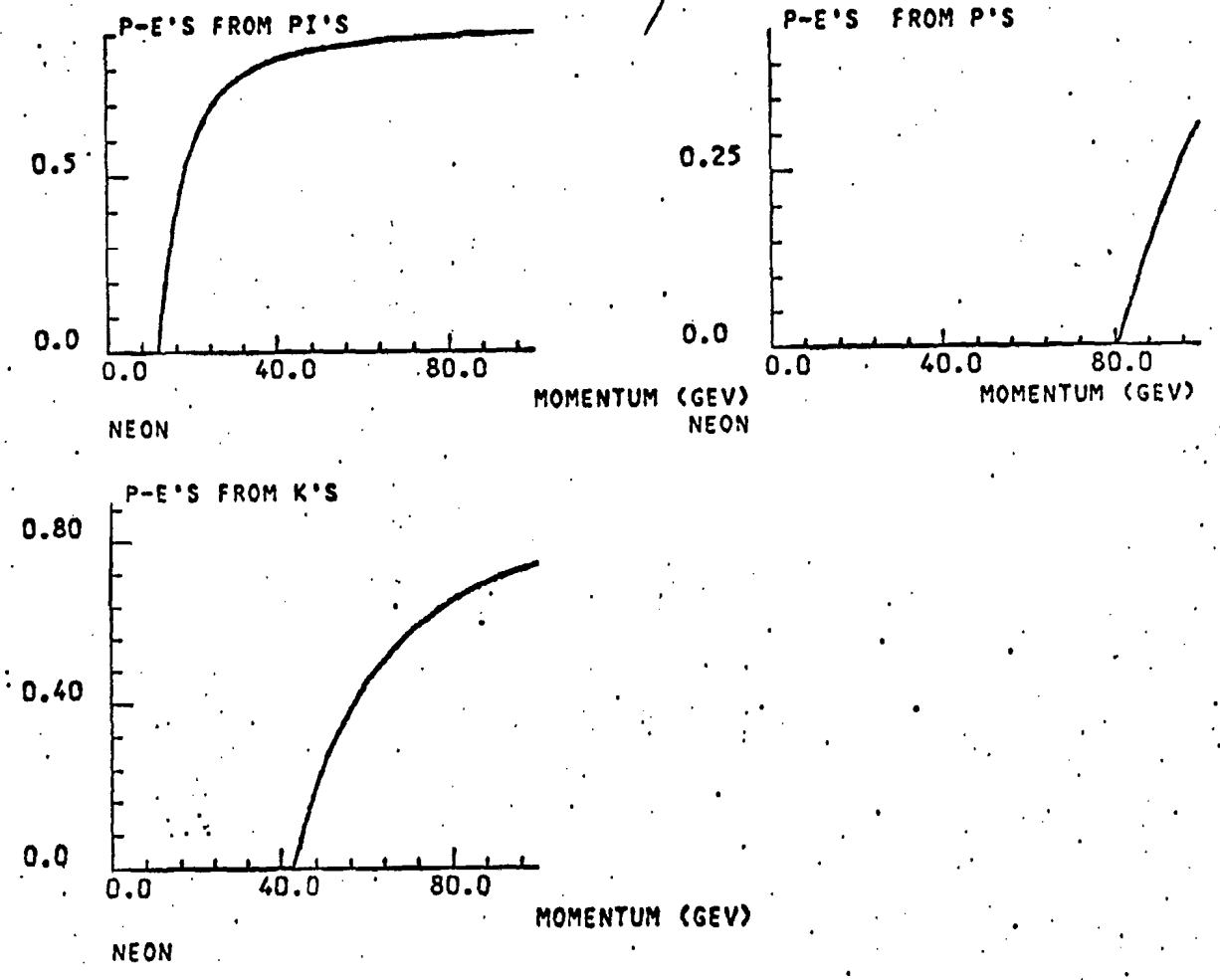

Fig. 5.16b

Photo-electrons from Freon 13 at Atmospheric Pressure

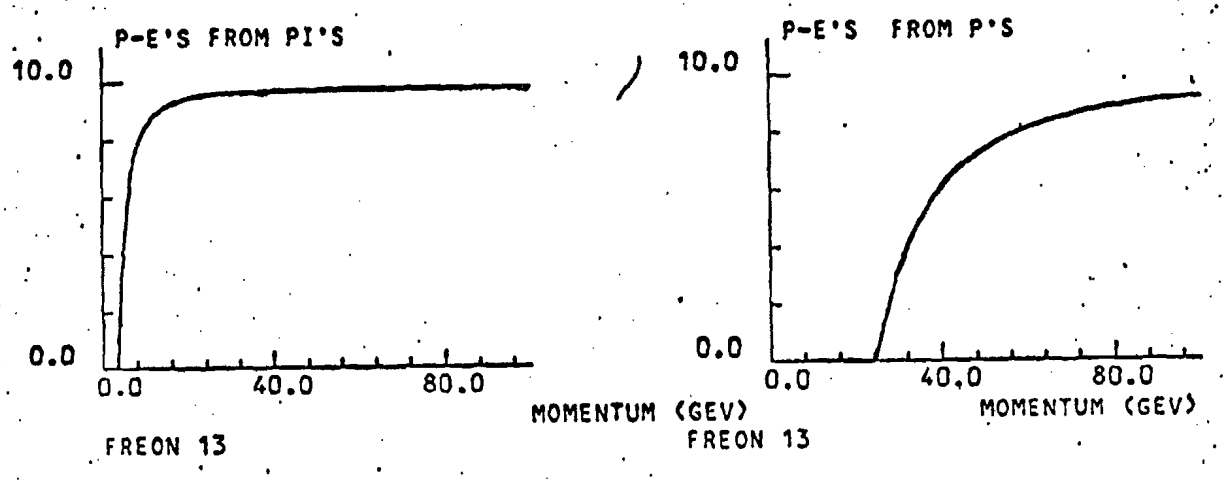

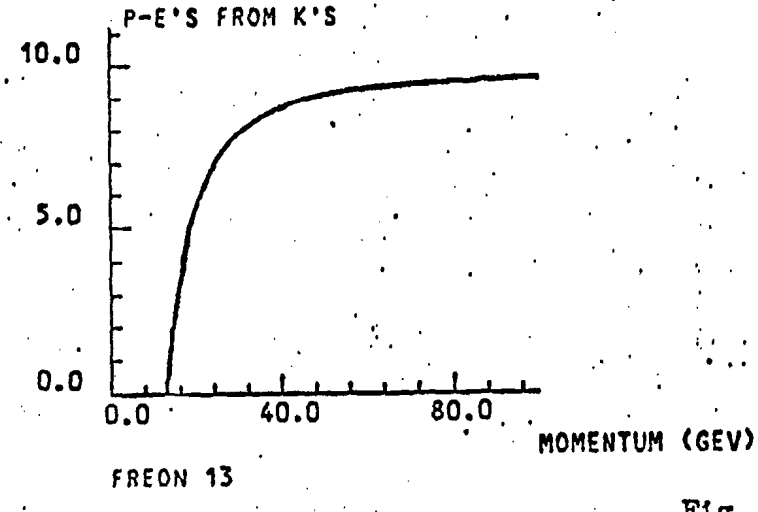

Fig. 5.16c

CHAPTER 6

SEARCH FOR CHARMED D-MESON PRODUCTION

6.1 INTRODUCTION

Experiments carried out in the last four years have established the existence of a new quantum number - charm. Initially this was inferred from di-muon production in ν, $\bar{\nu}$ interactions. Conclusive evidence was obtained from the discovery of long-lived high mass resonance states in e^+e^- annihilation, and electron-positron production in pp collisions - the ψ states.[52-55] These are interpreted as $q\bar{q}$ bound states of the quark associated with this new particle (analogous to the vector meson states ρ, ϕ, w etc.) and therefore have no net 'charm'. In addition to these states however, it is now believed that associated charmed meson production (the D-mesons) has also been observed in e^+e^- annihilation[56], and more recently in neutrino scattering.[57] At this time however, detailed investigation of these states is only possible in e^+e^- annihilation, in which the D mesons are identified with narrow resonances in $K\pi$, $K2\pi$ (and in general $Km\pi$) systems of mass $\sim$1.9 GeV/c^2 and widths a few keV.

Assuming the charm hypothesis, the strong decay of the lowest mass meson would be forbidden by charm conservation - and therefore the state would be long-lived. For charm changing decays, the Cabibbo favoured weak decay requires $\Delta C = \Delta S$ and therefore a strange particle in the final state - as observed experimentally. Electromagnetic production via a virtual photon would result in associated production of charm-anticharm pairs of mesons. The D-mesons are observed to recoil against a mass greater than 1.9 GeV/c^2 - supporting the hypothesis of associated production.

In addition, the charged D-mesons are observed to decay via an exotic mode (e.g. $D^+ \to K^-\pi^+\pi^+$ ($\Delta C = \Delta S$), rather than $K^+\pi^+\pi^-$ ($\Delta C = -\Delta S$)).

On this evidence, the D-mesons are strong candidates for (and have now been accepted as) states containing charm, i.e. with $C = \pm 1$. In the style of the quark model, one must now define the quark associated with this new particle. The quantum numbers of the charmed quark are:

$$B = \frac{1}{3}$$

$$I = 0$$

$$Q = +\frac{2}{3}$$

$$S = 0$$

$$C = 1$$

The introduction of a new quark has an important effect in deep-inelastic scattering. As was mentioned in Chapter 1, the structure function $F_2(x)$ must be modified to account for charmed quarks in the 'sea':

$$F_2^{p'}(x) = F_2^p(x) + x(c(x) + \bar{c}(x))$$

with the requirement that

$$\int_0^1 (c(x) - \bar{c}(x))dx = 0$$

where $c(x)$ is the momentum density of charmed quarks in the proton. In additic associated charm production must be expected in deep-inelastic scattering via the interaction of the virtual photon with a charmed quark in the sea. This quark can then combine with a second anti-quark from the proton 'bag' to form a charmed meson in the final state (Fig. 6.1). The residual quarks, missing a charmed quark, also have net charm and give rise to a second charmed meson of opposite charm to that of the struck quark. An estimate of this cross-section clearly requires some guess at the charmed part of the proton sea distribution. This will be discussed

further in Section 6.5 - rough estimates vary from 2-20% of the total cross-section below $x_{Bj} \sim 0.1$.

In addition to direct production of charmed particles, threshold effects as c(x) becomes important will give rise to apparent scaling violations. Clearly, as Q^2 and ν increase threshold effects will become less important and the structure functions should then re-scale.

Scaling violations of the order of 20% have been observed, and contradict the naive parton model. Alternative theories (Asymptotically Free Gauge Theories) can produce agreement with F_2 by allowing intrinsic scaling violation. The observed scaling violations can therefore be attributed to a mixtutre of intrinsic scaling violations and charm threshold effects, but the relative contributions are not well known. Investigation and measurement of direct charm production in deep-inelastic scattering can therefore remove some of this uncertainty.

Section 6.2 gives a description of an acceptance Monte Carlo for D-mesons and its use in the data analysis. Sections 6.2 and 6.3 present two approaches used to obtain invariant mass spectra for the D decay channels $K^{\pm}\pi^{\mp}$ and $K^{\pm}\pi^{\mp}\pi^{\mp}$. Finally, a summary of results and a brief comparison with theoretical predictions is given in Section 6.5.

6.2 SPECTROMETER ACCEPTANCE FOR D MESONS

The standard procedure used to identify resonance particles is by the enhancements they cause in the invariant mass spectra of their decay products. Having identified such an enhancement, a background subtraction can be made and a production cross-section calculated if the branching ratio for the decay channel observed and the acceptance of the apparatus for the decay products are both known. The mass of the D mesons, and the branching ratios of several of their decay channels are now reasonably well known. The only unknown required therefore, in a calculation of their production cross-section, is the acceptance of their decay products. Unfortunately, a calculation of the decay product acceptance is model dependent - both on the production mechanism and on the D decay scheme.

A description of the model used and the results obtained from it will be given in this section. An estimate of the model dependence will also be given. The philosophy used is straightforward. A Monte Carlo program is used to produce a D meson momentum vector distribution in the laboratory according to the model. The D is allowed to decay and the products tracked through the spectrometer to check for acceptance (Fig. 6.2).

D. Production Mechanism

Following the standard picture of deep-inelastic scattering, the incident muon beam is considered as a source of virtual photons defined by the variables Q^2 and ν. The reaction envisaged is thus

$$\gamma^* + p \rightarrow D + X$$

where γ^* represents the virtual photon

D represents the observed D meson

X represents all other hadrons produced

(conserving quantum numbers in the interaction).

Clearly, the ideas used in the production mechanism must be borrowed, at least to begin with, from normal (uncharmed) meson production. These can then be modified as necessary to account for any experimentally observed differences in charm production. In addition, angular and momentum dependence from the kinematics of the virtual photon must be included. A typical function for the D momentum vector might depend on the following (Fig. 6.3)

x_F - the modified Feynman x variable defined by

$$x_F = \frac{P_{11}}{(P^2_{max} - P^2_{\perp})^{\frac{1}{2}}}$$ where P_{11} is the momentum of the D in the direction of the virtual photon, and P_{max} the maximum momentum allowed.

$P^2_{\perp}$ - the squared transverse momentum of the D relative to the virtual photon direction.

ϕ_D - the azimuthal angle of the D momentum vector relative to the muon scattering plane.

Q^2, ν - the kinematics of the virtual photon.

ϕ_{γ^*} - the azimuthal angle of the virtual photon relative to a suitable plane in the experimental coordinate system (this is not a kinematic variable, but may affect acceptance).

The variables x_F, $P^2_{\perp}$ and ϕ_D are defined in the γ^*-proton centre of mass system. The variables Q^2, ν and ϕ_{γ^*} are defined in the laboratory system.

The kinematics of the virtual photon enter the description both via the determination of the direction vector of the centre of mass frame in the laboratory and in the determination of the value of P_{max}. The direction of the centre of mass frame relative to the incident muon particle is defined by $(\theta_s, \theta_{\gamma^*})$ where:

$$Q^2 = 4E(E - \nu)\sin^2\frac{\theta_s}{2} + \frac{m_\mu^2\nu^2}{E(E-\nu)}$$

with

E the incident beam energy

ϕ_s the scattering angle

m_μ the mass of the muon.

P_{max} is determined by having a D recoiling against a D-proton system moving at the same velocity. This gives:

$$P_{max} = \left[\frac{s}{4} + \left(\frac{(m_p + m_D)^2 - m_D^2}{4S}\right)^2 \frac{(m_p + m_D)^2 + m_D^2}{2}\right]^{\frac{1}{2}}$$

where

$s = m_p^2 + 2m_p\nu - Q^2$: centre of mass energy squared

m_p = proton rest mass

m_D = D meson rest mass

Clearly this requires an addition of a threshold such that:

$$s > s_{th} = (m_p + 2m_D)^2 \ (=21.8 \ (\text{GeV}/c^2)^2)$$

A simple step function was used since threshold behaviour should be relatively unimportant, typically $\nu \sim 150$ GeV/c^2 inside the experimental acceptance giving $s >> s_{th}$.

There are three further general points to note before discussing the exact model used:

(a) The D meson is an extremely narrow resonance (≤2-40 MeV) and it is reasonable to consider the mass as a delta-function at 1.87 GeV/c^2.

(b) Assuming a sea quark production mechanism, the charmed quark distribution functions are expected to cause some x_{Bj} dependence on the cross-section.

This analysis covers a small range of x_{Bj} ($0.0001 < x_{Bj} < 0.1$) and the charmed quark distribution was assumed to be constant.

(c) The variables chosen for the model are not unique. In some models, z ($= E_D/\nu$) is preferred to x_F and $P_\perp$ rather than $P_\perp^2$. Moreover, some Q^2 dependence might be required from charm threshold effects.

A discussion of the distributions of the variables used in the Monte Carlo, and the methods of obtaining them will now be given.

x_F Dependence

Uncharmed hadron production in muon scattering has an x_F dependence of the form e^{-bx_F} with $b \sim 3.5$.[58] There is some evidence however, that charmed particle production does not have an exponential x_F distribution but rather has a uniform z distribution[20]. For $z \gtrsim 0.2$, x_F and z are approximately identical and a uniform z distribution implies a uniform x_F distribution. The two distributions $D(x_F) = e^{-3.5x_F}$ and $D(x_F) =$ Constant were used to calculate the acceptance as a check on model dependence. Only the range $0 < x_F < 1.0$ (current fragmentation) was considered.

$P_\perp^2$ Dependence

This again requires consideration of uncharmed hadron production in deep-inelastic scattering, which has a dependence of the form $e^{-bP_\perp^2}$ with $b \sim 8$[59]. Model dependence was tested using two input distributions:

$$N(P_\perp) \sim e^{-8P_\perp^2} \quad , \quad n(P_\perp^2) = \text{Constant}$$

A cut-off at $P_\perp = P_{max}$ was applied.

ϕ_D Dependence

In the naive parton model, no azimuthal dependence is expected about the virtual photon axis, since the system has cylindrical symmetry. ϕ_D was therefore chosen uniformly in the range $0 < \phi_D < 2\pi$.

Q^2 and ν Dependence

Q^2 and ν must be chosen according to the cross-section $\frac{d^2\sigma}{dQ^2 d\nu}$ for deep-inelastic scattering, such that the scattered muon falls within the acceptance of the spectrometer. A cut was also imposed on Q^2 and ν corresponding to the cuts applied in the data analysis.

ϕ_{γ^*} Dependence

There is axial symmetry about the incident beam direction. ϕ_{γ^*} was chosen uniformly in the range $0 < \phi_{\gamma^*} < 2\pi$ relative to a known y axis perpendicular to the incident beam direction.

The methods chosen to generate these variables in the Monte Carlo were quite straightforward. A random number generator was used to provide the uniform ϕ distributions. A distribution of the form e^{-Ay} can be generated from the distribution $y = -\frac{1}{A} \ln y'$ where y' is chosen uniformly in the range $0 < y' < 1$. A cut-off was then applied at $x_F = 1$ and $P_\perp = P_{max}$.

A file containing all events used to measure $F_2(x)$ was used as a source for Q^2 and ν. Acceptance cuts on the scattered muon were then applied. To complete the description of the interaction, the vertex was chosen uniformly within the target volume, and the incident beam track

Having obtained the momentum vector of the D-meson in the γ^*-proton centre-of-mass frame, it is straightforward to transform into the laboratory system using standard rotation matrices and Lorentz transformations.

Decay-Product Generation

Only the decays $D^\circ \to K^-\pi^+$, $\overline{D^\circ} \to K^+\pi^-$ and $D^\pm \to K^\mp\pi^\pm\pi^\pm$ were considered. An isotropic decay distribution was used for the two body decay and a uniform phase space distribution for the three body decay. The decay products were considered to come directly from the interaction vertex. A simple hard core model was used to project the decay products through the spectrometer magnet. The particle trajectories could then be tested for acceptance. Additional cuts on momentum and opening angle could also be applied to 'particles' accepted by the apparatus as required.

General Results

The acceptance Monte Carlo served two purposes in the analysis. Its first objective was to obtain an acceptance for each of the four decay channels averaged over all kinematic variables. Its second function was to determine acceptance distributions for several of these variables. These distributions could then be used to determine data cuts which would maximise detection sensitivity.

An investigation into the model dependence in the Monte Carlo was carried out by considering two different functions for both the P_1^2 and x_F distributions:

(a) A uniform x_F distribution in the range $0 < x_F < 1.0$

(b) An exponential x_F distribution of the form $e^{-3.5x_F}$ in the range $0 < x_F < 1.0$.

(c) A uniform $P_\perp^2$ distribution in the range $0 < P_\perp^2 < 9$ $(GeV/c)^2$.

(d) An exponential $P_\perp^2$ distribution of the form $e^{-8P_\perp^2}$ in the range $0 < P_\perp < P_{max}$.

Each x_F distribution was used in conjunction with both $P_\perp^2$ distributions to produce four different functional inputs to the model.

The muon-kinematics acceptance distribution and the analysis cuts made on this also affect the resultant model distributions. The analysis cuts used were:

(a) $1 < Q^2 < 2$ $(GeV/c^2)^2$, $120 < \nu < 200$ GeV

(b) $0.5 < Q^2 < 1$ $(GeV/c^2)^2$, $140 < \nu < 200$ GeV

(c) $Q^2 > 2$ (GeV/c^2), $10 < \nu < 200$ GeV

These cuts correspond to a muon accpetance greater than 10% in all regions of the kinematic plane. The input z_D distributions obtained from each of the four $(x_F, P_\perp)$ distributions, are shown in Fig. 6.4 for $Q^2 > 1.0$ $(GeV/c^2)^2$. The results are weighted by the raw (Q^2,ν) distribution observed in the spectrometer following analysis cuts. The cut-off at $z_D \tilde{\approx} 0.1$ is a direct result of the muon kinematics. z_{min} is clearly obtained at $x_F = 0$, $P_\perp = 0$, $\nu = \nu_{max}$, $Q^2 = Q^2_{min}$, where the meson is produced at rest in the γ^*-proton centre of mass frame which has the highest energy possible. Retaining only terms in ν in the transformation to the laboratory frame gives

$$z_{min} \tilde{\approx} \frac{M_D}{\sqrt{2m_p\nu}} = 0.096$$

The uniform $P_\perp^2$ distribution clearly distorts the z distributions resulting from both x_F distributions. The acceptance as a function of

$p_\perp^2$ (and $P_\perp$) was found to be flat. Therefore, the observed differences are simply a result of the intrinsic $P_\perp$ dependence in x_F, which is most pronounced at high $P_\perp$ and low x_F. However, these distortions are the result of a violent change in the $P_\perp$ distribution. All measured uncharmed meson $P_\perp$ distributions show an exponential fall-off with $P_\perp$ which can be parameterised as a function of $P_\perp$ or $P_\perp^2$.[58] Any reasonable function of this type can be expected to give similar z distributions. Major differences will only occur as a result of improbably high values of $P_\perp$ or at low z (as can be seen in Fig. 6.4). Above $z \gtrsim 0.6$ the distributions are similar for both $P_\perp$ distributions.

The hadron arm in the downstream spectrometer was centred on the nominal beam centre of the apparatus. The geometric acceptance for positive and negative particles is therefore approximately the same, as should be the acceptance for the products in charge conjugate isotropic decays. Within statistics, all acceptance distributions (momentum, opening angle, x_F,z) were found to be the same for the charge conjugate decays. The average acceptance for charge conjugate decays agree to within ±0.02 for all models (Table 6.1). As this is the case, explicit reference to the sign of decay products will now be omitted in the remainder of this section. Thus the reference $D \to K\pi$ should be taken as referring to both decay channels ($D^\circ \to K^-\pi^+$, $\overline{D^\circ} \to K^+\pi^-$).

Since the spectrometer acceptance is flat as a function of $P_\perp$, the acceptance as a function of x_F (or z_D) determines the accepted $x_F(z_D)$ distributions resulting from the four input distributions. Figure 6.5 shows the acceptance as a function of x_F and z for the two input $P_\perp$ distributions (averaged over all accessible Q^2,ν). The acceptance follows the same trends for both $P_\perp^2$ distributions. At low x_F (or z_D)

the acceptance is poor, as would be expected in a downstream spectrometer. Acceptance increases rapidly with z_D as more decay products gain sufficient momentum to pass through the spectrometer magnet. The $K\pi\pi$ acceptance is consistently lower than that for $K\pi$, reflecting the lower average momentum of the decay products.

Convoluting the input x_F distribution with its acceptance will reproduce the x_F distribution observed downstream. The resulting z distributions for the four models are shown in Fig. 6.6. For the distributions obtained from a uniform x_F input distribution, the acceptance is clearly the dominating factor, weighting events to high z. In contrast it is the input $e^{-3.5x_F}$ distribution which is dominant over the acceptance and produces a distribution weighted to low z. As a result, the average acceptance in the two $e^{-3.5x_F}$ models is 30% lower than that in the models with a uniform x_F distribution (Table 6.1). Both the $K\pi$ and $K\pi\pi$ decays follow the same general shape.

The effect of spectrometer acceptance on two additional variables was investigated with regard to possible data cuts. These were the momentum distribution of the kaon and the angular distribution of the kaon relative to the momentum vector of the D in the γ^*-proton centre of mass frame (θ_K). θ_K is input as a uniform $\cos\theta_K$ distribution in both isotropic and phase space decay schemes. As was shown in Chapter 5, the momentum of the kaon must lie in a narrow band to obtain identification from the Cerenkov counter. The opening angle distribution is a standard procedure used to identify uncorrelated tracks which appear as spikes at $\cos\theta \sim \pm 1$.

The momentum distributions show the same trends for all models and in both decay channels. (Fig. 6.7) The kaon momentum peaks around 15 GeV/c and falls away slowly on a long tail out to 100 GeV/c. The

sharpest peak occurs in the distribution with both $e^{-8P_\perp^2}$ and $e^{-3.5x_F}$ as expected since this weights towards low x_F and $P_\perp$. Both uniform x_F, and uniform $P_\perp^2$ distributions tend to broaden this peak. As expected from the decay scheme, the kaon from the three body decay has a lower average momentum than that from the two body decay (Table 6.2). The peak in the momentum spectrum is also lower.

For all models, the opening angle distributions in both channels show a sharp fall-off at $\cos\theta_K \sim \pm 1$ (corresponding to forward-backward decay) (Fig. 6.8). Therefore, any opening angle cuts used to remove spikes will not greatly alter the overall acceptance. A cut in opening angle which removes all events where $|\cos\theta_K| > 0.90$ changes the overall spectrometer acceptance from 0.46 to 0.44 in the case D-Kπ, for $e^{-8P_\perp^2}$, uniform x_F input.

However, the effects of this cut must be considered in conjunction with the data analysis cuts used to obtain a cross-section. These also affect the angular acceptance and will be discussed as appropriate.

6.3 D-MESON ANALYSIS 1

As was outlined in Section 6.1, the aim of this analysis was to search for enhancements in $K^{\pm}\pi^{\mp}$ and $K^{\pm}\pi^{\mp}\pi^{\mp}$ invariant mass spectra in the neighbourhood of 1.8 GeV/c^2. In this search, the information provided by the Cerenkov counter was used to identify the kaons (since kaons with a momentum less than 21.2 GeV/c do not emit Cerenkov radiation in the counter). As was shown in Chapter 5, there are two backgrounds which also give this signal.

1. Protons. These also fail to emit Cerenkov radiation in this momentum range.
2. Pions. Inefficiency in the counter, particularly quantum inefficiency at low momentum can result in pions failing to emit Cerenkov radiation.

In the usual picture of deep-inelastic scattering, the downstream products come from the fragmentation of the virtual photon and the target proton is given little momentum. Baryon anti-baryon production from fragmentation should be highly suppressed relative to meson production and the target proton should rarely be seen by the downstream spectrometer. Proton contamination is therefore expected to be small. A measurement of proton production was made at higher momenta, at which protons can be identified unambiguously by the Cerenkov counter (Chapter 7). This was found to be consistent with background and therefore proton contamination was neglected in this analysis.

The mean π/K ratio observed in the experiment was approximately 6:1 (Chapter 7). A small inefficiency in the Cerenkov counter can therefore lead to a high background contamination in the kaon signal due to pions - an inefficiency of 5% corresponds to a contamination of over 20%. This effect determines the minimum momentum at which kaons can be identified for a given pion contamination.

Several schemes were used to classify particles:

A Particles with a momentum between 12.4 GeV/c and 21.2 GeV/c which fail to light the Cerenkov counter are classified as kaons, (corresponding to the 95% pion efficiency level and the kaon Cerenkov threshold respectively). All other hadrons are considered to be pions.

B Particles with a momentum between 8.0 GeV/c and 31.0 GeV/c which fail to light the Cerenkov counter are classified as kaons (corresponding to the 90% pion efficiency level and the 90% kaon efficiency level respectively). All other hadrons are classified as pions.

C Particles with a momentum between 12.4 GeV/c and 21.2 GeV/c which fail to light the Cerenkov counter are classified as kaons. Particles with a momentum less than 21.2 GeV/c which light the counter are classified as pions. No other particles considered.

Clearly, these examples form only a subset of the possible criteria which can be applied to the identification scheme. The choice of criteria used to obtain a final measurement was determined by the basic result of this analysis. No enhancement was observed in the vicinity of the D mass either in $K\pi$ or $K\pi\pi$ combinations. Schemes B and C above both suffer from the problem that the momentum dependent quantum inefficiency must be incorporated into the acceptance Monte Carlo. Scheme 'A' provides 100% acceptance for D decays producing a kaon within the given momentum range, provided all decay products are accepted by the spectrometer. This scheme was therefore chosen to obtain an upper limit on D-meson production.

The event kinematics and acceptance cuts used were:

(a) $10 < \nu < 200$ GeV, $2 < Q^2 < 80$ $(GeV/c^2)^2$

$120 < \nu < 200$ GeV, $1 < Q^2 < 2$ $(GeV/c^2)^2$

$140 < \nu < 200$ GeV, $0.8 < Q^2 < 1$ $(GeV/c^2)^2$

$160 < \nu < 200$ GeV, $0.5 < Q^2 < 0.8$ $(GeV/c^2)^2$

$170 < \nu < 200$ GeV, $Q^2 < 0.5$ $(GeV/c^2)^2$

(b) $x_{Bj} < 0.1$

(c) $W^2 > 22$ GeV^2

(d) The interaction vertex was required to lie inside the target area in x and y, and within three standard deviations of the target in z.

(e) The scattered muon was required to have Class 1 timing and both x and y links to proportional chamber tracks. The downstream muon track was required to pass outside the K-veto hodoscope and inside the outer limits of the M and M' hodoscopes. Finally, the downstream track was required to project within 3 cm of the interaction vertex in y.

Hadron identification was based on the tracksorting scheme described in Chapter 4. Only tracks with Class 1 timing were allowed. In addition to passing the duplicate and quality tests of the track sorter, hadron tracks were required to link to both x and y tracks in the proportional chambers. A pointing test was applied to these links, requiring:

$$(x_{proj} - x_{vert}) < 3\,\varepsilon_x + 8 \text{ mm}$$

$$(y_{proj} - y_{vert}) < 3\,\varepsilon_y + 8 \text{ mm}$$

where (x_{proj}, y_{proj}) are the (x,y) coordinates of the track at the vertex;

(x_{vert}, y_{vert}) the coordinates of the vertex; and $\epsilon_{x,y}$ is the error on the (x,y) coordinates of the vertex. The minimum value of 8 mm ensures that if the vertex is well determined, the track pointing requirements are not unreasonably strict (Fig. 6.9).

Candidates for kaon tracks were only selected from those hadron tracks which passed outside the Cerenkov beam deadener and inside the mirror 'window-frames' as described in Chapter 5. All hadrons which either failed this geometric test or the kaon criteria were classified as pions.

The invariant masses of the various combinations were then obtained for each event, and entered in the appropriate plots. Multiple entries were allowed for each event in different plots, e.g. a combination $K^+\pi^-\pi^-$ would enter once in the three particle plot, and twice in the two particle plot - this should only affect low mass background.

Data analysis was carried out in two regions of

$$Q^2 : Q^2 < 1.0 \ (GeV/c^2)^2 \ ; \ \ 1 < Q^2 < 80 \ (GeV/c^2)^2$$

High $Q^2 : 1 < Q^2 < 80$

A search for D meson production was made in this region following schemes A and B outlined above. An analysis of the four separate channels ($K^+\pi^-$, $K^-\pi^+$, $K^+\pi^-\pi^-$, $K^-\pi^+\pi^+$) could not be made as there was insufficient data. Following the symmetry arguments given earlier, charge conjugate decay channels were combined. The invariant mass spectra for $K\pi$, $K\pi\pi$ and their sum are shown in Figures 6.10 and 6.11 for schemes A and B. $Cos\theta_K$ distributions are shown for the two schemes in Figures 6.12 and 6.13, where θ_K is defined as the angle between the kaon momentum vector and that of the combined mass M in the laboratory, measured in the rest frame of M (Fig. 6.14). z_M distributions are shown,

in Figures 6.15 and 6.16, where z_M is defined as E_M/ν.

Schemes A and B were expected to give similar results. However, despite an increase in background from pion contamination, it was hoped that scheme B would give increased sensitivity (as it has a higher acceptance for kaons). The general features of the three distributions are the same for both schemes. No enhancements which cannot be attributed to simply statistical fluctuations are apparent in the mass range 1.6-2.0 GeV/c for either scheme. The observed opening angle distributions agree qualitatively with those obtained in the Monte Carlo. Features which might justify an opening angle cut on the data are not apparent (e.g. spikes at $\cos\theta_K \sim 1$), therefore no opening angle cut was used. The observed z_M distributions are also similar to those obtained from the Monte Carlo. This however, must simply be an effect of acceptance, and general meson production since it is clear from the scatter plots shown in Fig. 6.17 that low z entries in the data come predominantly from low mass combinations. The only reasonable conclusion from this analysis is that there is no observable D-meson production. The following scheme was then used to calculate an upper limit on D-meson production. This was only carried out for scheme A, as it was only for this scheme that the acceptance could be calculated with confidence..

The overall spectrometer acceptance (α) for the four decay channels is shown in Table 6.3. The D-meson production model used was a uniform x_F distribution and an $e^{-8P_\perp^2}$ distribution. The branching ratios for the decay channels (B) and the values $\alpha.B$ are also shown in Table 6.3. It is apparent that within errors, all channels have the same $\alpha.B$. Since charged and neutral D-meson production should occur with equal probability and have nearly the same mass, it is a reasonable approximation to sum all four channels (which will increase sensitivity).

The resultant distribution - D - can then be assigned a mean $\alpha.B$ for use in calculation of the cross-section upper limit. This however, also requires an estimate of the maximum number of D-meson events. It was chosen to estimate this, by the number required to give a 1.64 standard deviation above background (90% confidence level) in the region of the D mass (1.87 GeV/c^2) within the resolution of the spectrometer.

The combined invariant mass plot is shown in Fig. 6.10. The background under the D is fairly flat and was estimated by the average number of events in the range 1.75-1.95 GeV/c^2. The mass resolution of the spectrometer was measured to be 40 MeV/c^2 σ_{rms} from the width of K^o_s(38). The background estimate is therefore given by the total number of events in the range 1.83-1.91 GeV/c^2. The results are shown in Table 6.5. An upper limit of 2200 D-mesons produced in this data set was obtained. Cerenkov counter information was available for only a section of the total data and comprised of an integrated flux of 3.95×10^{10} μ's in which there were a total of 4398 deep-inelastic scattering events. (A discussion of the normalisation is given in Chapter 8, and results in Tables 8.1 and 8.3.)

The 90% confidence level on the total cross-section $\mu + p \rightarrow \mu + D + X$ based on this analysis, in the region $1 < Q^2 < 80$ $(GeV/c^2)^2$, $10 < \nu < 200$ G is

$$23.4 \pm 7.6 \text{ nbarns}$$

and the contribution of charm production to the total cross-section in this region

$$50 \pm 16.3\%$$

The error in the measured branching ratios (26%) was combined in quadrature with an estimated error due to averaging $\alpha.B$ (33%) to obtain the relative error in the cross-section.

Low Q^2 : $Q^2 < 1.0$ GeV/$c^2)^2$

The results of the high Q^2 analysis indicated that no increase in sensitivity would be obtained by identification scheme B. Therefore only identification scheme A was used in the low Q^2 analysis. Again, statistics limited the investigation to the combined decay channels $K^{\pm}\pi^{\mp}$, $K^{\pm}\pi^{\mp}\pi^{\mp}$.

The invariant mass spectra for $K\pi$, $K\pi\pi$ and their sum are shown in Fig. 6.18, z_M and $\cos\theta_K$ distributions are shown in Figures 6.19 and 6.20. Again, no enhancements in the invariant mass spectra which are not consistent with statistical fluctuations are observed. The z_M and $\cos\theta_K$ distributions show no anomalous behaviour, and again no opening angle cut was applied to the data. An upper limit on the D-production cross-section was therefore calculated, following the procedure described in the high Q^2 analysis.

From Fig. 6.18 it is clear that the background in the vicinity of the D-mass, for the summed 4 channel plot, is relatively flat. The average number of events in the range 1.7-2.0 GeV/c^2 was used as an estimate of background. The spectrometer acceptance α, and $\alpha.B$ are shown in a Table 6.4 for this Q^2 range. A large variation is apparent for the four channels, but errors are also large and the approximation that these be represented by an average value is not unreasonable (particularly as the analysis is an estimate of an upper limit). The results obtained are shown in Table 6.5. An upper limit of 1642 D-mesons produced in this kinematic region was obtained. This corresponds to a total cross-section for D-meson production of 14.8 ± 3.9 nbarns, and corresponds to a contribution of 34 ± 8.9% to the total deep-inelastic cross-section in this region. The error, due to averaging $\alpha.B$ was combined in quadrature with that in the measured branching ratios to obtain the quoted errors.

6.4 D-MESON ANALYSIS 2

The D-meson acceptance Monte Carlo predicted a large fraction of decays, which were fully accepted by the spectrometer but in which the $\bar{K}$ kaon had a momentum greater than 21.2 GeV/c (Fig. 6.7, Table 6.6). Since the analysis which used the Cerenkov counter identification of the kaon had resulted in too small an acceptance to provide a useful upper limit, a scheme involving these high momentum kaons was considered. The only major problem to be overcome is that of multiple combinations as some 30% of the hadrons observed in the spectrometer had a momentum greater than 21 GeV/c (Fig. 6.21).

The general method used was to consider each hadron with a momentum greater than 21.2 GeV/c as a kaon and combine this with all other hadrons in the event. Distributions for $K\pi$ and $K\pi\pi$ using this simple method are shown in Figures 6.21 and 6.22. Clearly a detailed understanding of the background resulting from multiple combinations is required before a reliable estimate of D production can be made. This indicated the use of a second Monte Carlo, and therefore the simple approach was rejected.

The general characteristics of D-meson production, predicted from the Monte Carlo were used to remove the effects of multiple combinations in a second approach. As the spectrometer acceptance was predominantly at high z (Fig. 6.5) it is reasonable to assume that only one of the pair of D mesons can be observed in the spectrometer. It was therefore chosen to make only <u>one</u> entry per event in any of the plots - the combination with the mass closest to the D-meson mass was selected.

The event and hadron selection criteria given in Section 6.3 were also applied in this analysis. Plots were accumulated for the following classes in each event:

1. The two particle mass closest to 1.86 GeV/c^2.
($K^-\pi^+$ or $K^+\pi^-$ but not both).

2. The three particle mass closest to 1.86 GeV/c^2.
($K^-\pi^+\pi^+$, $K^+\pi^-\pi^-$ but not both).

3. The invariant mass combination closest to 1.86 GeV/c^2.

4. Results were further classified in two z_M bins:
$0 < z_M < 0.4$; $0.4 < z_M < 1.0$.

High Q^2 : $1 < Q^2 < 4$ (GeV/c^2)^2; $4 < Q^2 < 80.0$ (GeV/c^2)^2

The invariant mass distributions for decay channels containing either a K^+ (i.e. $K^+\pi^-$ or $K^+\pi^-\pi^-$) or a K^- (i.e. $K^-\pi^+$ or $K^-\pi^+\pi^-$), resulting from this procedure are shown in Fig. 6.23, for $z_m > 0.4$. In both plots, but particularly in that for the channel containing a K^-, there is an enhancement in the vicinity of 1.85 GeV/c^2. It was then necessary to determine whether this was a real D-meson signal, or a result of the mass selection procedure. To investigate this, a second series of plots were obtained in which:

A only hadrons with momenta greater than 21.2 GeV/c were chosen as kaons

B Only hadrons with momenta less than 21.2 GeV/c were chosen as kaons.

The momentum cut of 21.2 GeV/c was chosen to allow the use of the Cerenkov counter to reject pions in Class B ultimately.

Fig. 6.24 shows the invariant mass distributions for K^+ and K^- in the two momentum bands for $z_M > 0.4$. The enhancement is clearly visible in the K^- plot at low momentum, and perhaps also in K^+. However, no enhancement is apparent in either plot for selection A above.

Fig. 6.25 shows $\cos\theta_K$ distributions obtained using selection A for masses greater than 1 GeV/c^2, clearly indicating a preference towards forward decay. However, no anomalous behaviour is apparent. An upper limit could therefore be obtained from scheme A, further investigation was required for scheme B.

A first stage in investigating the enhancement observed in scheme B was to obtain finer mass binning. This is shown for the summed distribution ($K^+ + K^-$) in Fig. 6.26 for the ranges $0 < z_m < 0.4$, $z_m > 0.4$, $1 < Q^2 < 4$ (GeV/c^2)^2, $4 < Q^2 < 80$ (GeV/c^2)^2. No Q^2 or z dependence is apparent, and the enhancement is no longer clear. This suggested that the enhancement was a statistical fluctuation amplified by binning and mass selection. Nevertheless, a second stage of investigation was pursued using the Cerenkov counter information to reject pions (unfortunately also reducing the data set available). The object was to detect as many pions as possible and no geometric cuts were applied to tracks (such as in Chapter 5). Selecting only those hadrons which also failed to light the Cerenkov counter as kaon candidates clearly produces a much purified sample, even allowing for detection efficiency (a minimum of 50-60% kaons). Fig. 6.27 shows the result of this cut on the invariant mass distributions. The most striking fact is the large reduction in the number of entries (a factor of 10). A comparison of z_m and $\cos\theta_K$ distributions, with and without pion rejection, are shown in Figures 6.28 and 6.29. In both cases, the cut does not affect the general shape of the distributions, and both are in semi-quantitative agreement with Monte Carlo predictions (particularly the observed peaking at $\cos\theta_K \sim 1$). The breakdown of the summed distributions into z and Q^2 bins is shown in Fig. 6.30. Statistics are very poor, and no conclusions can be drawn.

As was the case in Analysis 1, the conclusion of this analysis is therefore that there is no observable D-meson signal in the four channels $K^+\pi^-$, $K^-\pi^+$, $K^+\pi^-\pi^-$, $K^-\pi^+\pi^+$. An upper limit will be estimated following the procedure given in Section 6.3. This will be made for the following criteria:

(a) $P_K > 21.2$ GeV/c, $z > 0.4$, $Q^2 > 1$ (A2)

(b) $P_K < 21.2$ GeV/c, $z > 0.4$, $Q^2 > 1$ using Cerenkov counter rejection of pions (B2)

(c) $P_K < 21.2$ GeV/c, All z, $Q^2 > 1$ using Cerenkov rejection of pions (C2)

(d) $P_K < 21.2$ GeV/c, All z, $Q^2 > 1$, without rejection of pions. (D2)

(a) $P_K > 21.2$ GeV/c, $1 < Q^2 < 80$ $(GeV/c^2)^2$, $z > 0.4$

The four channel summed distribution for this class is shown in Fig. 6.31. The distribution is relatively flat in the range 1.75-1.95 GeV/c^2 and the average value in this range was chosen as an estimate of the background. A table of acceptance for this class of events is given in Table 6.6 from which a mean value of $\alpha.B$ was obtained. Details of the results are given in Table 6.8. An upper limit of 1760 ± 526 D-mesons was obtained. The full data set was used for this measurement, and the normalisation is given in Tables 8.1 and 8.3 (Data set A).

The 90% confidence level on the total cross-section for D-meson production is 9.9 ± 3.0 nbarns, corresponding to a contribution to the total deep-inelastic cross-section of 21.2 ± 6.3%.

(b) $P_K < 21.2$ GeV/c, $z > 0.4$, $1 < Q^2 < 80$ (GeV/c^2) - Including pion Rejection.

The acceptance for this class is given in Table 6.7. Summed distributions for the four channels are shown in Fig. 6.27. The invariant mass distribution is flat and the average in the range 1.5-2.2 GeV/c^2 was used to estimate the background. Details are given in Table 6.8, the 90% confidence level was measured to be 1281 ± 478 D-mesons. Normalisation is from Data Set B in Tables 8.1 and 8.3. A limit on the total cross-section of 7.2 ± 2.7 nbarns corresponding to 15.4 ± 5.8% of the total deep-inelastic cross-section is obtained in this region.

(c) $P_K < 21.2$ GeV/c, All z, $1 < Q^2 < 80$ (GeV/c^2) - Including pion Rejection.

The Monte Carlo calculation of acceptance for this class is given in Table 6.7. The four channel summed invariant mass distribution is shown in Fig. 6.32. Again, this distribution is flat and the average value in the range 1.6-2.0 GeV/c^2 was used to estimate background. A 90% confidence level of 1340 ± 413 D-mesons was obtained (details are given in Table 6.7). The relevant normalisation is Data Set B in Tables 8.1 and 8.3. This gives a 90% confidence level on the total charm production cross-section of 14.2 ± 4.4 nbarns, corresponding to 30.5 ± 9.4% of the total deep-inelastic cross-section.

(d) $P_K < 21.2$ GeV/c, All z, $1 < Q^2 < 80$ (GeV/c^2)^2 - No pion Rejection

The aim in calculating an upper limit from this class was to use the full data set in an attempt to obtain a consistency estimate with those previously given.

The acceptance for this class is given in Table 6.7. The summed invariant mass distribution is shown in Fig. 6.33. This is not wholly consistent with a flat distribution, but for an estimate of the background in the vicinity of 1.85 GeV/c^2, it would be reasonable to take the average value of the distribution in the range 1.75-1.95 GeV/c^2. Details are given in Table 6.8, a 90% confidence level of 2978 ± 918, D-mesons was obtained. The normalisation is given in Tables 8.1 and 8.3 for Data Set 8. This gives the 90% confidence level for the total D meson cross-section of 16.7 ± 5.2 nbarns, corresponding to a contribution of 35.9 ± 11.1% to the total deep-inelastic cross-section.

Low Q^2 : $Q^2_{min} < Q^2 < 1.0$ $(GeV/c^2)^2$:

Only two categories were investigated in this region:

1. The kaon chosen only from hadrons with momenta greater than 21.2 GeV/c (where no pion rejection is possible).
2. The kaon chosen only from hadrons with momenta less than 21.2 GeV/c which failed to light the Cerenkov counter (using the loose cuts of this section).

A comparison between the invariant mass spectra of K^+ and K^- channels for the above categories and $z_M \gtrless 0.4$ is shown in Figures 6.34 and 6.35. Scatter plots against z for $z_M > 0.4$ are shown in Fig. 6.36. No statistically significant enhancements in the vicinity of 1.85 GeV/c^2 are apparent in any of these distributions. The most striking feature is that pion rejection again reduces the number of entries in the plots for classification 2 to approximately $^1/10^{th}$ of those for classification 1. An interesting background is apparent in the scatter plots where elastic ρ events are clearly visible at $z \sim 1$ and a mass of $M \sim m_p + m_K - m_\pi$. Fig. 6.37 shows a comparison of the $\cos\theta_K$ distributions for $P_K > 21.2$ GeV/c and $P_K < 21.2$ GeV/c. No significant deviations from Monte Carlo predictions

were apparent, therefore no opening angle cut was applied to the data.

Again, the conclusion of this analysis was that no observable D-meson signal was apparent in the data, and an upper limit on the cross-section was obtained following the procedure described in Section 6.3. This was carried out for the four classifications:

(a) $P_K > 21.2$ GeV/c, $Q^2_{min} < Q^2 < 1.0$ (GeV/c^2)^2, $0 < z_m < 1$

(b) $P_K > 21.2$ GeV/c, $Q^2_{min} < Q^2 < 1.0$ (GeV/c^2)^2, $0.4 < z_m < 1$

(c) $P_K < 21.2$ < GeV/c, $Q^2_{min} < Q^2 < 1.0$ (GeV/c^2)^2, $D < z_m < 1$ - using pion rejection,

(d) $P_K < 21.2$ GeV/c, $Q^2_{min} < Q^2 < 1.0$ (GeV/c^2)^2, $0.4 < z_m < 1$ - using pion rejection.

The four channel summed invariant mass distributions for these classifications are shown in Fig. 6.38. Tables 6.9 and 6.10 give the acceptance values from the Monte Carlo using a uniform x_F distribution and an $e^{-8P_\perp^2}$ distribution as input. The errors on $\langle\alpha.B\rangle$ in these tables are calculated from the spread in $\alpha.B$, and the measured error in B combined in quadrature. Results are given in Table 6.11, background estimates were taken as the average number of events in the ranges indicated on Fig. 6.38. The normalisation given in Tables 8.1 and 8.3 for the appropriate data sets gives the following upper limits on D-meson production for $Q^2 < 1.0$ (GeV/c^2)^2:

(a) $P_K > 21.2$ GeV/c, $0 < z_m < 1.0$ (E2):

A total D cross-section of 8.0 ± 2.5 nbarns, corresponding to 18.8 ± 5.9% of the deep-inelastic cross-section.

(b) $P_K > 21.2$ GeV/c, $0.4 < z_m < 1.0$ (F2):

A maximum D production cross-section of 6.9 ± 2.2 nbarns, corresponding to 16.2 ± 5.2% of the deep-inelastic cross-section.

(c) $P_K < 21.2$ GeV/c, $0 < z < 1$ (G2):

A maximum D production cross-section of 11.2 ± 4.2 nbarns, corresponding to 26.3 ± 9.9% of the deep-inelastic cross-section, was obtained though statistics are poor in this plot.

(d) $P_K < 21.2$ GeV/c, $0.4 < z < 1$ (H2):

There are very few entries in this plot. A maximum D production cross-section of 8.2 ± 3.5 nbarns, corresponding to 19.3 ± 8.2% of the deep-inelastic cross-section.

6.5 DISCUSSION OF RESULTS

The calculation of the charm contribution to deep-inelastic scattering is important in the understanding of the scaling violations observed in the inelastic structure functions at small x. A comparison of the upper limit obtained in this analysis with various theoretical estimates will be made. Some recent experimental results will also be given.

A summary of the results obtained in Sections 6.3 and 6.4 is given in Table 6.12. It is clear from this analysis that the spectrometer had a very low efficiency for the detection of the hadronic decays of D-mesons. Moreover, the Monte Carlo used to calculate final values of acceptance was the most favourable possible - if D-mesons are produced with an x_F distribution similar to non-charmed hadrons, (i.e. weighted towards low x_F) then the acceptance is essentially zero. In addition, coupled to this low acceptance there is the disastrously low branching ratios of the two and three body hadronic decay channels of 2-4%. The probability of observing a D-meson decay is therefore a number of order 0.1 x 0.03, and the results reflect the very low sensitivity. A single event therefore represents an enormous cross-section - most of the limits obtained would correspond to an observed signal of only 10 events but nevertheless represent a contribution to the total cross-section of some 20-30%.

The various estimates of an upper limit on charm production do not represent independent measurements: rather they represent measurements on the same data using analyses of different sensitivities. Therefore, it is reasonable to take the lowest 90% cl in each Q^2 region as a best estimate on charm production (since this corresponds to the analysis with highest sensitivity).

Explicitly defining the regions of integration (corresponding to the analysis cuts) gives:

$$\int_{Q^2_{min}}^{1.0} \int_{\nu\nu 140,\ x_{Bj}<0.1}^{200} \frac{d^2\sigma}{dQ^2 d\nu}(\mu p \to \mu + D + X) \lesssim 6.9 \text{ nbarns}$$

(representing 16.2% of the total cross-section in this region).

$$\int_{Q^2=1}^{80} \int_{\nu=10,\ x_{Bj}<0.1}^{200} \frac{d^2\sigma}{dQ^2 d\nu} (\mu p \to \mu + D + X) \lesssim 7.2 \text{ nbarns}$$

(representing 15.4% of the total cross-section in this region). However, the errors on these limits are some 30-40%. The means of the kinematic variables in these regions are:

(a) $Q^2 = Q^2_{min} - 1.0$ $(GeV/c^2)^2$

$\langle Q^2 \rangle = 0.25$ $(GeV/c^2)^2$

$\langle \nu \rangle = 183$ GeV

$\langle s \rangle = 344$ GeV^2

$\langle x \rangle = 0.0007$

(b) $Q^2 = 1.0 - 80.0$ $(GeV/c^2)^2$

$\langle Q^2 \rangle = 5.1$ $(GeV/c^2)^2$

$\langle \nu \rangle = 141$ GeV

$\langle s \rangle = 200$ GeV^2

$\langle x \rangle = 0.023$

Other Experimental Results

One other experiment has estimated the contribution to the deep-inelastic cross-section from charmed D-meson production.[20] This estimate was inferred from the observed rate of dimuon production relative to the normal deep-inelastic process which gives a single muon in the final state (i.e. $\frac{\sigma(\mu^+ + p \to \mu^+ + \mu^\pm + X)}{\sigma(\mu^+ + p \to \mu^+ + X)}$)

However, again this result relies on a model dependent calculation of acceptance for the muon from D-decay. An upper limit on the contribution from charm production in deep-inelastic scattering of 5% was obtained.

Although the processes are not directly related to deep-inelastic muon scattering, it is interesting to compare the cross-sections obtained for D-meson production in e^+e^- annihilation and neutrino scattering with the results presented in this thesis. The vector meson $\psi(3772)$ lies just above D threshold and decays completely into $D^\circ\overline{D^\circ}$. The total cross-section for this reaction[56] is

$$e^+ + e^- \rightarrow \psi(3772) \text{ is } 9.1 \pm 2 \text{ nbarns}$$

at a centre of mass energy of 3.772 GeV. The branching ratios to the two possible decay channels were also measured:

$$B[\psi(3772) \rightarrow D^\circ\overline{D^\circ}] = 0.56$$

$$B[\psi(3772) \rightarrow D^+D^-] = 0.44$$

(where the difference is a result of a slight mass difference). D° and $\overline{D^\circ}$ production have been observed in neutrino scattering, directly from their hadronic decays[57] (it is interesting to note that the charged meson $D^\pm$ has not been observed within the experimental resolution). A contribution from D° production to the deep-inelastic neutrino scattering of 17.5% was obtained. However, as was already mentioned, neither of these results can be directly related to charm production in muon scattering. In e^+e^- annihilation the picture is of resonance production via the $\psi(3772)$ and would only be relevant in some G.V.M.D. model of diffractive D production where the virtual photon 'turns into' a vector meson ($\psi(3772)$ or higher mass), which then decays to D mesons. In neutrino scattering, the interaction is mediated by the weak current and comparison of results requires quantitative predictions in a unified gauge theory of weak and electromagnetic interactions.

Theoretical Estimates of Charm Production

Estimates of charm production have been calculated in two basic models: the Generalised Vector Meson Dominance model and asymptotically free gauge theories such as Q.C.D.

G.V.M.D.[59] predicts a contribution to the cross-section from charm production of ∿13% for large Q^2 and ν at $x \sim 0$. At finite Q this result must be reduced by a factor

$$\frac{M_\rho^2 + Q^2}{M_\psi^2 + Q^2}$$

Thus in the region $Q^2 < 1.0(\text{ GeV}/c^2)^2$ G.V.M.D. predicts a contribution of ∿1%, and in the region $1 < Q^2 < 80\ (\text{GeV}/c^2)^2$ 6-7%.

Several field theory calculations are available. Gluck and Reya[60] calculate a contribution of 50% from charm production at $x \lesssim 0$ and ∿30% at $x \sim 0.1$ (assuming a small uncharmed SU(3) symmetric sea and a charmed sea component consistent with neutrino data). Barger and Phillips[61] estimate $\sigma_c/\sigma_{All} = 0.09$ for $\langle x \rangle = 0.05$, $\langle \nu \rangle = 140$ GeV, $\langle Q^2 \rangle = 6.5\ (\text{GeV}/c^2)^2$, using a quark parton model with an SU(4) symmetric sea. (This calculation was relevant to the results presented in reference 20). In a recent publication by Leveille and Weiler[62], both the total charm production cross-section and the contribution to F_2 are calculated for $Q^2 \gtrsim 2.5(\text{GeV}/c^2)^2$. (Moreover, the results are presented in a form which facilitates comparison with experiment.) They calculate a contribution to F_2 at $x \sim 0.1$, $Q^2 \sim 5\ (\text{GeV}/c^2)^2$ of 0.022 from charm production. The value of F_2 at the mean value of x and Q^2 used in this analysis (high Q^2) is 0.4[9]. Therefore, the calculated contribution corresponds to ∿6% of the total cross-section.*

* Unfortunately, there appears to be an error in the paper in the value of the total cross-section. In the text a value of ∿23 nbarns is quoted for muoproduction at a laboratory energy of 275 GeV whereas a figure (Fig. 3) in the paper gives ∿2 nbarns. The correct value is 2.3 nbarns.[75]

The limits on charm production are in agreement with that obtained by Chen et al[20]. The results are also in semi-quantitative agreement with theoretical predictions. However, a true test of these predictions and of the models used can only be obtained from a measurement of the Q^2 dependence of charm production.

TABLE 6.1

MODEL DEPENDENCE OF AVERAGE SPECTROMETER ACCEPTANCE

Acceptance for Channel Input Distributions	K^-K^+	$K^+\pi^-$	$K^-\pi^+\pi^+$	$K^+\pi^-\pi^-$
$e^{-3.5x_F}$, $e^{-8P_\perp^2}$	0.46	0.30	0.15	0.15
Uniform x_F, $e^{-8P_\perp^2}$	0.46	0.46	0.31	0.32
$e^{-3.5x_F}$, Uniform $P_\perp^2$	0.25	0.25	0.14	0.15
Uniform x_F, Uniform $P_\perp^2$	0.42	0.42	0.28	0.29

TABLE 6.2

Accepted Kaon Momentum Distributions: a, b GeV/c, mean kaon momentum, and standard deviation respectively

Channel Input Distribution	$K^-\pi^+$	$K^+\pi^-$	$K^-\pi^+\pi^+$	$K^+\pi^-\pi^-$
$e^{-3.5x_F}$, $e^{-8P_\perp^2}$	30.3,24	28.1,20	24.3,17	24.3,17
Uniform x_F, $e^{-8P_\perp^2}$	44.2,33	38.5,27	34.7,24	32.6,21
$e^{-3.5x_F}$, Uniform $P_\perp^2$	33.3,24	33.0,24	27.4,19	27.3,19
Uniform x_F, Uniform $P_\perp^2$	35.9,24	35.3,24	45.0,32	44.4,31

TABLE 6.3

Spectrometer Acceptance: $1 < Q^2 < 80$ $(GeV/c^2)^2$ (using Cerenkov Counter Identification Scheme A)

Channel	Acceptance α	Branching Ratio B	$\alpha.B$ $(x10^3)$
$K\pi$	0.08	0.022	1.76
$K\pi\pi$	0.06	0.039	2.34

$\langle\alpha.B\rangle = 2.05 \pm 0.67 \times 10^{-3}$ (error in B combined in quadrature with variance of $\alpha.B$)

TABLE 6.4

Spectrometer Acceptance: $Q^2 < 1.0$ $(GeV/c^2)^2$ (using Cerenkov Counter Identification Scheme A)

Channel	Acceptance α	$\alpha.B$ $x10^3$
$K^+\pi^-$	0.098	2.2
$K^-\pi^+$	0.071	1.6
$K^+\pi^-\pi^-$	0.084	3.3
$K^-\pi^+\pi^+$	0.076	3.0

$\langle\alpha.B\rangle = 2.52 \pm 0.66 \times 10^3$ (error in B combined in quadrature with variance of $\alpha.B$).

TABLE 6.5

Upper Limits on Charmed Meson Production (Analysis 1 for an integrated flux of 3.95×10^{10} μ's)

Q^2 $(GeV/c^2)^2$	Background Estimate	Events for 1.64 Deviation	$\langle\alpha.B\rangle$ ($\times 10^3$)	90% c.l. (Events)
Q^2_{min} - 1.0	6.4	4.14	2.52	1642 ± 430
1.0-80.0	7.2	4.4	2.05	2200 ± 719

TABLE 6.6

Spectrometer Acceptance for Analysis 2: $p_K > 21.2$ GeV/c, $1 < Q^2 < 80$ $(GeV/c^2)^2$, $z > 0.4$

Channel	Acceptance α	α.B ($\times 10^3$)
$K^-\pi^+$	0.30	6.6
$K^+\pi^-$	0.32	7.0
$K^-\pi^+\pi^+$	0.19	7.4
$K^+\pi^-\pi^-$	0.19	7.4

$\langle\alpha.B\rangle = 7.1 \pm 2.1 \times 10^{-3}$ (error in B combined in quadrature with variance of α.B).

TABLE 6.7

Spectrometer Acceptance for Analysis 2: $p_K < 2.12$ GeV/c,

$1 < Q^2 < 80$ (GeV/c^2)^2

Channel	Acceptance α ($0 < z < 1$)	α_z ($0.4 < z < 1$)	α.B ($\times 10$)	α_z.B ($\times 10$)
$K^-\pi^+$	0.135	0.076	2.97	1.67
$K^+\pi^-$	0.148	0.089	3.26	1.96
$K^-\pi^+\pi^+$	0.114	0.080	4.45	3.12
$K^+\pi^-\pi^-$	0.119	0.085	4.64	3.32

$\langle\alpha.B\rangle = 3.83 \pm 1.18 \times 10^{-3}$

$\langle\alpha_z.B\rangle = 2.52 \pm 0.94 \times 10^{-3}$ (error in B combined in quadrature with variance of α, α_z.B).

TABLE 6.8

Upper Limits on Charmed Meson Production Using Analysis 2:

$1 < Q^2 < 80$ (GeV/c^2)^2

Kinematic Cuts	Background Estimate	Events for 1.64 σ Deviation	$\langle\alpha.B\rangle$ ($\times 10^3$)	90% c.l. Events
$p_K > 21.4$, $z > 0.4$	57.9	12.5	7.1	1760 ± 526
$p_K < 21.4$, $z > 0.4$	3.88	3.23	2.52	1281 ± 478
$p_K < 21.4$, $z > 0.4$ +C	9.8	5.13	3.83	1340 ± 413
$p_K < 21.4$, $z > 0$	48.4	11.4	3.83	2978 ± 918

C denotes rejection of pions on Cerenkov information.

TABLE 6.9

Spectrometer Acceptance for Analysis 2: $p_K > 21.2$ GeV/c, $Q^2 < 1.0$ (GeV/c^2)^2

Channel	Acceptance α (0 < z < 1)	α_z (0.4 < z < 1)	α.B (x 10^2)	α_z.B (x 10^2)
$K^-\pi^+$	0.52	0.42	1.14	0.92
$K^+\pi^-$	0.49	0.38	1.08	0.84
$K^-\pi^+\pi^+$	0.36	0.33	1.40	1.29
$K^+\pi^-\pi^-$	0.36	0.33	1.40	1.29

$\langle\alpha.B\rangle = 1.29 \pm 0.29 \times 10^{-2}$

$\langle\alpha_z.B\rangle = 1.08 \pm 0.34 \times 10^{-2}$ (error in B combined in quadrature with variance of α, α_z.B).

TABLE 6.10

Spectrometer Acceptance for Analysis 2: $p_K < 21.2$ GeV/c, $Q^2 < 1.0$ (GeV/c^2)^2

Channel	Acceptance α (0 < z < 1)	α_z (0.4 < z < 1)	α.B (x 10^3)	α_z.B (x 10^3)
$K^-\pi^+$	0.15	0.06	3.30	1.32
$K^+\pi^-$	0.16	0.07	3.52	1.54
$K^-\pi^+\pi^+$	0.13	0.06	5.07	2.34
$K^+\pi^-\pi^-$	0.14	0.07	5.46	2.73

$\langle\alpha.B\rangle = 4.34 \pm 1.63 \times 10^{-3}$

$\langle\alpha_z.B\rangle = 1.98 \pm 0.84 \times 10^{-3}$ (error in B combined in quadrature with variance of α, α_z.B).

TABLE 6.11

Upper Limits on Charmed Meson Production Using Analysis 2:

$Q^2 < 1.0\ (GeV/c^2)^2$

Kinematic Cuts	Background Estimate	Events for 1.64 σ Deviation	$\langle \alpha.B \rangle$ ($\times 10^3$)	90% c.l. (Events)
$p_K > 21.2,\ z > 0$	120.5	18.0	10.8	1667 ± 525
$p_K > 21.2,\ z > 0.4$	90.5	15.6	10.8	1444 ± 455
$p_K < 21.2,\ z > 0$	10.8	5.4	4.34	1244 ± 467
$p_K < 21.2,\ z > 0.4$	1.15	1.81	1.98	914 ± 388

TABLE 6.12

SUMMARY OF RESULTS

Description of Analysis Scheme	90 c.l. on Cross-Section (nbarns)	90% c.l. on Contribution (%)
Analysis 1, $1 < Q^2 < 80\ (GeV/c^2)^2$	23.4 ± 7.6	50 ± 16.3
Analysis 1, $Q^2 < 1.0\ (GeV/c^2)^2$	14.5 ± 3.8	34 ± 8.9
Analysis 2, $1 < Q^2 < 80\ (GeV/c^2)^2$, A2	9.9 ± 3.0	21.2 ± 6.3
Analysis 2, $1 < Q^2 < 80\ (GeV/c^2)^2$, B2	7.2 ± 2.7	15.4 ± 5.8
Analysis 2, $1 < Q^2 < 80\ (GeV/c^2)^2$, C2	14.2 ± 4.4	30.5 ± 9.4
Analysis 2, $1 < Q^2 < 80\ (GeV/c^2)^2$, D2	16.7 ± 5.2	35.9 ± 11.1
Analysis 2, $Q^2 < 1.0\ (GeV/c^2)^2$, E2	8.0 ± 2.5	18.8 ± 5.9
Analysis 2, $Q^2 < 1.0\ (GeV/c^2)^2$, F2	6.9 ± 2.2	16.2 ± 5.2
Analysis 2, $Q^2 < 1.0\ (GeV/c^2)^2$, G2	11.2 ± 4.2	26.3 ± 9.9
Analysis 2, $Q^2 < 1.0\ (GeV/c^2)^2$, H2	8.2 ± 3.5	19.3 ± 8.2

Flow Diagram of Acceptance Monte Carlo

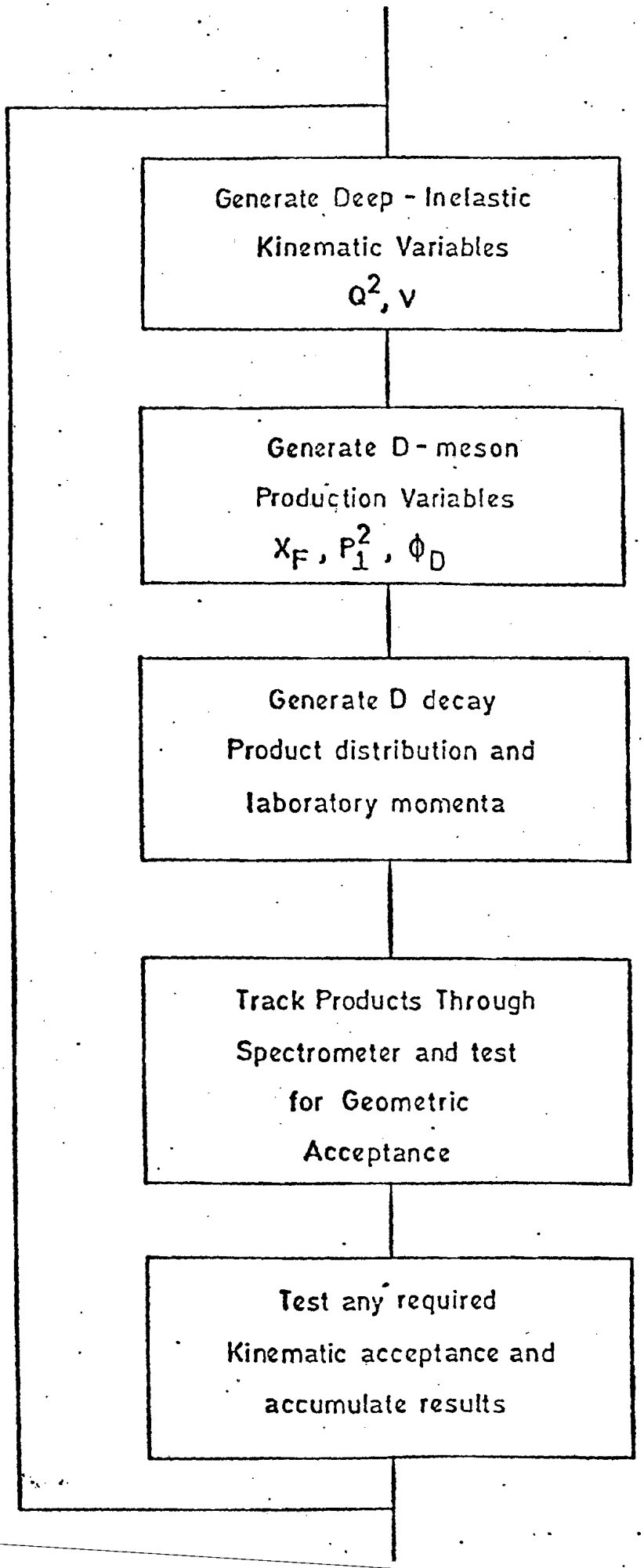

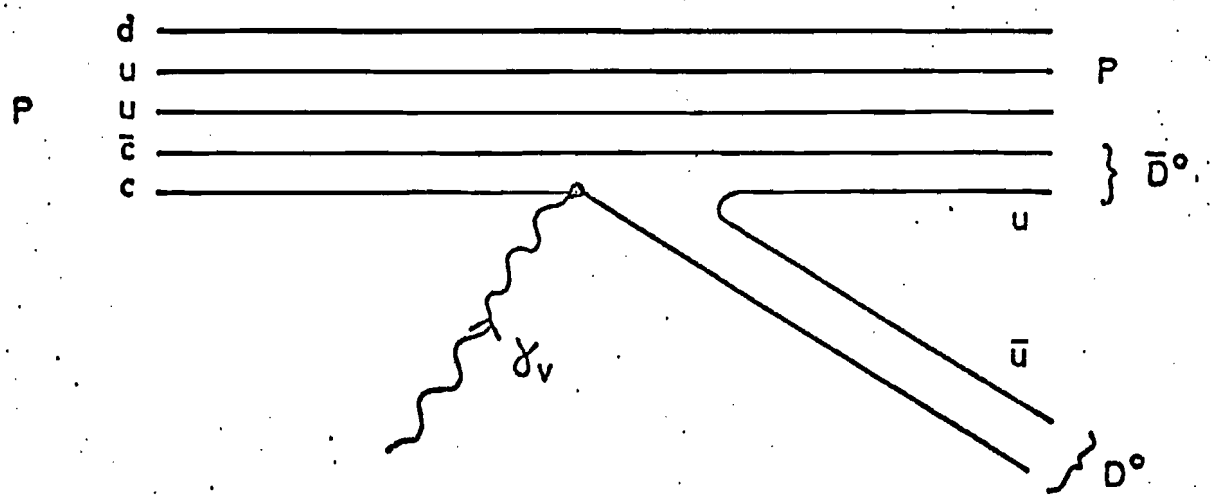

Fig. 6.1

Fig. 6.3

Kinematic variables used in Monte - Carlo

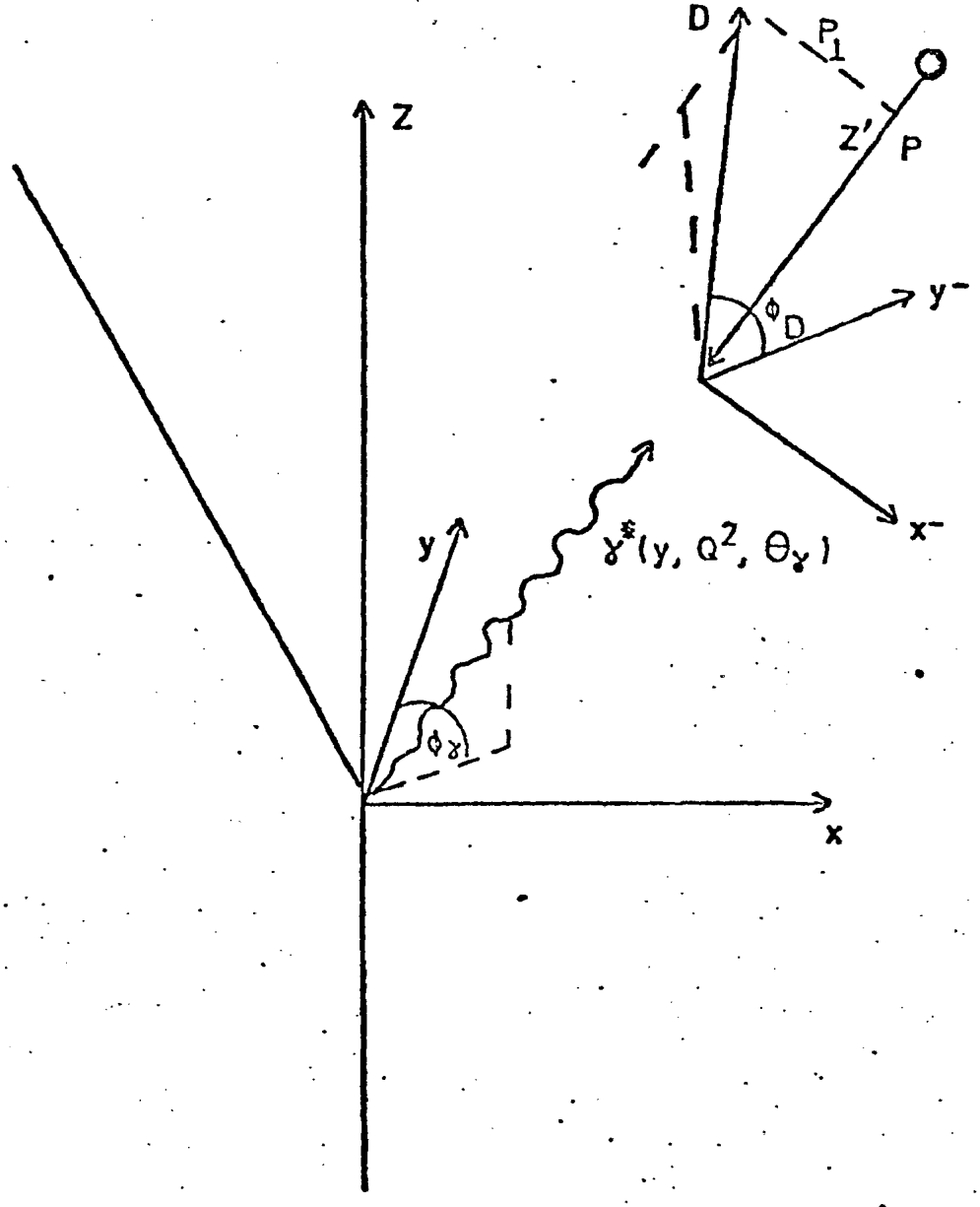

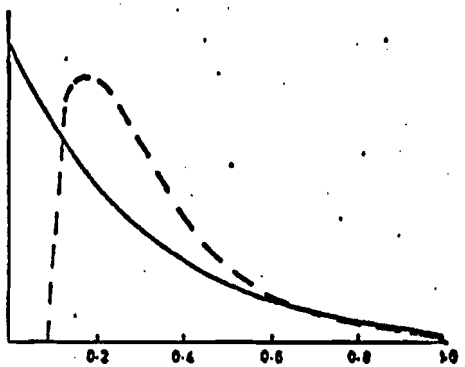

For $d^6P^2_{\perp}$, Uniform X_{BJ}

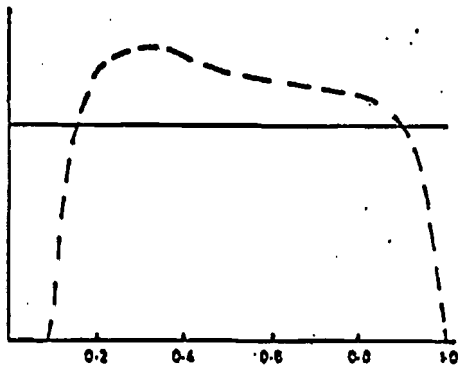

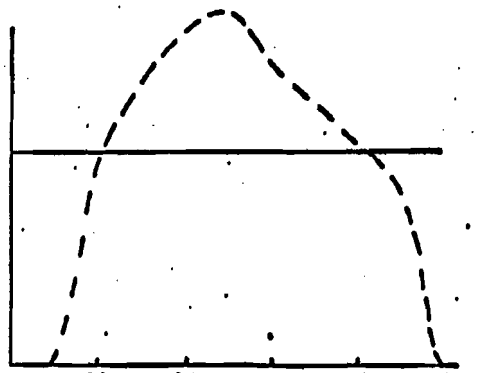

$0 < P^2_{\perp} < 9$ Dist

Uniform x_p

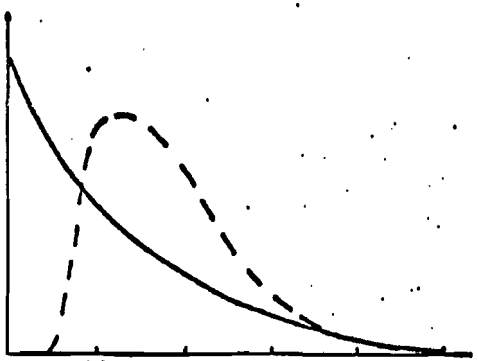

$0 < P^2_{\perp} < 9$ Uniform Distribution

$e^{-3.5x_p}$

Fig. 6·4

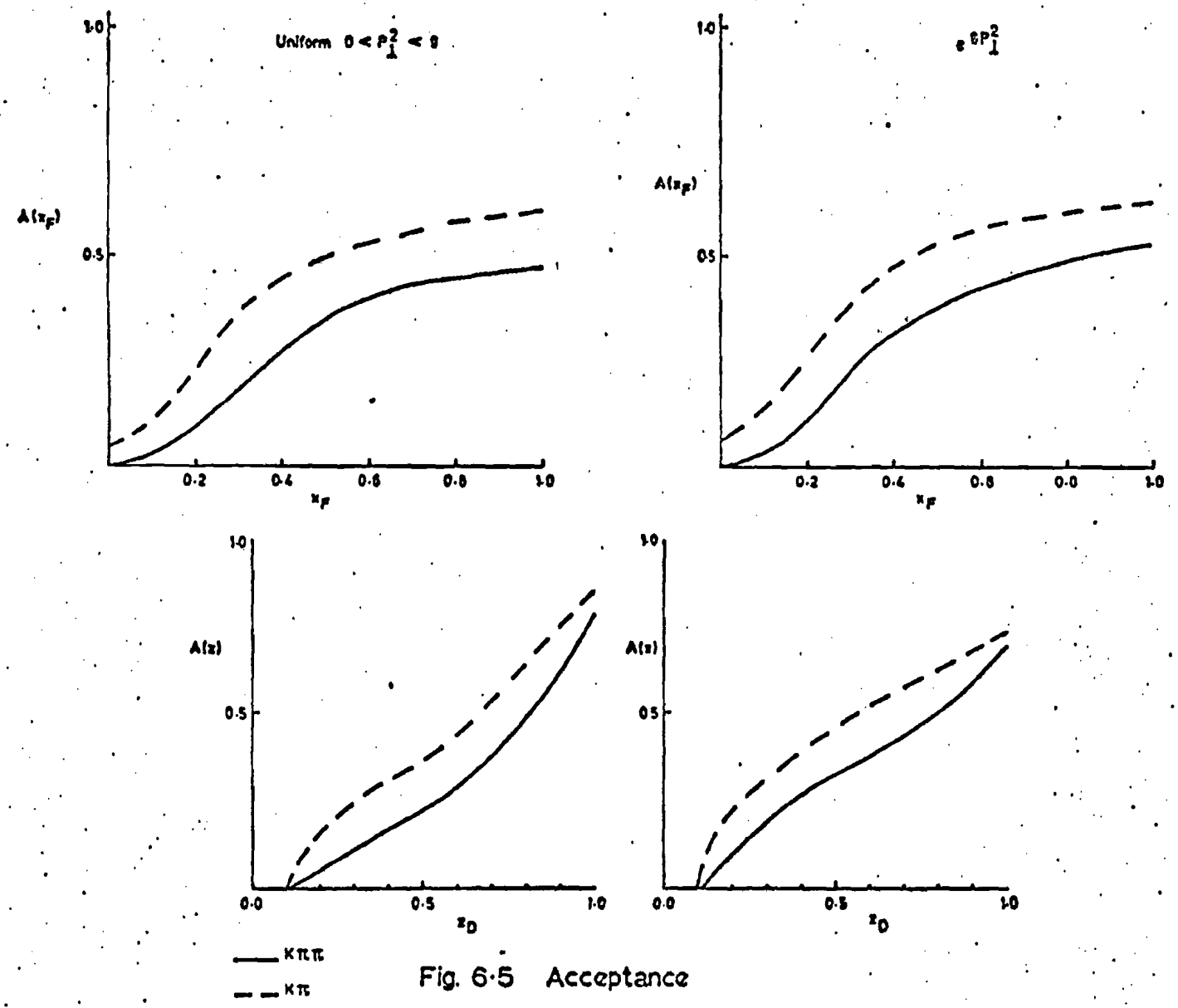

Fig. 6·5 Acceptance

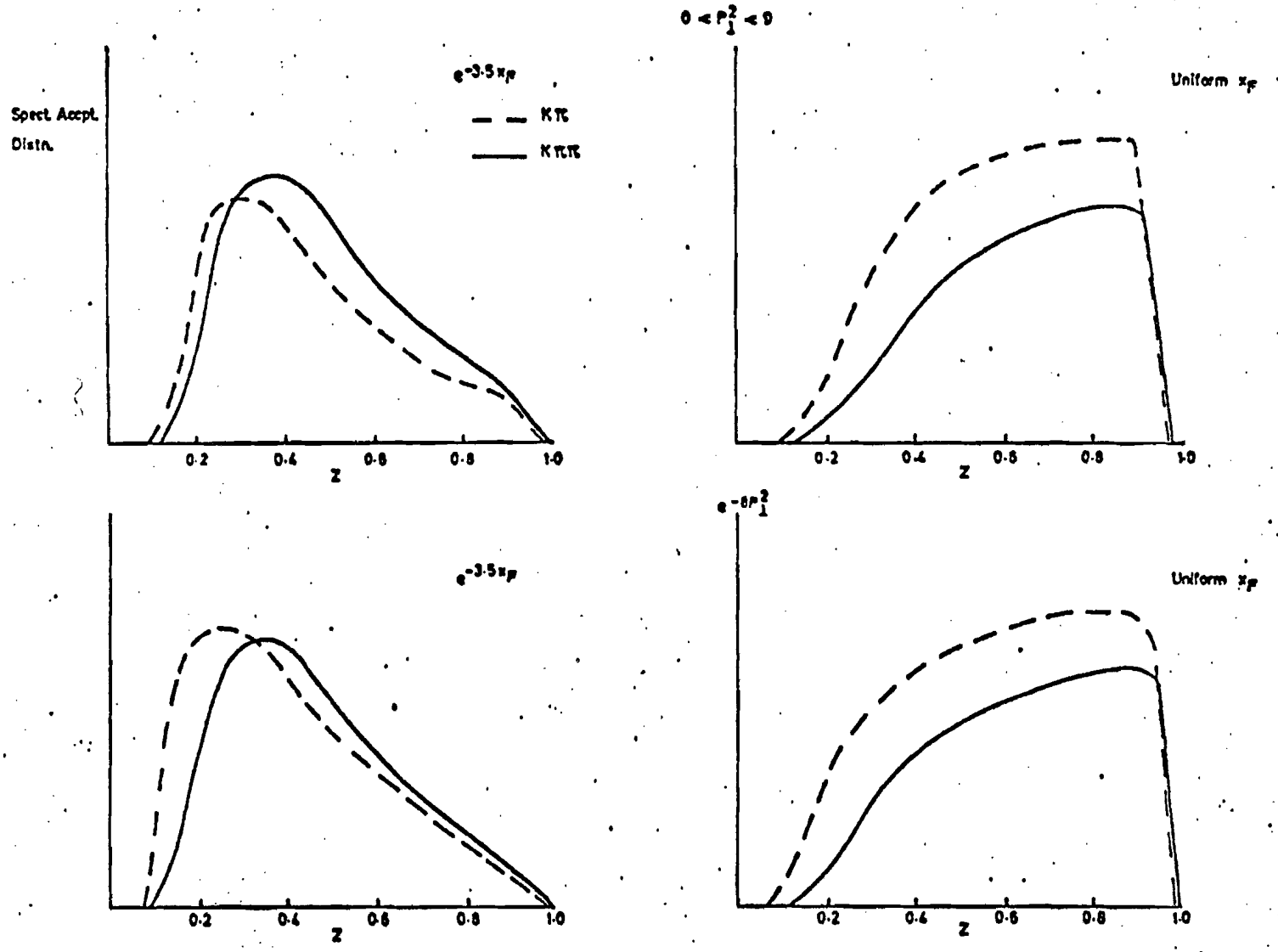
$0 < P_\perp^2 < 9$
Spect. Accpt.
Distn.
$e^{-3.5x_F}$
Kπ
Kππ
Uniform x_F
$e^{-8P_\perp^2}$
Z
0·2
0·4
0·6
0·8
1·0

Fig. 6·6

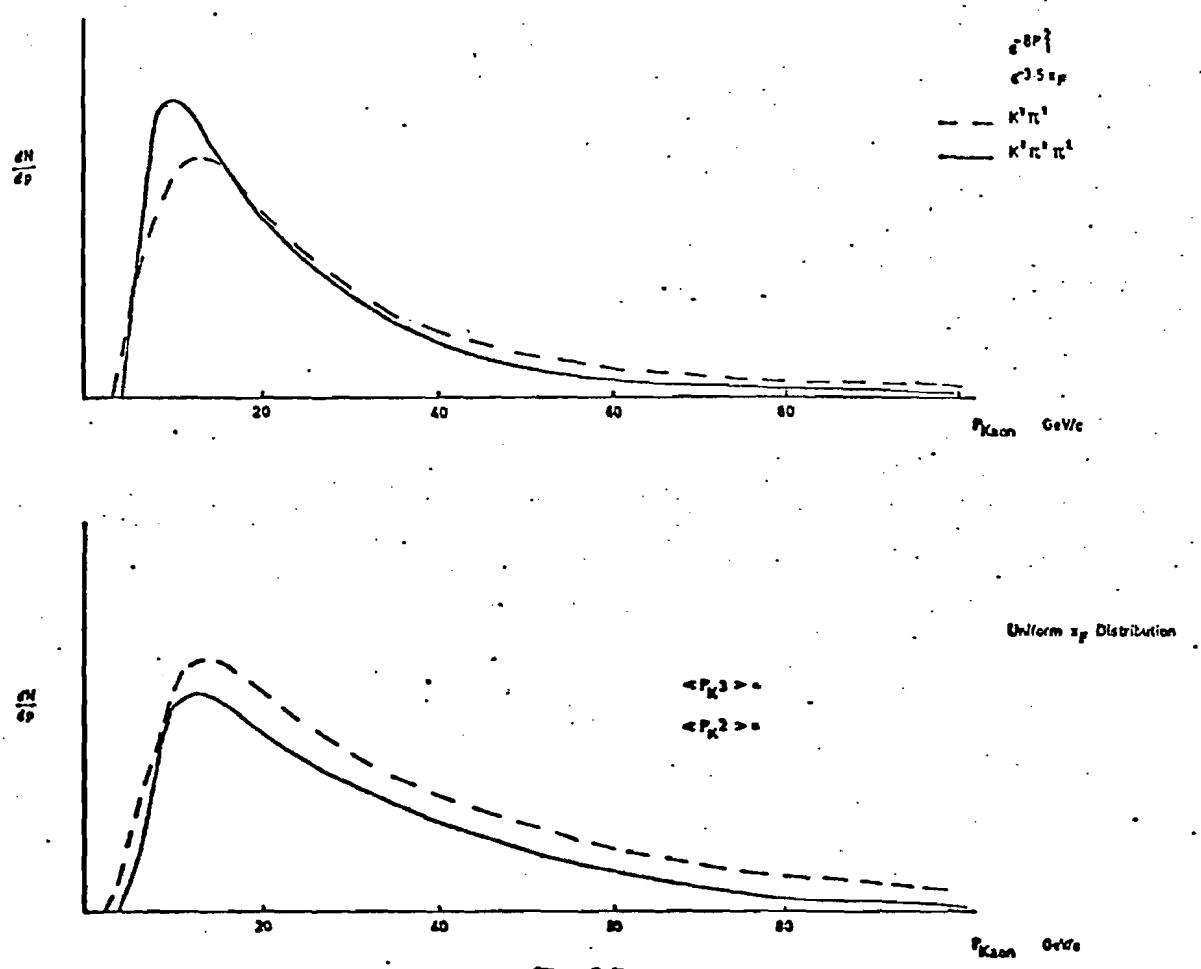

Fig. 6-7a

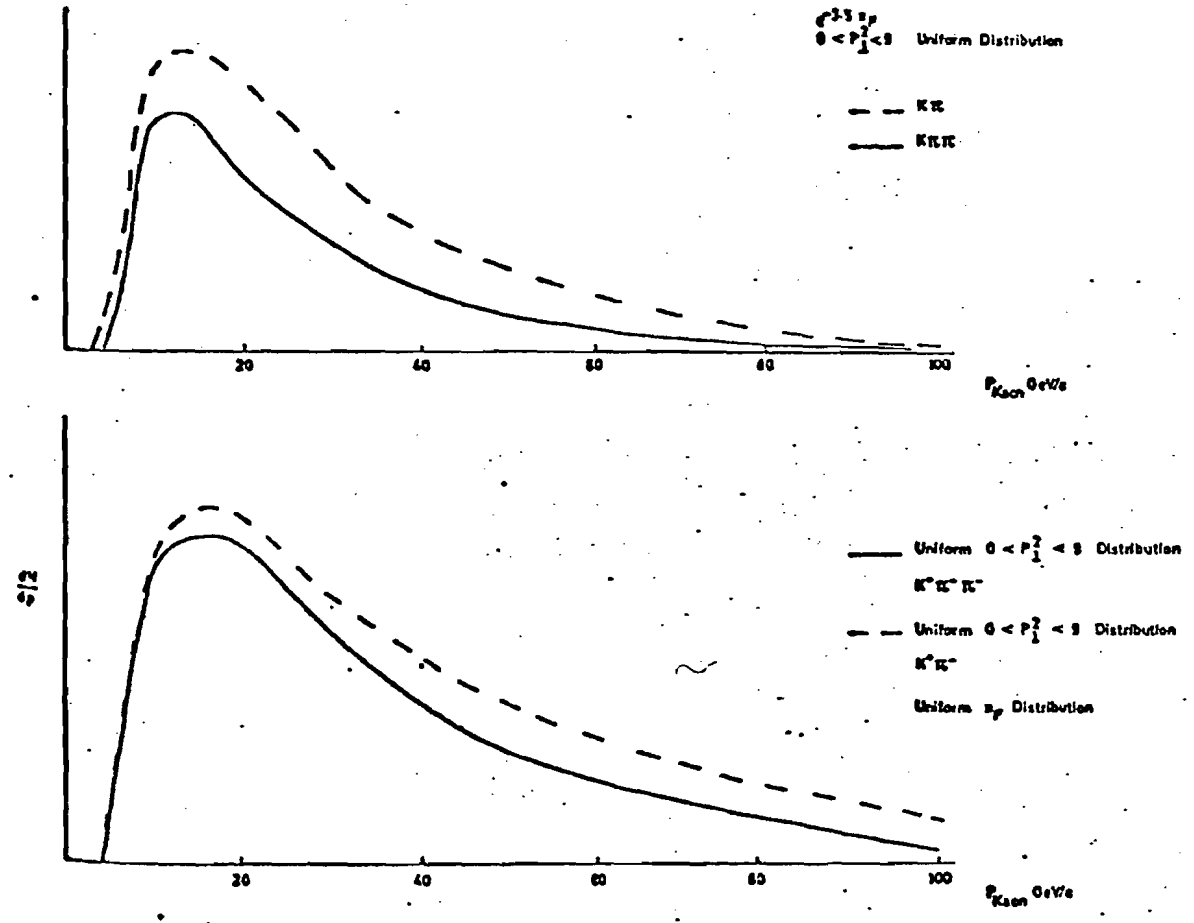

Fig. 6-7b

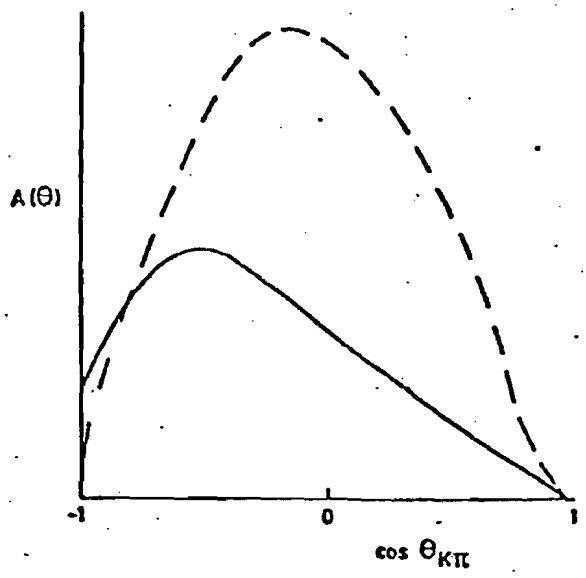

$e^{-3.5\,x_F}$, $e^{-8P_\perp^2}$, Uniform x_{Bj}

For D's accepted by spectrometer

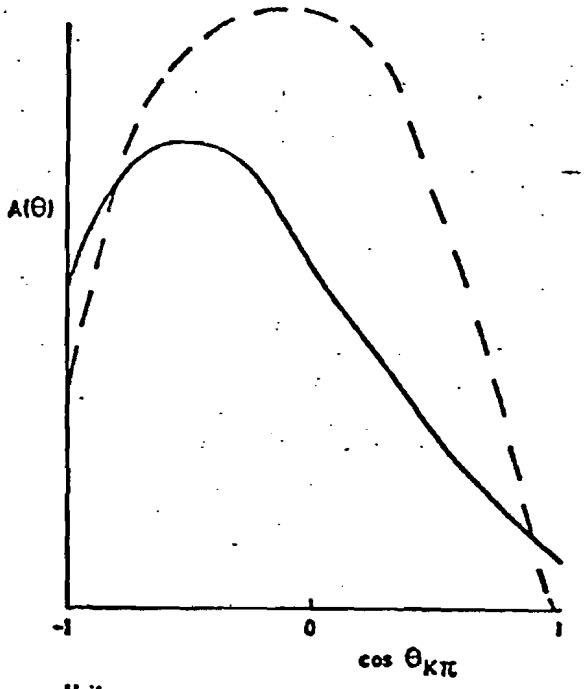

Uniform x_F $e^{-8P_\perp^2}$

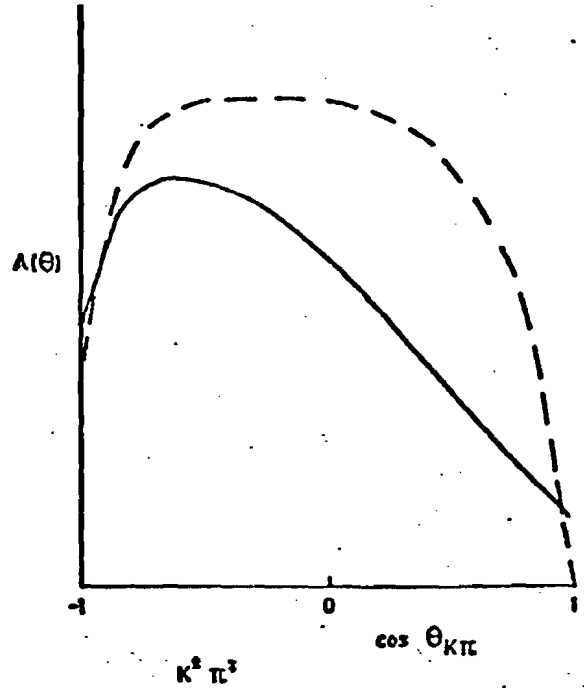

$K^\pm\pi^\mp$

$K^\pm\pi^\mp\pi^\mp$

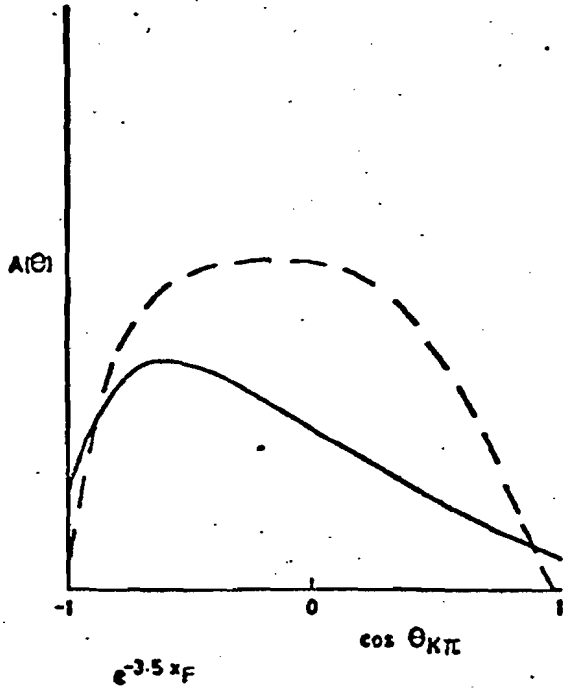

$e^{-3.5\,x_F}$

$0 < P_\perp^2 < 9$

Uniform x_F, Uniform $0 < P_\perp^2 < 9$

For D's accepted by spectrometer

Fig. 6·8

Vertex - Pointing Distributions for Upstream MWPC Tracks.

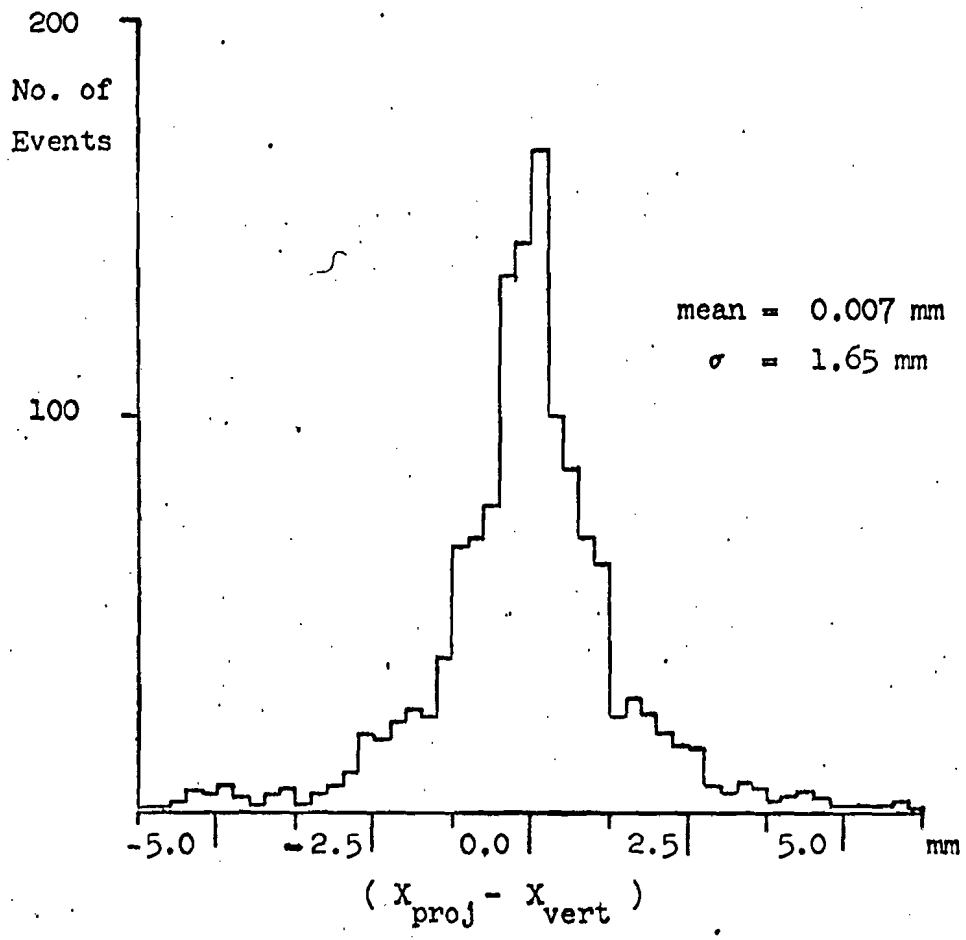

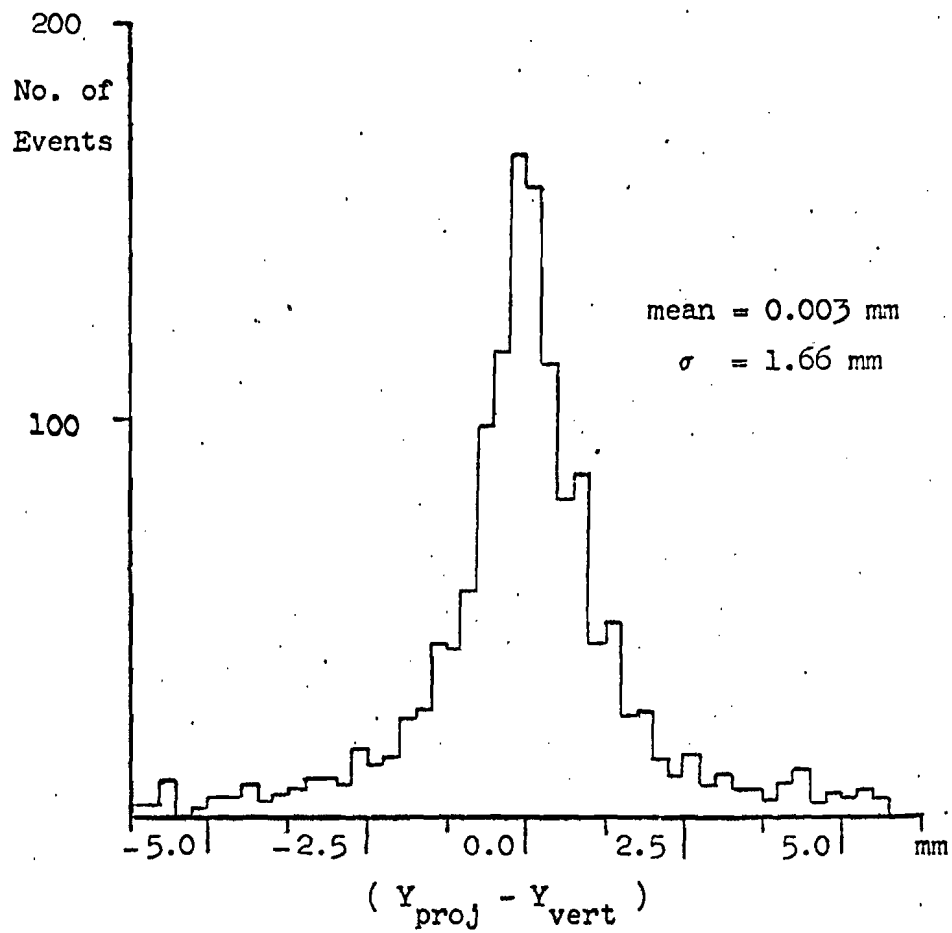

Fig. 6.9

Invariant Mass Distributions.
Analysis 1, Scheme A

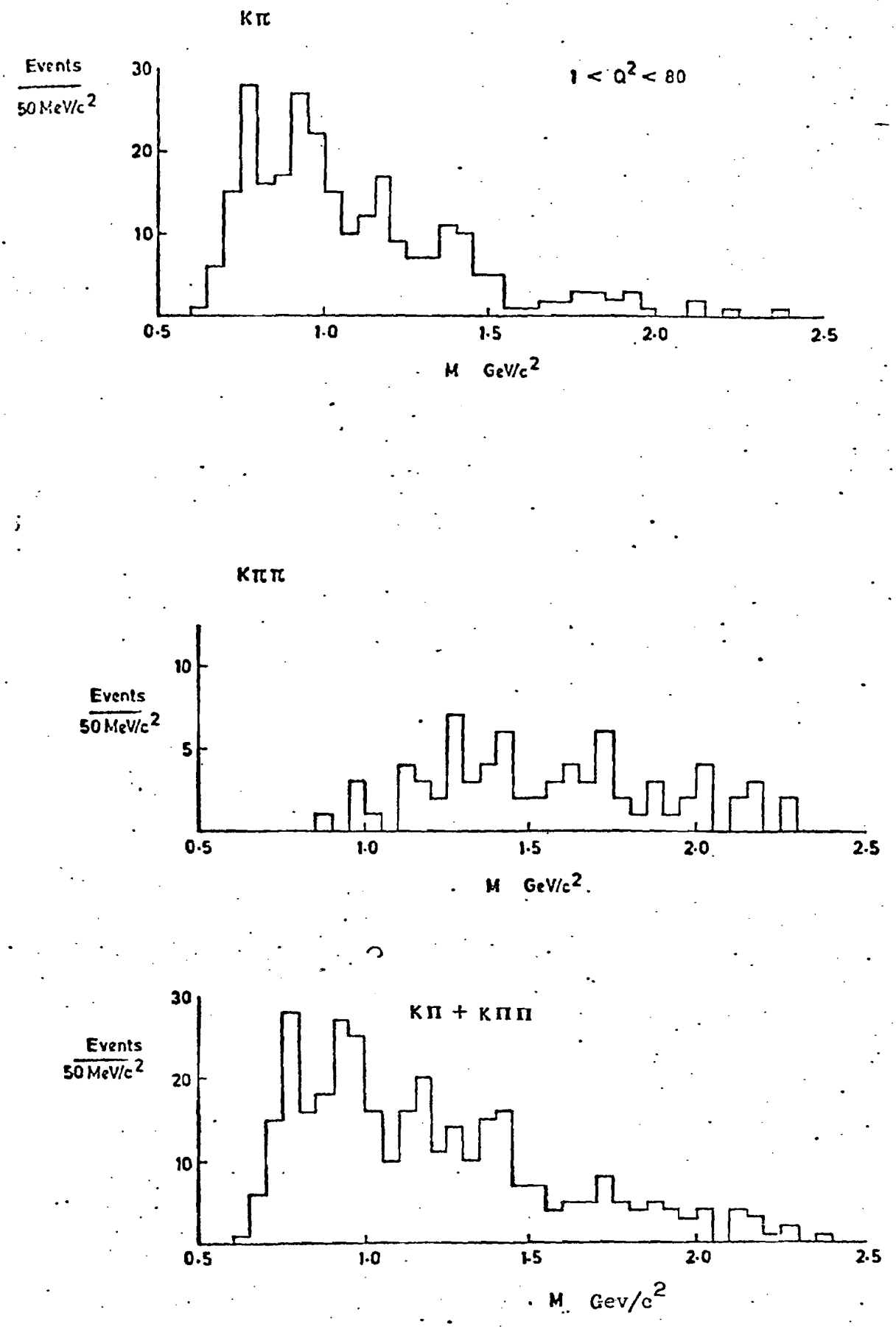

Fig. 6·10

Invariant Mass Distributions.

Analysis 1, Scheme B

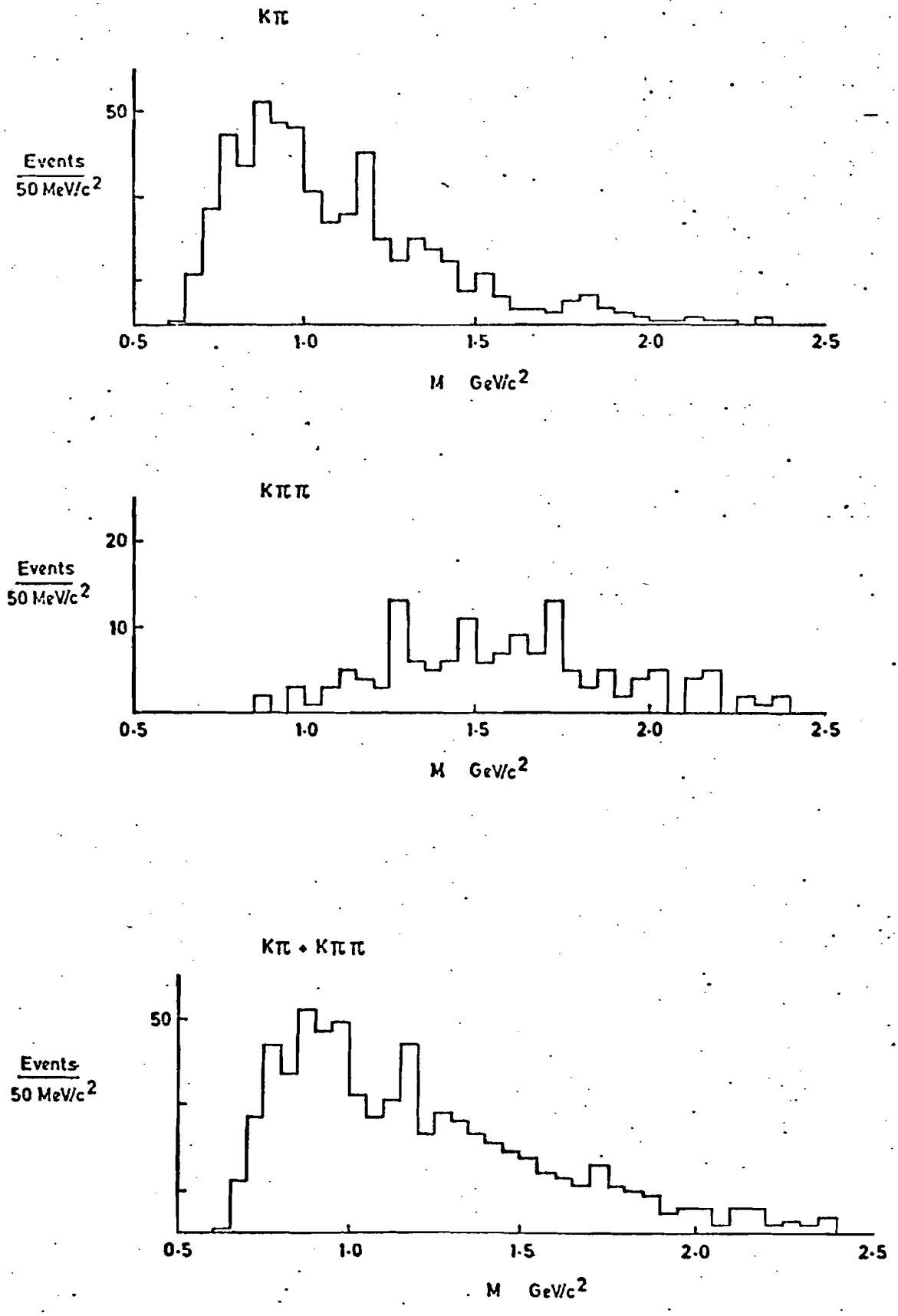

Fig. 6·11

Analysis 1, Scheme A

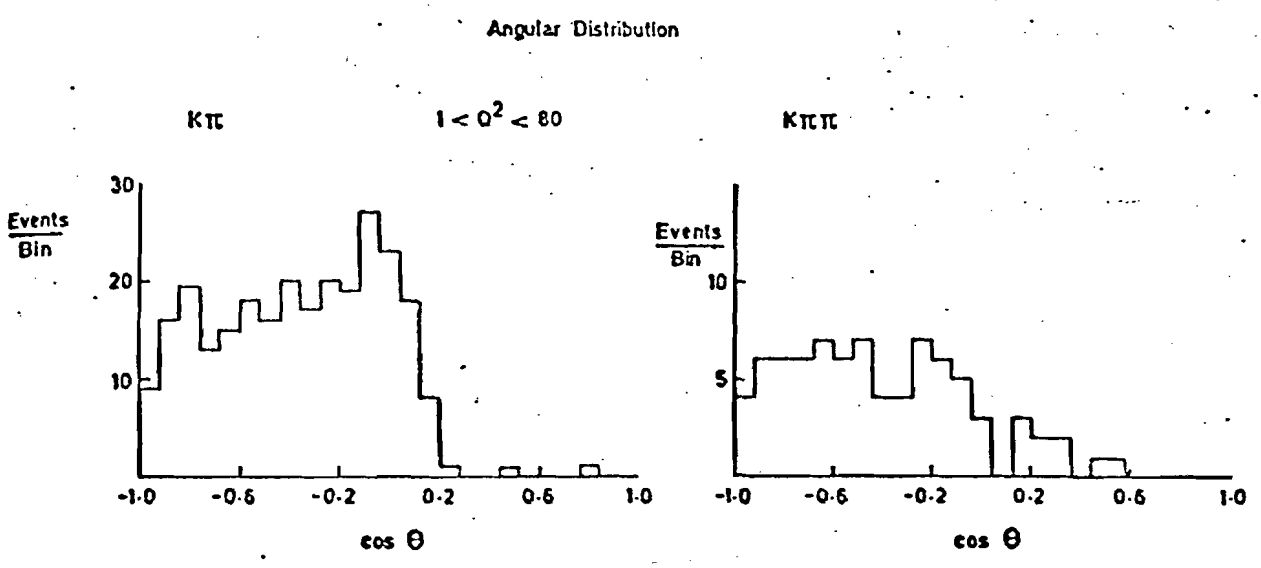

Fig. 6·12

Analysis 1, Scheme B

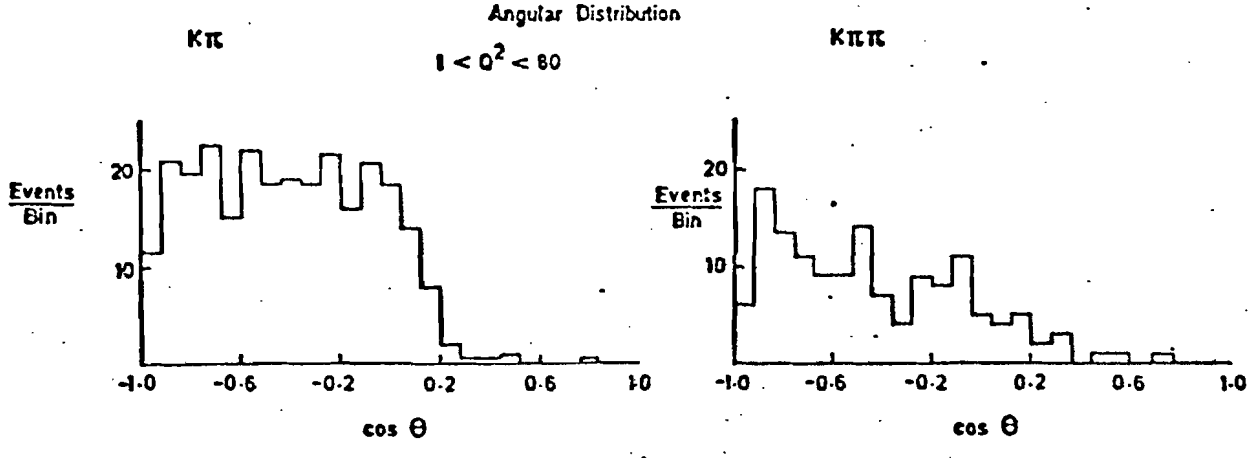

Fig. 6·13

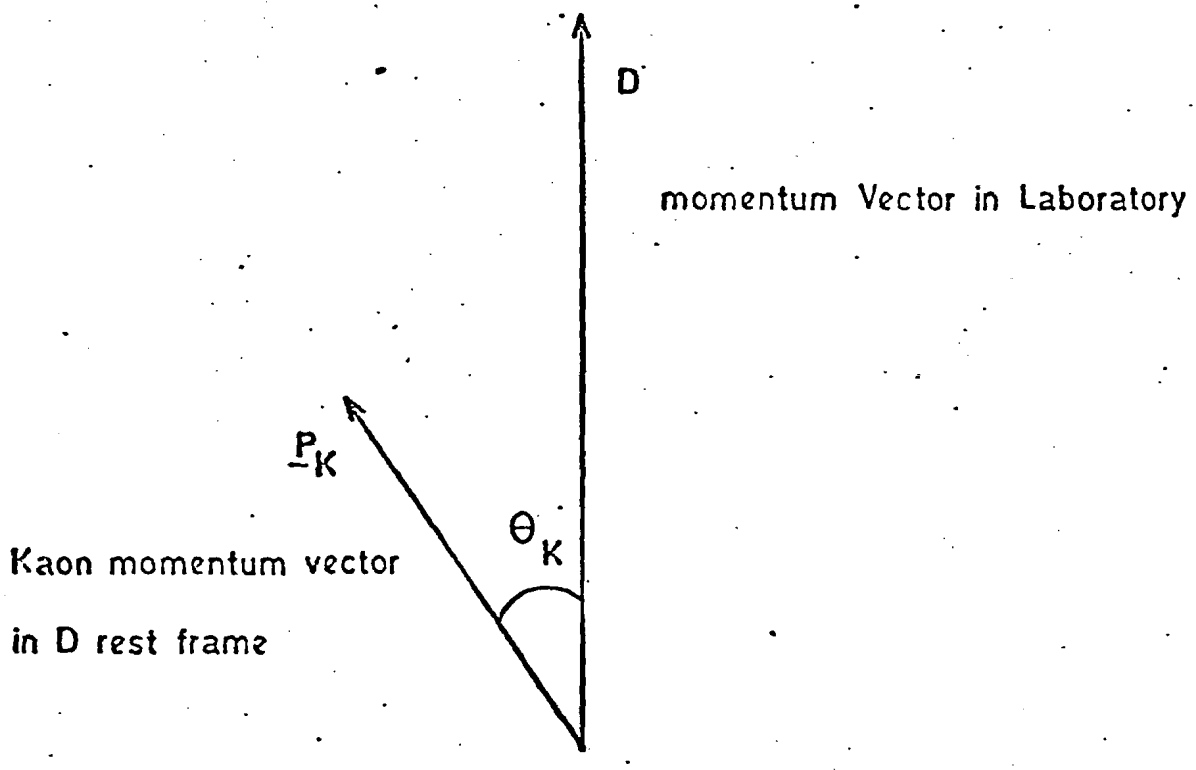
D
momentum Vector in Laboratory
$\underline{P}_K$
θ_K
Kaon momentum vector
in D rest frame

Fig. 6.14

Analysis 1, Scheme A

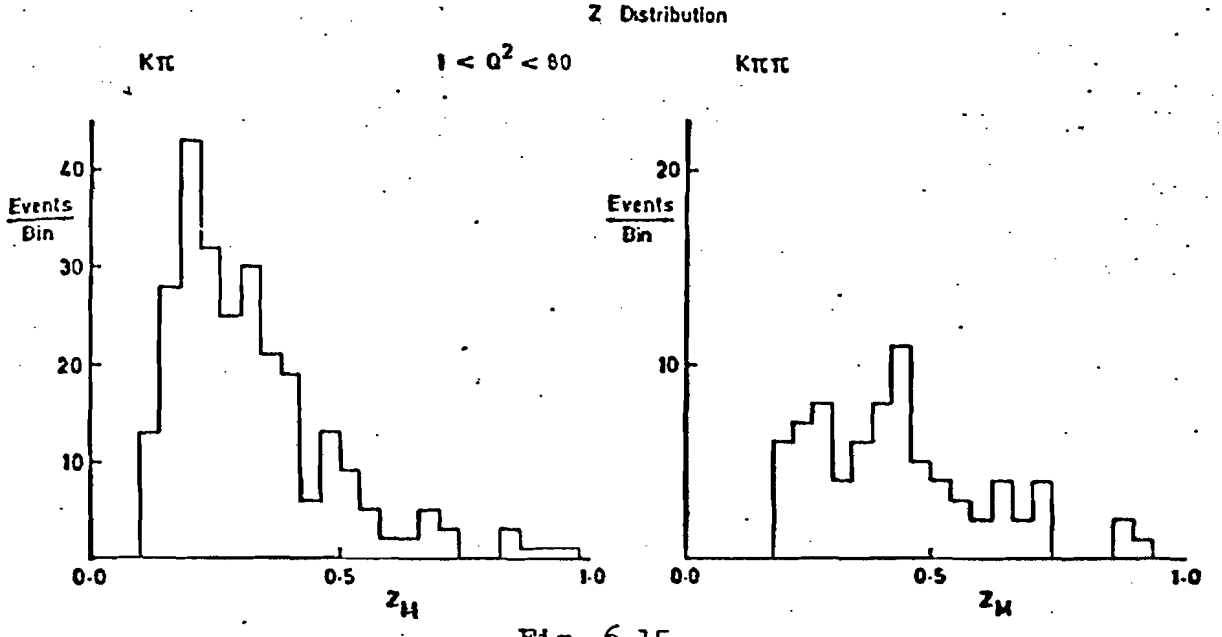

Fig. 6.15

Analysis 1, Scheme B

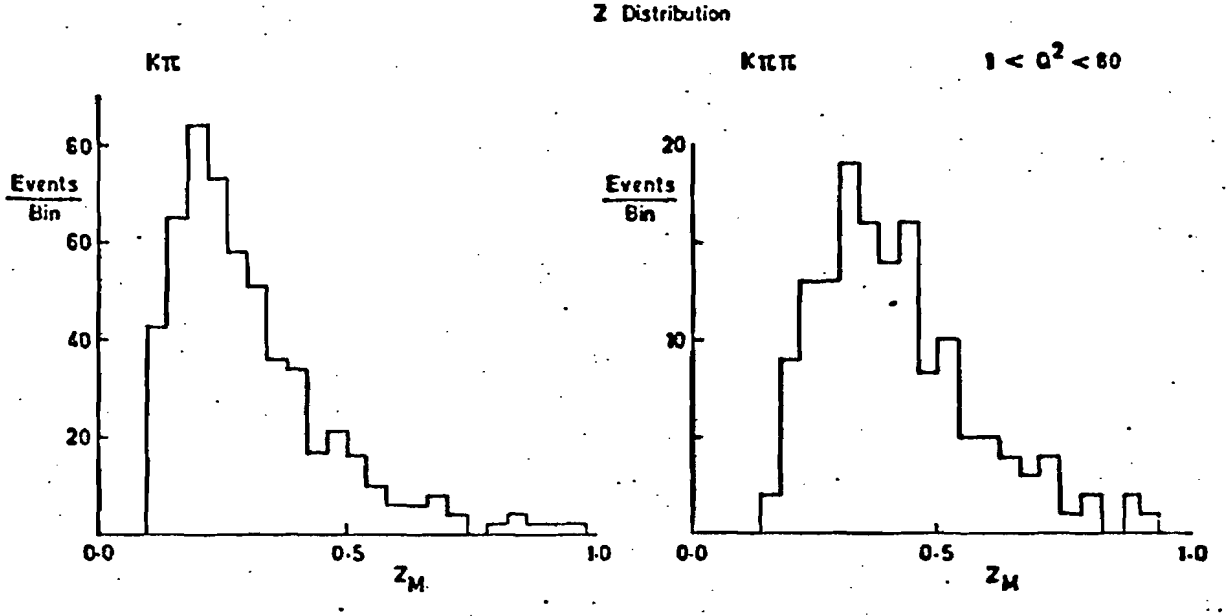

Fig. 6·16

$M_{K\Pi}$ vs Z_M

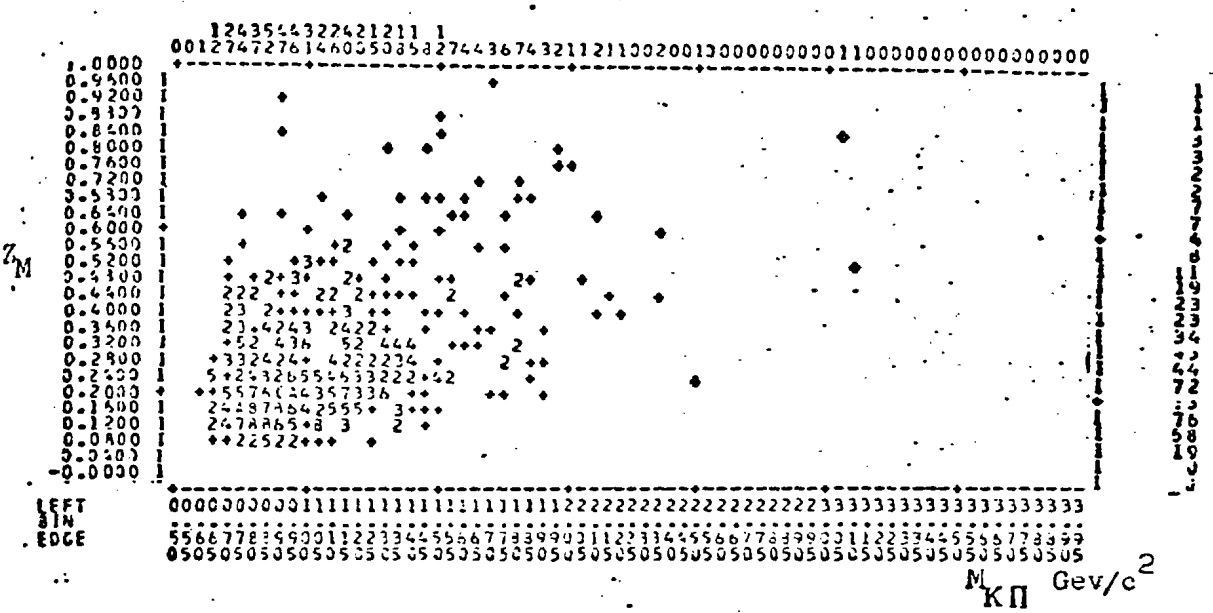

$M_{K\Pi\Pi}$ vs Z_M

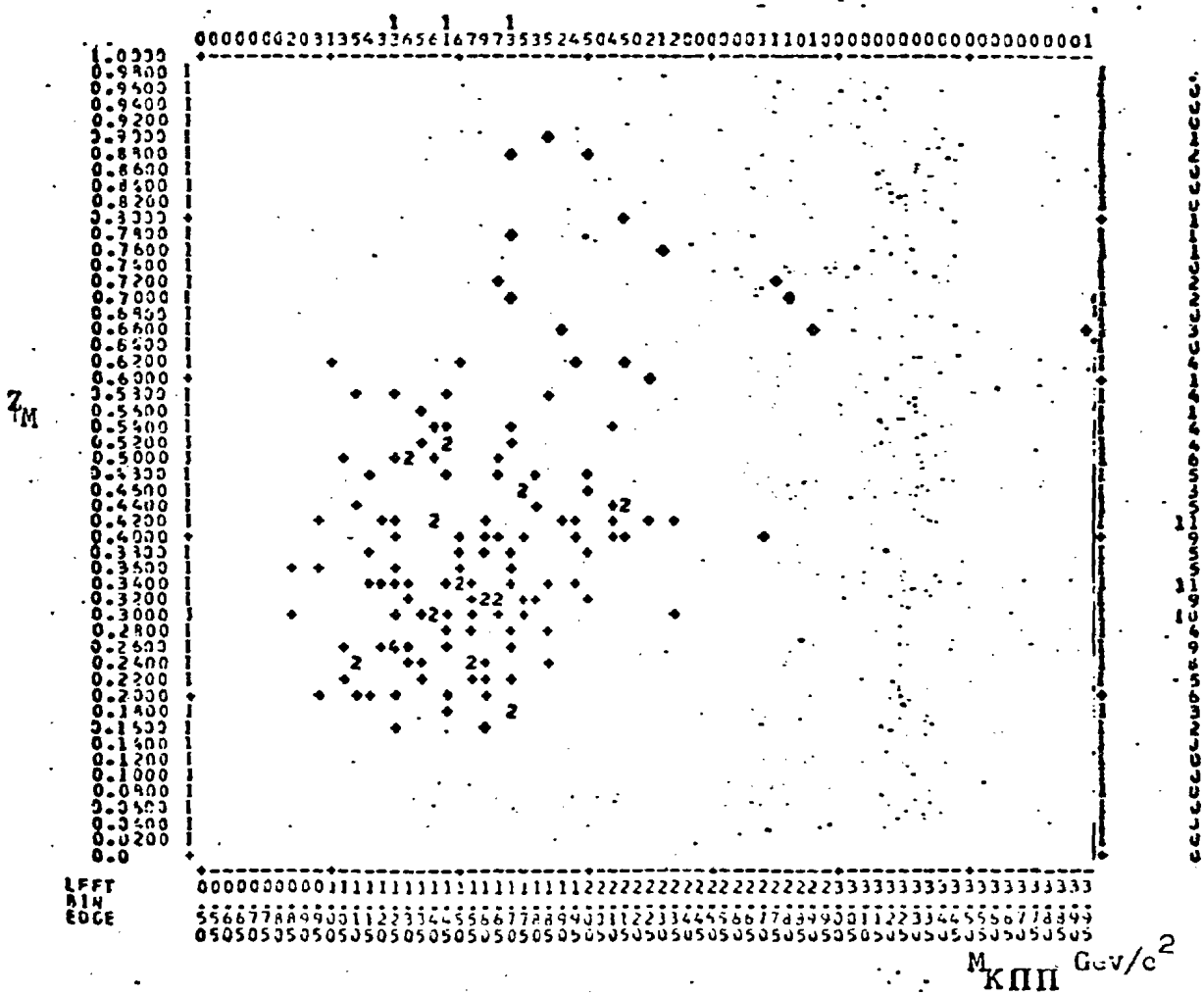

Fig. 6.17a

$M_{K\Pi}$ vs Z_M

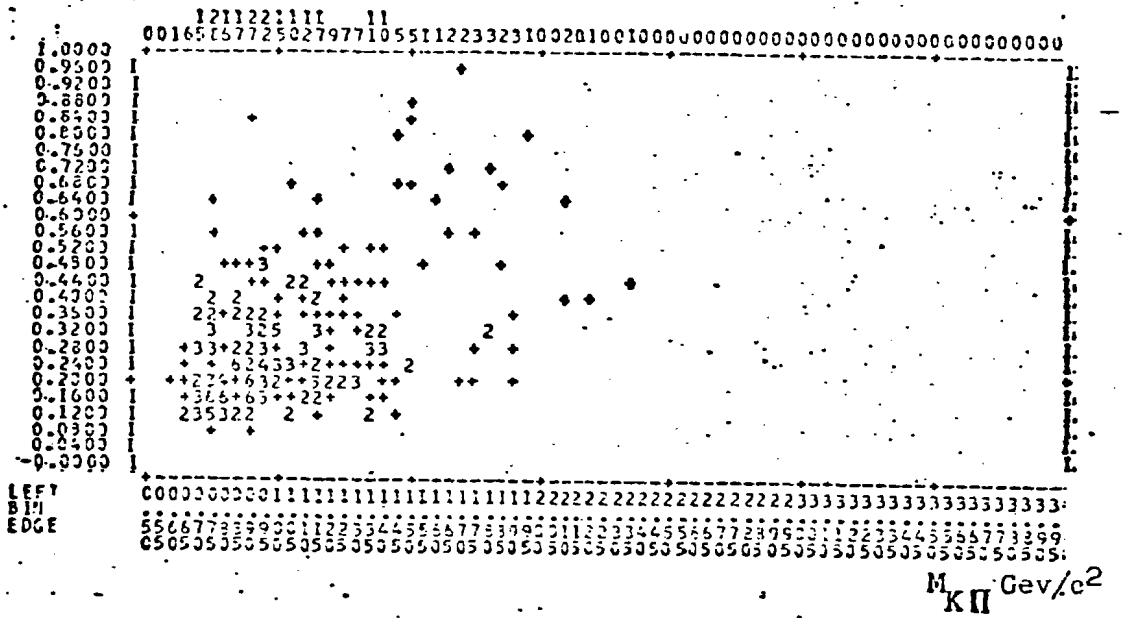

$M_{K\Pi\Pi}$ vs Z_M

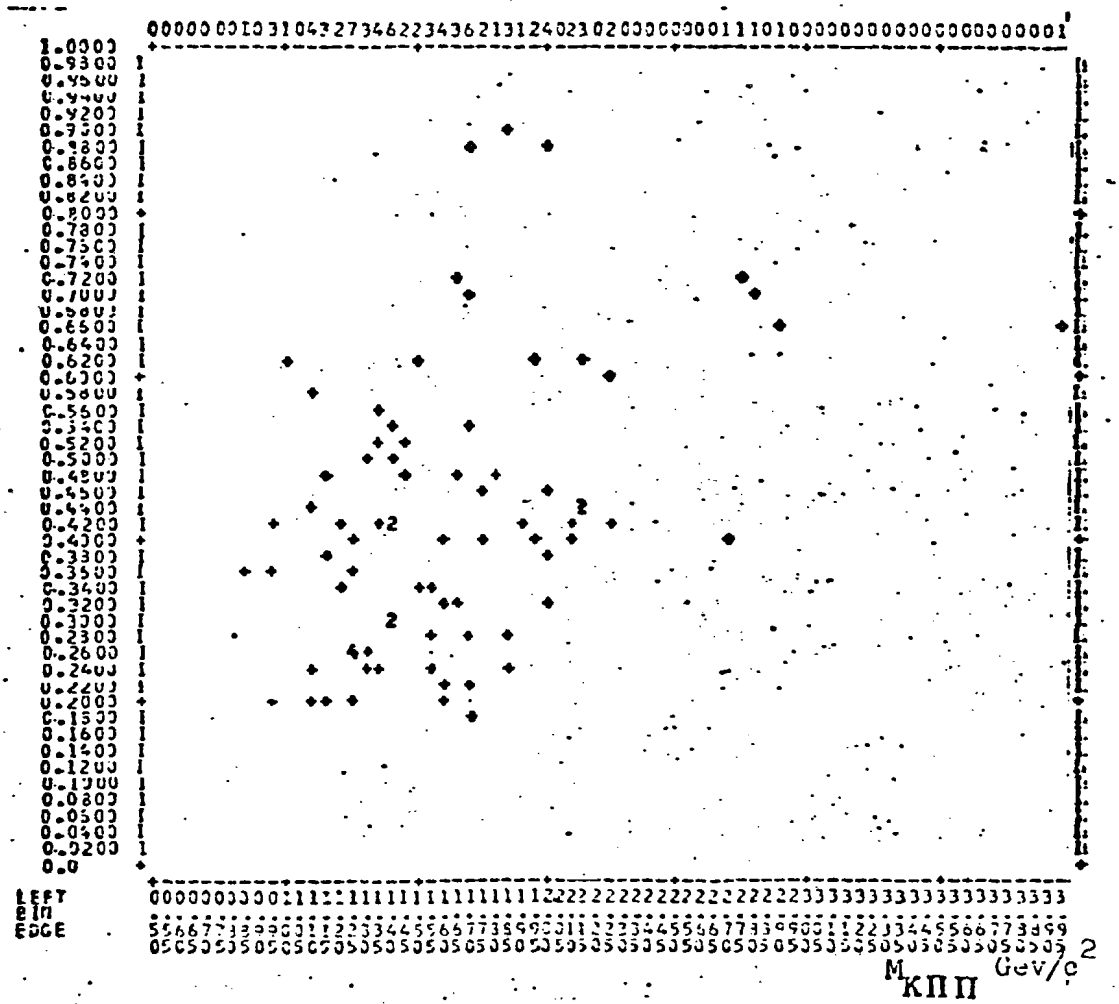

Fig. 6.17b

Analysis 1

Invariant Mass, Scheme A, $Q^2 < 1.0$

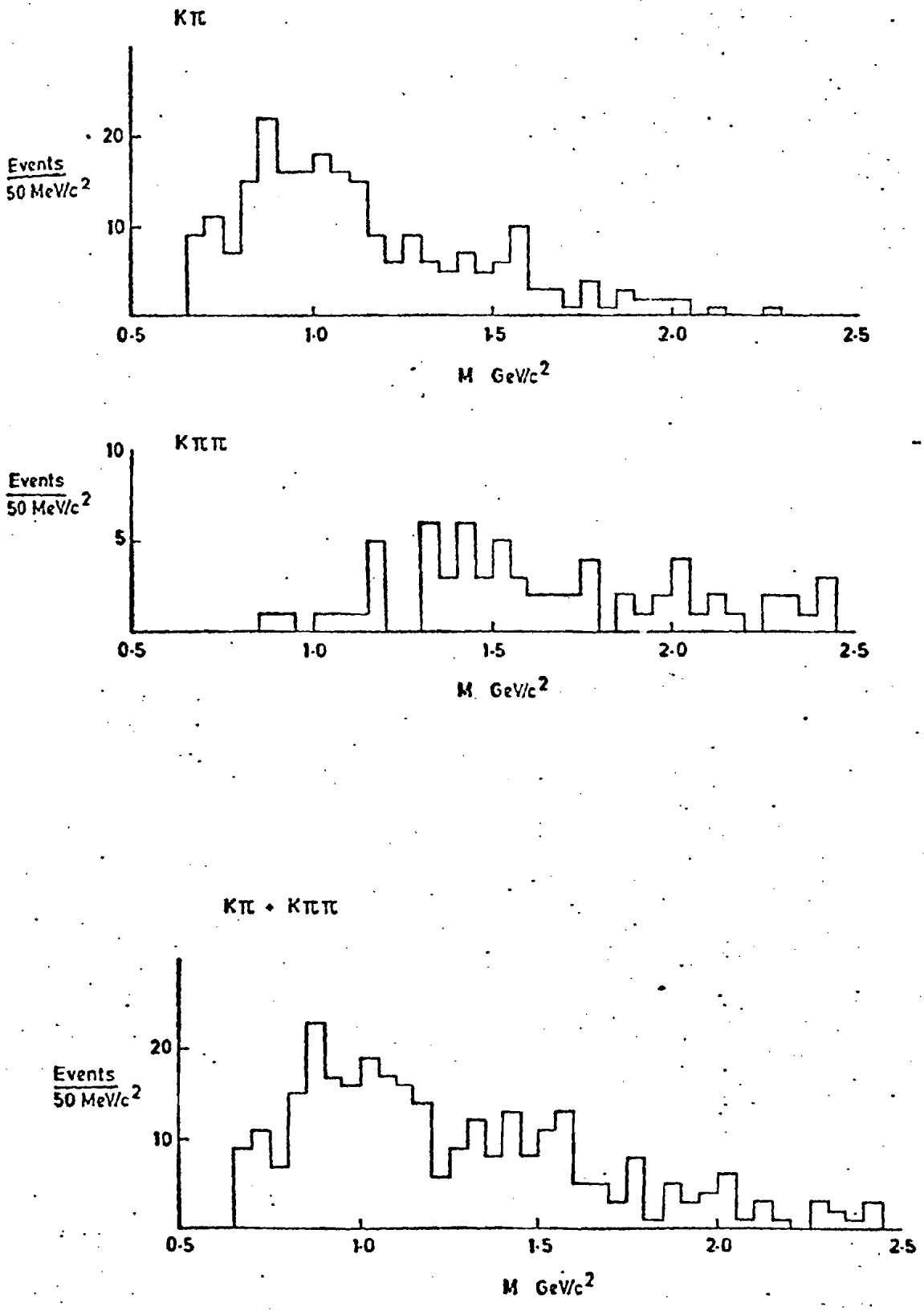

Fig. 6·18

Analysis 1

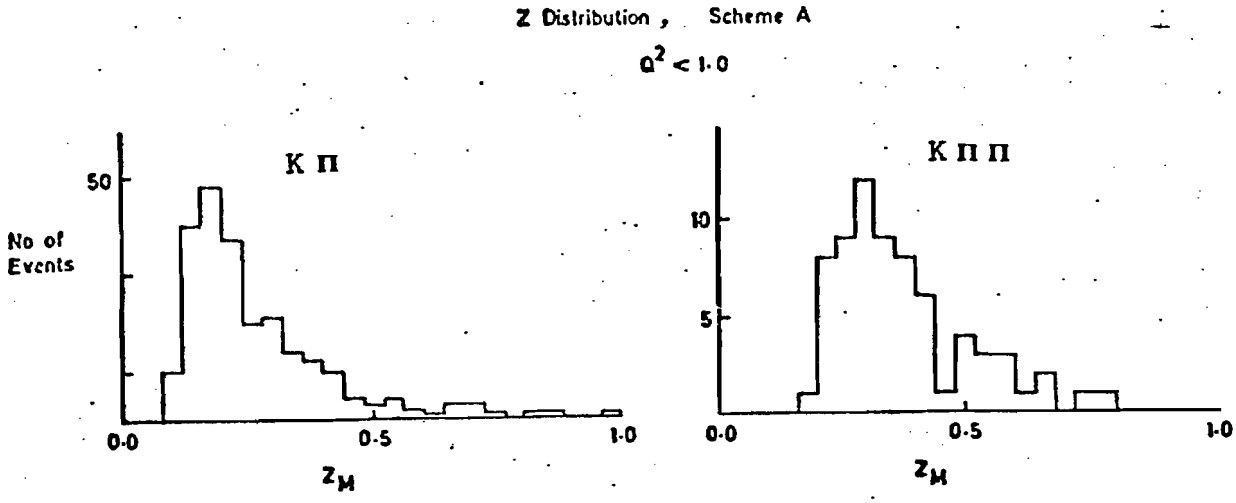

Fig. 6·19

Analysis 1

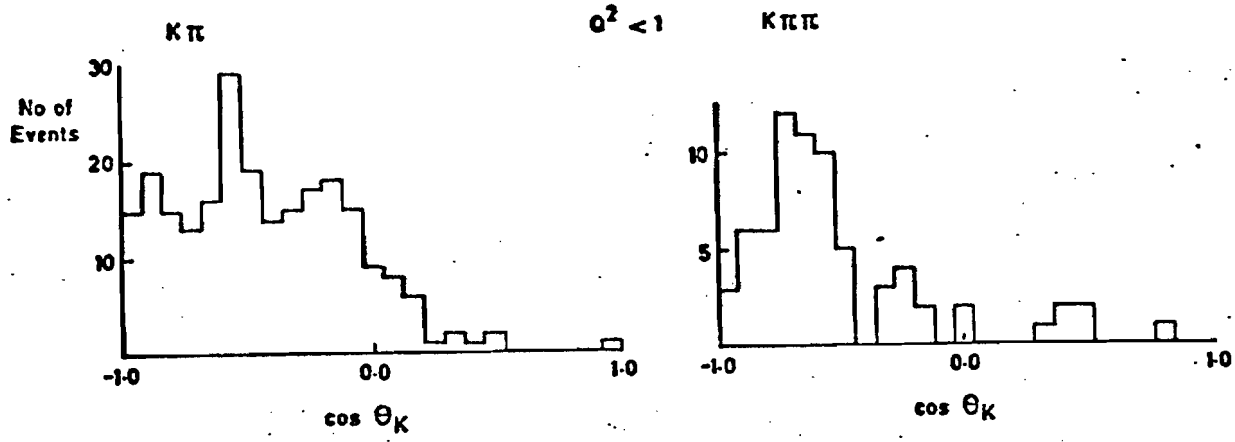

Fig. 6·20

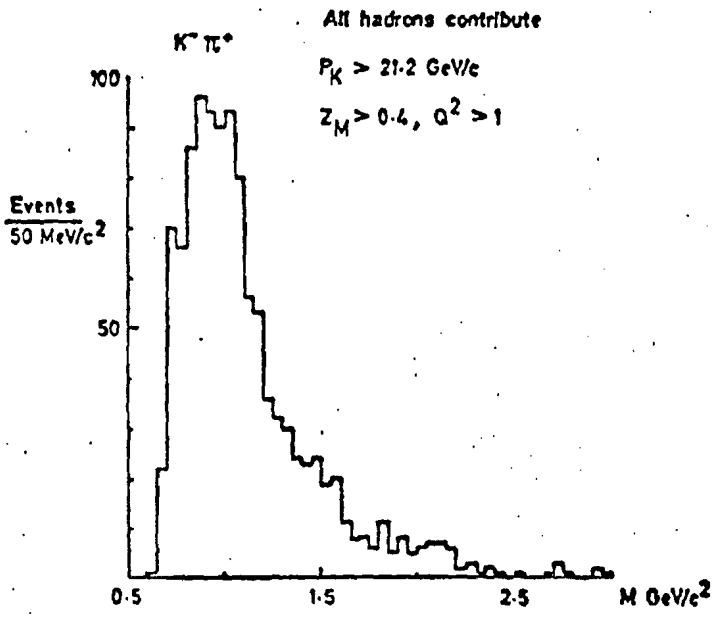
All hadrons contribute
$K^-\pi^+$
$P_K > 21{\cdot}2$ GeV/c
$Z_M > 0{\cdot}4$, $Q^2 > 1$
Events / 50 MeV/c^2
100
50
0·5
1·5
2·5
M GeV/c^2

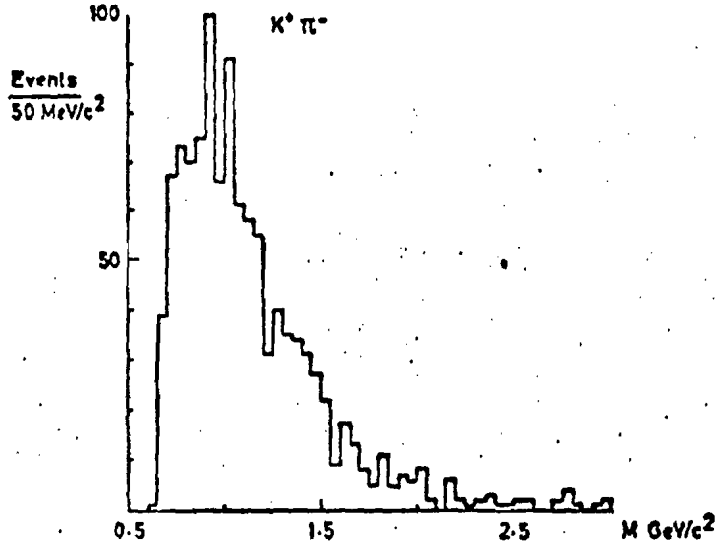
$K^+\pi^-$
Events / 50 MeV/c^2
100
50
0·5
1·5
2·5
M GeV/c^2

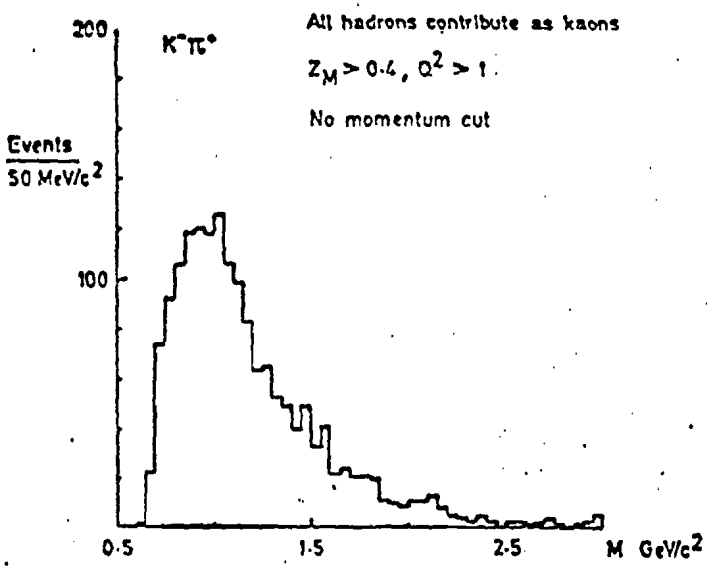
All hadrons contribute as kaons
$K^-\pi^+$
$Z_M > 0{\cdot}4$, $Q^2 > 1$
No momentum cut
Events / 50 MeV/c^2
200
100
0·5
1·5
2·5
M GeV/c^2

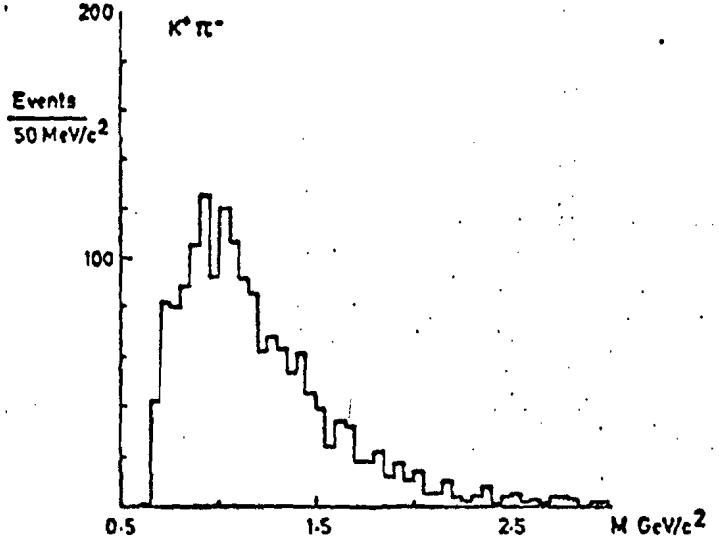
$K^+\pi^-$
Events / 50 MeV/c^2
200
100
0·5
1·5
2·5
M GeV/c^2

Fig. 6·21

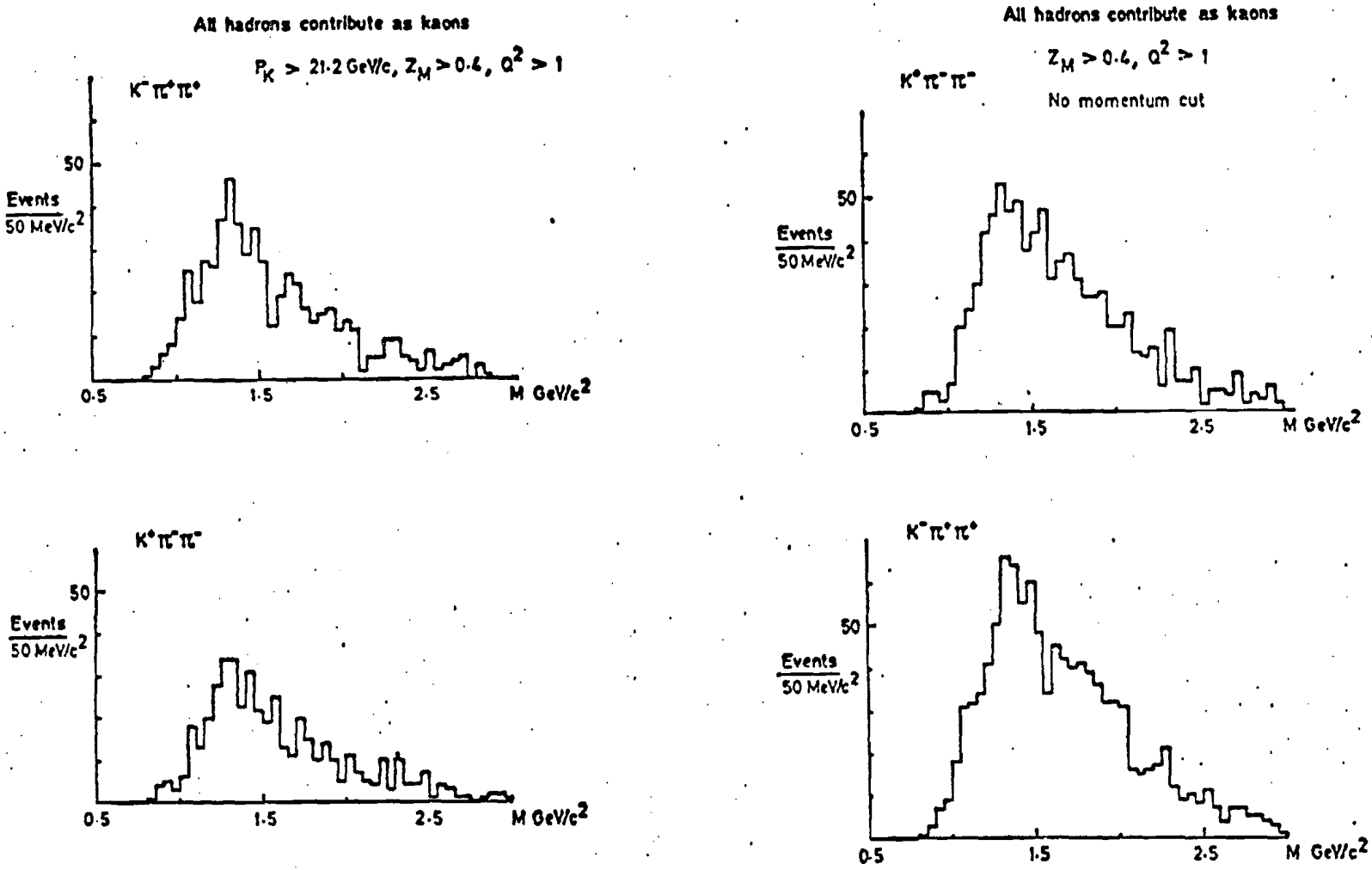
All hadrons contribute as kaons
$P_K > 21{\cdot}2$ GeV/c, $Z_M > 0{\cdot}4$, $Q^2 > 1$
$K^-\pi^+\pi^+$
50
Events / 50 MeV/c^2
0·5
1·5
2·5
M GeV/c^2
All hadrons contribute as kaons
$Z_M > 0{\cdot}4$, $Q^2 > 1$
No momentum cut
$K^+\pi^-\pi^-$
50
Events / 50 MeV/c^2
0·5
1·5
2·5
M GeV/c^2
$K^+\pi^-\pi^-$
50
Events / 50 MeV/c^2
0·5
1·5
2·5
M GeV/c^2
$K^-\pi^+\pi^+$
50
Events / 50 MeV/c^2
0·5
1·5
2·5
M GeV/c^2

Fig. 6·22

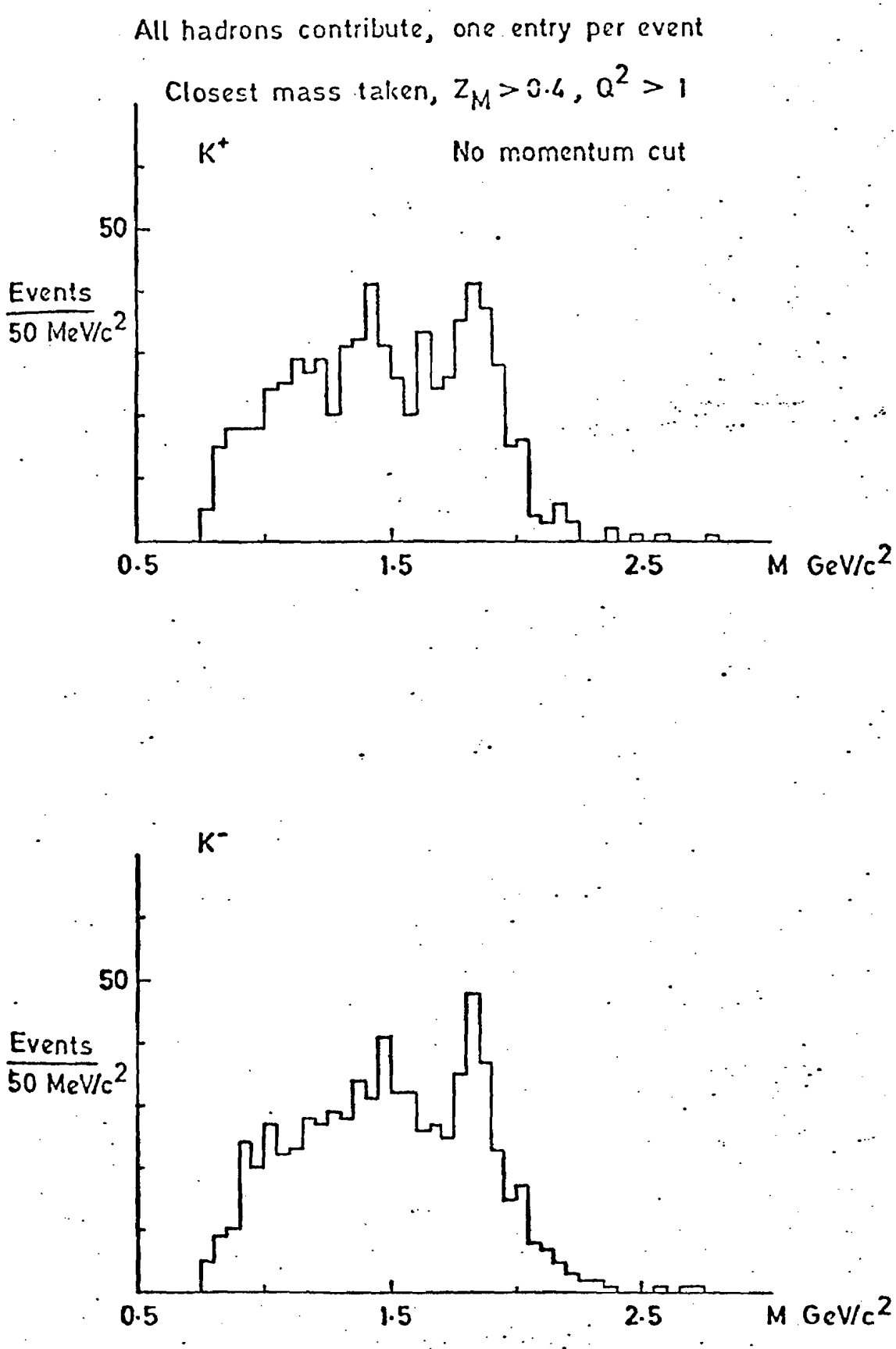
All hadrons contribute, one entry per event
Closest mass taken, $Z_M > 0.4$, $Q^2 > 1$
K^+
No momentum cut
50
Events
50 MeV/c^2
0·5
1·5
2·5
M GeV/c^2
K^-
50
Events
50 MeV/c^2
0·5
1·5
2·5
M GeV/c^2

Fig. 6·23

All hadrons contribute, only one entry per event

Closest mass taken $Z_M > 0.4$, $Q^2 > 1$

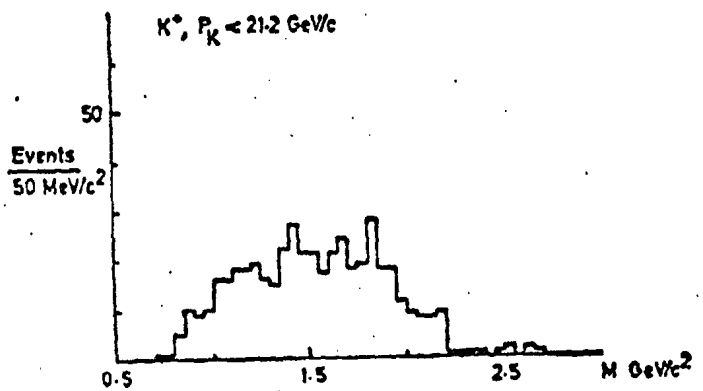

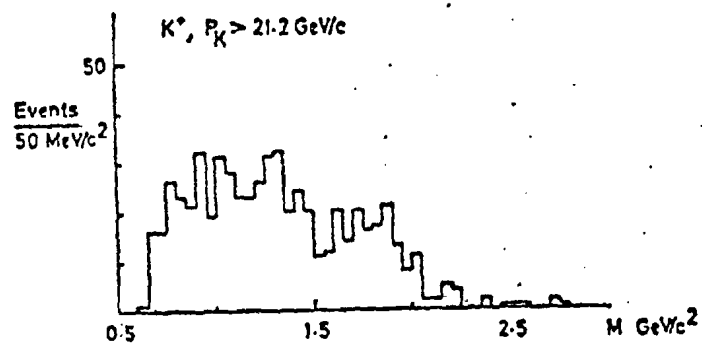

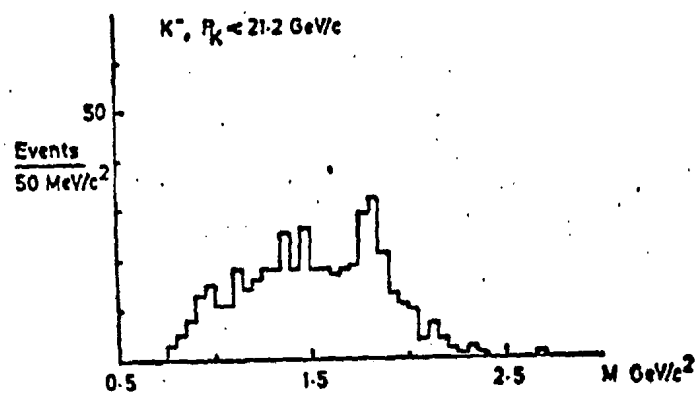

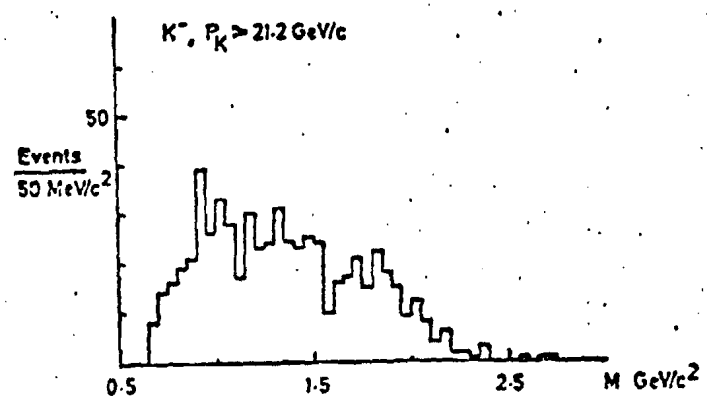

Fig. 6·24

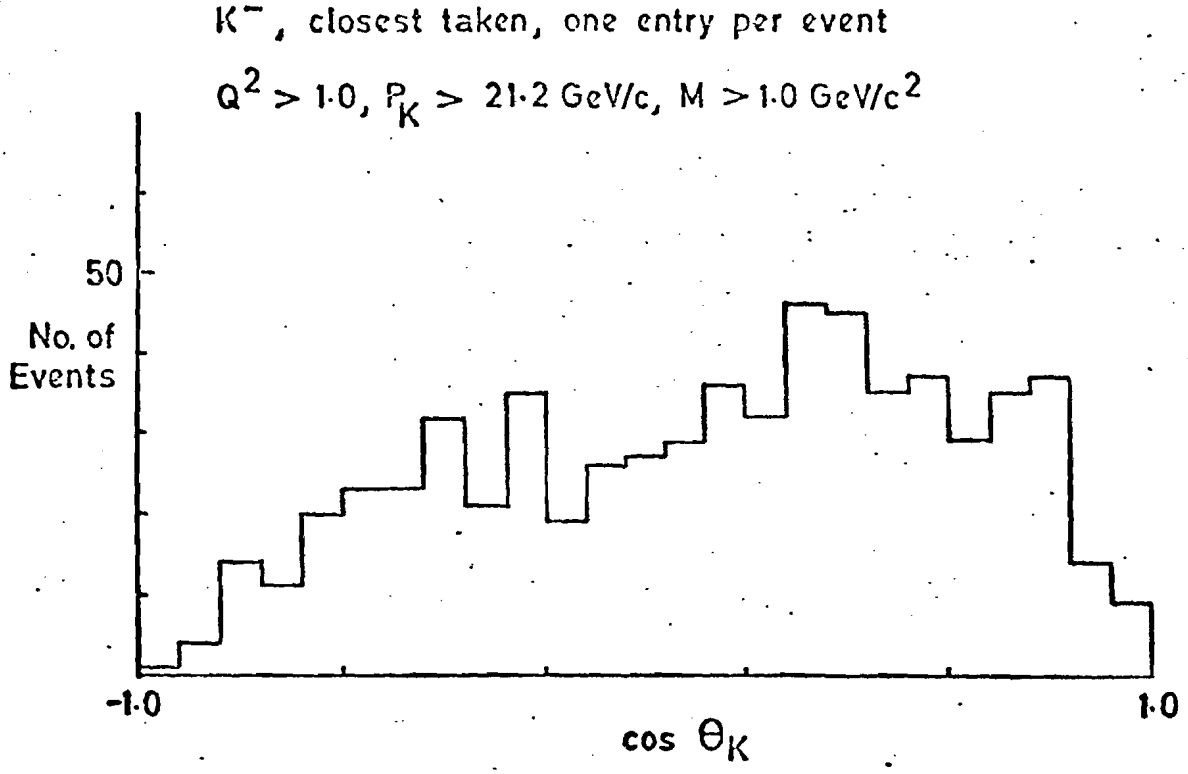
K^-, closest taken, one entry per event
$Q^2 > 1.0$, $P_K > 21.2$ GeV/c, $M > 1.0$ GeV/c^2
50
No. of Events
-1.0
1.0
cos θ_K

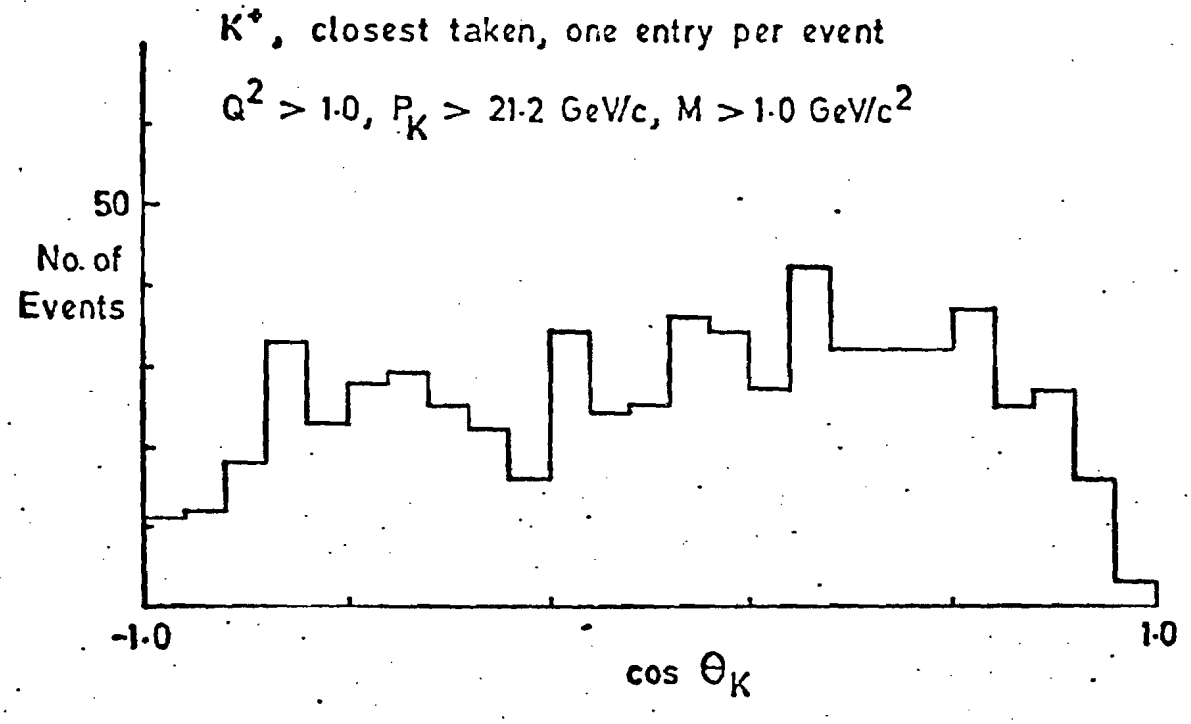
K^+, closest taken, one entry per event
$Q^2 > 1.0$, $P_K > 21.2$ GeV/c, $M > 1.0$ GeV/c^2
50
No. of Events
-1.0
1.0
cos θ_K

Fig. 6.25

$1 < Q^2 < 4.0$ Closest $P_K < 21.2$, One entry/event

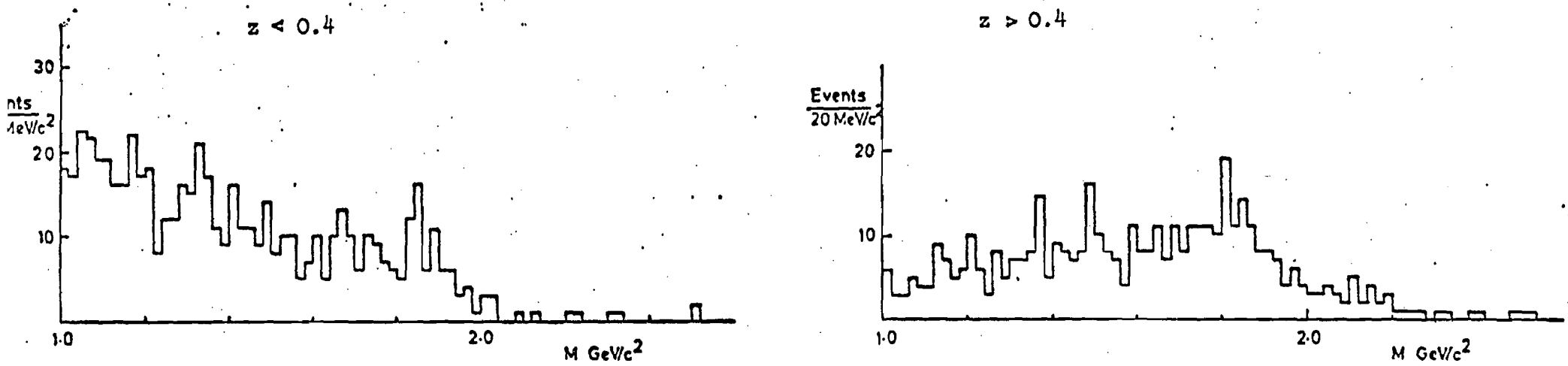

$4 < Q^2 < 80$, Closest $P_K < 21.2$, One entry/event

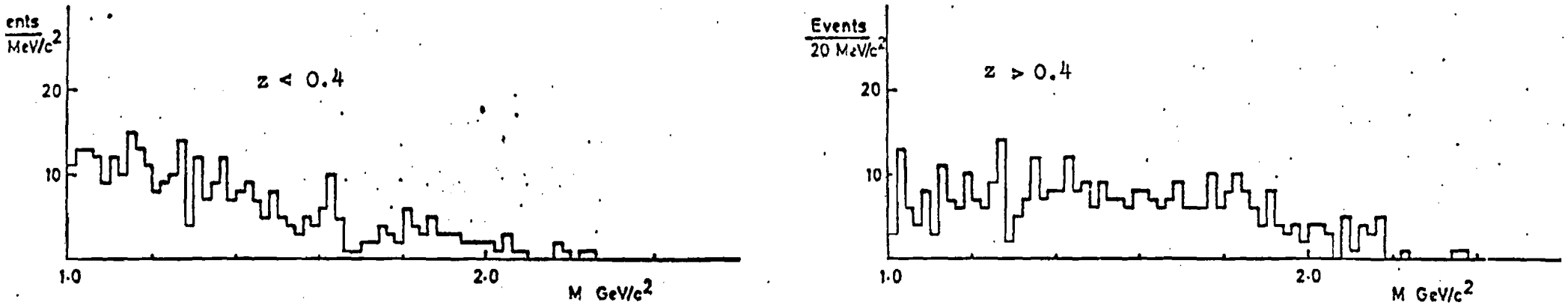

Fig. 6·26

Closest mass taken, one entry per event $P_K < 21.2$, Pions rejected using $\check{C}$ $Z_{\pi\mu} > 0.4$, $Q^2 > 1.0$

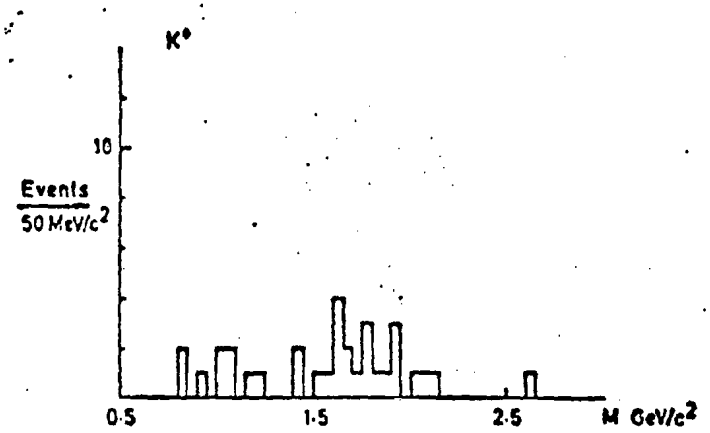

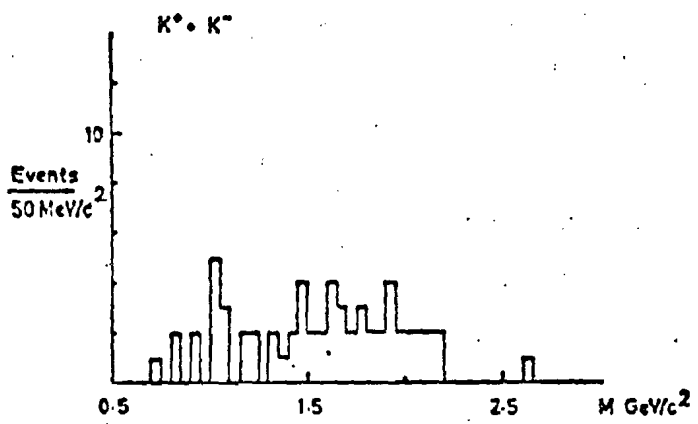

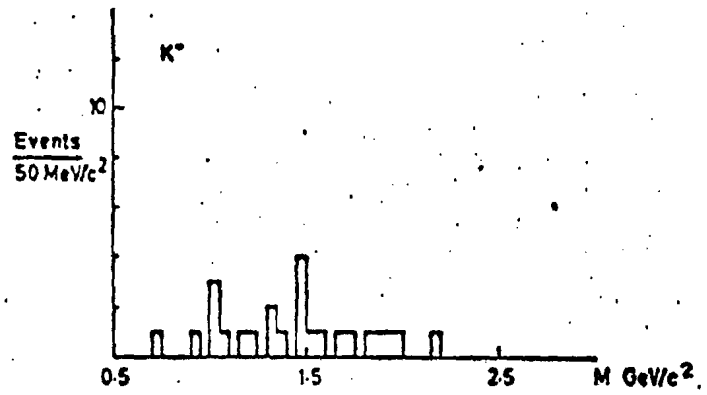

Fig. 6·27

Closest $P_K < 21.2$ Pion rejected using $\check{C}$ $Z > 0.4$

$1 < Q^2 < 80$

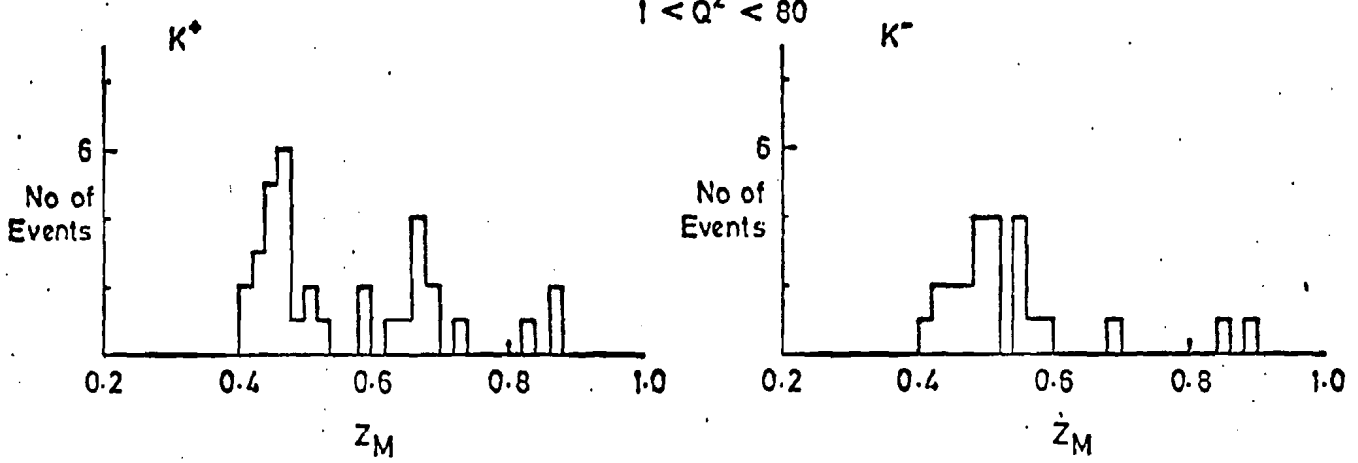

Closest $P_K < 21.2$ $1 < Q^2 < 80$ No rejection $Z > 0.4$

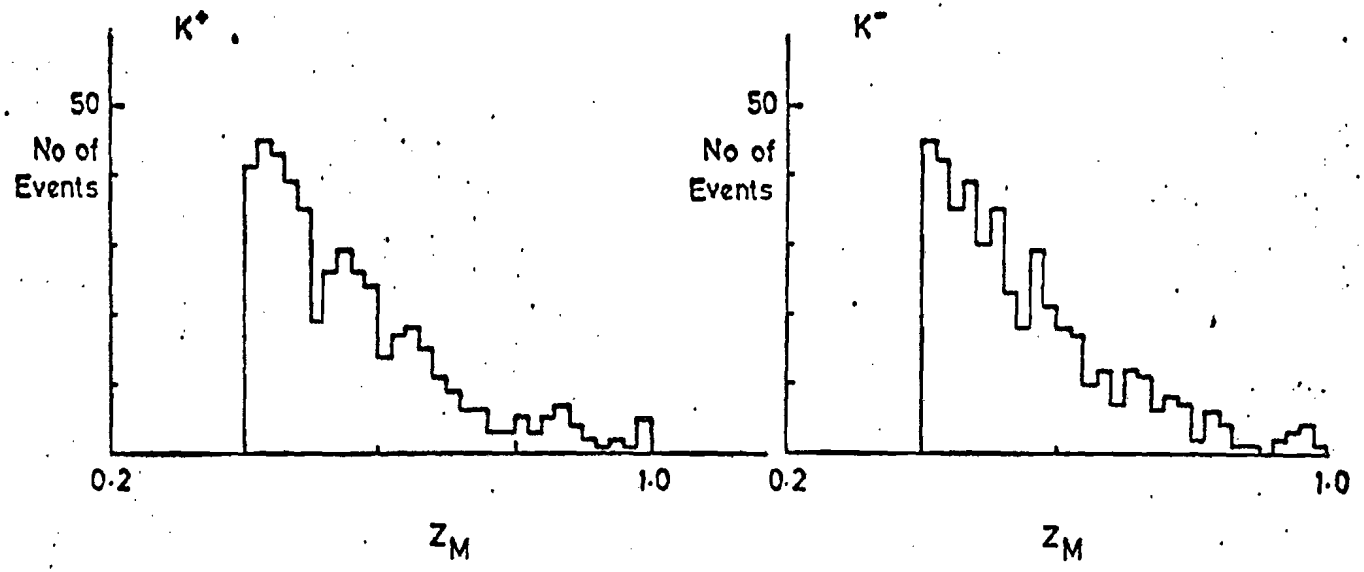

Fig. 6.28

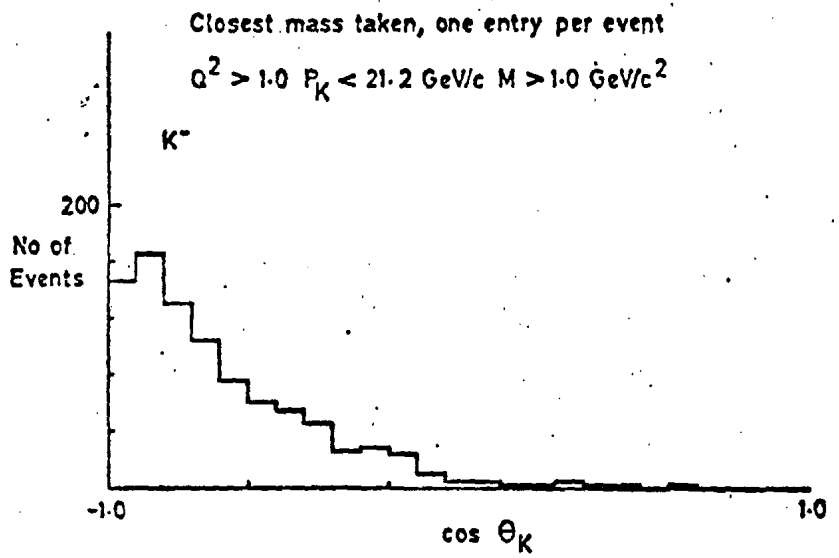
Closest mass taken, one entry per event
$Q^2 > 1.0$ $P_K < 21.2$ GeV/c $M > 1.0$ GeV/c^2
K^-
200
No of Events
-1.0
1.0
cos θ_K

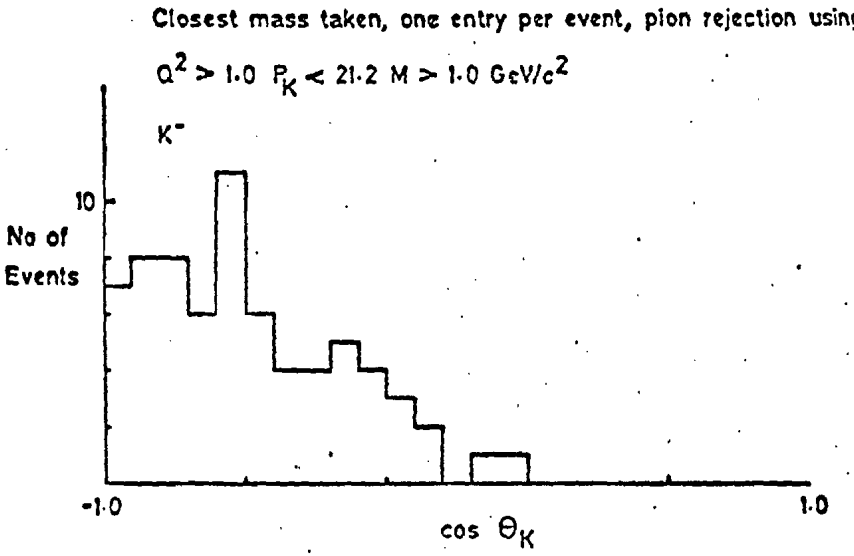
Closest mass taken, one entry per event, pion rejection using χ^2_c
$Q^2 > 1.0$ $P_K < 21.2$ $M > 1.0$ GeV/c^2
K^-
10
No of Events
-1.0
1.0
cos θ_K

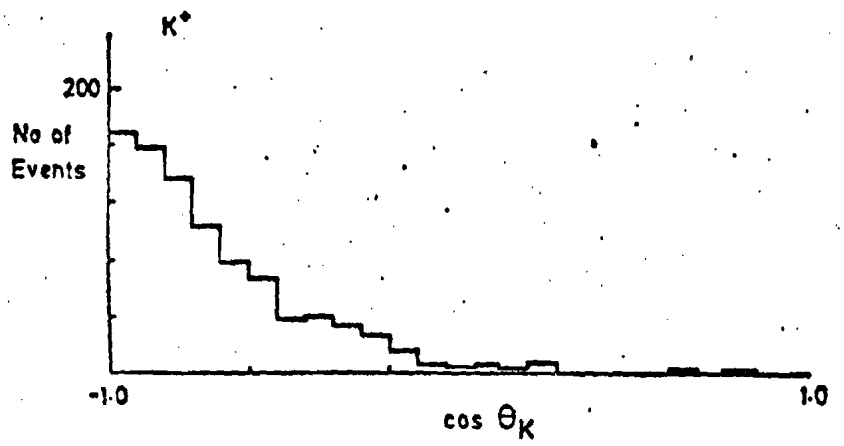
K^+
200
No of Events
-1.0
1.0
cos θ_K

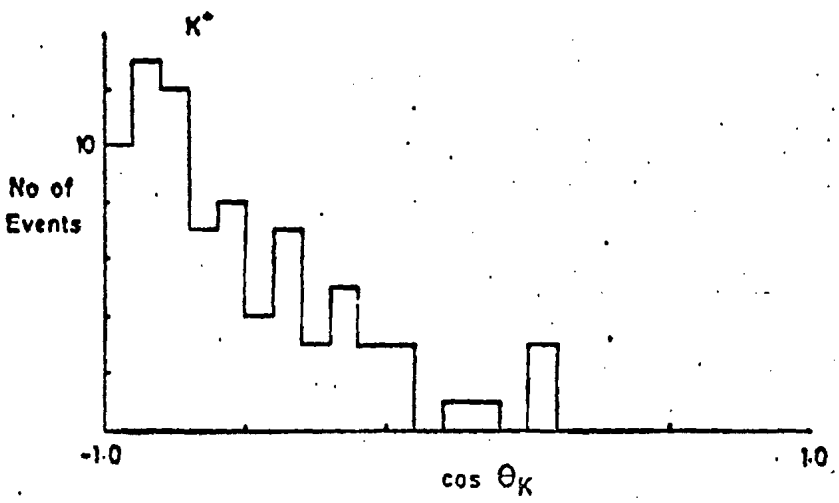
K^+
10
No of Events
-1.0
1.0
cos θ_K

Fig. 6·29

P < 21·2, Pions removed using $\check{C}$, one entry/event, closest taken

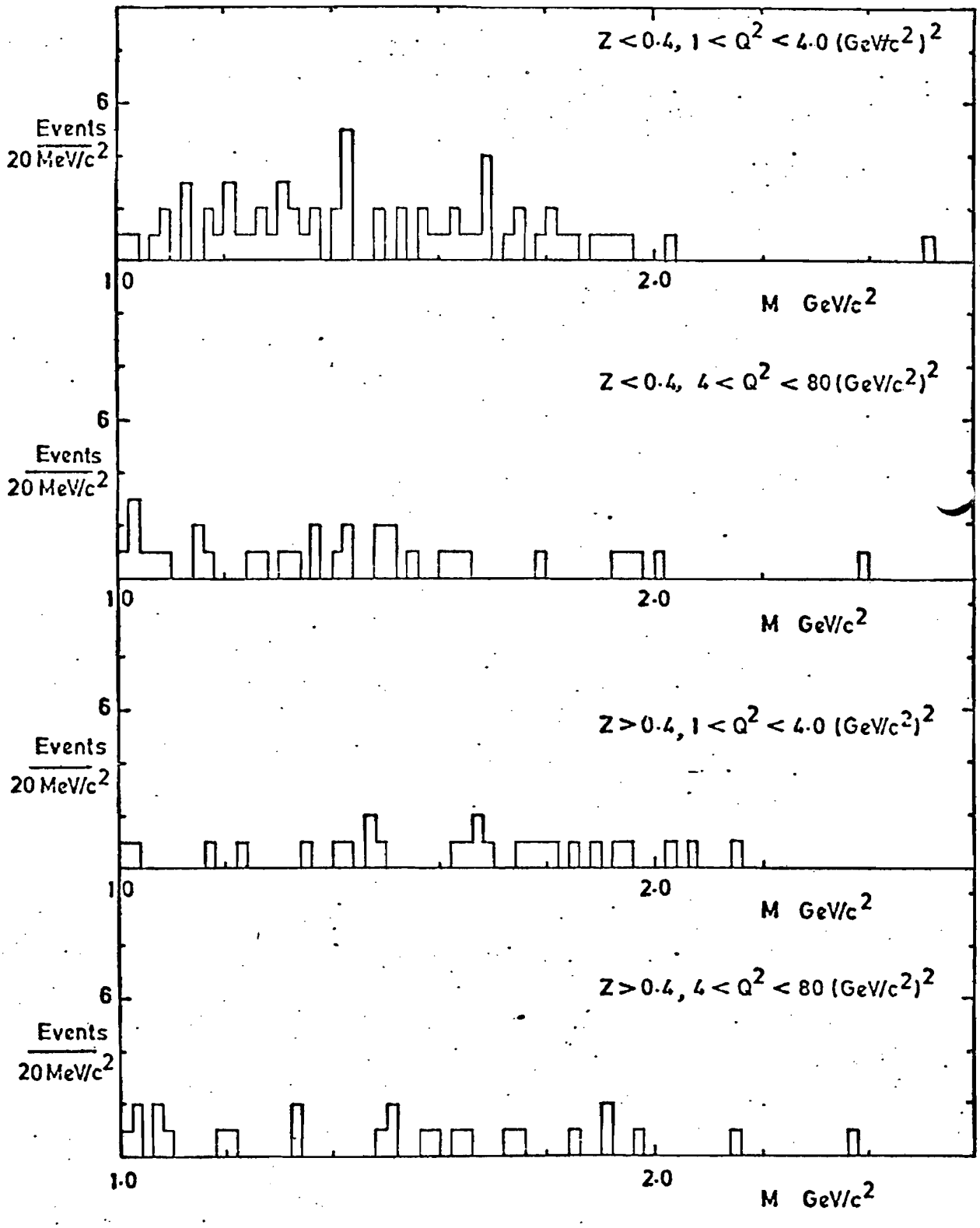

Fig. 6·30

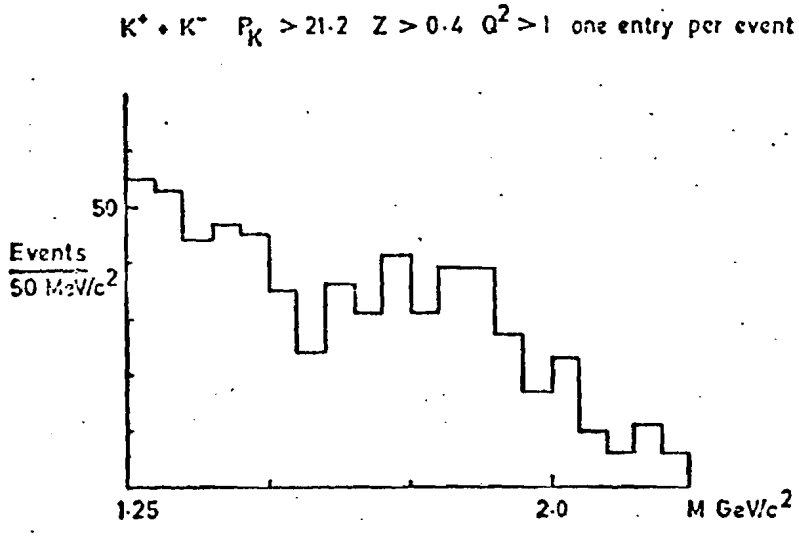

Fig. 6·31

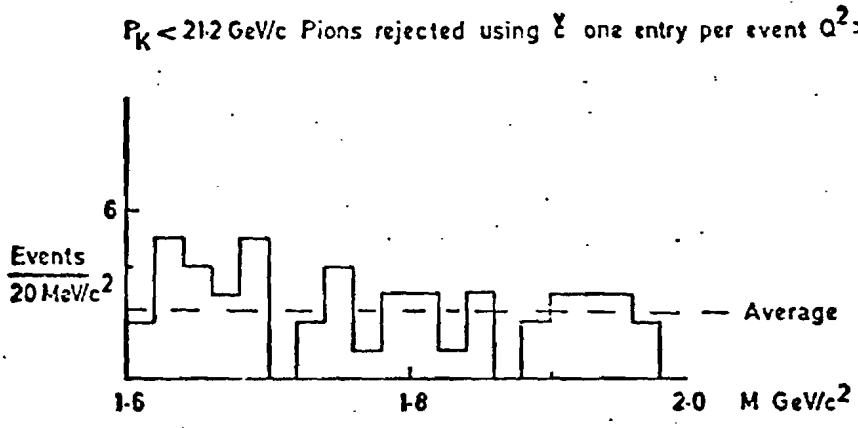

Fig. 6·32

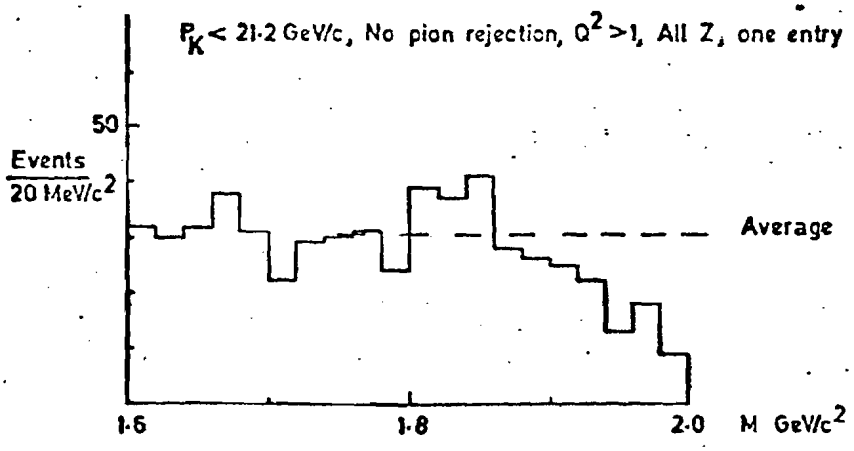

Fig. 6·33

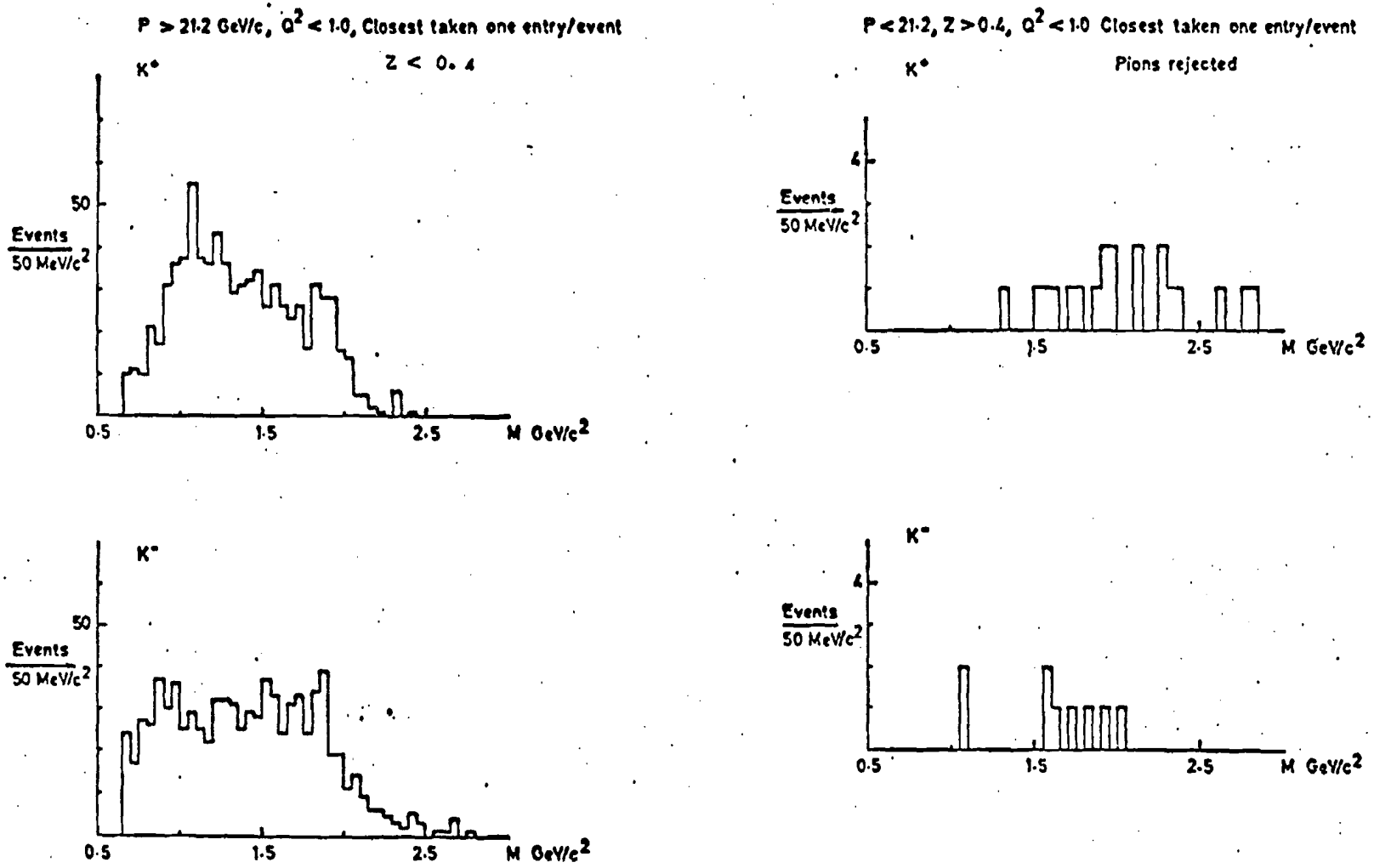
P > 21·2 GeV/c, Q² < 1·0, Closest taken one entry/event
K⁺
Z < 0·4
50
Events
50 MeV/c²
0·5
1·5
2·5
M GeV/c²
K⁻
50
Events
50 MeV/c²
0·5
1·5
2·5
M GeV/c²
P < 21·2, Z > 0·4, Q² < 1·0 Closest taken one entry/event
K⁺
Pions rejected
4
Events
50 MeV/c²
0·5
1·5
2·5
M GeV/c²
K⁻
4
Events
50 MeV/c²
0·5
1·5
2·5
M GeV/c²

Fig. 6·34

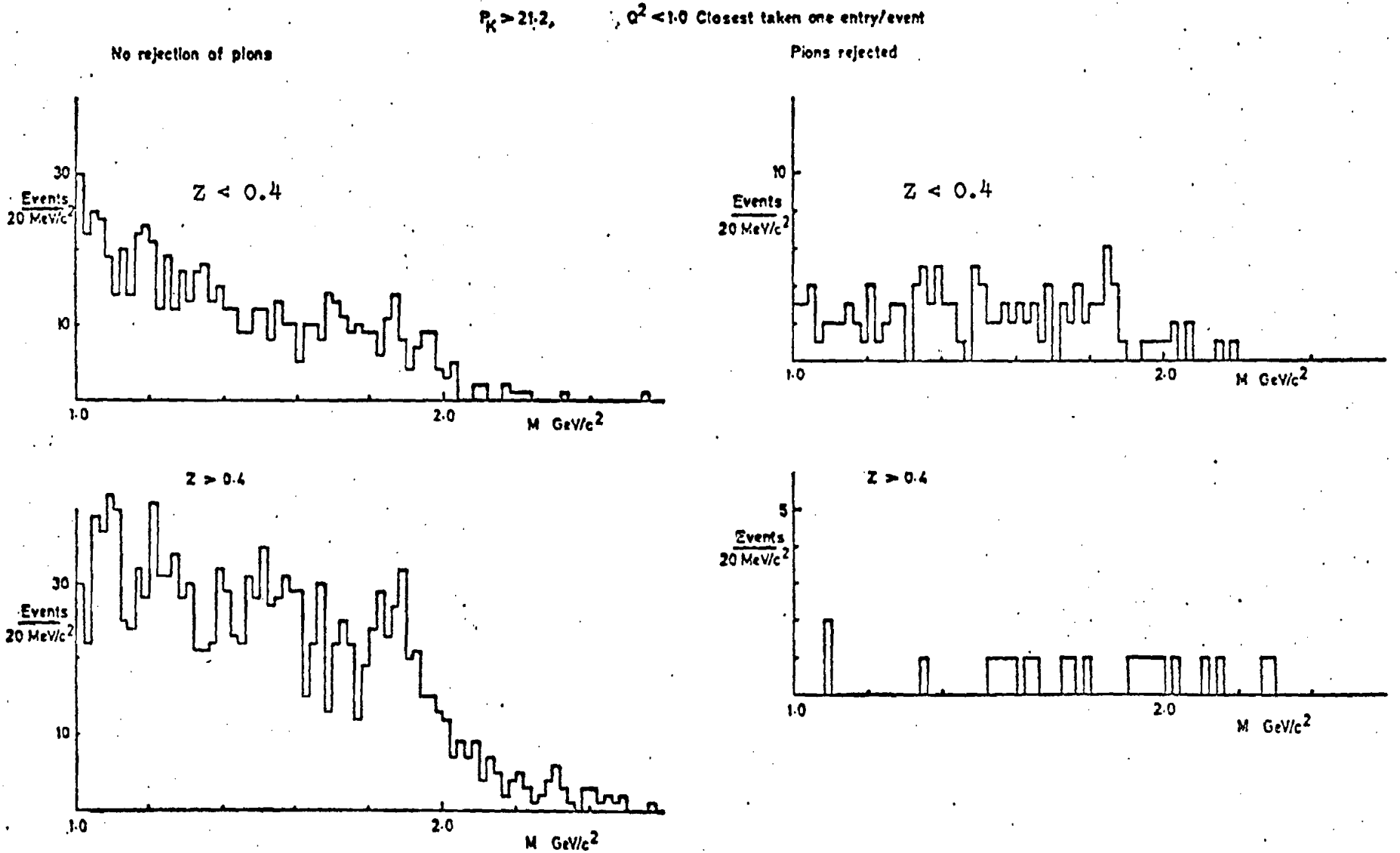
$P_K > 21.2$, $Q^2 < 1.0$ Closest taken one entry/event
No rejection of pions
Pions rejected
Z < 0.4
Z > 0.4
Events
20 MeV/c²
M GeV/c²
1.0
2.0
30
10
5

Fig. 6·35

$K^-\pi^+ + K^-\pi^+\pi^+$

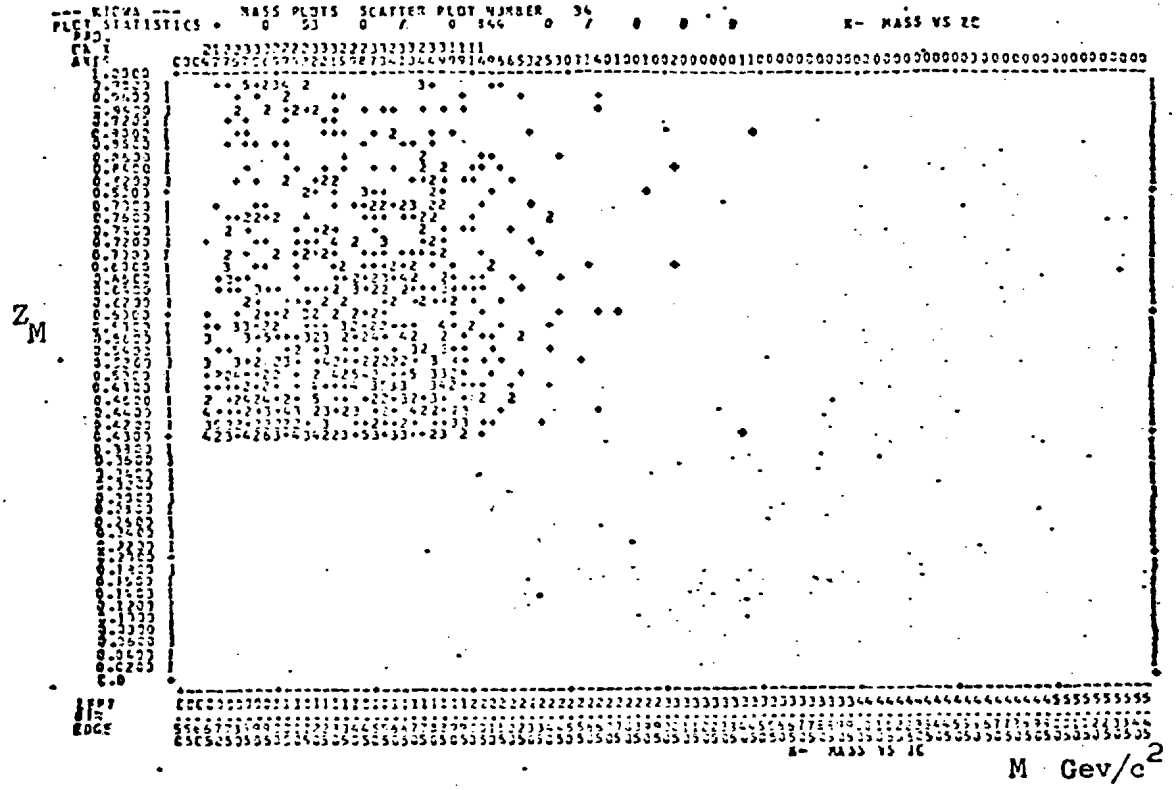

$K^+\pi^- + K^+\pi^-\pi^-$

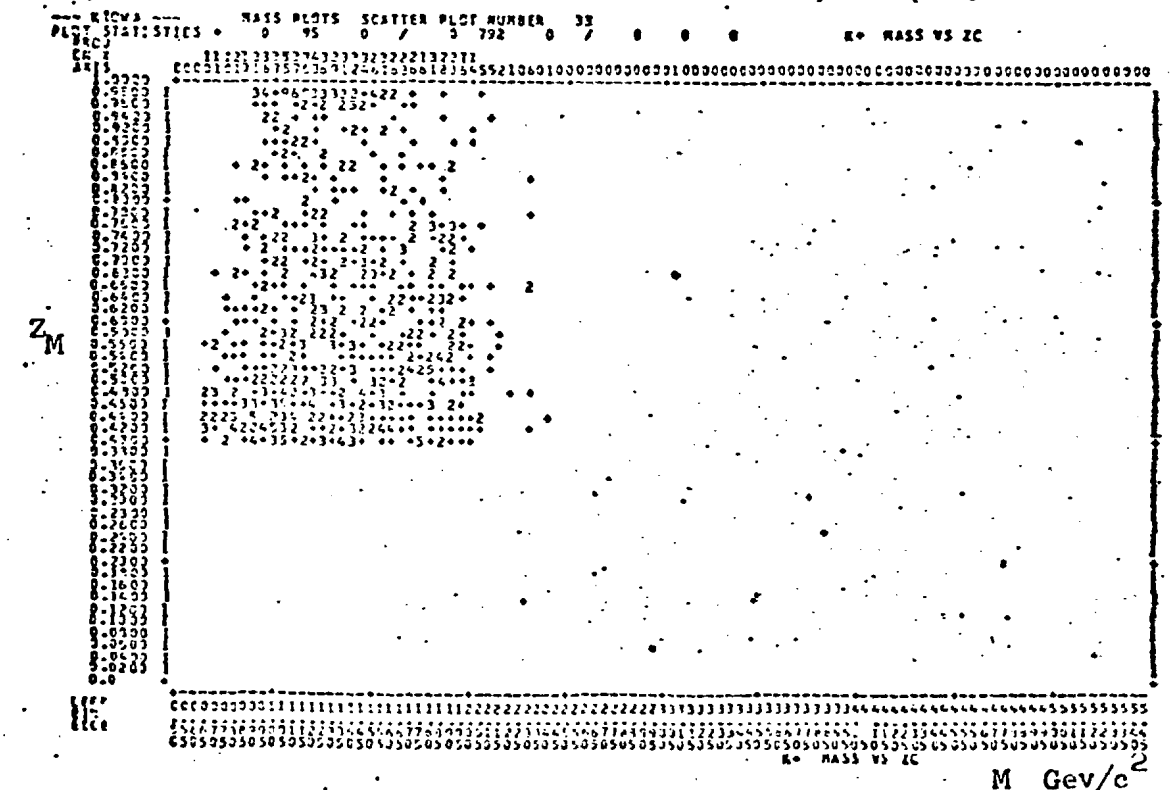

Fig. 6.36a

$K^-\Pi^+ + K^-\Pi^+\Pi^+$

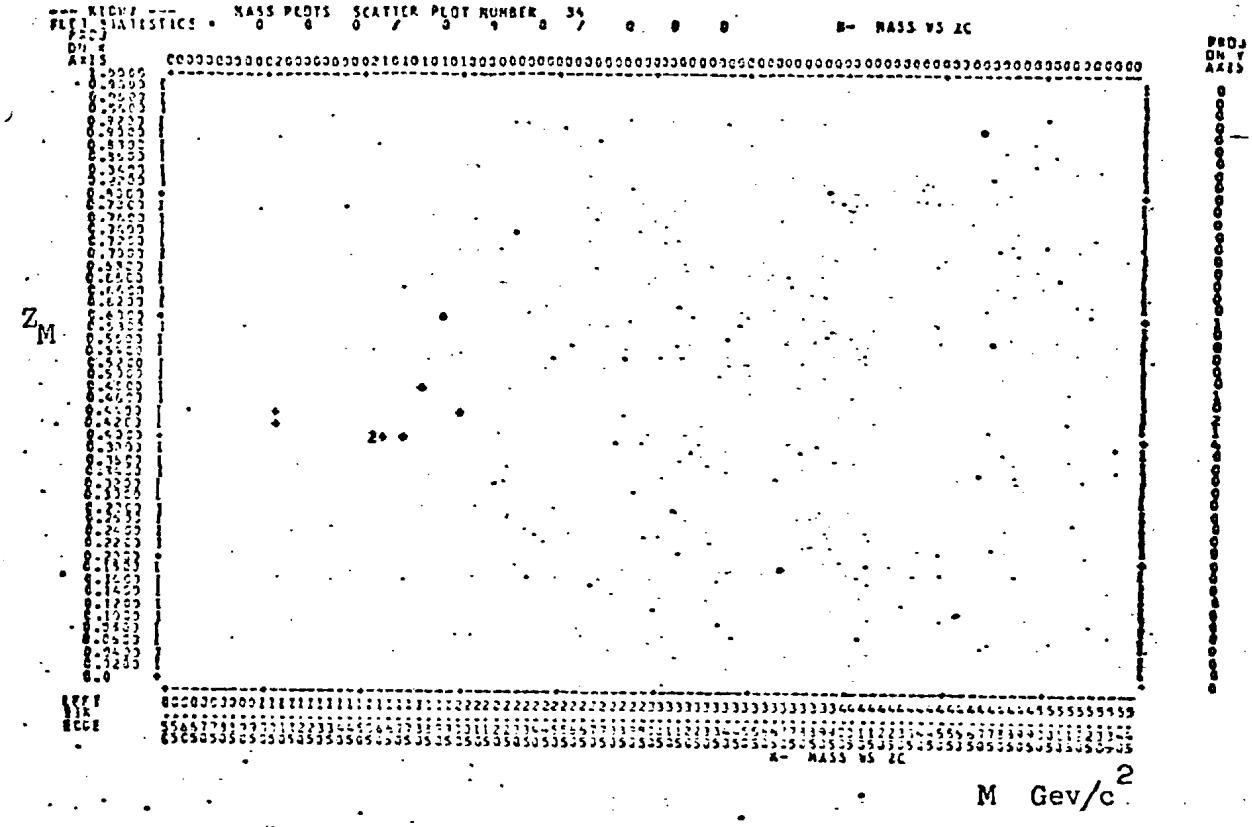

$K^+\Pi^- + K^+\Pi^-\Pi^-$

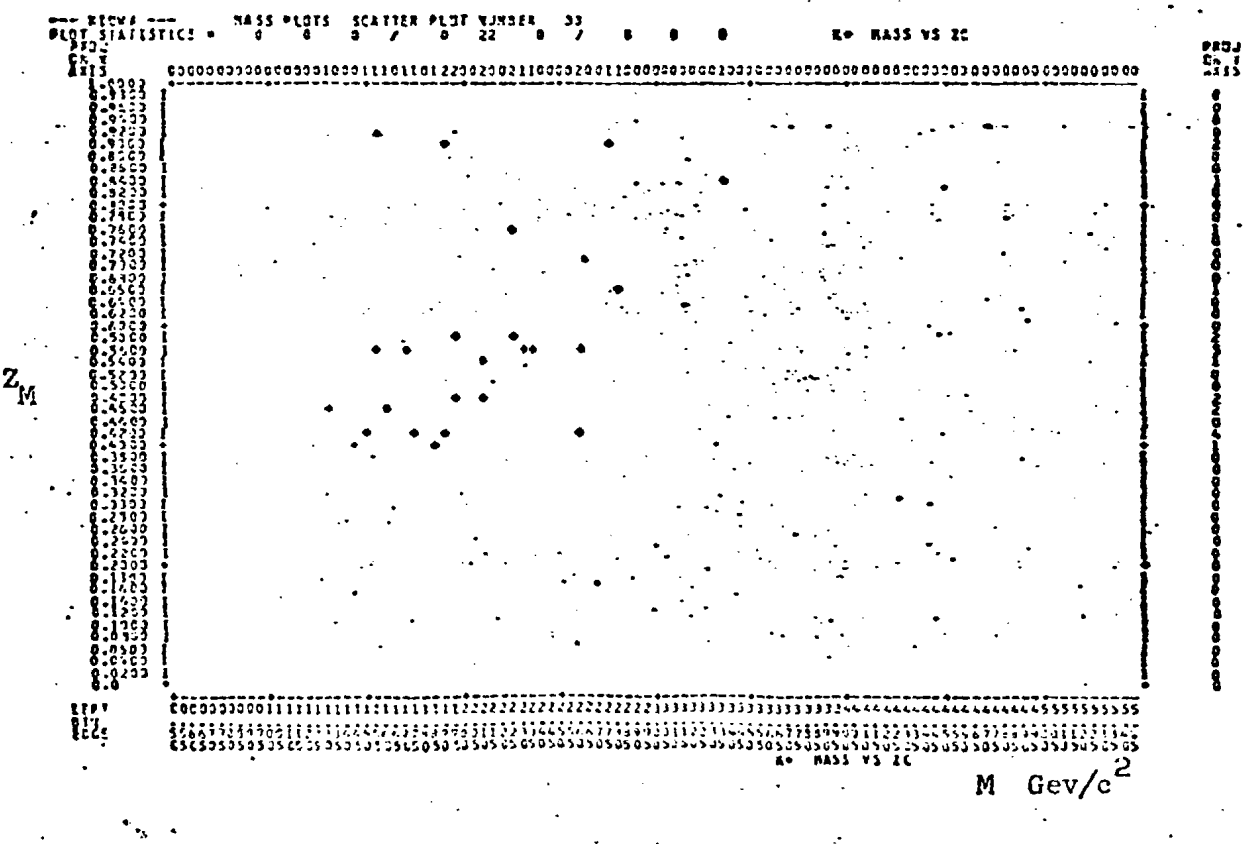

Fig. 6.36b

Analysis 2, $Q^2 < 1.0$ (Gev/c^2)^2, $M > 1.0$ Gev/c^2

$P_K > 21.2$ Gev/c

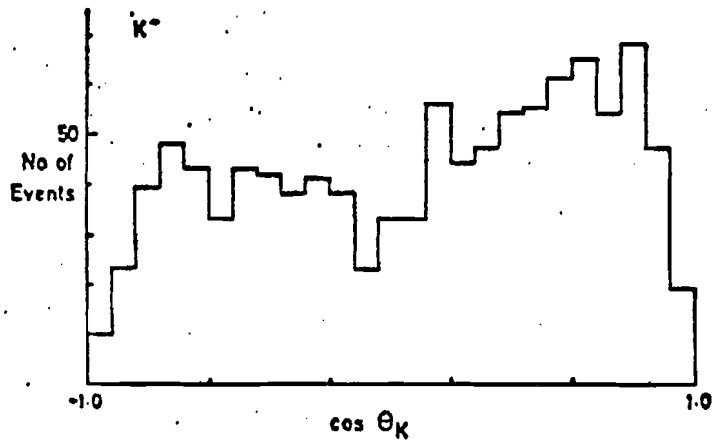

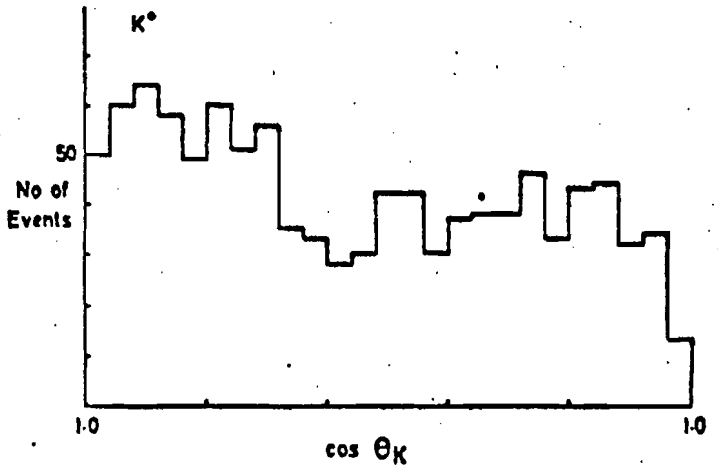

$P_K < 21.2$ Gev/c

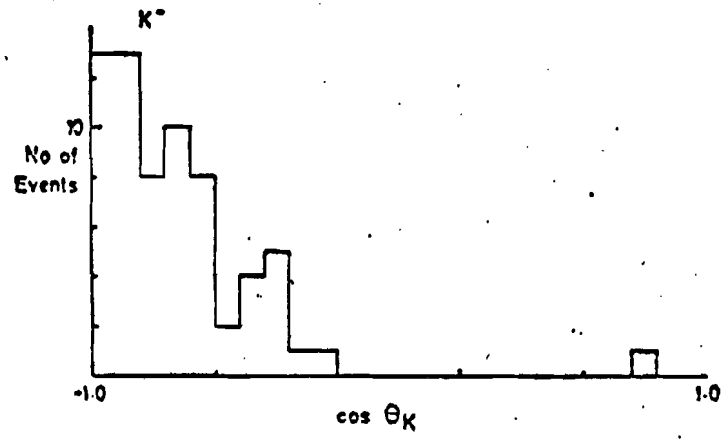

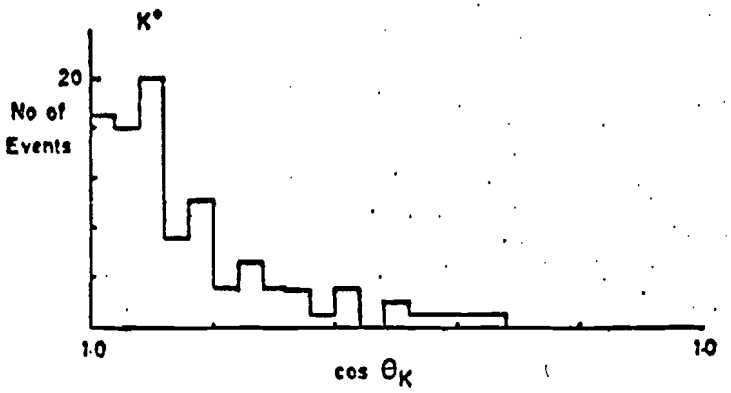

Fig. 6·37

Analysis 2, $Q^2 < 1.0$ (Gev/c^2)^2

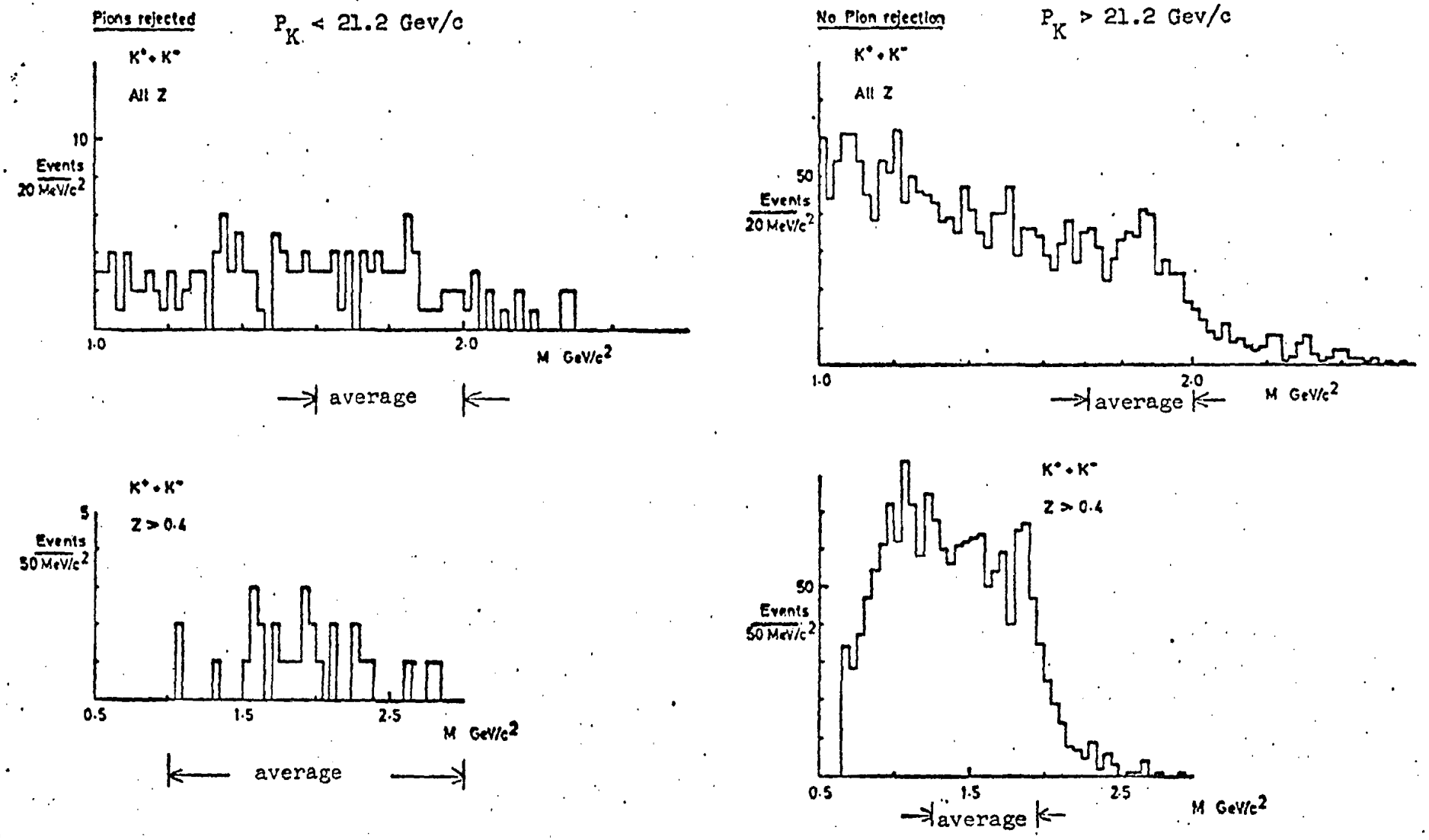

Fig. 6·38

CHAPTER 7

PARTICLE FLUXES

7.1 INTRODUCTION

As was observed in Chapter 5, the Cerenkov counter yielded efficient pion identification in one narrow momentum band (12.4-21.2 GeV/c) and fair proton identification in a second, higher momentum hand (31.4-38.2 GeV/c). This identification makes possible a first measurement of particle fluxes at a large centre of mass energy in deep-inelastic scattering. There are three problems associated with this measurement:

(a) Inefficiency in the Cerenkov counter can cause pions to be misidentified as kaons or protons, and kaons to be misidentified as protons. The magnitude of this effect can be estimated from the measured Cerenkov counter inefficiency, and a correction applied to the data.

(b) Although the downstream hadron chambers were aligned symmetrically about the beam axis, the Cerenkov counter beam deadener, and the deadener in the six metre spark chambers resulted in different acceptances for positive and negative hadrons. The hadron acceptance was not calculated in this analysis and therefore a measurement of the positive to negative ratio was not possible. However, the ratio of positive to positive and negative to negative is independent of acceptance and these ratios can therefore be obtained.

(c) Electrons from the large number of μ-e scatters observed in the data (see Chapter 8) would be mis-identified as pions and would completely swamp the pion signal at low Q^2. The μ-e filter developed for use in extracting the structure functions was only 75% efficient. This was not sufficient to recover the pion

signal. The region below Q^2 of 1.0 $(GeV/c^2)^2$ was therefore removed from the analysis to avoid contamination.

Measurements of K^+/π^+, K^-/π^-, P/π^+, $\bar{P}/\pi^-$ as a function of z will be presented in Section 7.2 and as a function of $P_\perp^2$ in Section 7.3. The muon kinematics cuts used were:

$$1 < Q^2 < 80 \ (GeV/c^2)^2$$

$$10 < \nu < 200 \ GeV$$

This resulted in

$$\langle s \rangle = 252.4 \ GeV^2$$

$$\langle Q^2 \rangle = 6.7 \ (GeV/c^2)^2$$

$$\langle \nu \rangle = 141 \ GeV$$

$$\langle x_{Bj} \rangle = 0.033$$

Subsidiary cuts on Q^2 were made for one section of the analysis. For the region Q^2 = 1.0-4.0 $(GeV/c^2)^2$, the means of the kinematic variables were:

$$\langle s \rangle = 288 \ GeV^2$$

$$\langle Q^2 \rangle = 2.1 \ (GeV/c^2)^2$$

$$\langle \nu \rangle = 154 \ GeV$$

$$\langle x_{Bj} \rangle = 0.009$$

For the region Q^2 = 4.0-80 $(GeV/c^2)^2$, the means of the kinematic variables were:

$$\langle s \rangle = 214 \ GeV^2$$

$$\langle Q^2 \rangle = 11.7 \ (GeV/c^2)^2$$

$$\langle \nu \rangle = 120 \ GeV$$

$$\langle x_{Bj} \rangle = 0.06$$

Conclusions and comments will be given in Section 7.4.

7.2 PARTICLE FLUXES AS A FUNCTION OF z

The standard definition of z applies to this analysis

$$z = \frac{P_{had}}{\nu} \approx \frac{E_{had}}{E_T}$$

where E_{had} is the energy of the hadron, P_{had} its momentum and E_T is the energy given to the hadronic system in the laboratory. It is seen that for $z > 0.2$, z corresponds to the Feynman scaling.

Having obtained the momentum bands in which particle identification was possible, the procedure used to obtain particle fluxes was quite straightforward. The event selection criteria applied to the scattered muon track were the same as those used in Chapter 6. Good hadron tracks were then identified using the hadron selection criteria given in Chapter 6. These hadron tracks were then required to pass outside the beam deadener, within 80 cm of the central edges of the Cerenkov counter mirrors and also within their window frames (as described in Chapter 4). The selected hadrons were then subdivided into the two momentum bands in which identification was possible and the remainder rejected. Hadrons were then further divided into two classes for each momentum band: those which had lit the Cerenkov, and those which had not. Finally, these classes were binned as a function of z and charge, where the z bins were chosen to provide reasonable statistics.

Therefore, neglecting inefficiency in the Cerenkov counter, this classification scheme provides the following information:

(a) 12.4-21.2 GeV/c

Lit tracks are pions, unlit tracks are kaons or protons. Therefore in this band the ratio $\text{Unlit}^{\pm}(z)/\text{Lit}^{\pm}(z)$ gives an upper limit on the ratio $K^{\pm}/\pi^{\pm}$, or $\frac{K}{All}$, $\frac{\pi}{All}$ as desired.

(b) 31.4-38.2 GeV/c

Lit tracks are pions or kaons, unlit tracks are protons. Therefore in this band the ratio $^{Unlit^{\pm}}(z)/Lit^{\pm}(z)$ gives an upper limit on the ratio $^{p^{\pm}}/(\pi + K)^{\pm}$.

The raw event distributions for these classifications are shown in Fig. 7.1-7.4. A note on the binning is necessary.

The minimum z in Figures 7.1 and 7.2 is determined by the minimum momentum (12.4 GeV/c) and the maximum ν (200 GeV) giving roughly $z_{min} \tilde{\sim} 0.05$. Similarly in Figures 7.3 and 7.4, z_{min} is determined by the kinematics to be roughly 0.15.

It is immediately apparent from these distributions that proton production is at best only 10% of kaon production which is itself only roughly 15% of pion production.

A convenient distribution is the particle flux ratios relative to all hadrons produced in the interaction. The flux ratios $^{\pi}$/All, ^{K}/All, ^{p}/All are shown in Fig. 7.5, extracted from the raw event distributions before correction for Cerenkov counter inefficiency. At this point, it is necessary to digress into a brief review of the quark parton description of meson production in deep-inelastic processes given in Section 1.3, in order to explain Fig. 7.5c. In this model, the virtual photon interacts with a single quark in the proton, which is then dressed with other quarks to form the mesons observed in the final state. Thus z is the fraction of the momentum of the struck quark carried off by the observed meson. This fraction is given a 'fragmentation function' D(z), which represents the probability of obtaining a given meson with a fraction z of the momentum of the struck quark. In the model, D(z) depends on the flavour of the quark struck and on the final state meson produced, but not on the energy or momentum given to the struck quark (Q^2, ν) - i.e. D(z) scales in the variable z. Therefore the ratio

$\frac{P}{All}(z)$, $\frac{\pi}{All}(z)$, $\frac{K}{All}(z)$ are independent of the momentum at which they were measured and have the relationship:

$$\frac{P}{All}(z) + \frac{\pi}{All}(z) + \frac{K}{All}(z) = 1$$

for all values of z, if it is assumed that only protons, pions and kaons are being produced. This assumption is correct to within 10% at least, given the results on charmed meson production obtained in Chapter 5. A bin-by-bin subtraction of the proton contribution from the pion failure distribution then provides the kaon distribution (Fig. 7.5c).

In addition, an estimate can also be obtained for the fluxes

$$\frac{\pi^+ + \pi^-}{\text{All Hadrons}} \quad , \quad \frac{K^+ + K^-}{\text{All Hadrons}} \quad \text{and} \quad \frac{P + \bar{P}}{\text{All Hadrons}}$$

If the acceptance for positive particles is α^+ and that for negative particles is α^- and one defines $\alpha = \frac{\alpha^+}{\alpha^-}$ then,

$$\left(\frac{\pi^+ + \pi^-}{\text{All Hadrons}}\right)_{\text{True}} = \frac{\alpha^+\pi^+}{\alpha^+ All^+}_{obs} + \frac{\alpha^-\pi^-}{\alpha^- All^-}_{obs}$$

$$= \frac{\alpha\pi^+ + \pi^-}{\alpha All^+ + All^-}_{obs}$$

At low momentum, differences in acceptance for positive and negative particles should be negligible as all hadrons will be bent away from the deadeners by the spectrometer magnet. Therefore,

$$\left(\frac{\pi^+ + \pi^-}{\text{All Hadrons}}\right)_{\text{True}} \approx \frac{\pi^+ + \pi^-}{All^+ + All^-}_{obs}$$

and similarly for kaons.

This equality is not necessarily correct in the momentum region in which protons can be identified, but should still remain a reasonable approximation for the calculation of the ratio P/All. These distributions

are shown in Fig. 7.6, where again a bin-by-bin subtraction has been used to obtain the kaon flux.

Identification Efficiency

At this stage however, the results, especially those shown in Fig. 7.5b and 7.5c were open to question as the data had not been corrected for Cerenkov inefficiency. In the momentum range 12.4-21.2 GeV/c, the relevant inefficiency measurements are given in Table 5.5. These measurements were obtained from the pulse height distribution in the cells. The average inefficiency was estimated from the average number of photo-electrons collected in each cell. The average number of photo-electrons collected and its error is given by:

$$\mu = \frac{\sum_i \frac{N_i}{E_i^2}}{\sum_i \frac{1}{E_i^2}} \qquad \text{The mean number of photo-electrons collected}$$

$$\frac{1}{\sigma^2} = \sum_i \frac{1}{E_i^2} \qquad \text{The variance of the mean}$$

where N_i is the mean number of photo-electrons collected by each cell, and E_i is the error on this measurement. Moreover, as the errors, E_i, were obtained statistically from the populations in each cell, this automatically weights the estimate of μ by the observed event distribution. From the results given in Table 5.5:

$$\mu_1 = 3.38$$

$$\sigma_1 = 0.14$$

Similarly, Table 5.6 gives the results relevant to the proton identification range:

$$\mu_2 = 3.58$$

$$\sigma_2 = 0.17$$

These results give the following inefficiencies (%):

1. 12.4-21.2 GeV/c: $= 3.40^{+0.51}_{-0.40}$

2. 31.4-38.2 GeV/c: $= 2.79^{+0.36}_{-0.44}$

Corrected Results

Fig. 7.5b is clearly consistent with a flat z distribution. The average values obtained, using all points are:

$$\frac{P}{All^+} = 0.064 \pm 0.015$$

$$\frac{\bar{P}}{All^-} = 0.062 \pm 0.016$$

These values are only two standard deviations above the rate expected from the measured inefficiency in this region. The result is therefore compatible with background. If however, this result represents a true proton signal, then a maximum contribution is of the order 1-2% with large errors. Further comments on this result will be given in Section 7.4.

Since evidence to the contrary is unconvincing, in the extraction of the corrected kaon distributions the proton distribution function was taken as zero for all z. This assumption immediately implies, for Fig. 7.5a, that those hadrons which fail to light the Cerenkov counter are either kaons, or pions which failed through inefficiency. A bin-by-bin correction for a flat 3% inefficiency (ε) was applied to the data using the prescription:

$$N^{\pi}_{true} = N^{\pi}_{obs}(1 + \varepsilon)$$

$$N^{K}_{true} = N^{K}_{obs} - \varepsilon N^{\pi}_{obs}$$

neglecting terms of order ε^2.

The resulting corrected distributions are shown in Fig. 7.7. Clearly, there has been no change in shape as a result of this correction, indicating that the results obtained are not an effect of the Cerenkov inefficiency.

Figs. 7.8 and 7.9 show, for comparison, the corrected and uncorrected K/π flux ratios assuming no contribution from protons. It is seen that the correction for Cerenkov misidentification results in a 2% reduction in relative normalisation, with no change in overall shape. The $K^{\pm}/\pi^{\pm}$ corrected flux ratios are shown in Fig. 7.10 and show a similar behaviour.

It was also possible to investigate the K/π ratios in two z and two Q^2 bins. The results are given in Table 7.1. Statistics are poor at high z and the results are inconclusive. Assuming no variation with Q^2 or charge gives an average value for the K/π ratio in the region $0.3 < z < 0.9$, $1 < Q^2 < 80$ $(GeV/c^2)^2$:

$$\frac{K^+}{\pi^+} = \frac{K^-}{\pi^-} = 0.33 \pm 0.07$$

At low z ($0.1 < z < 0.3$) statistics are reasonable and there is apparently a variation with Q^2 which is roughly a 3 standard deviation effect for the positive charge ratio. It is possible that there are systematic errors which have not been considered in this region and the result requires a more accurate measurement of the fluxes before any effect can be claimed. Clearly, such a result is important as it contradicts one of the hypotheses of the quark model- namely independence of Q^2. Investigation into the effect of ν could not be carried out, since it was impossible to obtain two non-overlapping ν bands which could provide sufficient statistics.

Systematic and Statistical Errors

This analysis relies on the measured efficiency of the Cerenkov counter. This was estimated from pulse height distributions, which may result in a bias due to the trajectories and momenta of the particles selected. However, as the measurements were chosen to correspond to the momentum ranges used in the analysis, such a bias if it exists should be small. Clearly, statistical errors on the measured average efficiency are small and would cause no significant changes in the results. Quantum inefficiency has been automatically included in the measured efficiency. Overall, an error of 1-2% would represent a reasonable estimate of these cumulative effects. There is also an error introduced by the neglect of proton contribution, which may be 1-3% at low z. Therefore, overall systematics may be as high as 1-5% in the low z region.

Further discussion and comments on these results will be given in Section 7.4.

7.3 PARTICLE FLUXES AS A FUNCTION OF $P_\perp^2$

The second interesting variable in understanding hadron production in the quark-parton model is the transverse momentum of the observed meson with respect to the momentum vector of the struck quark. In deep-inelastic scattering, as the virtual photon only interacts with a single quark, the momentum vector of the struck quark is that of the virtual photon. This is measured, and therefore the transverse momentum of the mesons produced can be calculated. Whether one uses the variable $P_\perp$ (= transverse momentum) or $P_\perp^2$ is a matter of choice (and model). The standard parameterisation of $P_\perp$ distributions at low $P_\perp$ is as a function $Ae^{-P_\perp^2}$ (where A is a constant), therefore the fluxes were presented as a function of $P_\perp^2$. Moreover, this is the standard variable of Q.C.D.

A similar procedure to that used to obtain the z particle ratio distributions, was used to obtain $P_\perp^2$ distributions out to a value of $P_\perp^2$ of 1.6 $(GeV/c)^2$ for $1 < Q^2 < 80$ $(GeV/c^2)^2$ in the regions $z < 0.3$, $z > 0.3$. Statistics limited the maximum $P_\perp$ used in the analysis. Poor statistics also prevented investigation of 'protons' for $z > 0.3$. The raw event distributions and particle flux ratios obtained from them are shown in Fig. 7.11-7.13. In accordance with the results obtained in Section 7.2, no proton contribution was considered in the kaon fluxes. However, this conclusion can also be drawn from the measured $P_\perp$ distributions. From Fig. 7.13 the mean values of the flux ratios in the proton identification region are:

$$\frac{\text{Unlit}^+}{\text{All}^+} = 0.033 \pm 0.014$$

$$\frac{\text{Unlit}^-}{\text{All}^-} = 0.037 \pm 0.015$$

These are clearly consistent with the background estimate due

to inefficiency given in Section 7.2. Moreover, for both charges, the $P_\perp^2$ ratio distributions are consistent with being flat, which would be expected if the source of the failures was detection inefficiency. The fluxes shown in Fig. 7.11 and 7.12 were therefore obtained from the raw data assuming no proton contribution. The expected relative increase with $P_\perp$ of kaons over pions is clearly shown in the raw data at low z - it will be shown that this effect is not a result of Cerenkov counter inefficiency.

A bin-by-bin correction for a 3% inefficiency was applied in the same fashion as for the z flux distributions. The corrected data and the ratios of K/π as a function of $P_\perp^2$ are shown in Fig. 7.14-7.16. Again, the only significant effect of the correction procedure is a relative reduction in the ratio $\frac{K}{\pi}$ by 2%. The relative increase in kaons over pions with increasing $P_\perp^2$ is still apparent at low z. For $z < 0.3$, a straight line fit of the form:

$$\frac{K}{\pi}(P_\perp^2) = a_1 + a_2 P_\perp^2$$

gave the following results:

1. $\frac{K^+}{\pi^+}$: $a_1 = 0.14 \pm 0.03$
   $a_2 = 0.14 \pm 0.10$

2. $\frac{K^-}{\pi^-}$: $a_1 = 0.10 \pm 0.02$
   $a_2 = 0.12 \pm 0.09$

For $z > 0.3$ the position is unclear as errors are large. The $\frac{K^+}{\pi^+}$ distribution is significantly higher than the $\frac{K^-}{\pi^-}$ distribution. Both however, are consistent with being flat as a function of $P_\perp^2$ and have large errors. Improved data are clearly necessary in this region before a reasonable interpretation can be made, as the differences may simply be statistical fluctuations.

7.4 COMPARISON OF RESULTS WITH THEORETICAL PREDICTIONS AND OTHER EXPERIMENTS

As has been shown, apart from inefficiency in the Cerenkov counter, only kaons and protons should fail to light the Cerenkov counter in the momentum band 12.4-21.2 GeV/c. In this region, 17.7 ± 1.2% of all charged hadrons were observed to fail to light the counter, compared with a measured inefficiency of 3.4 ± 0.2%. Correcting for this inefficiency gives the rate for proton and kaon production as 14.9 ± 1.4%. It was also possible to separate protons from pions and kaons in the momentum band 31.4-38.2 GeV/c, since in this region only protons should fail to light the Cerenkov counter. A failure rate of 6.0 ± 1.1% was observed in this region, compared with a measured inefficiency of 3.6 ± 0.2%. The maximum level of proton production is therefore 2.6 ± 1.3% of all charged hadrons, and is consistent with background.

Further separation can be obtained if:

(a) Feynman scaling is assumed to hold throughout the accessible kinematic region;

(b) Scaling violations in deep-inelastic scattering are neglected (a 10-20% effect).

The particle ratio distributions are then independent of Q^2 and ν, and of the momentum band used for identification. Separation of the particle production fractions is then possible. This gives the fraction of all charged hadrons (f_π, f_K, f_p) as:

$$f_\pi = 0.854 \pm 0.014$$

$$f_K = 0.120 \pm 0.027$$

$$f_p = 0.026 \pm 0.013$$

Assumptions (a) and (b) are necessary in the extraction of particle ratio distributions as a function of z and $P_\perp^2$. In particular, if

assumption (a) is incorrect then the distributions as a function of z are implicit functions of ν. The variation of acceptance then results in these distributions also having a Q^2 dependence (i.e. low ν corresponds to high Q^2, and high ν to principally low Q^2).

Comparisons with Other Experiments

Having made the above assumptions, it is reasonable to compare the data with other experiments of a similar nature.[63,64,65] A recent experiment has reported on proton production in deep-inelastic electron scattering[63]. However, the centre of mass energy in this experiment is considerably lower than that for the data presented in this thesis (s = 7-31 GeV^2 c.f. $\langle s \rangle$ = 252 GeV^2). In addition, the results are principally concerned with residual anti-proton production in the target fragmentation region. For positive z in the range 0.1-0.3, they obtain the result $\bar{p}/\pi^- = 0.041 \pm 0.007$, which is higher than that obtained in this analysis. The data are at low s and some overspill from the target fragmentation into positive z may occur. However, no data on proton production was presented in this paper and a firm conclusion cannot be drawn.

It is also possible to compare this data to that obtained in e^+e^- annihilation, with three further assumptions:

1. Quark fragmentation functions are only dependent on the quark flavour, and not on any particular interaction (implicit in the quark cascade model for hadron production).
2. Valence quark contribution is unimportant:-
   as the majority of the data is at low z, this is valid if hadron production proceeds via a cascade type process such as described in Section 1.4.
3. Sea quark distributions of the proton are approximately the same

as the probability distributions for creating $q\bar{q}$ pairs from the vacuum (- this assumption can be neglected if assumption 2 is valid).

Inclusive hadron production in e^+e^- annihilation at $\langle s \rangle = 53^2 GeV^-$ has been reported by D.G. Aschman et al.[64] A comparison of the particle production fractions obtained by Aschman et al with the fractions obtained in this analysis is given in Table 7.2.

Good general agreement is apparent. Moreover, as is clear from Figures 7.1-7.4, the data presented in this thesis is at predominantly low z ($z < 0.3$). This region corresponds approximately to the low momentum data of reference 64, which is in excellent agreement with this experiment and provides supporting evidence for the assumptions made in this analysis. In addition, the proton contribution is confirmed to be small, justifying its neglect in calculating kaon distributions.

A comparison of the z distribution of the ratio $K^{\pm}/\pi^{\pm}$ could also be obtained from the data of Aschman et al. By definition

$$\frac{K^{\pm}}{\pi^{\pm}} = \frac{d^3\sigma^K}{d\Omega dp} \Big/ \frac{d^3\sigma^{\pi}}{d\Omega dp}$$

The comparison is shown in Fig. 7.17, where the approximation $z \approx {}^{2P}/\sqrt{s}$ has been used to extract the data from reference 64. Excellent agreement is obtained for all points. The data thus show a remarkable agreement with Feynman scaling and the quark fragmentation hypothesis (assumption (1) above).

Finally, data on inclusive $K^{\pm}$ electroproduction is also available[65] (Martin et al). This however, is again obtained at a much lower centre of mass energy than the data presented in this thesis, but provides information on both $z(\tilde{\sim}x_F)$ and $P_\perp^2$ distributions of the flux ratios $\frac{K^+}{\pi^+}$, K^-/π^-. A comparison of the z distributions is shown in Fig. 7.18. The data sets appear to be inconsistent, both in the magnitude of the ratios

and their general trends (particularly K^-/π^-). The interpretation of the $P_\perp^2$ distributions obtained in the two experiments is even more difficult. This analysis has observed a slight rise with $P_\perp^2$ for both K^+/π^+ and K^-/π^- at low z, and a flat $P_\perp^2$ distribution at high z. Martin et al observed a rising $P_\perp^2$ distribution for K^+/π^+ but a flat distribution for K^-/π^-. The results could therefore indicate z dependence in the $P_\perp$ distributions. However, the differences may simply be due to resonance production at low energies.

To summarise briefly, the only data with which a comparison can be made have been taken at centre of mass energies which are considerably lower than those of data in this thesis. Some quantitative agreement is obtained with hadron distributions in e^+e^- annihilation at $\langle s \rangle = 53$ GeV^2, whereas some discrepancies are apparent in lower energy leptoproduction data ($\langle s \rangle = 21$ GeV^2). Possible causes of this inconsistency could be: a violation of Feynman scaling at low energies; or confusion with resonance production. However, errors are large in all four experiments, particularly at large z and high $P_\perp$. Further confirmation of these results is therefore required.

Theoretical Predictions for Hadron Distributions

Hadron distributions have been calculated mainly within two theoretical frameworks: either using a full Q.C.D. treatment or using the simpler impulse approximation of the quark-parton model. However, both methods are complex, and only a semi-quantitative comparison will be given.

Various authors[66,67,68] have calculated quark fragmentation functions $D_{qi}^h(z)$ in quark cascade models similar to that described in Section 1.4. These models have the common characteristic that the cascade process is a function of only one variable - the fraction of momentum of

the quark carried off by the meson (z), or the fraction of momentum left with the cascade ($\eta = 1-z$), i.e. all models assume Feynman scaling. In general, the models contain several adjustable parameters, and these are obtained by fits to experimental data.

The fragmentation functions $D_u^{\pi^\pm}(z)$ and $D_u^{K^\pm}(z)$ have been calculated in a simple cascade model[66] for a comparison with the hadron distributions produced in deep-inelastic anti-neutrino scattering (in which u quark scattering dominates by virtue of the Cabibbo coupling). However, these results are also relevant to muon scattering, since for reasonably equal quark distributions, u quark scattering should dominate the process by virtue of its charge. The particle ratios $R(\pi^+/\pi^-)$, $R(\pi^+/K^+)$, $R(\pi^+/K^-)$ are calculated in reference 66, where

$$R\left(\frac{\pi^+}{m_i}\right) = \frac{\int_{0.4}^{0.9} D_u^{\pi^+}(z)dz}{\int_{0.4}^{0.9} D_u^{m_i}(z)dz}$$

The ratios $R(\pi^+/K^+)$ and $R(\pi^-/K^-)$ were measured in this experiment and are compared in Table 7.4 with the values given in reference 66 There is remarkable agreement between calculated and measured values, particularly considering the simplicity of the model and the assumption of u quark dominance.

A more intricate model for the calculation of quark fragmentation functions is given in reference 67. In this model, the fragmentation functions are calculated in a quark cascade model assuming:

(a) the probability of forming $q\bar{q}$ pairs in the colour field of a quark 'a' is independent of the flavour of quark 'a'.

(b) SU(3) symmetry is broken - the probability of forming the pair $s\bar{s}$ is half the probability of forming $u\bar{u}$ or $d\bar{d}$ (following a fit to high $P_\perp$ data in pp collisions).

(c) Feynman scaling is assumed to hold.

(d) Quarks are given a mean $P_\perp$ corresponding to the observed transverse-momentum of hadrons - $\langle P_\perp^2 \rangle_{\pi^\pm} = 0.245$, following a gaussian distribution.

(e) Gluons can be neglected.

A comparison at the limits $z \to 1$, and $z \to 0$, and with the calculated value of $\langle P_\perp^2 \rangle^K / \langle P_\perp^2 \rangle$ will be given.

Assumption (b) above leads to the requirement that $D_u^{K^\pm}(z)/D_u^{\pi^\pm}(z) \to \frac{1}{2}$ as $z \to 1$. This does not appear to agree with the observed results, but errors are extremely large in this region and the limit $z \to 1$ is determined mainly by extrapolating low z data. A check on the sensitivity of this limit on the quark content of the proton was made following the prescription of Farrar[69].

$$x\bar{u}(x) = c(1 - x)^{10} \; ; \quad x\bar{d}(x) = c(1 - x)^7$$

$$xs(x) = x\bar{s}(x) = 0.1\,(1 - x)^8$$

$$xu(x) = a + b\sqrt{x} \; ; \quad xd(x) = a + b'\sqrt{x}$$

where $a = 0.17$, $b = 1.69$, $b' = 0.78$, $c = 0.17$.

Calculating these probability distributions for a value of $x = 0.033$, and assuming that in the limit $z \to 1$, the observed meson must contain the struck quark leads to:

$$D^{\pi^+}(z \to 1) = 4\gamma u(x) + 1.\gamma\bar{d}(x)$$

$$D^{\pi^-}(z \to 1) = 1.\gamma d(x) + 4\gamma\bar{u}(x)$$

$$D^{K^+}(z \to 1) = 4(1 - 2\gamma)u(x) + 1.\gamma s(x)$$

$$D^{K^-}(z \to 1) = 4(1 - 2\gamma)\bar{u}(x) + 1.\gamma\bar{s}(x)$$

where γ is the probability of producing a $u\bar{u}$ pair and is 0.4. This gives

$$\frac{K^+(z)}{\pi^+(z)} \xrightarrow[z \to 1]{} 0.51 \quad ; \quad \frac{K^-(z)}{\pi^-(z)} \xrightarrow[z \to 1]{} 0.41$$

$$\frac{K^{\pm}(z)}{\pi^{\pm}(z)} \xrightarrow[z \to 1]{} 0.48$$

Clearly the predictions are insensitive to such a change of input quark distributions.

At low z, the model predicts $D_u^{K^{\pm}}(z)/D_u^{\pi^{\pm}}(z) \to 0.2$ as $z \to 0$. Moreover, as a result of the cascade process and assumption 'a', this relation holds for all quark flavours. The limit at low z is therefore independent of the quark content of the proton. The experimental results give:

$$\frac{K^+}{\pi^+}(z \sim 0.05) = 0.15 \pm 0.03 \quad ; \quad \frac{K^-}{\pi^-}(z \sim 0.05) = 0.11 \pm 0.03$$

The model is therefore in qualitative agreement with the data, although the data would suggest a slightly lower limit than the predicted value of 0.2.

A final comparison is possible with the ratio $\frac{\langle p_1^2 \rangle_{K^{\pm}}}{\langle p_1^2 \rangle_{\pi^{\pm}}}$ predicted in reference 67, with the observed rise in the ratio K/π with P_1 at low z. A fit to the P_1 ratio distributions for $z < 0.3$ of the form $Ae^{bP_1^2}$ gave:

$$A = 0.15 \pm 0.03, \; b = 0.68 \pm 0.4 \text{ for } K^+/\pi^+$$

$$A = 0.10 \pm 0.02, \; b = 0.80 \pm 0.5 \text{ for } K^-/\pi^-$$

Averaging these results gives $\bar{A} = 0.13 \pm 0.02$, $\bar{b} = 0.75 \pm 0.31$. Assuming both pions and kaons to follow a P_1 distribution of the form $Ae^{-P_1^2}$ with the input value of Field and Feynman for $\frac{1}{\alpha_\pi} = \langle p_1^2 \rangle_\pi = 0.245$, (noting that $\bar{b} = \alpha_K - \alpha_\pi$) gives:

$$\frac{\langle p_1^2 \rangle_K}{\langle p_1^2 \rangle_\pi} = 1.22 \pm 0.12$$

The value for this ratio calculated in reference 67, was 1.20. The measured result is therefore in good agreement with the calculated value, although with a large error (reflecting the large errors in the measurement of the slope).

Gluons

The major omission in the fragmentation models described in this section has been the effect of gluon fragmentation on the hadron distributions. This is particularly significant as it has been shown that gluons carry a large fraction of the momentum of the proton. Their effect, however, must be calculated using the full machinery of QCD to calculate hadron distributions[70]. Quantitative comparisons are extremely difficult to compute and are outside the scope of this thesis. However, it is possible to explain the increase in the ratio K/π with $P_\perp$ on a superficial level by considering the gluon contribution. In QCD gluons form an SU(3) symmetric colour octet whose probability of dissociation into $q\bar{q}$ pairs increases with $P_\perp$. As gluons are SU(3) symmetric, they populate $u\bar{u}$, $d\bar{d}$ and $s\bar{s}$ equally, and it is this more 'democratic' population of $s\bar{s}$ at high $P_\perp$ which leads to a relative increase in kaon production.

Summarising, the data exhibits qualitative agreement with both parton model and QCD predictions.

TABLE 7.1

PARTICLE RATIO DISTRIBUTIONS AS A FUNCTION OF Q^2

$0.1 < z < 0.3$

Charge	Q^2 Range $(GeV/c^2)^2$	Raw Data Lit	Raw Data Unlit	Corrected Data Lit	Corrected Data Unlit	K/π
+	1.0-4.0	221	39	228	31	0.14 ± 0.03
-	1.0-4.0	231	42	238	35	0.15 ± 0.03
+	4.0-80.0	260	69	268	61	0.23 ± 0.03
-	4.0-80.0	209	46	215	40	0.19 ± 0.03

$0.3 < z < 0.9$

Charge	Q^2 Range $(GeV/c^2)^2$	Raw Data Lit	Raw Data Unlit	Corrected Data Lit	Corrected Data Unlit	K/π
+	1.0-4.0	20	8	20.6	7.4	0.36 ± 0.15
-	1.0-4.0	20	1	20.6	0.4	0.02 ± 0.04
+	4.0-80.0	25	17	26	16	0.61 ± 0.19
-	4.0-80.0	20	6	21	5	0.24 ± 0.12

TABLE 7.2

COMPARISON WITH DATA OF ASCHMAN ET AL.

	Aschman et al $0.4 < P < 1.0$ GeV/c	Aschman et al $p > 1.0$ GeV/c	This Experiment
f_π	0.87 ± 0.01	0.76 ± 0.02	0.854 ± 0.014
f_K	0.12 ± 0.02	0.16 ± 0.03	0.120 ± 0.027
p	0.0014 ± 0.0005	0.07 ± 0.02	0.026 ± 0.013

TABLE 7.3

COMPARISON WITH DATA OF MARTIN ET AL.

(Function $R(\pi^\pm/K^\pm)$ is Defined in Text)

	Measured	Calculated
$R(\pi^+/K^+)$	2.0 ± 0.5	3.0
$R(\pi^-/K^-)$	6.0 ± 1.9	4.7

Raw Event Distribution, 12·4 < P < 21·2 GeV/c

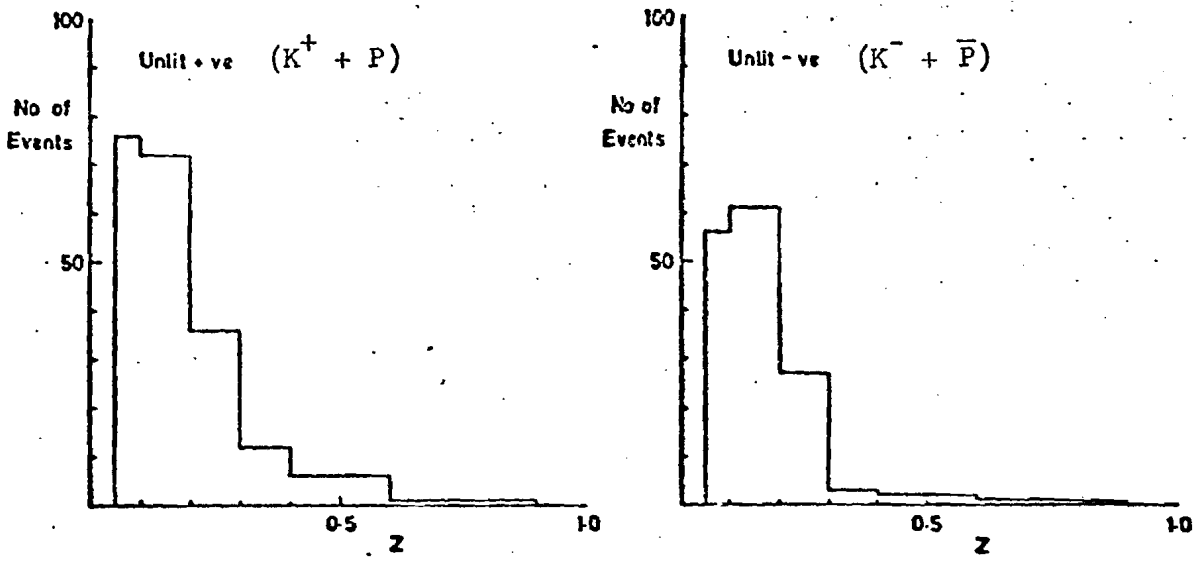

Fig. 7·1

Raw Event Distribution 12.4 < P < 21.2 Gev/c

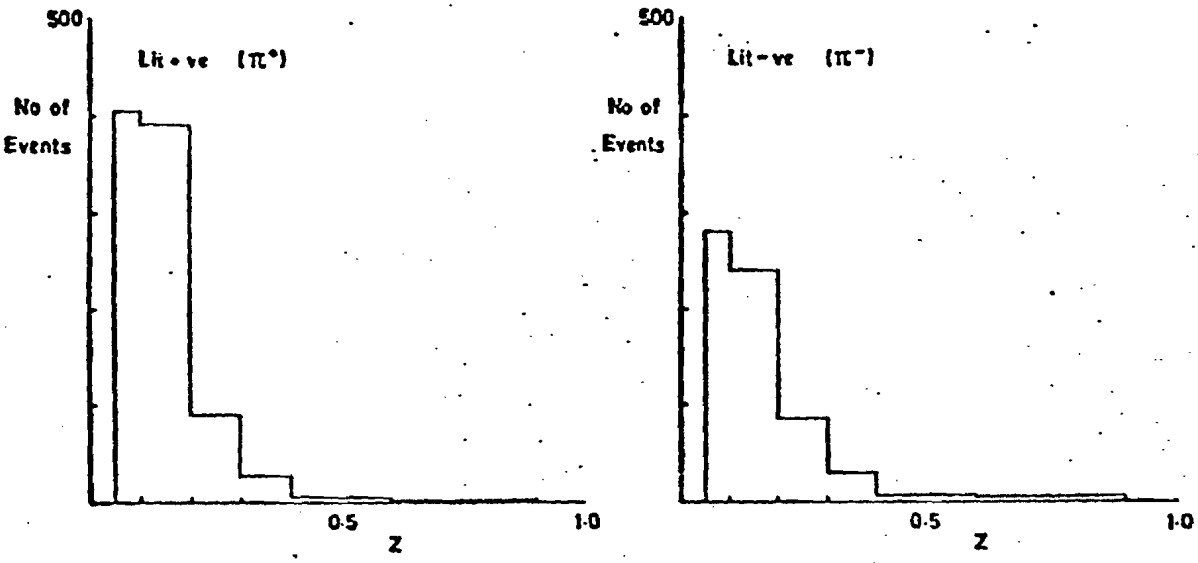

Fig. 7·2

Raw Event Distribution $31.4 < P < 38.2$ Gev/c

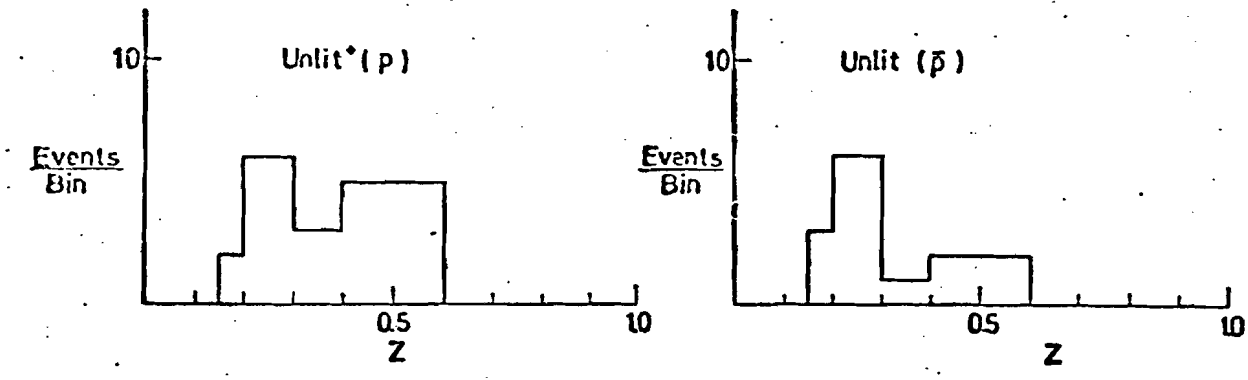

Fig. 7.3

Raw Event Distribution $31.4 < P < 38.2$ Gev/c

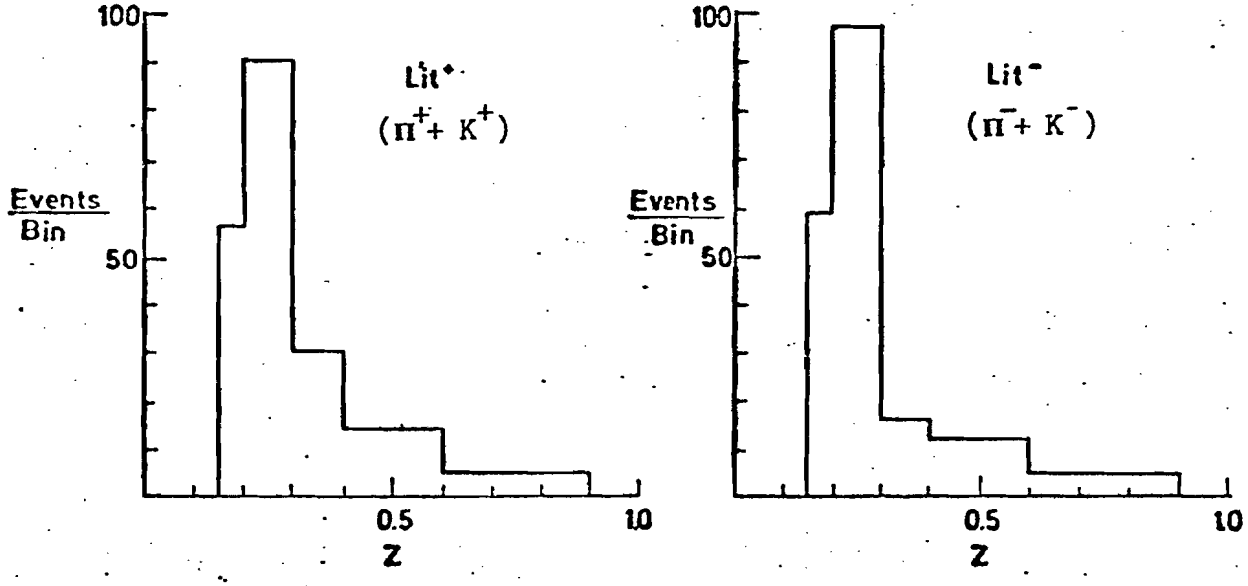

Fig. 7.4

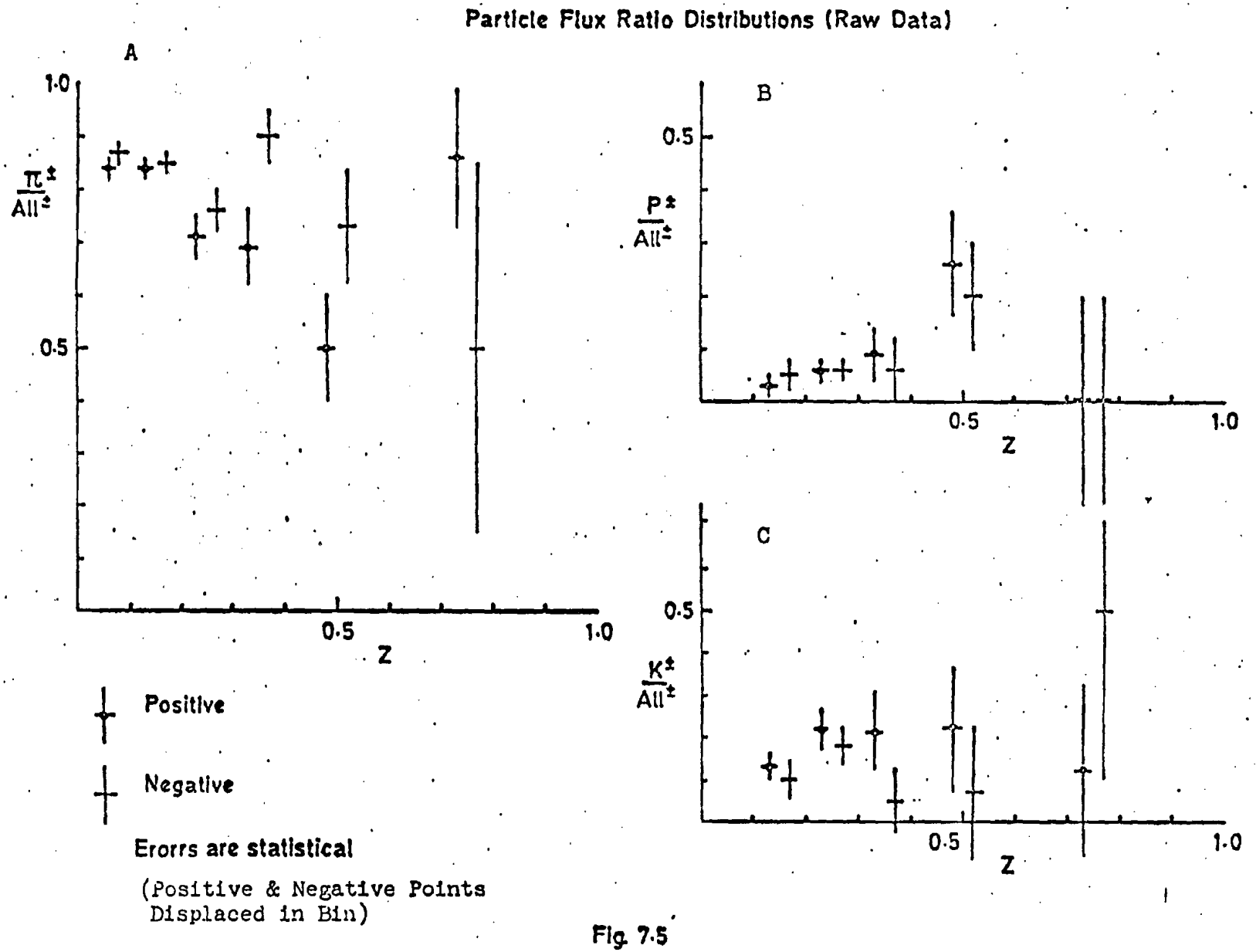
Particle Flux Ratio Distributions (Raw Data)
A
1·0
0·5
$\frac{\pi^{\pm}}{All^{\pm}}$
0·5
1·0
Z
B
0·5
$\frac{P^{\pm}}{All^{\pm}}$
0·5
1·0
Z
C
0·5
$\frac{K^{\pm}}{All^{\pm}}$
0·5
1·0
Z
Positive
Negative
Erorrs are statistical
(Positive & Negative Points Displaced in Bin)

Fig. 7.5

Particle Flux Ratio Distributions (Raw Data)

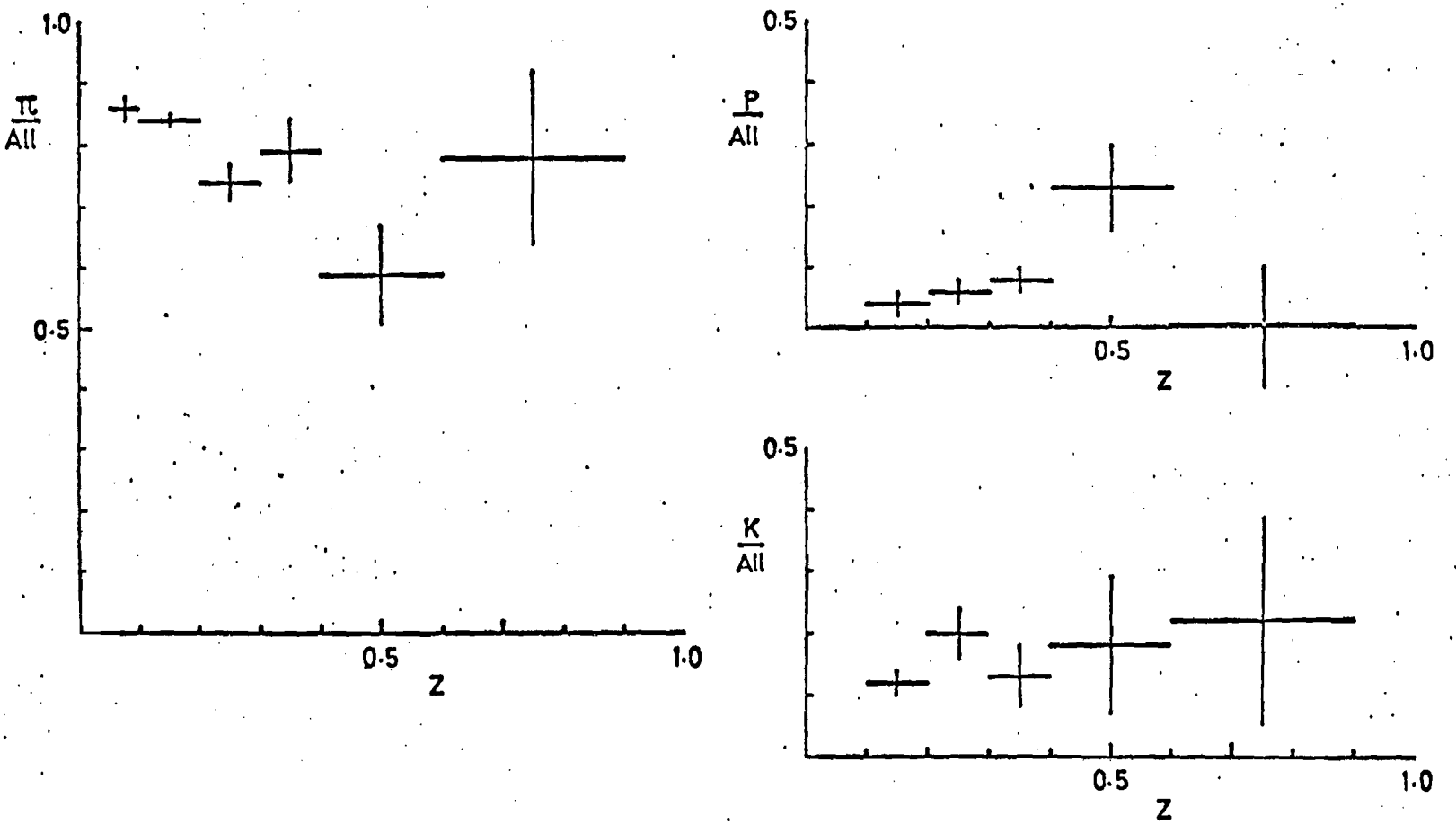

Fig. 7·6

Corrected Event Distributions $12{\cdot}4 < P < 21{\cdot}2$ GeV/c

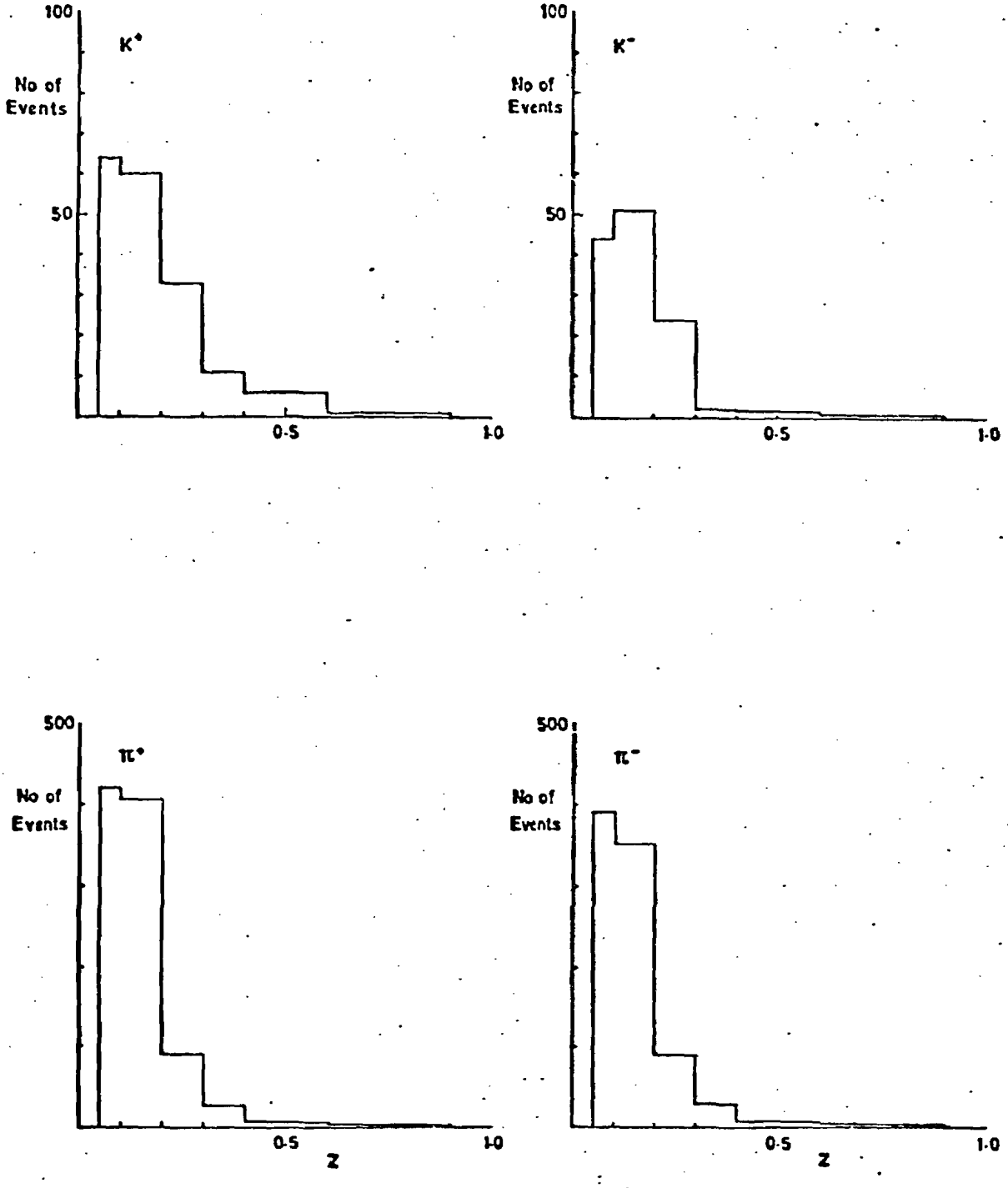

Fig. 7·7

Particle Flux Ratio Distribution, Assuming no p Contribution
(Raw Data)

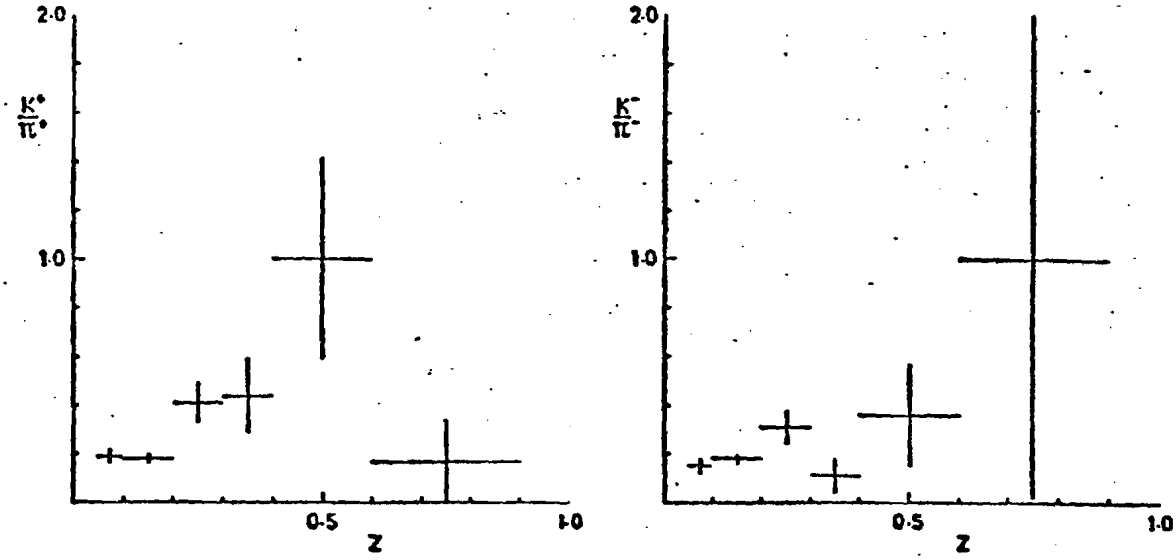

Fig. 7·8

Corrected Particle Flux Distribution, Assuming no P Contribution

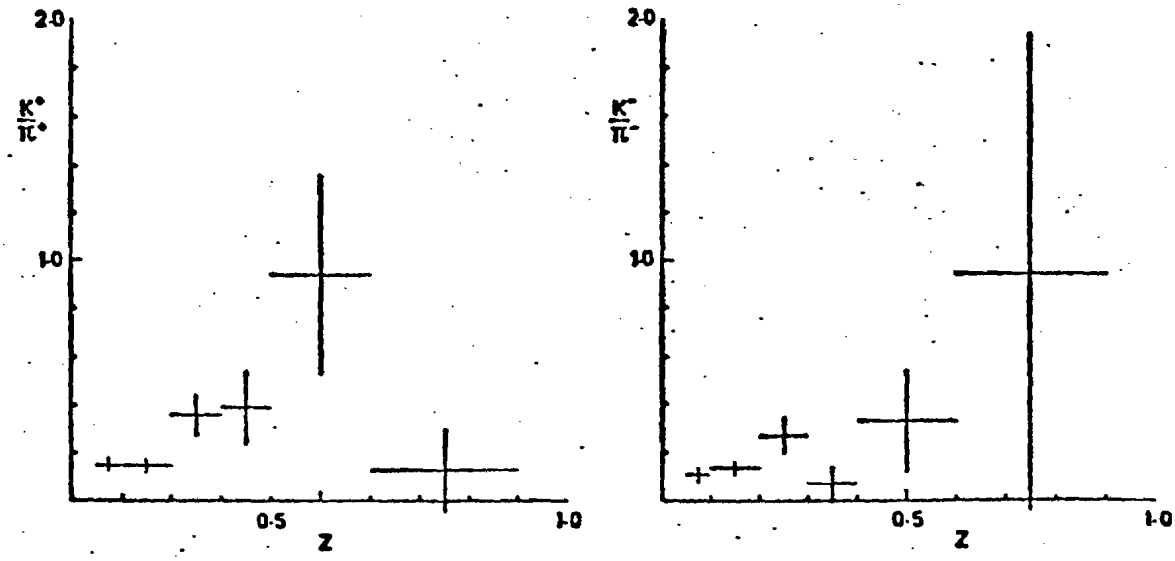

Fig. 7·9

Particle Flux Ratio Distributions, Assuming no p Contribution (Corrected Data)

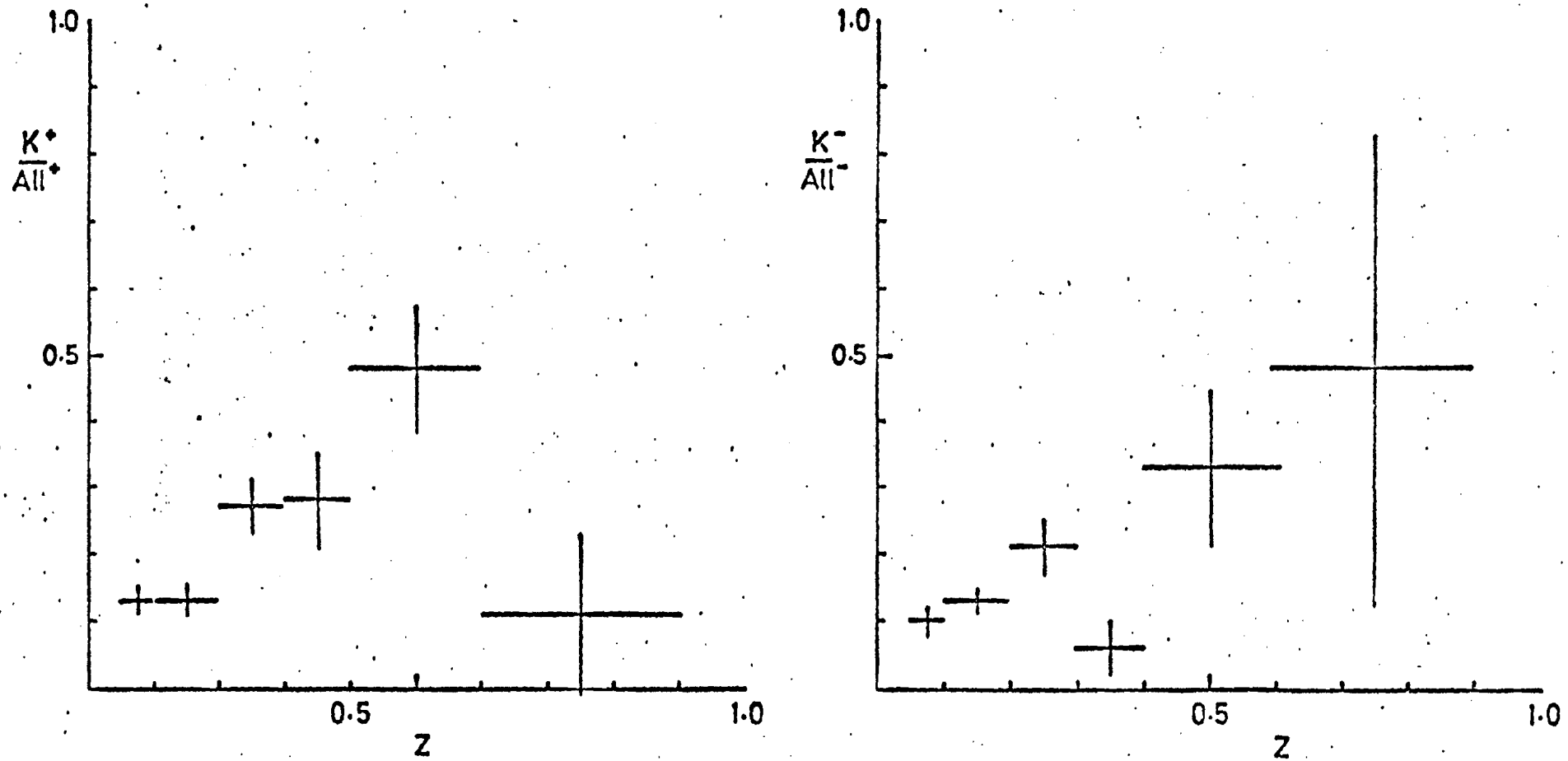

Fig. 7.10

Raw Event Distribution $Z < 0.3$, $12.4 < P < 21.2$ Gev/c

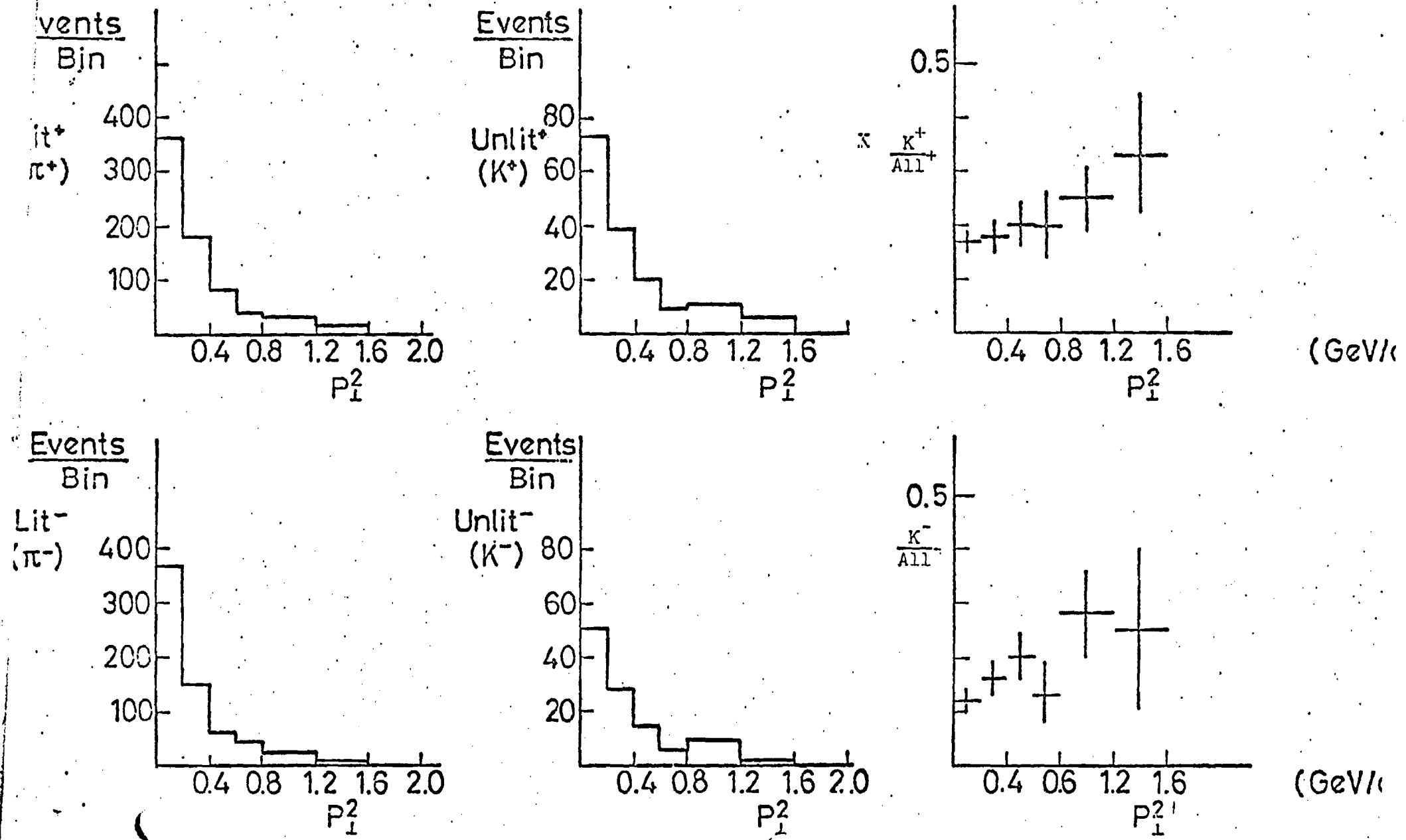

Fig. 7.11

Raw Event Distribution $Z > 0.3$, $12.4 < P < 21.2$ Gev/c

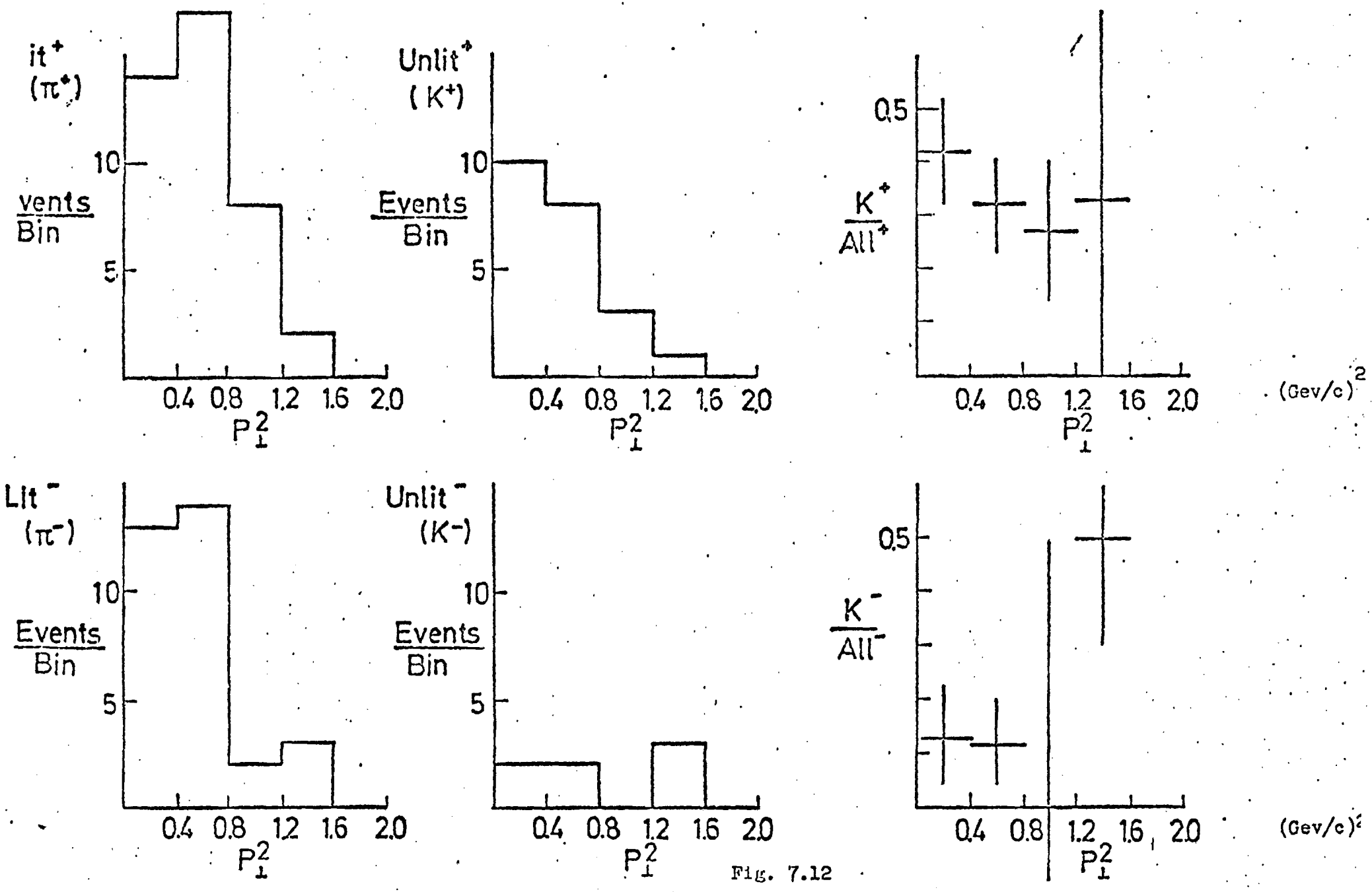

Fig. 7.12

Raw Event Distributions $Z < 0.3$, $31.4 < P < 38.2$ Gev/c

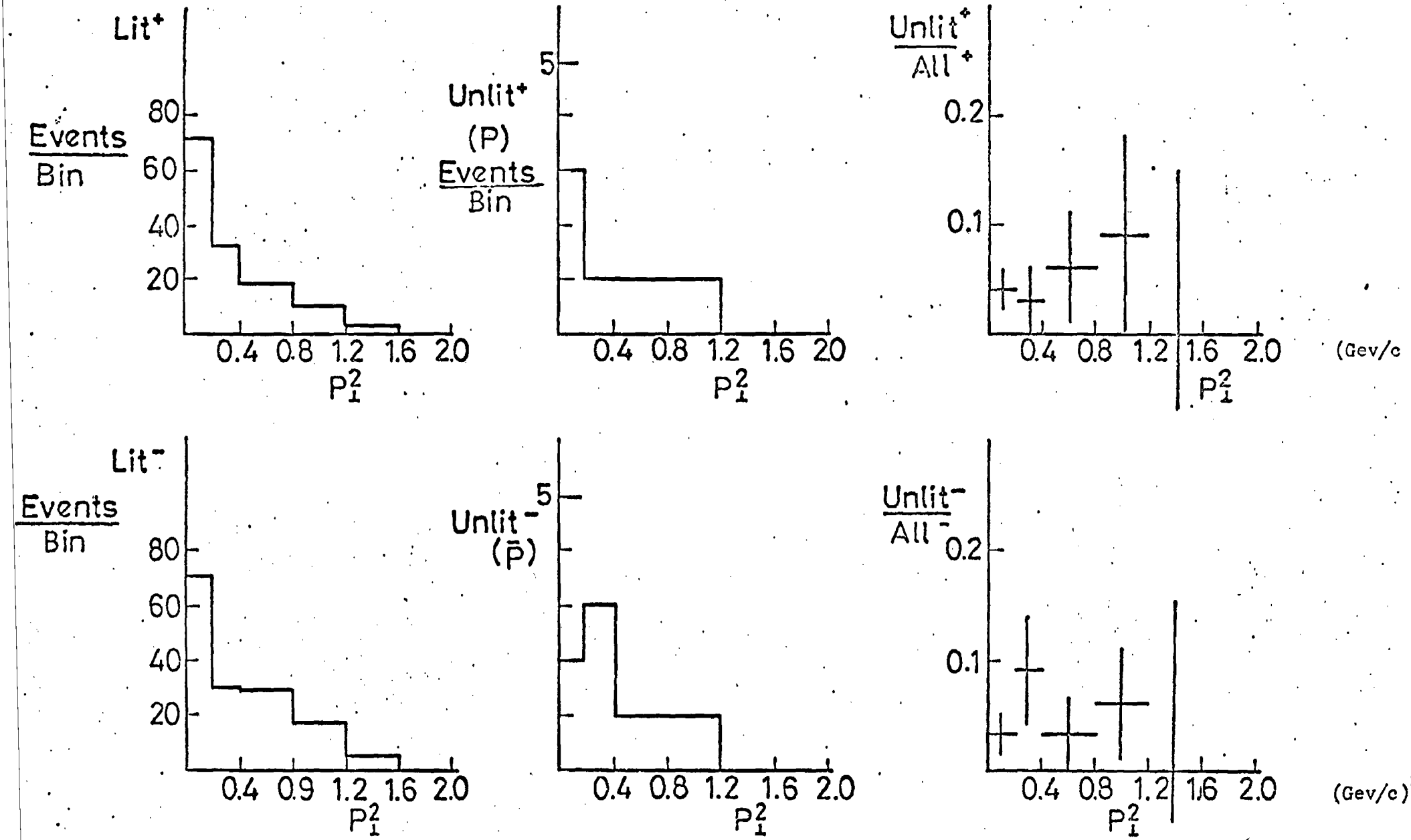

Fig. 4.13

Corrected Event Distribution $Z < 0.3$, $12.4 < P < 21.2$ Gev/c

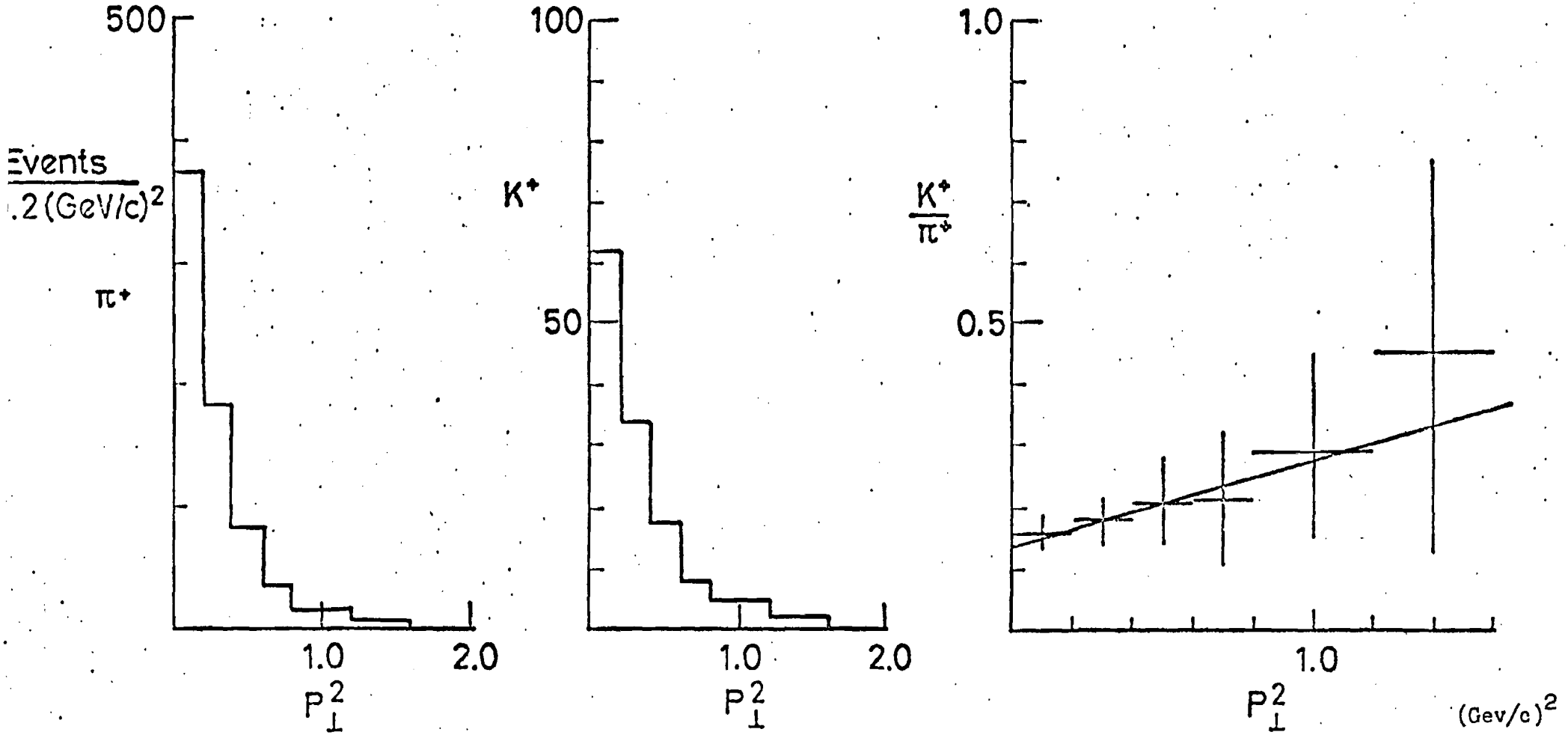

Fig. 7.14

Corrected Event Distribution $Z < 0.3$, $12.4 < P < 21.2$ Gev/c

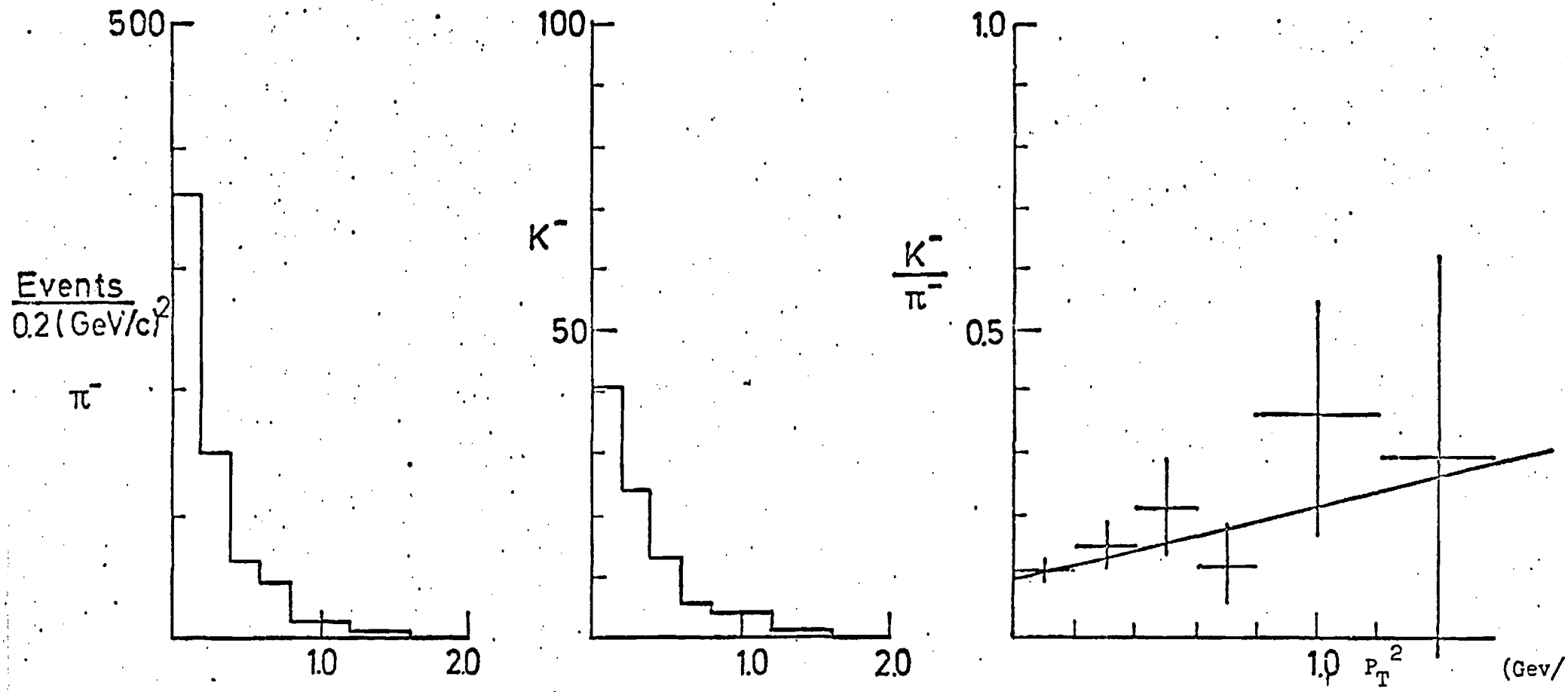

Fig. 7.15

Corrected Event Distributions $Z > 0.3$, $12.4 < P < 21.2$ Gev/c

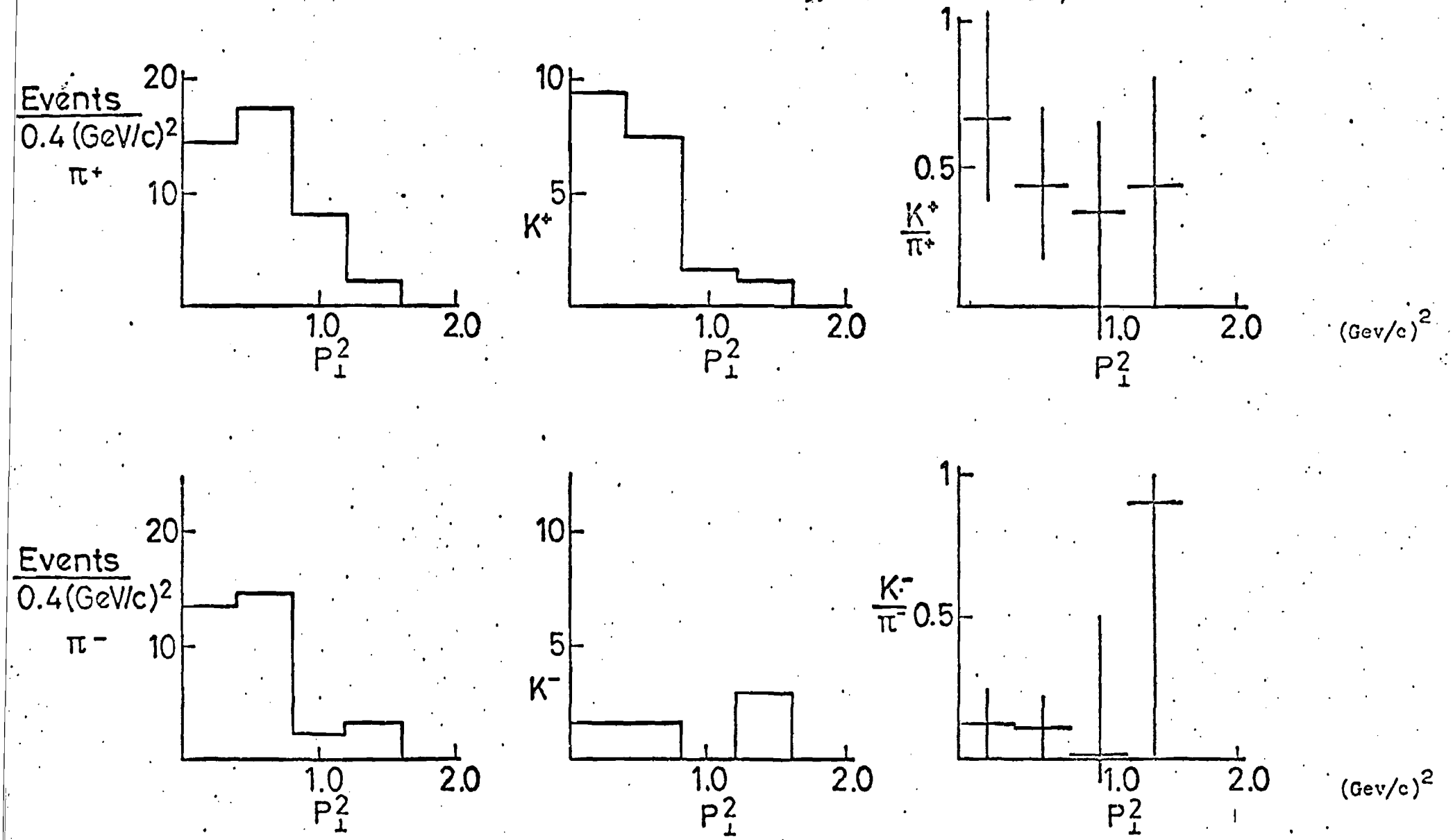

Fig. 7.16

Comparison with Aschman et al

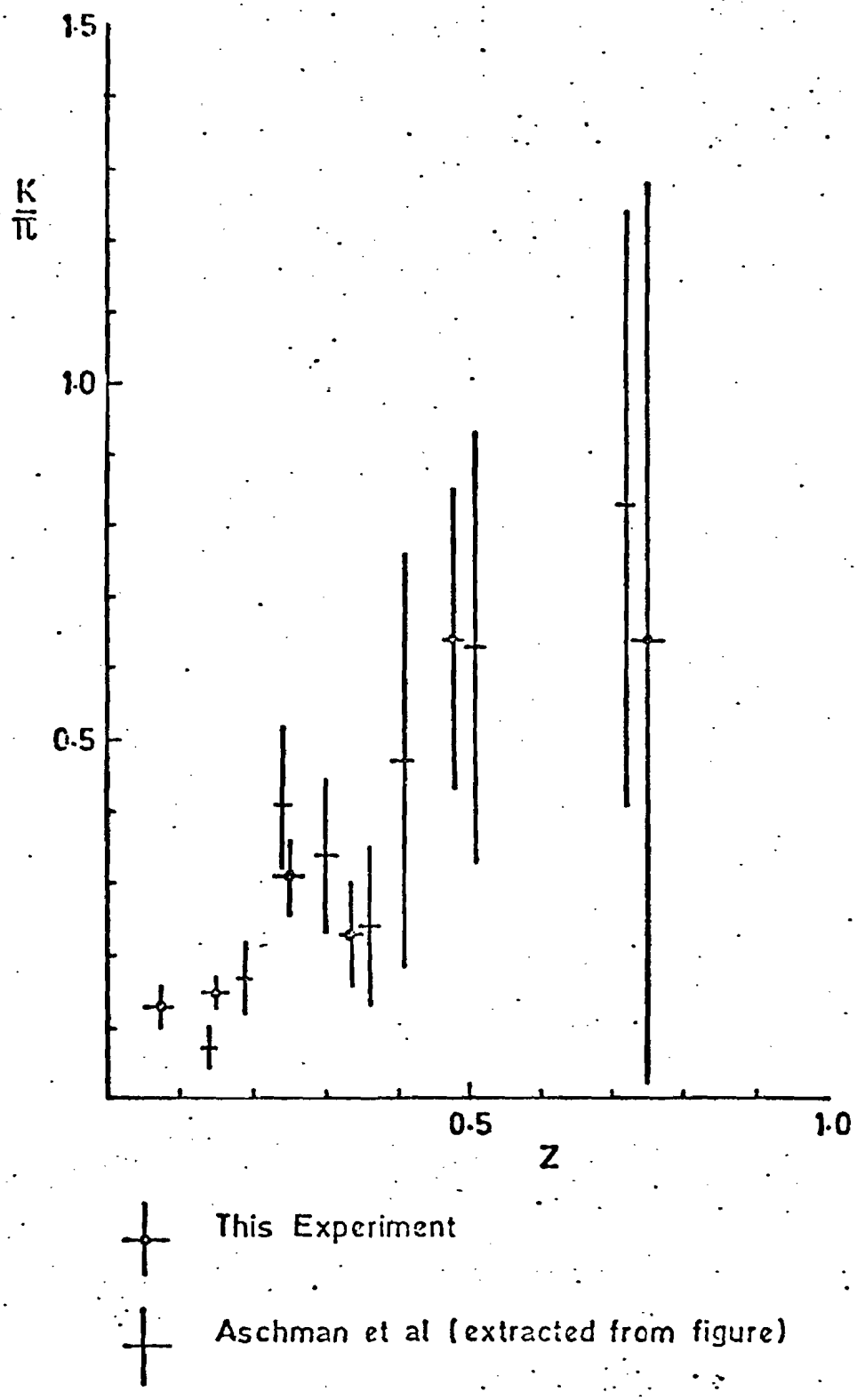

Fig. 7-17

Comparison with Martin et al

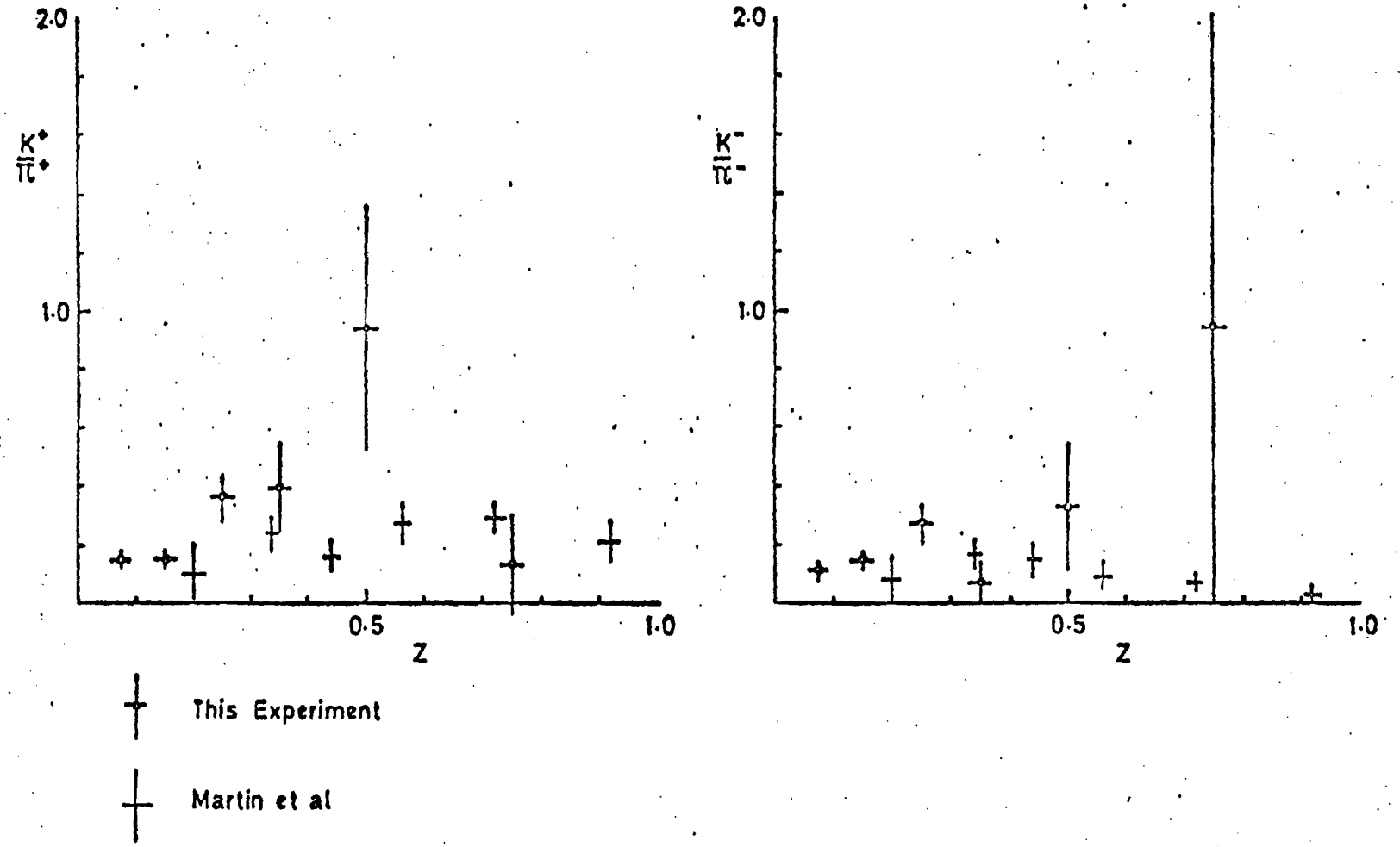

Fig. 7·18

CHAPTER 8

NORMALISATION AND RELATED TOPICS

8.1 INTRODUCTION

In Chapter 6, upper limits on D-meson production were presented in terms of two processes:

$$\mu + p \rightarrow \mu + D + \text{anything}$$

$$\gamma^* + p \rightarrow D + \text{anything}$$

That is to say relative to the total muon cross-section and relative to the virtual photon cross-section. Normalisation to the deep-inelastic cross-section is straightforward and depends simply on the luminosity. However, normalisation to the virtual photon cross-section, particularly at low Q^2 ($Q^2 < 1.0$ $(GeV/c^2)^2$) is more involved as it is necessary to correct for radiative effects, and subtract the contribution from μ-e scattering in order to obtain the true deep-inelastic cross-section. Much of the analysis in this region relied heavily on work by other members of the collaboration which is described in detail in references 9, 38, 43. The principal addition was that of a more reliable scheme for identifying μ-e scatters solely from measurement of the scattering angle and therefore not relying on clear identification of the electron. As an important by-product, it was also possible to extrapolate the deep-inelastic cross-section to the limit $Q^2 = 0$. In addition, the charge on the electron was measured by evaluating the integral

$$\int_0^1 F_2^e(x)\,dx$$

However, the main aim of the analysis was to calculate the total number of deep-inelastic scatters in the regions

$$Q^2_{min} < Q^2 < 1.0 \ (GeV/c^2)^2$$

$$1.0 < Q^2 < 80.0 \ (GeV/c^2)^2.$$

The normalisation to the total muon flux will be given in Section 8.2, and to the virtual photon flux in Section 8.3. Measurement of the charge on the electron, the total μ-e cross-section, and the extrapolation of the virtual photon cross-section to zero Q^2 will be given in Section 8.4

8.2 NORMALISATION RELATIVE TO THE TOTAL MUON FLUX

It was only possible to measure the upper limit on the cross-section for D-meson production within a large range of Q^2 and ν. Therefore, if

$$\frac{d^2\sigma^D}{dQ^2 d\nu}(Q^2,\nu)$$

represents the differential cross-section for D-meson production in deep-inelastic scattering then in general, the number of events observed in any Q and ν range is given by

$$N\ (Q^2_{12},\nu_{12}) = \mathcal{L} C_I \int_{Q_1}^{Q_2} \int_{\nu_1}^{\nu_2} \frac{d^2\sigma^D}{dQ^2 d\nu}(Q^2,\nu)\ A(Q^2,\nu)\ F(Q^2,\nu) dQ^2 d\nu \qquad 8.1$$

where Q_1^2-Q_2^2 = range in Q^2

ν_1-ν_2 = range in ν

$\mathcal{L}$ = the luminosity of the experiment (= incident flux times scattering centres per unit area)

C_I = correction factors independent of kinematic variables

$A(Q^2,\nu)$ = geometric acceptance for both the scattered muon muon and the hadrons produced from the D-meson decay.

$F(Q^2,\nu)$ = a function containing all remaining factors which depend upon kinematic variables.

The true number of events is given by:

$$I = \mathcal{L} \int_{Q_1^2}^{Q_2^2} \int_{\nu_1}^{\nu_2} \frac{d^2\sigma^D}{dQ^2 d\nu} \qquad 8.2$$

and this must be evaluated from Equation 8.1. However, unlike the measurement of the differential cross-section for deep-inelastic scattering, that for D-meson production is greatly simplified, particularly

as the measurement was of an upper limit in a completely specified model. The measurement did not justify the computation required to accurately estimate all factors and where possible, approximations were used.

In D production, only deep-inelastic radiative corrections (Fig. 8.1) and smearing resulting from the finite resolution of the spectrometer need be considered in $F(Q^2,\nu)$. Fig. 8.2 shows the angular resolution and Q^2 resolution obtained using the standard momentum measurement scheme for elastic muon-electron scatters. Equations 4.7 and 4.8 were used to obtain the calculated values of Q^2 and ν. Equation 4.1 gives

$$\delta p = P\delta\theta \qquad 8.3$$

and therefore for momenta below 100 GeV/c, the error is less than 0.5 GeV/c. The standard deviation in Q^2 is 0.034 $(GeV/c^2)^2$ and therefore smearing corrections can be neglected as the Q^2 and ν ranges are large compared to the resolution of the spectrometer. Internal bremmstralung can shift events in the Q^2 and ν plane. However, the Q^2 and ν ranges are large (particularly ν) and therefore this effect will also be neglected.

The model used for the calculation of the D-meson acceptance included no explicit Q^2 and ν dependence. A simple step function on the total centre of mass energy was used to require sufficient energy for production of a $D\bar{D}$ pair. This condition has only a very minor effect at low ν and can be neglected. Therefore, in this model

$$\frac{d^2\sigma^D}{dQ^2 d\nu} = C_2 \frac{d^2\sigma}{dQ^2 d\nu} \qquad 8.4$$

where C_2 is a constant and

$$\frac{d^2\sigma}{dQ^2 d\nu}$$

is the deep-inelastic differential cross-section.

Equation 8.1 therefore reduces to

$$N(Q^2_{12},\nu_{12}) = \mathcal{L} C_I \int_{Q_1^2}^{Q_2^2}\int_{\nu_1}^{\nu_2} C_2 dQ^2 d\nu \int_{Q_1}^{Q_2}\int_{\nu_1}^{\nu_2} \frac{d^2}{dQ^2 d\nu} A(Q^2,\nu) dQ^2 d\nu \qquad 8.5$$

or

$$\frac{N(Q^2_{12},\nu_{12})}{\int_{Q_1^2}^{Q_2^2}\int_{\nu_1}^{\nu_2} \frac{d^2\sigma}{dQ^2 d\nu} A(Q^2,\nu) dQ^2 d\nu} \cdot \frac{1}{\mathcal{L} C_I} = \int_{Q_1^2}^{Q_2^2}\int_{\nu_1}^{\nu_2} C_2 dQ^2 d\nu$$

The acceptance $A(Q^2,\nu)$ can be separated into a product of the acceptance of scattered muon with that of hadrons produced from the decay of the D-meson.

$$A(Q^2,\nu) = A_M(Q^2,\nu) . A_D(Q^2,\nu) \qquad 8.6$$

The acceptance for the scattered muon is given in Figure 8.3. In the low Q^2 region ($Q^2 < 1.0$ (GeV/c)^2, $170 < \nu < 200$ GeV). The acceptance is 100% for most of the range. Therefore, no significant error will be introduced by taking the approximation $A_M(Q^2,\nu) = 1$ in this region. The position at high Q^2 is more complicated as there are large variations in acceptance over the Q^2,ν plane, and in addition to the differential cross-section, the effect of the analysis cut $x_{Bj} < 0.1$ must also be considered. The Q^2 and ν analysis cuts used were:-

$2.0 < Q^2 < 80.0$ (GeV/c^2)^2, $10 < \nu < 200$ GeV

$1.0 < Q^2 < 2.0$ (GeV/c^2)^2, $10 < \nu < 200$ GeV

Observed event distributions are shown in Fig. 8.4a. Clearly a large fraction of the low Q^2, low ν region will be removed by the x_{Bj} cut. At high ν both the acceptance and the event distribution are slowly varying as functions of Q^2 and therefore a reasonable approximati would be to pick a central value in this region and again consider $A_M(Q^2,\nu)$ as constant. The acceptance of 0.85 in the region $Q^2 \sim 3$ (GeV/c^2)^2, $\nu \sim 170$ GeV was chosen and should introduce at most a systematic error

of 10% in the normalisation. The quantity

$$I_1 = \int_{Q_1^2}^{Q_2^2}\int_{\nu_1}^{\nu_2} \frac{d^2\sigma}{dQ^2 d\nu} A(Q^2,\nu)\, dQ^2 d\nu$$

in Eqn. 8.5 therefore reduces to

$$I_1 = A_M \int_{Q_1^2}^{Q_2^2}\int_{\nu_1}^{\nu_2} \frac{d^2\sigma}{dQ^2 d\nu} A_D(Q^2,\nu)\, dQ^2 d\nu \qquad 8.7$$

$A_D(Q^2,\nu)$ is dependent on the model used to generate a D-meson and its decay products. The integral I_1 was calculated using the Monte-Carlo technqiue described in Chapter 6. For the region $Q^2 < 1.0$ $(GeV/c^2)^2$, A_M has the value 1.0 and for region $1 < Q^2 < 80$ $(GeV/c^2)^2$ A_M takes the value 0.85.

As was discussed in Section 4.6, inefficiency in the spectrometer and analysis routines (clearly independent of kinematics) can be considered as an effective reduction in flux by an amount 0.549 ± 0.01. These are the only factors which are independent of kinematics and therefore the constant C_I also has the value 0.549 ± 0.01. In Chapter 6, upper limits were calculated in terms of the quantity

$$N' = \frac{N(Q_{12}^2,\ \nu_{12})}{\int_{Q_1^2}^{Q_2^2}\int_{\nu_1}^{\nu_2} \frac{d^2\sigma}{dQ^2 d\nu} A_D(Q^2,\nu)\, dQ^2 d\nu} \qquad 8.8$$

which is the calculated number of events in Q^2 and ν range from D-meson production given that the scattered muon has been accepted by the spectrometer. The normalisation is therefore (taking $C_2 = 1$) determined by the effective luminosity

$$\mathcal{L}' = A_M C_I = A_M C_I . B\rho_H . \ell N_A \qquad 8.9$$

where

B = total muon flux

ρ_H = density of liquid hydrogen (0.0708 gm/cm^2)

ℓ = target length (120 cm)

N_A = Avogadros number

The data sets used in the analysis contained an integrated flux $B_1 = 7.45 \times 10^{10}$ and $B_2 = 3.95 \times 10^{10}$. The effective luminosity at low Q^2 is therefore:

$$\mathcal{L}_1 = 2.09 \times 10^{35}$$

$$\mathcal{L}_2 = 1.11 \times 10^{35}$$

and at high Q^2

$$\mathcal{L}_1 = 1.78 \times 10^{35}$$

$$\mathcal{L}_2 = 0.94 \times 10^{35}.$$

The cross-section per event ($\frac{1}{\mathcal{L}}$) is given in Table 8.1

It should be noted that no target empty subtraction could be carried out as no D-meson signal was observed. This subtraction can also be considered partially as reduction in flux and its omission leads to a possible systematic error in the cross-section estimated at 5%.

8.3 NORMALISATION RELATIVE TO THE VIRTUAL PHOTON CROSS-SECTION

The number of deep-inelastic scattering events observed in each of the kinematic regions of the D-meson analysis gives the normalisation relative to the virtual photon cross-section. In the model used to simulate D-meson production the differential cross-section for D production is simply a fraction of the deep-inelastic differential cross-section above threshold (Section 8.2). Therefore, the ratio n_D/n_I (the contribution to deep-inelastic scattering from D production) is independent of the scattered muon acceptance, where n_D is the calculated number of D-mesons produced in the kinematic region given that the scattered muon was accepted by the spectrometer and n_I is the number of deep-inelastic events observed in the spectrometer in that kinematic region. n_D is obtained from Equation 8.8 and as we have seen was calculated in a plausible model using a Monte-Carlo method in Chapter 6. Extraction of n_I is not straightforward as it requires careful consideration of the contributions from several processes to the observed cross-section and will be discussed in some detail.

If σ is taken to represent the differential cross-section for some process (or equally the number of events in a given Q^2 and ν range resulting from that process) then the observed cross-section can be written as

$$\sigma_{obs} = \sigma_{DI} + \sigma_{MT} + \sigma_{ER} + \sigma_{IR} + \sigma_{ME} \qquad 8.10$$

where

σ_{obs} = observed cross-section

σ_{DI} = true deep-inelastic cross-section

σ_{MT} = empty target background

σ_{ER} = elastic radiative tail contribution to the cross-section.

σ_{IR} = deep-inelastic radiative tail correction

σ_{ME} = elastic muon-electron scattering cross-section.

Clearly the contribution from each of the above corrections depends on the kinematic region. Extraction of the true deep-inelastic cross-section for the data analysed in this thesis is described in refs. 9 and 43 for values of Q^2 above 1.0 (GeV/c^2) . The results obtained were the basis of the analysis described here to obtain normalisation factors for the D-meson cross-section limits and brief discussion of the procedure used will be given. Extension of the results to low Q^2 was required where μ-e scattering is an important process and the procedure used to remove the μ-e background will be given.

σ_{DI} This is clearly the required cross-section and therefore Equation 8.10 must be inverted to obtain it.

σ_{MT} This is background associated with scatters outside the target flask and general fake events resulting from halo triggers. Special runs were carried out with the target empty to estimate this background. Triggers for a total flux of 7.45×10^{10} muons were obtained (Fig. 8.5). Correction for the effect of hydrogen vapour in the flask corresponded to a reduction in flux of 0.977.

σ_{ER} Elastic μ-p scattering can populate deep-inelastic regions of the Q^2,ν plane if the muon also emits a photon (or photons) either before, during or after interacting with the proton. Photon emission before or after the interaction is termed "straggling" and emission during the interaction "internal bremmstrahlung" (Fig. 8.1). This contribution to the observed cross-section is referred to as the "elastic radiative tail".

Processes in which two or more photons are emitted are suppressed by additional powers of α and the contribution σ_{ER} was calculated exactly using the method of Mo and Tsai[71] assuming single photon emission. The measured values of the proton elastic form factors were used in this procedure to generate a table of numbers of events in

appropriate Q^2 and ν bins resulting from the elastic radiative tail (Fig. 8.6).

σ_{IR} In a similar way to the elastic radiative tail, straggling or internal bremmstrahlung during an inelastic interaction will shift the observed values of Q^2 and ν from their true values. Given the true deep-inelastic cross-section it is possible to obtain the radiated cross-section. However, the reverse process is not straightforward. The iterative procedure of Mo and Tsai was used to generate a table of correction factors η for an array of points in the Q^2,ν plane (Fig. 8.7) where

$$\eta = \frac{\text{True Deep-Inelastic Cross-Section}}{\text{Measured Deep-Inelastic Cross-Section}} \qquad 8.11$$

and

Measured Deep-Inelastic Cross-Section =

[Observed Cross-section - Calculated Elastic Radiative Tail]

Basically, this method starts with a guess for the structure functions which are then used to calculate the true deep-inelastic cross-section (True) and radiatively degraded deep-inelastic cross-section (Rad). This then provides initial values for $\eta = \frac{\text{True}}{\text{Rad}}$ which are then used to correct the observed cross-section to the true observed deep-inelastic cross-section. This is then fitted to the structure functions until no significant change is observed. The inelastic structure functions measured in earlier data[17] were used as starting values and only a single iteration was required.

The details of the procedure used to obtain the above radiative corrections can be found in references 37, 42,43.

ME The kinematics for elastic muon-electron scattering are completely specified (Eqns. 4.7 and 4.8). However, as was seen in Fig. 8.2 the finite resolution of the spectrometer causes a smearing in the measurement of the scattering angle and in Q^2. Muon-electron

scattering events therefore populate a large fraction of the Q^2 range below $Q^2 = 1(GeV/c^2)^2$ but can be neglected above this.

Routines which tracked particle trajectories through the spectrometer magnet using the complete field map were developed for the analysis of tracks found in the MWPCs positioned in the magnetic field[38] (referred to in future as the "Illinois trackfinding analysis"). These provided better angular resolution than the standard programs and were used to improve the angular resultuion of the scattered muon track (Fig. 8.8). The improved measurement of Q^2 resulting from this restricted the range of Q^2 populated by muon-electron scatters to less than 0.08 $(GeV/c^2)^2$ compared with roughly 0.13 $(GeV/c^2)^2$ in the standard analysis. The scheme used was: identify μ-e events using Q^2, θ_S and event signature; estimate the efficiency of the identification scheme; remove μ-e events from the data then correct for inefficiency on a bin-by-bin basis. The improved Q^2 resolution therefore restricted large corrections to a few bins. In addition, it enabled an accurate estimate of the filter efficiency to be made.

Muon-Electron Filter

Elastic μ-e scatters were selected on the basis of the following criteria:

1. A muon plus one negatively charged "hadron" downstream of the C.C.M.
2. Energy Imbalance $(1 - \frac{E_{had}}{\nu})$ less than 0.1
3. The transverse momentum of the "hadron" relative to the virtual photon less than 0.2 GeV/c.
4. At most three tracks in either x or y views upstream with $n_{Tx} \cdot n_{Ty} > 2$ where n_{Tx} and n_{Ty} are the numebrs of x or y tracks respectively.

Figures 8.9-8.11 show raw event distribution as a function of Q^2 before and after subtraction of events identified by the filter. The μ-e elastic peak is clearly visible, as is the fact that the filter is considerably less than 100% efficient.

The efficiency of the filter was estimated from the range ν = 170-180 GeV where the μ-e peak falls largely in the range $0.15 < Q^2 < 0.20$ $(GeV/c^2)^2$. The main problem is the fact that the bins on either side also contain a large number of μ-e events and therefore a simple background subtraction seems impossible at first. However, in this region, the μ-e elastic cross-section is clearly very much larger than the deep-inelastic cross-section (up to a factor of 20). Therefore, assuming a reasonably slow variation of the deep-inelastic cross-section in this region (Chapter 8.4) the efficiency of the filter can be measured from the signal remaining in the bins 0.15-0.20 $(GeV/c^2)^2$ relative to the mean level in the bins on either side (predominantly also μ-e). The background was taken as the average of the contents in bins 0.125-0.15 $(GeV/c^2)^2$ and 0.20-0.225 $(GeV/c^2)^2$ and was estimated to be 1400 events with the filter "on" and 2600 events with the filter "off". The filter efficiency was measured to be $\varepsilon_{\mu e} = 0.75 \pm 0.04$. The major systematic error would appear to be in the estimate of the background with the μ-e filter on, where the variation between the two bins is large. A systematic error of 15% in the measurement of the background with the filter on was added in quadrature with the statistical error.

Equation 8.10 can now be re-written as

$$\sigma_{DI} = (\sigma_{obs} - \sigma_{ER} - \sigma_{ME} - \sigma_{MT}) . \eta \qquad 8.12$$

where σ now represents the number of events in the appropriate region of Q^2 and ν. It is possible to correct for acceptance if required by instead calculating

$$\sigma_{DI} = (\sigma_{obs} - \sigma_{ME} - \sigma_{MT}) \cdot \frac{\sigma_{calc}}{(\sigma_{calc} + \sigma_{ER})} \cdot \eta \qquad 8.13$$

where σ_{calc} is the calculated true number of events in the region. However, as was seen in Section 8.2 the acceptance in the two regions considered is relatively uniform. Therefore since the limits on D production were quoted given that the scattered muon was accepted, this acceptance cancels and Equation 8.12 can be used to calculate the correct normalisation.

σ_{MT} and σ_{ER} can be obtained directly from Figures 8.5 and 8.6 by summing events in the required kinematic region. An appropriate expression for η can be used to correct for deep-inelastic radiative effects. Correction for μ-e scattering can be obtained by analysing the data with the filter on and with it off to obtain

$$\sigma_{ME} = \frac{(n_{OFF} - n_{ON})}{\epsilon_{\mu e}} \qquad 8.14$$

for the low Q^2 region

Normalisation for Region Q^2 = 1.0-80 $(GeV/c^2)^2$

As can be seen from Fig. 8.6 the contribution from elastic radiative tail can be neglected in this region, as can that from μ-e scatters. Equation 8.11 therefore reduces to

$$\sigma_{DI} = (\sigma_{obs} - \sigma_{MT})\eta$$

σ_{MT} was obtained from the observed target empty events weighted by a factor 7.5 to account for the relative fluxes between full and empty data sets. An approximate parameterisation of the deep-inelastic radiative correction table was used (Table 8.2). σ_{DI} was then obtained by the net sum of events with $x_{Bj} < 0.1$ weighted accordingly. For the full data set this was measured to be 8885 events (for a total flux of 7.45×10^{10} μ's).

For the data set in which Cerenkov information was available this number was measured to be 4728 events (for a total flux of 3.85×10^{10} μ's). The average deep-inelastic radiative correction was 0.865.

Normalisation for the Region $Q^2 = Q^2_{min} - 1.0$ $(GeV/c^2)^2$

In this region the full expression for σ_{DI} (Eqn.. 8.12) must be used. However, some simplification results from the restricted ν range, 170-200 GeV.

Event distributions obtained with and without subtraction of μ-e events identified by the filter are shown in Fig. 8.4. It is clear that the vast majority of the deep-inelastic contribution to this kinematic region lies in the Q^2 range 0.1-0.2 $(GeV/c^2)^2$. The deep-inelastic radiative correction is reasonably uniform in this region and the value of η used was its average value - 0.857. As all events in this region have $x_{Bj} < 0.1$ the numbers σ_{obs}, σ_{ER} and σ_{MT} were simply obtained by summing from Figs. 8.4-8.6:

σ_{obs} = 49794 events

σ_{ER} = 9810

σ_{MT} = 24650 (corrected for flux)

Figures 8.12-8.14 show the effect of the μ-e filter in finer binning. The shape of the distributions for events removed at low Q^2 indicates that the filter is removing some real events. The total number of μ-e events was therefore obtained from the sum of events removed by the filter in the range Q^2 = 0.1-0.3 $(GeV/c^2)^2$ giving a total number of identified μ-e's of 16982 in the region ν = 170-200 GeV. This therefore gives (Eqn.. 8.14)

$$\sigma_{ME} = 5661 \text{ events}$$

Equation 8.12 can now be used to give the required normalisation to the virtual photon cross-section

σ_{DI} = 8290 events (for a total flux of 7.45 x 10^{10} μ's).

This can then be scaled to give the corresponding normalisation for the second data set

σ_{DI} = 4398 events (for a total flux of 3.95 x 10^{10} μ's).

The results of this section are summarised in Table 8.3.

8.4 TOPICS RELATED TO THE CROSS-SECTION AT LOW Q^2

The use of a reliable μ-e filter, and more particularly the compression of the μ-e elastic peak into a very small range of Q^2 allowed extrapolation of the cross-section to $Q^2 = 0$. In addition, as a check on possible systematics, the criterion for μ-e scattering

$$M_e = \frac{Q^2}{2\nu}$$

could be used to check the momentum calibration of the Illinois track-finding analysis. An estimate of $\int_0^1 F_2 dx$ for the electron and the total μ-e cross-section could also be made. These three measurements will be described in this section.

Extrapolation of the Cross-Section to Zero Q^2

The analysis routines described in reference 43 calculated the virtual photon cross-section down to Q^2_{min}. However, as the standard momentum analysis did not allow an accurate estimate of μ-e contamination, an estimate of the cross-section below $Q^2 = 1$ $(GeV/c^2)^2$ was not quoted. The use of the 'Illinois' trackfinding routines with their superior resolution both confined μ-e contamination to a small range in Q^2 and allowed an accurate estimate to be made of the μ-e contamination resulting from inefficiency in the filter. It was then a simple matter to correct for this contamination as before and extrapolate the cross-section to zero Q^2.

Limited statistics prevented an investigation as a function of W^2 in the fine Q^2 binning required to allow accurate extrapolation. Table 8.4 presents the values of the cross-section integrated over the range W^2 = 319-375 GeV^2 obtained with and without use of the μ-e filter. The parameterisation of Brasse[72] was used to remove resonance contributions from the elastic radiative tail. Correction for the filter

inefficiency was made according to the prescription

$$\sigma_{corrected} = \sigma_{ON} - \frac{(1 - \varepsilon_{\mu e})}{\varepsilon_{\mu e}} (\sigma_{OFF} - \sigma_{ON})$$

As the values of σ_{OFF} and σ_{ON} come from essentially the same data sets, their difference should not depend on the statistical errors in σ_{OFF} and σ_{ON}. The error in the difference was neglected and the statistical error in σ_{ON} combined in quadrature with that in $\varepsilon_{\mu e}$ to give the error in the corrected cross-section.

The corrected values of the cross-section are shown in Fig. 8.15. The curve is a fit to the form

$$\sigma(\nu, Q^2) = A(\nu)\left(\frac{1}{1 + Q^2/\Lambda^2}\right) \mu\text{barns}$$

in the range $Q^2 = Q^2_{min}$ - 0.4 $(GeV/c^2)^2$. The values obtained were

$$A = 132 \pm 13 \ \mu\text{barns}$$

$$\Lambda^2 = 0.09 \pm 0.03 \ (GeV/c^2)^2$$

giving a chisquared of 11.3 for 10 degrees of freedom.

Following the alternative description of deep-inelastic scattering in which the muon beam is considered a source of virtual photons (Chapter 1.1) the virtual photon cross-section is given by

$$\sigma_{meas} = \sigma_T(1 + (\varepsilon + \delta)R)$$

where $R = \sigma L/\sigma_T$

$$= \frac{2M^2\mu}{Q^2}(1 - \varepsilon)$$

$$= \frac{1}{1 + \frac{2(Q^2 + \nu^2)\tan^2\theta/}{Q^2(1 - Q^2_{min}/Q^2)}}$$

For the region of interest (ν = 170-200 GeV) the mean value of Q^2_{min} is 0.0516. At $Q^2 = Q^2_{min}$ $\varepsilon = 0$ and $\delta = 0.435$.
Typical values obtained for R are [8, 9] $R_{min} = 0.25$, $R_{max} = 0.44$ giving $\sigma_T(0)$ = 119 ± 13 μb and 111 ± 13 μb respectively.

These results are in good agreement with the total photon cross-

section at this energy[73] which is 118 ± 0.5 μbarns.

Momentum Calibration of the Illinois Analysis

The calibration of the Illinois analysis can be checked using the μ-e scatters selected by the filter which should satisfy the relation $Q^2 = 2 m_e \nu$.

The Q^2 distributions of events selected by the μ-e filter in three ν ranges are shown in Figures 8.12-8.14. The elastic μ-e peak is clearly visible. From the shape of the distributions above $Q^2 = 0.2$ $(GeV/c^2)^2$ (expected to be approximately gaussian) it is apparent that the filter is selecting some deep-inelastic events below $Q^2 = 0.15$. The means of the distributions were taken in the ranges indicated to exclude this region. The results obtained are shown in Table 8.5 and show excellent agreement with the measured value of m_e ($\sim$0.511 MeV/c^2) from the measured mean value of Q^2 and the bin centre value of ν. The main source of errors are the measurement of ν and its spread within each bin (3% maximum) and the statistical error of 1.3% in the mean value of Q^2 in each range. Measurements in the three ranges were combined in quadrature to obtain an average value of $m_e = 0.505 \pm 0.011$ MeV/c^2. This result therefore confirms that the alignment of the Illinois trackfinding routines with the experimental coordinate system to within 1%.

Measurement of the Charge of the Electron

At the current time, all experimental evidence supports the fact that the electron is a point particle[2]. Therefore, for μ-e scattering the integral of the structure function $F_2^2(x)$ yields the $(\text{charge})^2$ of the electron i.e. (from Eqn. 1.8)

$$e^2 = \int_0^1 F_2^e(x) \left(x - \frac{Q^2}{2\nu}\right) dx = 1$$

in units where $e = h = c = 1$.

Any deviation from the expected value of 1 would imply internal structure in the electron.

Structure functions were evaluated using the procedure described in reference 43 with the only change being the use of the Illinois trackfinding to obtain improved resolution of the scattered muon. There are two problems which must be considered:

1. Results were obtained as a function of $x^{p}_{Bj} = \frac{Q^2}{2M_p \nu}$ where M_p = proton mass. Therefore, a correction factor $\frac{M_p}{M_e}$ must be applied to obtain x^{e}_{Bj}.

2. Deep-inelastic radiative corrections have been applied to all events and to obtain the cross-section, therefore the cross-section must be re-corrected to remove these. The average value of η in the region of interest (Q^2 = 0.125-0.225 $(GeV/c^2)^2$, ν = 170-200 GeV) is 0.860 with a variance $\sigma^2 = 1.27 \times 10^{-3}$ corresponding to a mean deviation of 3.5%. The deep-inelastic radiative correction factor is very uniform in this region and its effect can be removed quite accurately by multiplying the measured value of $\int_0^1 F_2 dx$ by $\frac{1}{0.86}$.

The scheme used to extract $F_2^e(x)$ essentially inverts the procedure used to remove μ-e background from deep-inelastic cross-section. The results obtained are shown in Table 8.6. The corrected electron structure function values in the x ranges were obtained simply from

$$F_2^e(x) = \frac{(F_2^{OFF}(x) - F_2^{ON}(x))}{\epsilon_{\mu e}}$$

using the value of $\epsilon_{\mu e}$ measured in Section 8.3. The error in $\epsilon_{\mu e}$ was combined in quadrature with the statistical errors in F_2^{OFF} to obtain the error in F_2^e.

Again as in Section 8.3 the error in the difference was neglected. It is clear from the data that the contribution from $F_2^e(x)$ is essentially zero for $x^p > 10 \times 10^{-4}$. The integral

$$I = \int_0^1 F_2^e(x^p)dx^p$$

was evaluated from the sum

$$S = \sum_{x^p=0\text{-}10^{-3}} F_2^e(x^p)\Delta x^p$$

in obvious notation.

The integral of the electron elastic structure function $F_2^e(x^e)$ over the range x^e = 0-1 is then given by

$$\int_0^1 F_2^e(x^e)dx^e = \frac{M_p}{m_e} \cdot \frac{1}{0.86} \cdot S$$

where $x^e = Q^2/2m_e\nu$.

This integral was measured to be 1.01 ± 0.04, where the error is obtained from the statistical error in the sum S combined in quadrature with the error in the radiative correction factor.

The inclusion of this measurement is therefore that no deviation from point-like behaviour has been observed out to a value of Q^2 = 0.2 $(GeV/c^2)^2$ in the space-like region. Experiments have revealed no internal structure in the electron out to a value of Q^2 = 27 $(GeV/c^2)^2$. The result obtained therefore allows a limit on the internal structure of the muon to be estimated. Parameterising the deviation from point-like behaviour in the standard form

$$f_\mu(Q^2) = f_\mu(0)(1 \pm Q^2/\Lambda^2)$$

where
$$F_\mu(0) = 1$$
$$Q^2/\Lambda^2 = 0.01 \pm 0.04.$$

Clearly, the sign of the deviation cannot be determined from this measurement. However, the expected deviation is a reduction in the effective charge, i.e. $f(Q^2) = f_\mu(0)(1 - Q^2/\Lambda^2)$. The upper limit on Λ^2 is infinity since the denominator passes through zero. The lower limit on Λ^2 is obtained from $Q^2/\Lambda^2 = 0.01 \pm 0.04$. This gives Λ^2_{min} = 4.7 $(GeV/c^2)^2$ for a mean value of Q^2 of 0.189 $(GeV/c^2)^2$.

Radiative corrections to μ-e scattering have been neglected in the estimate of F_2^e. These can have an effect of 1%[74].

μ-e Total Cross-Section

A measurement of the μ-e total cross-section can also be obtained from the data. Fig. 8.16 shows the weighted event distribution obtained without use of the μ-e filter after corrections for elastic radiative tail and spectrometer acceptance have been made. Fig. 8.17 shows the calculated deep-inelastic event distribution after deep-inelastic radiative corrections and correction for resolution smearing. Subtraction of the calculated deep-inelastic contribution from the corrected observed distribution for $Q^2 < 1.0$ $(GeV/c^2)^2$ will therefore give the μ-e total cross-section in the range ν = 170-200 GeV. This was measured to be 23902 ± 2390, where the error quoted is an estimate of the error in calculating deep-inelastic radiative corrections of ∿10%.

The μ-e total cross-section can be calculated exactly[1] if radiative effects are neglected by (Equations 1.3 and 1.5)

$$\frac{d\sigma}{d\nu} = \frac{4\pi\alpha^2}{Q^4} \frac{m_e}{E^2} \frac{\frac{Q^2}{2m_e} G_M\left(\frac{Q^2}{2} - m_\mu^2\right) + \frac{G_E^2 + \tau G_M^2}{1+\tau}}{\left(1 - \frac{m_\mu^2}{E^2}\right)} \qquad 8.14$$

where $\tau = Q^2/4m_e^2$

For an effective beam flux of 4.24×10^{10} μ's and the remaining luminosity parameters given in Section 8.2, Eqn.. 8.14 gives 23668 ± 710 events in the range ν = 170-200 GeV for an incident beam energy of 219 GeV. Where the quoted error is obtained from an estimated error of 3% in calculation of the radiative corrections to μ-e scattering. The measured result is therefore in good agreement with the calculated value. A limit on the Q^2 variation of the muon form factor can again be obtained

assuming

$$G_M(Q^2) \equiv 1$$

$$G_E(Q^2) = G_E(0)\ (1 - Q^2/\Lambda^2)$$

where $G_E(0) \equiv 1$ and Q^2/Λ^2 is also assumed small. Including an error of 3% from μ-e radiative corrections in quadrature with that from the measured cross-section gives a one standard deviation from the mean of 2495 events. Assuming this deviation to be wholly from a deviation of G_E from 1 gives

$$\Delta n = 6.1 \times 10^5\ Q^2/\Lambda^2$$

substituting $Q^2 = 0.189$ (GeV/c^2) and the above value for Δn gives a lower limit on Λ^2 of 46.2 $(GeV/c^2)^2$.

An alternative formulation can be used to obtain an estimate of Λ^2:

$$G_E^2(0)\left(1 + \frac{Q^2}{\Lambda^2}\right) = \frac{\sigma_{meas}}{\sigma}$$

This has the advantage that a straightforward estimate of the error in Λ^2 can be obtained from the relative errors of σ_{meas}, and σ_{pred} and gives $\Lambda^2 = 38.0 \pm 5.0$. The result is in good agreement with the previous measurement. Taking a conservative view therefore gives $\Lambda^2_{min} = 33$ $(GeV/c^2)^2$.

TABLE 8.1

D-MESON NORMALISATION - TO TOTAL FLUX

Data Set	Q^2 Range $(GeV/c^2)^2$	Total Flux $(x10^{-10})$	Cross-Section/Event (pbarns/event)
A	$Q^2 < 1.0$	7.45	4.78
B	$Q^2 < 1.0$	3.95	9.01
A	$Q^2 > 1.0$	7.45	5.62
B	$Q^2 > 1.0$	3.95	10.64

TABLE 8.2

APPROXIMATE VALUES FOR DEEP-INELASTIC RADIATIVE CORRECTIONS

ν (GeV)	$\sigma_{true}/(\sigma_{meas}-\sigma_{ER})$ (RC)
10-80	1.00
80-85	0.99
85-90	0.975
95-100	0.95
100-105	0.92
105-110	0.86
110-200	0.75

TABLE 8.3

NORMALISATION TO VIRTUAL PHOTON CROSS-SECTION

Q^2 $(GeV/c^2)^2$	Integrated Flux $(x10^{-10})$	Data Set	σ_{DI}
Q^2_{min}-1.0	7.45	A	8885
Q^2_{min}-1.0	3.95	B	4728
1.0-80.0	7.45	A	8290
1.0-80.0	3.95	B	4398

TABLE 8.4

VIRTUAL PHOTON CROSS-SECTION INTEGRATED OVER THE RANGE W = 319-325 (GeV)

Q^2 $(GeV/c^2)^2$	No Filter σ(μbarns)	$\pm$/-	Filtered σ(μbarns)	$\pm$/-	Corrected σ(μbarns)	$\pm$/-
0.025-0.05	170.5	37.9	141.9	37.2	132.2	38.2
0.05-0.075	147.3	18.5	121.6	18.1	112.9	19.0
0.075-0.100	155.3	19.6	119.0	18.9	106.0	20.1
0.100-0.125	231.9	17.7	168.0	16.8	146.4	19.0
0.125-0.150	269.9	18.7	159.0	16.2	121.4	20.0
0.150-0.175	782.4	24.8	272.6	18.7	99.9	36.0
0.175-0.200	1446.4	29.6	472.6	19.7	142.8	52.7
0.200-0.225	892.1	25.7	316.0	18.1	112.2	37.4
0.225-0.250	278.5	17.8	123.2	16.0	70.6	21.3
0.250-0.275	94.5	17.4	52.4	16.0	38.2	17.4
0.275-0.300	99.7	16.5	60.0	16.1	56.6	17.4
0.300-0.400	100.9	7.4	71.6	7.0	63.0	8.0
0.400-0.600	71.2	5.3	50.7	5.1	43.8	5.5
0.600-0.800	32.2	5.1	28.3	5.0	26.9	5.2
0.800-1.00	40.05	4.4	39.1	4.4	38.8	4.4

TABLE 8.5

MASS OF THE ELECTRON

ν (GeV)	$\langle Q^2 \rangle$ $(GeV/c^2)^2$	+/-	$\langle Q^2 \rangle / 2\nu$ MeV/c^2	+/-
170-180	0.175		0.500	0.02
180-190	0.188		0.508	0.02
190-200	0.198		0.508	0.02

$$\overline{\frac{Q^2}{2\nu}} \equiv M_e = 0.505 \pm 0.011 \text{ MeV/c}^2.$$

TABLE 8.6

$F_2(x)$ For ν_e Scattering (Integrated over range Q^2_{min}-80$(GeV/c^2)^2$)

x^P $(x10^4)$ $(Q^2/2M\nu)$	$F_2(x)$ +/- (No Filter) $(x10^{-3})$		$F_2(x)$ +/- (Filtered) $(x10^{+3})$		$F_2^e(x)$ +/- ($\epsilon_{\nu e}$ = 0.75) $(x10^{-3})$	
0.67-1.33	83	33	69	33	19	33
1.33-2.00	61	10	48	10	17	10
2.00-2.63	119	16	97	14	29	16
2.63-3.33	216	18	165	17	68	18
3.33-4.00	289	23	193	21	128	23
4.00-4.65	512	32	238	27	365	34
4.65-5.41	2142	49	682	34	1947	76
5.41-6.06	2807	60	962	38	2460	95
6.06-6.67	1188	50	413	40	1033	59
6.67-7.47	458	42	224	37	312	43
7.47-8.00	277	48	171	45	141	48
8.00-10.00	339	28	238	26	135	28
10.0-16.7	321	22	222	21	0	
16.7-25.0	310	25	270	24	0	
25.0-41.7	313	24	313	24	0	
41.7-62.5	426	39	423	24	0	
62.5-83.3	316	40	314	40	0	
83.3-125.0	409	29	407	29	0	
125.0-167.0	367	28	362	28	0	
167.0-1000.0	388	10	387	10	0	

Internal Bremmsträlung

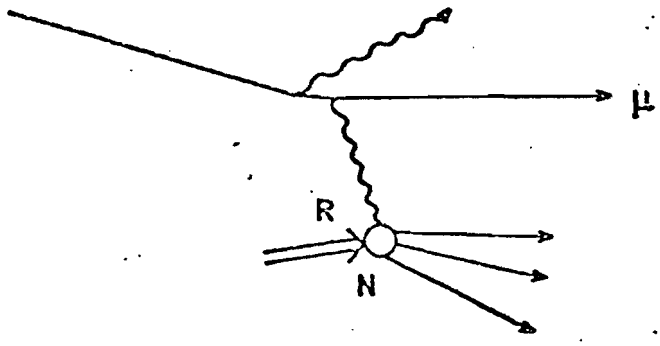

R denotes the fact that the bremmsträlung is emmitted in the field of the nuclear with which the virtual photon interacted

Straggling

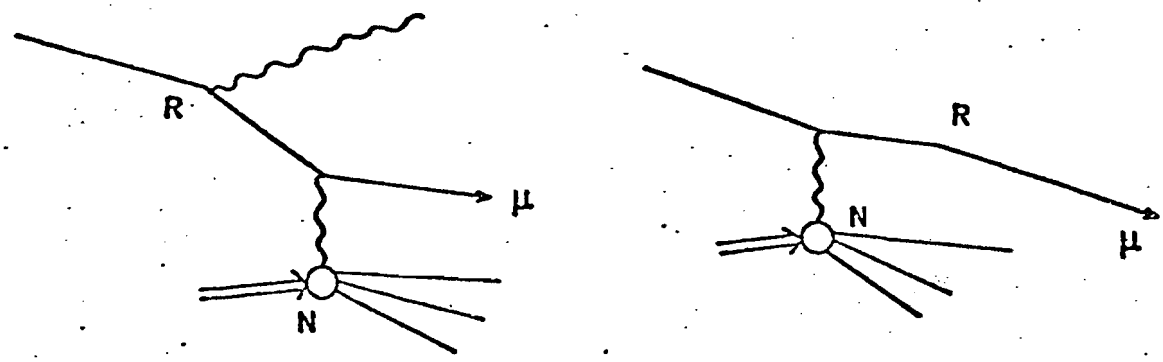

In this case the muon radiates in the field of a nucleus before or after that with which it interacts

Fig. 8.1

Angular Resolution of Standard Momentum Analysis

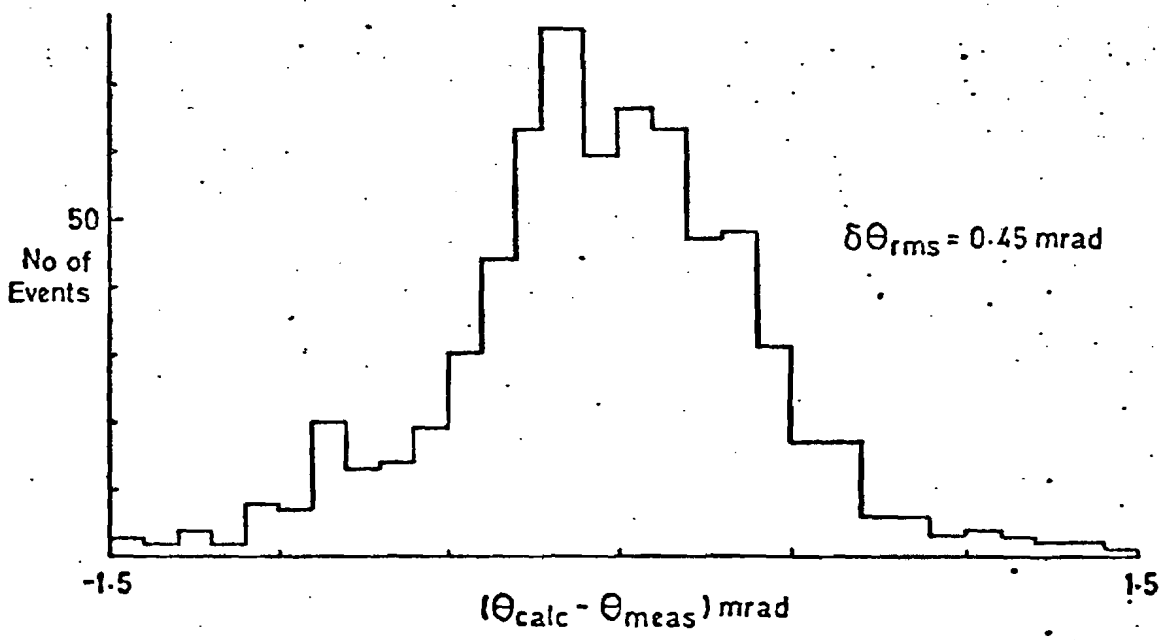

Q^2 Resolution of Standard Momentum Analysis

Using Elastic μ - e's

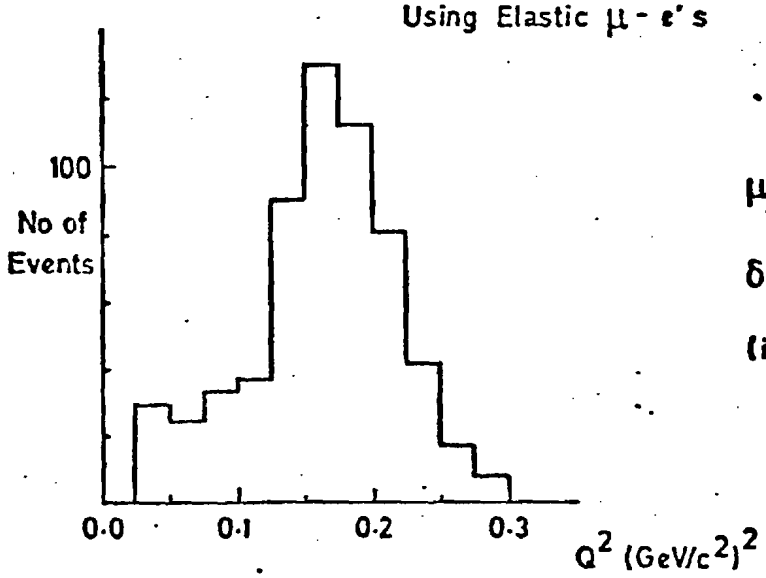

μ_{Q^2} = 0·187 $(GeV/c^2)^2$

δQ^2_{rms} = 0·034

(in indicated range)

Fig. 8·2

Acceptance Distribution for Scattered Muon

ASSUMED ACCEPTANCE FOR PHI DISTRIBUTIONS E = 222.37 GEV

TH	PHI																
0	5.0																
	95.00	0.0	0.0	0.0	0.0	0.0	0.635	0.675	0.532	0.455	0.347	0.134	0.002	0.0	0.002	0.011	0.014
	85.00	0.0	0.0	0.0	0.0	0.882	0.761	0.664	0.589	0.524	0.430	0.278	0.018	0.007	0.021	0.040	0.023
	75.00	0.0	0.0	0.0	0.0	0.969	0.896	0.750	0.641	0.563	0.473	0.375	0.090	0.054	0.083	0.054	0.022
	65.00	0.0	0.0	0.0	0.0	0.988	0.977	0.886	0.755	0.614	0.516	0.458	0.159	0.123	0.113	0.070	0.022
	55.00	0.0	0.0	0.0	1.000	1.000	1.000	0.966	0.844	0.705	0.575	0.554	0.244	0.131	0.119	0.073	0.025
	47.50	0.0	0.0	0.0	1.000	1.000	1.000	0.999	0.975	0.928	0.656	0.511	0.295	0.142	0.116	0.077	0.029
	42.50	0.0	0.0	0.0	1.000	1.000	1.000	1.000	0.997	0.926	0.719	0.544	0.347	0.140	0.135	0.075	0.034
	37.50	0.0	0.0	0.0	1.000	1.000	1.000	1.000	1.000	0.986	0.814	0.593	0.396	0.154	0.131	0.083	0.033
	32.50	0.0	0.0	0.0	1.000	1.000	1.000	1.000	1.000	1.000	0.945	0.674	0.435	0.178	0.126	0.085	0.032
	27.50	0.0	0.0	0.987	0.997	1.000	1.000	1.000	1.000	1.000	0.992	0.802	0.504	0.194	0.140	0.091	0.039
	22.50	0.0	0.0	0.955	0.978	0.997	1.000	1.000	1.000	1.000	1.000	0.937	0.592	0.229	0.155	0.105	0.050
	17.50	0.0	0.0	0.888	0.914	0.960	0.994	1.000	1.000	1.000	1.000	0.948	0.726	0.290	0.191	0.134	0.076
	12.50	0.0	0.852	0.853	0.852	0.879	0.931	0.986	1.000	1.000	1.000	0.985	0.900	0.453	0.270	0.182	0.122
	8.50	0.0	0.814	0.820	0.831	0.840	0.860	0.912	0.968	0.996	0.975	0.924	0.931	0.652	0.359	0.247	0.169
	6.50	0.0	0.799	0.805	0.804	0.817	0.845	0.897	0.969	0.992	0.944	0.910	0.926	0.720	0.410	0.299	0.222
	7.50	0.0	0.765	0.780	0.775	0.796	0.815	0.846	0.924	0.965	0.914	0.894	0.929	0.782	0.473	0.363	0.271
	5.50	0.0	0.721	0.729	0.738	0.763	0.755	0.783	0.856	0.898	0.882	0.902	0.922	0.846	0.512	0.390	0.320
	5.50	0.0	0.626	0.654	0.663	0.680	0.645	0.707	0.755	0.851	0.855	0.839	0.920	0.871	0.561	0.389	0.316
	5.75	0.0	0.545	0.553	0.579	0.588	0.637	0.629	0.682	0.804	0.844	0.872	0.920	0.885	0.570	0.394	0.317
	4.25	0.474	0.466	0.480	0.515	0.546	0.571	0.596	0.654	0.762	0.841	0.865	0.923	0.891	0.581	0.399	0.319
	3.75	0.390	0.399	0.409	0.435	0.455	0.516	0.553	0.612	0.742	0.824	0.855	0.927	0.894	0.584	0.400	0.323
	3.25	0.285	0.295	0.320	0.345	0.377	0.429	0.472	0.529	0.659	0.815	0.856	0.924	0.901	0.591	0.403	0.311
	2.75	0.212	0.218	0.213	0.237	0.276	0.337	0.381	0.461	0.583	0.774	0.859	0.926	0.905	0.593	0.402	0.307
	2.25	0.123	0.127	0.134	0.151	0.193	0.224	0.264	0.348	0.488	0.738	0.859	0.922	0.913	0.601	0.403	0.307
	1.75	0.059	0.056	0.063	0.074	0.095	0.125	0.177	0.258	0.471	0.542	0.774	0.922	0.910	0.606	0.406	0.305
	1.25	0.014	0.010	0.015	0.021	0.032	0.050	0.078	0.122	0.187	0.447	0.709	0.907	0.910	0.607	0.406	0.305
	0.95	0.004	0.003	0.004	0.006	0.011	0.018	0.029	0.046	0.092	0.277	0.553	0.905	0.922	0.611	0.402	0.303
	0.85	0.002	0.002	0.002	0.002	0.007	0.012	0.020	0.036	0.070	0.226	0.649	0.906	0.923	0.615	0.399	0.303
	0.75	0.0	0.001	0.001	0.002	0.004	0.005	0.010	0.022	0.045	0.155	0.541	0.897	0.923	0.617	0.401	0.301
	0.65	0.0	0.0	0.0	0.0	0.001	0.003	0.004	0.014	0.024	0.120	0.603	0.909	0.922	0.616	0.404	0.301
	0.55	0.0	0.0	0.0	0.0	0.0	0.001	0.002	0.006	0.013	0.088	0.530	1.000	0.923	0.626	0.410	0.301
	0.45	0.0	0.0	0.0	0.0	0.0	0.0	0.001	0.002	0.005	0.069	0.572	1.000	0.925	0.644	0.427	0.0
	0.35	0.0	0.0	0.0	0.0	0.0	0.0	0.0	0.0	0.001	0.034	0.554	1.000	0.924	0.659	0.472	0.0
	0.25	0.0	0.0	0.0	0.0	0.0	0.0	0.0	0.0	0.0	0.020	0.587	1.000	0.927	0.724	0.401	0.0
	0.15	0.0	0.0	0.0	0.0	0.0	0.0	0.0	0.0	0.0	0.011	0.631	1.000	1.000	1.000	0.225	0.0
VJ		2.5	7.5	15.0	30.0	50.0	70.0	90.0	110.0	130.0	150.0	170.0	190.0	202.5	207.5	212.5	217.5

Fig. 8.3

Observed Event Distribution (mu - e filter on)

EVENTS SEEN BEAM CORRECTION = 1.0000 CCM CORRECTION = 1.0000

Q^2 Gev^2																
5.00 - 80.00	555	697	1603	1098	917	622	525	434	376	175	133	157	154	98	34	7578
4.00 - 5.00	219	270	492	242	183	136	108	104	89	44	43	54	52	54	8	2098
3.00 - 4.00	332	410	514	321	223	179	121	158	119	72	69	73	106	69	12	2778
2.00 - 3.00	432	484	602	321	258	224	185	215	303	143	142	149	183	153	15	3809
1.50 - 2.00	376	399	437	259	241	257	222	285	462	331	380	463	568	492	53	5249
1.00 - 1.50	34	41	23	34	25	27	45	68	127	143	176	231	265	218	15	1451
0.80 - 1.00	32	11	19	22	9	20	34	49	141	226	255	311	415	368	34	1945
0.60 - 0.80	13	5	7	13	9	18	13	42	167	317	527	749	867	698	49	3474
0.40 - 0.60	29	4	6	4	5	2	5	3	96	229	502	674	892	645	68	3202
0.35 - 0.40	9	1	2	1	1	1	0	1	33	74	181	281	234	262	20	1118
0.31 - 0.35	7	2	3	5	2	2	0	0	22	88	218	305	356	349	28	1387
0.27 - 0.31	7	0	4	2	1	3	1	0	31	126	297	433	572	573	53	2109
0.23 - 0.27	8	1	4	3	3	1	2	0	34	183	541	871	1277	1104	96	5125
0.19 - 0.23	5	1	3	3	3	2	5	0	61	375	1104	1534	1486	1025	88	5689
0.15 - 0.19	8	0	2	2	1	0	2	1	80	566	1172	1182	1221	967	48	5442
0.10 - 0.15	13	1	0	2	2	3	2	2	111	480	870	1126	1456	916	6	4992
0.13 - 0.10	5	0	1	2	2	0	3	1	71	429	1152	1712	2175	620	0	8178
0.10 - 0.07	9	0	2	1	2	4	3	1	78	651	1955	2591	2509	173	0	8518
0.07 - 0.05	12	4	6	1	2	2	2	1	108	1169	3504	4549	1000	1	0	10393
0.05 - 0.02	13	5	4	5	4	5	4	3	318	2559	4751	1176	2	0	0	9349
0.02 - 0.00	25	1	2	5	6	1	3	5	68	20	0	0	0	0	0	139
	2145	2327	3734	2546	1897	1504	1310	1374	2902	8620	17952	18746	15842	8795	618	24576

NU GEV -10.0 10.0 20.0 40.0 60.0 80.0 100.0 120.0 140.0 160.0 170.0 180.0 190.0 200.0 210.0 230.0

Fig. 8.4a

Observed Event Distribution (mu - e filter off)

EVENTS SEEN BEAM CORRECTION = 1.0000 CCM CORRECTION = 1.0000

Q^2 Gev^2																
5.00 - 80.00	555	697	1605	1101	919	623	525	435	376	175	134	158	155	98	34	7590
4.00 - 5.00	219	271	492	242	183	138	108	104	90	44	43	54	52	54	9	2103
3.00 - 4.00	332	410	515	323	223	180	121	158	121	74	69	73	105	69	12	2766
2.00 - 3.00	433	484	609	321	258	227	184	215	304	144	143	150	186	158	15	3029
1.50 - 2.00	376	399	441	260	242	253	224	265	407	331	382	468	575	503	55	5330
1.00 - 1.50	34	41	23	34	25	27	45	68	129	147	176	234	270	224	16	1483
0.80 - 1.00	32	11	19	22	9	20	34	49	144	230	278	324	425	380	37	2036
0.60 - 0.80	13	5	7	13	9	18	13	42	179	381	644	841	972	727	54	3908
0.40 - 0.60	29	4	6	4	5	2	5	3	104	287	623	812	1029	787	72	3770
0.35 - 0.40	9	1	2	1	1	1	0	1	32	89	229	328	348	330	25	1397
0.31 - 0.35	7	2	3	5	2	2	0	0	29	112	282	389	451	427	31	1742
0.27 - 0.31	7	0	4	2	1	1	0	1	41	182	461	674	950	973	101	3409
0.23 - 0.27	8	1	2	4	3	1	1	0	54	317	1183	2371	3062	2724	228	9678
0.19 - 0.23	5	1	3	3	3	2	2	0	121	953	3045	4090	3519	1823	122	13570
0.15 - 0.19	8	0	2	2	1	0	2	1	205	1740	3094	2411	1820	1114	61	10541
0.10 - 0.15	13	1	0	2	2	3	2	2	240	1053	1413	1576	1725	1033	7	7022
0.13 - 0.10	5	0	1	2	2	0	3	1	123	805	1408	1966	2391	627	0	7104
0.10 - 0.07	9	0	2	1	2	4	3	1	89	744	2129	2922	2703	190	0	8778
0.07 - 0.05	12	4	6	1	2	2	2	1	118	1219	3789	4818	1062	1	0	11038
0.05 - 0.02	13	5	4	5	4	5	4	3	330	2877	4985	1240	2	0	0	9477
0.02 - 0.00	29	1	2	5	6	1	4	5	71	22	0	0	0	0	0	145
	2146	2329	3743	2352	1900	1512	1314	1376	3517	11746	24510	25589	21811	12292	879	-14056

NU GEV -10.0 10.0 20.0 40.0 60.0 80.0 100.0 120.0 140.0 160.0 170.0 180.0 190.0 200.0 210.0 230.0

Fig. 8.4b

Empty Target Event Distribution (mu - e filter on)

EMPTY TARGET EVENTS FOR 0.992E+10 BEAM WITH FULL/EMPTY BEAM RATIO= 7.5.0

SMOOTHED BACKGROUND FRACTION =****** FOR Q SQRD GT 0.5 AND NU LT 100 GEV

Q² GeV²	NU GEV	-10.0	10.0	20.0	40.0	60.0	80.0	100.0	120.0	140.0	160.0	170.0	180.0	190.0	200.0	210.0	230.0	
5.00-	80.00	16	11	31	32	20	15	14	7	15	3	1	3	5	2	1		176
4.00-	5.00	7	7	14	11	7	4	5	3	0	1	1	1	1	0	1		63
3.00-	4.00	7	11	13	11	5	2	7	4	2	4	0	6	2	4	0		78
2.00-	3.00	14	8	21	10	7	8	3	7	6	5	2	4	3	7	2		112
1.80-	2.00	8	14	16	5	12	5	5	10	17	11	8	23	22	24	6		186
1.60-	1.80	5	3	2	0	2	2	2	1	5	5	7	9	5	15	3		63
1.40-	1.60	5	1	0	0	1	1	0	1	10	7	11	14	31	22	3		104
1.20-	1.40	7	2	1	2	1	2	1	2	6	14	23	33	50	49	12		203
1.00-	1.20	7	2	1	1	1	0	0	1	4	17	19	32	44	51	8		143
0.90-	1.00	0	0	0	0	0	0	0	0	2	5	11	18	21	20	3		80
0.80-	0.90	0	0	0	0	1	0	0	0	1	5	6	23	35	31	3		105
0.70-	0.80	0	1	1	0	0	0	0	0	0	6	12	24	31	41	7		123
0.60-	0.70	2	0	0	0	0	1	0	0	1	12	22	37	41	51	4		171
0.50-	0.60	1	0	0	1	0	0	0	1	4	16	25	52	75	74	14		263
0.45-	0.50	3	0	1	1	0	0	0	1	2	18	48	58	84	74	9		295
0.40-	0.45	2	0	1	1	0	0	0	0	2	19	40	88	81	89	1		324
0.35-	0.40	2	1	1	0	0	0	0	0	7	19	61	106	168	83	0		448
0.30-	0.35	0	1	0	0	0	1	0	0	5	41	143	199	253	28	0		670
0.25-	0.30	2	0	2	0	0	0	0	0	12	61	238	409	122	0	0		846
0.20-	0.25	3	0	0	1	0	2	0	0	30	222	428	126	1	0	0		814
0.00-	0.02	3	0	0	1	0	0	0	0	7	4	0	0	0	0	0		15
		83	56	106	75	58	43	38	37	138	495	1106	1265	1080	675	77		5332

------ OVERALL NORMALIZATION CORRECTIONS -------
TOTAL FLUX RECORDED WAS 7.4458E+10 MUONS
THE BEAM EFFICIENCY WAS 0.616
THE MWPC EFFICIENCY WAS 0.971
THE DAS EFFICIENCY WAS 0.925
RANDOMS CORRECTION WAS 0.899
CORRECTION FOR GAS IN EMPTY TARGET 0.977 GIVING AN EFFECTIVE FLUX OF 0.4325E+11 MUONS

Fig. 8.5

EMPTY TARGET EVENTS FOR 0.992E+10 BEAM WITH FULL/EMPTY BEAM RATIO= 7.33

SMOOTHED BACKGROUND FRACTION =******* FOR Q SQRD GT 0.5 AND NU LT 100 GEV

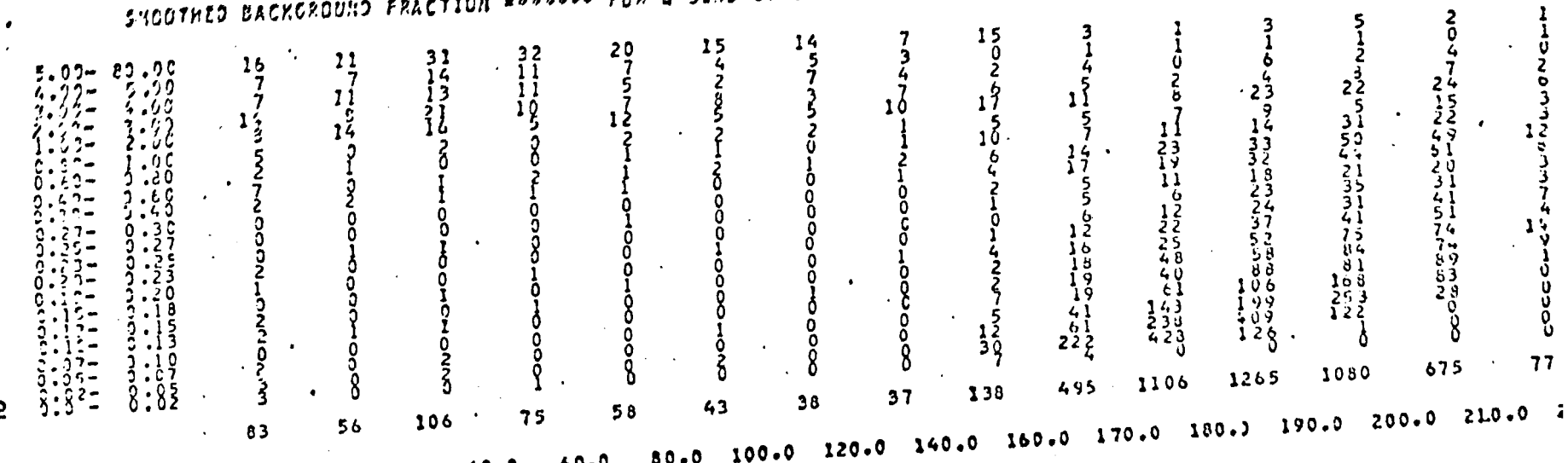

------ OVERALL NORMALIZATION CORRECTIONS ------

0.958E+10 MUONS

TARGET 0.977 GIVING AN EFFECTIVE FLUX OF 0.4325E+11 MUONS

FIG. 8.5

Calculated Elastic Radiative Tail Events

NORMALISATION CORRECTIONS

0.616 BEAM RECONSTRUCTION EFFICIENCY
******* MWPC TRACK EFFICIENCY X AND(JR) Y
0.995 DOWNSTREAM TRACK EFFICIENCY

0.977 CORRECTION FOR GAS DENSITY IN EMPTY TARGET

0.999 CORRECTION FOR RANDOM N VETOING OF GOOD EVENTS

VING AN EFFECTIVE FLUX OF 4.3246E+10 MUONS

DOWNSTREAM TRACK FINDING CORRECTION IN OPERATION

CALCULATED RADIATIVE TAIL EVENTS

5.00-	A0.00	0	0	0	1	2	3	5	8	12	8	11	15	23	0	0	88
4.00-	5.00	0	0	0	1	1	1	2	3	5	3	4	6	9	0	0	36
3.00-	4.00	0	0	1	1	2	3	4	4	9	6	8	11	16	0	0	67
2.00-	3.00	0	2	3	4	5	7	10	14	21	14	18	24	36	0	0	157
1.00-	2.00	0	0	0	0	0	0	0	53	75	49	41	84	122	0	0	445
0.80-	1.00	0	0	0	0	0	0	0	0	41	27	33	44	63	0	0	208
0.60-	0.80	0	0	0	0	0	0	0	0	0	46	57	75	107	0	0	285
0.40-	0.60	0	0	0	0	0	0	0	0	0	38	47	152	215	0	0	522
0.30-	0.40	0	0	0	0	0	0	0	0	0	0	178	153	216	0	0	444
0.27-	0.30	0	0	0	0	0	0	0	0	0	0	43	56	79	0	0	178
0.25-	0.27	0	0	0	0	0	0	0	0	0	0	52	66	94	0	0	212
0.23-	0.25	0	0	0	0	0	0	0	0	0	0	63	81	114	0	0	258
0.20-	0.23	0	0	0	0	0	0	0	0	0	0	79	101	142	0	0	322
0.18-	0.20	0	0	0	0	0	0	0	0	0	0	100	129	182	0	0	411
0.15-	0.18	0	0	0	0	0	0	0	0	0	0	132	171	240	0	0	544
0.13-	0.15	0	0	0	0	0	0	0	0	0	0	182	236	325	0	0	743
0.10-	0.13	0	0	0	0	0	0	0	0	0	0	246	353	440	0	0	1063
0.07-	0.10	0	0	0	0	0	0	0	0	0	0	436	581	502	0	0	1518
0.05-	0.07	0	0	0	0	0	0	0	0	0	0	851	870	184	0	0	1905
0.02-	0.05	0	0	0	0	0	0	0	0	0	0	1107	204	0	0	0	1311
0.0 -	0.02	0	0	0	0	0	0	0	0	0	0	0	0	0	0	0	0
		0	2	4	7	10	15	21	85	163	191	3737	3412	3109	0	0	10756

NU GEV	-10.0	10.0	20.0	40.0	60.0	80.0	100.0	120.0	140.0	160.0	170.0	180.0	190.0	200.0	210.0	230.0

Fig. 8.6

Deep-Inelastic Radiative Corrections (η)

RADIATIVE CORRECTIONS FOR INELASTIC REGION CALCULATED FROM DATA FIT
RATIO OF TRUE/(MEASURED-ELASTIC RADIATIVE TAIL)

Q SQRD																
45.000	0.0	0.0	1.200	1.052	0.989	0.941	0.935	0.929	0.923	0.915	0.905	0.892	0.876	0.852	0.812	0.744
25.000	0.0	1.158	1.074	1.014	0.966	0.918	0.912	0.906	0.898	0.888	0.875	0.860	0.840	0.810	0.767	0.697
15.000	0.0	1.081	1.038	0.993	0.950	0.901	0.894	0.887	0.877	0.866	0.853	0.835	0.813	0.782	0.738	0.663
10.000	0.0	1.051	1.018	0.979	0.940	0.889	0.882	0.874	0.863	0.852	0.838	0.820	0.797	0.765	0.722	0.657
7.500	1.136	1.036	1.007	0.971	0.933	0.881	0.874	0.866	0.855	0.844	0.829	0.811	0.788	0.758	0.716	0.650
5.000	1.086	1.018	0.993	0.961	0.925	0.873	0.866	0.858	0.846	0.834	0.820	0.803	0.781	0.753	0.710	0.645
4.000	1.069	1.010	0.986	0.956	0.922	0.869	0.861	0.855	0.843	0.832	0.818	0.801	0.780	0.754	0.719	0.654
3.500	1.061	1.005	0.982	0.953	0.920	0.867	0.860	0.855	0.842	0.831	0.817	0.800	0.780	0.755	0.723	0.661
3.000	1.050	0.997	0.976	0.948	0.916	0.865	0.857	0.853	0.839	0.828	0.815	0.799	0.780	0.757	0.727	0.669
2.750	1.046	0.995	0.974	0.946	0.913	0.863	0.856	0.853	0.839	0.828	0.815	0.800	0.784	0.759	0.730	0.675
2.500	1.041	0.992	0.971	0.945	0.912	0.863	0.856	0.853	0.838	0.828	0.815	0.801	0.783	0.761	0.735	0.681
2.250	1.036	0.988	0.969	0.942	0.911	0.862	0.855	0.847	0.838	0.828	0.816	0.802	0.785	0.764	0.740	0.688
2.000	1.031	0.985	0.966	0.940	0.911	0.862	0.855	0.846	0.839	0.828	0.817	0.803	0.788	0.769	0.746	0.696
1.750	1.026	0.982	0.963	0.938	0.910	0.861	0.900	0.847	0.839	0.830	0.819	0.805	0.791	0.774	0.753	0.705
1.500	1.020	0.978	0.960	0.937	0.909	0.862	0.855	0.848	0.840	0.832	0.822	0.810	0.796	0.780	0.761	0.715
1.250	1.014	0.974	0.958	0.935	0.907	0.868	0.856	0.850	0.843	0.835	0.826	0.815	0.803	0.789	0.771	0.727
1.000	1.007	0.969	0.955	0.933	0.909	0.864	0.855	0.853	0.846	0.839	0.831	0.822	0.811	0.799	0.783	0.739
0.800	1.003	0.967	0.953	0.932	0.909	0.866	0.861	0.856	0.850	0.843	0.836	0.827	0.817	0.805	0.790	0.746
0.700	1.000	0.965	0.952	0.933	0.905	0.868	0.864	0.859	0.853	0.847	0.840	0.833	0.824	0.813	0.798	0.773
0.600	0.997	0.963	0.951	0.932	0.905	0.871	0.867	0.863	0.858	0.852	0.846	0.839	0.831	0.822	0.808	0.779
0.550	0.993	0.961	0.947	0.929	0.906	0.875	0.871	0.867	0.863	0.858	0.852	0.846	0.838	0.828	0.815	0.784
0.500	0.989	0.958	0.948	0.928	0.926	0.879	0.876	0.872	0.868	0.864	0.859	0.853	0.845	0.835	0.820	0.784
0.450	0.985	0.956	0.945	0.930	0.910	0.884	0.881	0.878	0.875	0.871	0.866	0.860	0.853	0.842	0.823	0.771
0.400	0.980	0.955	0.944	0.930	0.911	0.891	0.888	0.887	0.882	0.877	0.873	0.867	0.859	0.849	0.836	0.793
0.375	0.979	0.954	0.944	0.931	0.915	0.892	0.889	0.887	0.883	0.879	0.874	0.868	0.858	0.848	0.809	0.656
0.350	0.978	0.954	0.945	0.931	0.915	0.894	0.891	0.888	0.885	0.881	0.875	0.868	0.858	0.840	0.798	0.773
0.325	0.977	0.954	0.945	0.932	0.917	0.896	0.893	0.890	0.886	0.882	0.876	0.868	0.857	0.835	0.778	0.740
0.300	0.976	0.954	0.946	0.934	0.919	0.897	0.894	0.892	0.887	0.882	0.876	0.868	0.854	0.826	0.741	0.0
0.275	0.975	0.955	0.947	0.935	0.921	0.899	0.896	0.894	0.888	0.883	0.875	0.865	0.848	0.808	0.651	0.0
0.250	0.977	0.955	0.948	0.937	0.923	0.900	0.897	0.897	0.888	0.881	0.872	0.858	0.833	0.769	0.319	0.0
0.225	0.975	0.956	0.950	0.940	0.926	0.901	0.898	0.892	0.886	0.877	0.865	0.845	0.802	0.658	0.0	0.0
0.200	0.975	0.959	0.953	0.944	0.930	0.909	0.896	0.889	0.880	0.868	0.848	0.811	0.707	0.0	0.0	0.0
0.175	0.975	0.962	0.957	0.953	0.936	0.898	0.890	0.880	0.864	0.840	0.794	0.670	0.0	0.0	0.0	0.0
0.150	0.977	0.967	0.966	0.956	0.943	0.885	0.868	0.842	0.794	0.663	0.093	0.0	0.0	0.0	0.0	0.0
0.125	0.981	0.975	0.973	0.969	0.955	0.677	0.0	0.0	0.0	0.0	0.0	0.0	0.0	0.0	0.0	0.0
NU	5.0	15.0	25.0	50.0	100.0	160.0	165.0	170.0	175.0	180.0	185.0	190.0	195.0	200.0	205.0	210.0

Fig. 8.7

Angular Resolution of Improved Track Analysis (Illinois)

Using Elastic μ - e events

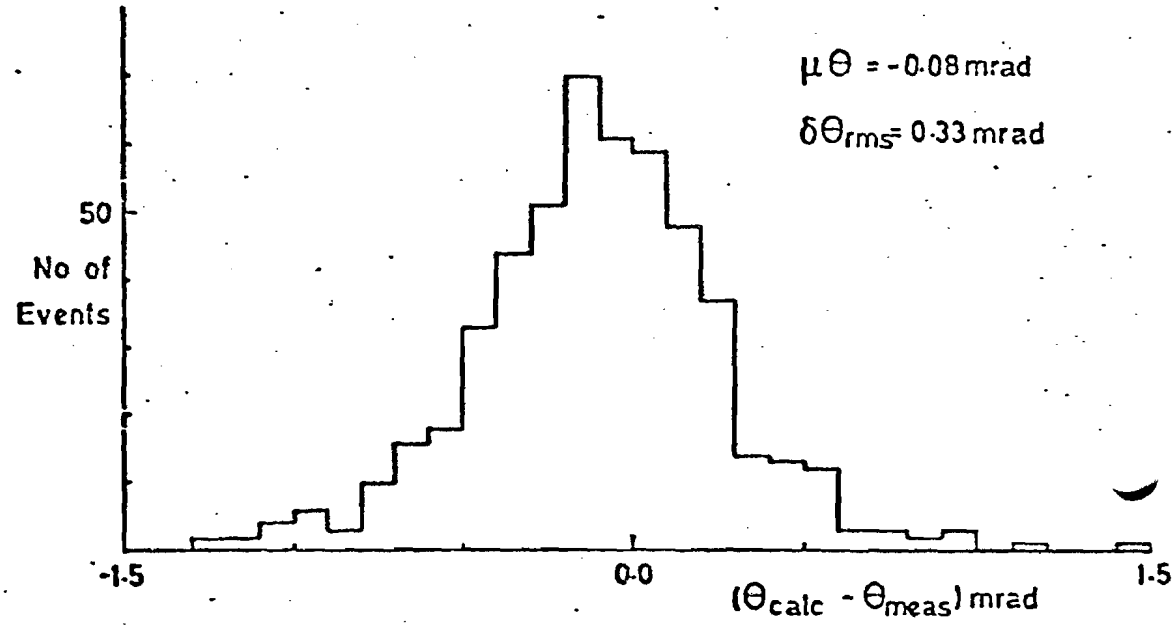

Q^2 Resolution of Elastic μ - e Events (Illinois Track Analysis)

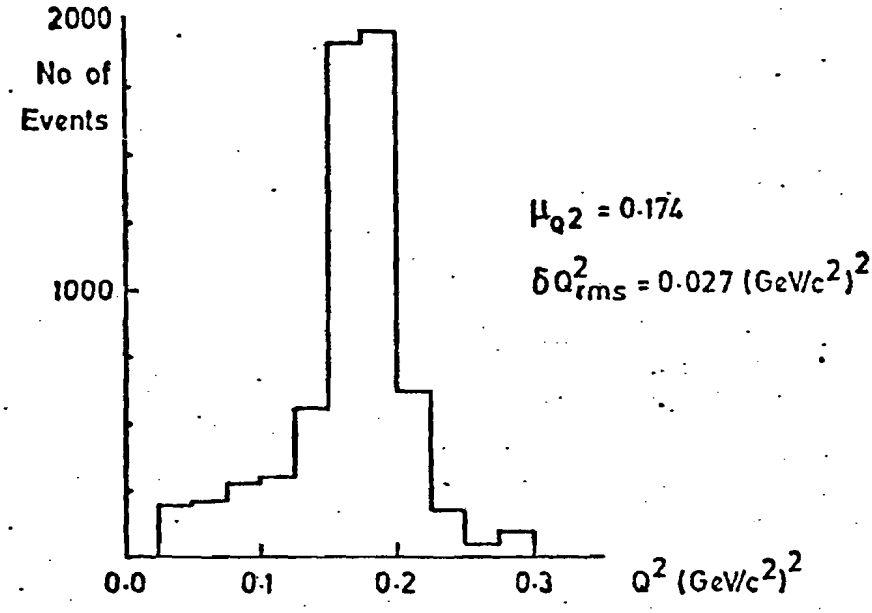

Fig. 8.8

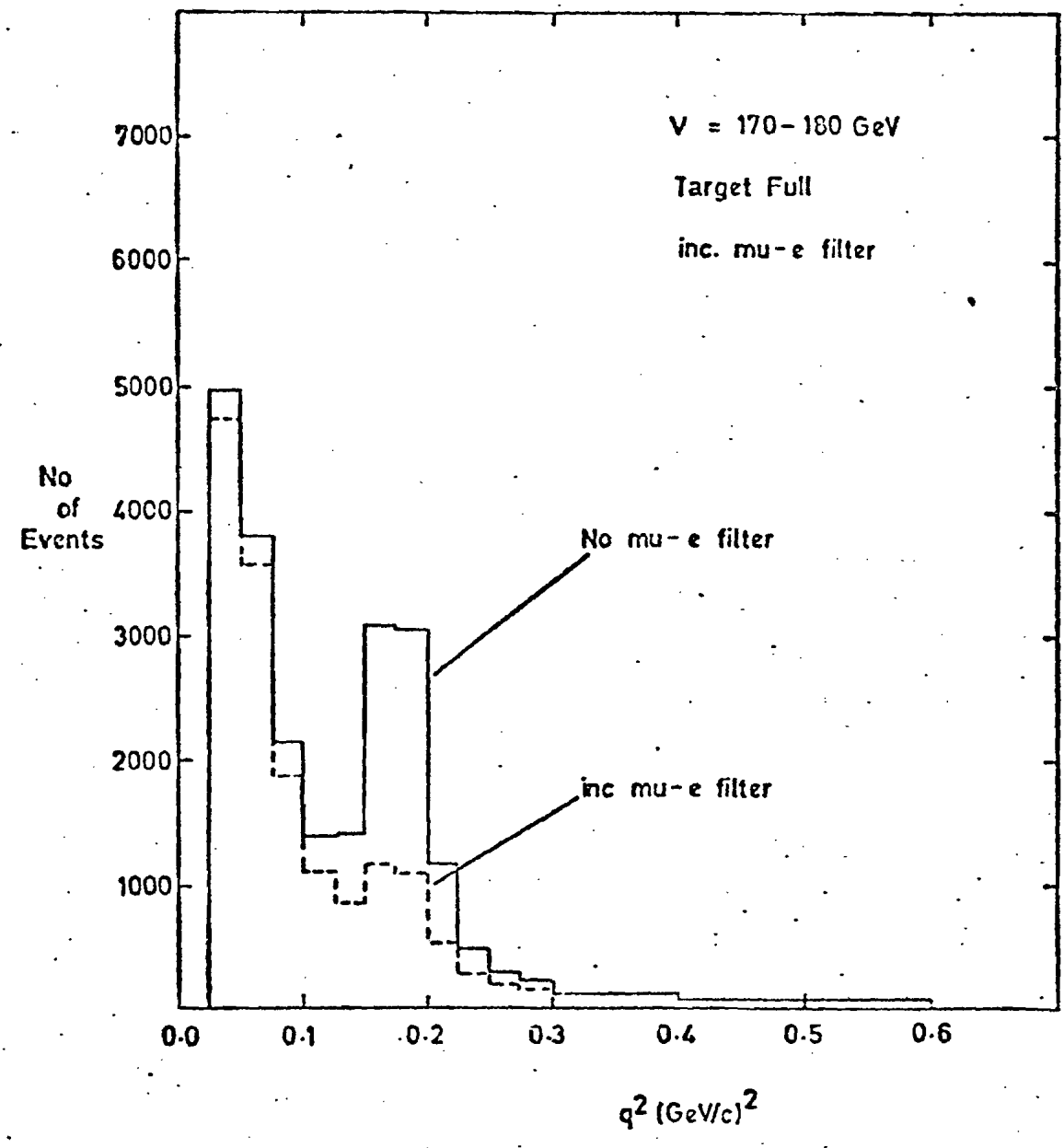
V = 170 – 180 GeV
Target Full
inc. mu – e filter
No mu – e filter
inc mu – e filter
No of Events
7000
6000
5000
4000
3000
2000
1000
0·0
0·1
0·2
0·3
0·4
0·5
0·6
q^2 (GeV/c)^2

Fig. 8·9

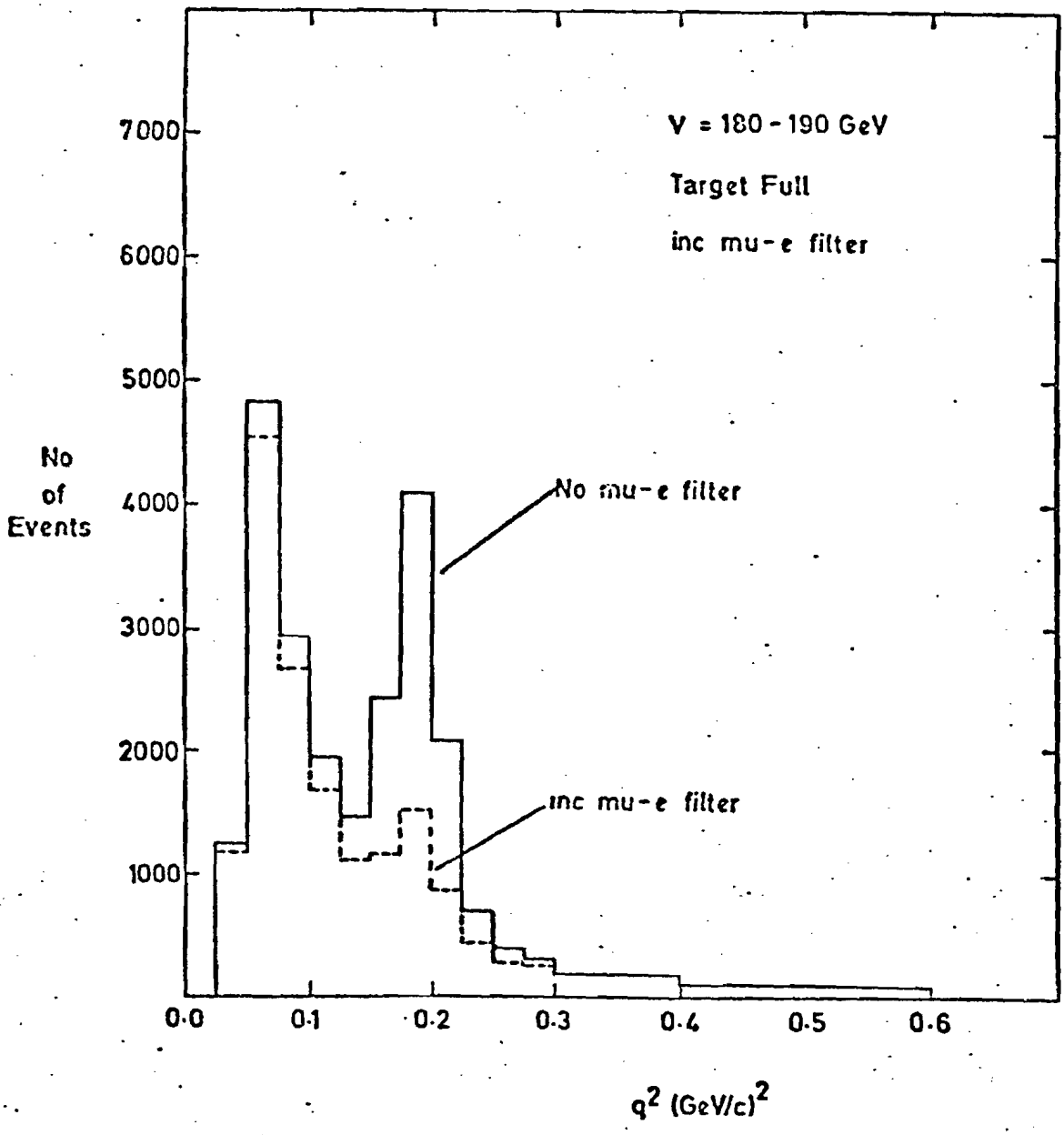
V = 180 - 190 GeV
Target Full
inc mu-e filter
No mu-e filter
inc mu-e filter
No of Events
7000
6000
5000
4000
3000
2000
1000
0.0
0.1
0.2
0.3
0.4
0.5
0.6
q^2 (GeV/c)^2

Fig. 8.10

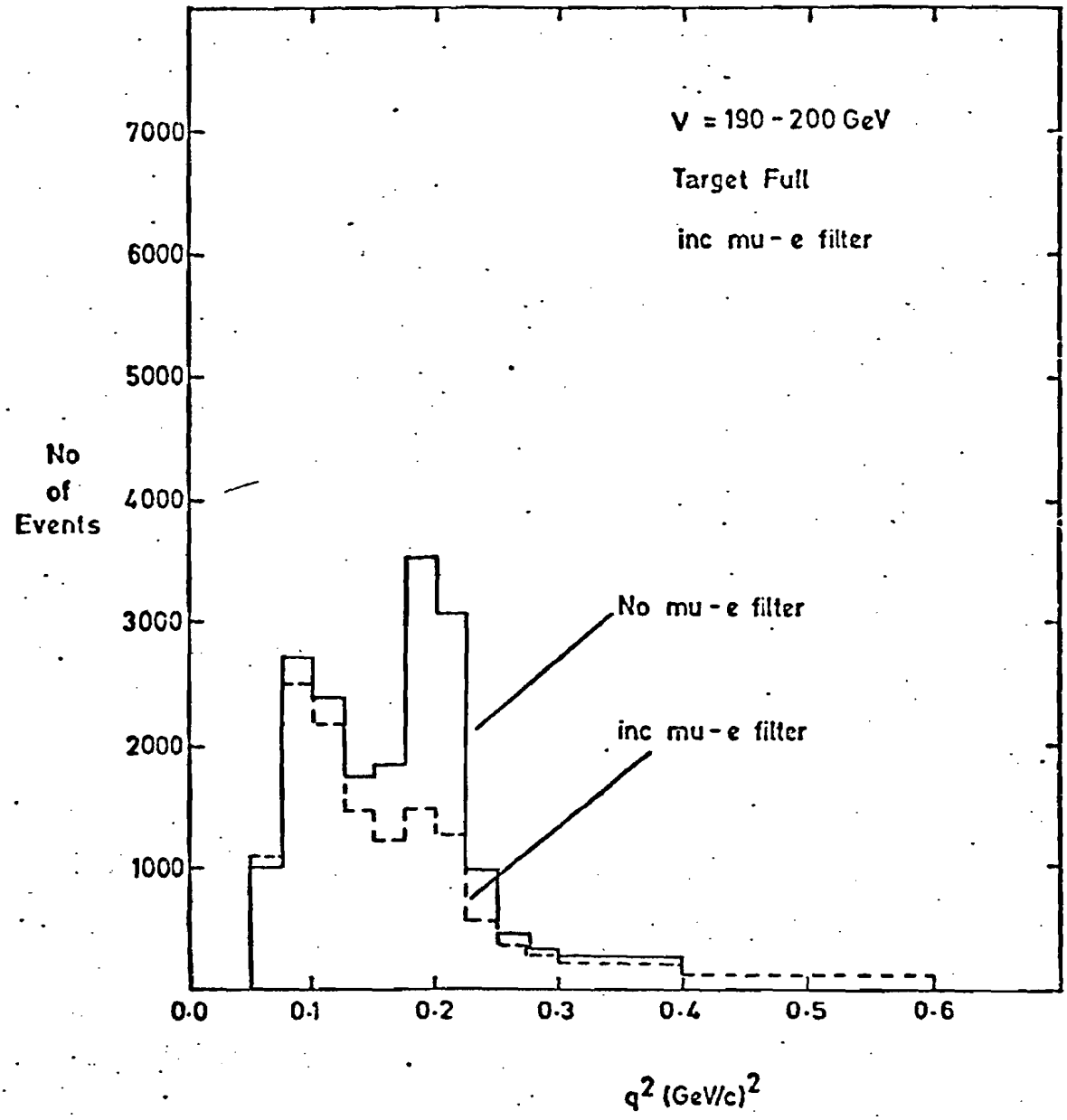
ν = 190 - 200 GeV
Target Full
inc mu - e filter
No mu - e filter
inc mu - e filter
No of Events
7000
6000
5000
4000
3000
2000
1000
0·0
0·1
0·2
0·3
0·4
0·5
0·6
q^2 (GeV/c)^2

Fig. 8·11

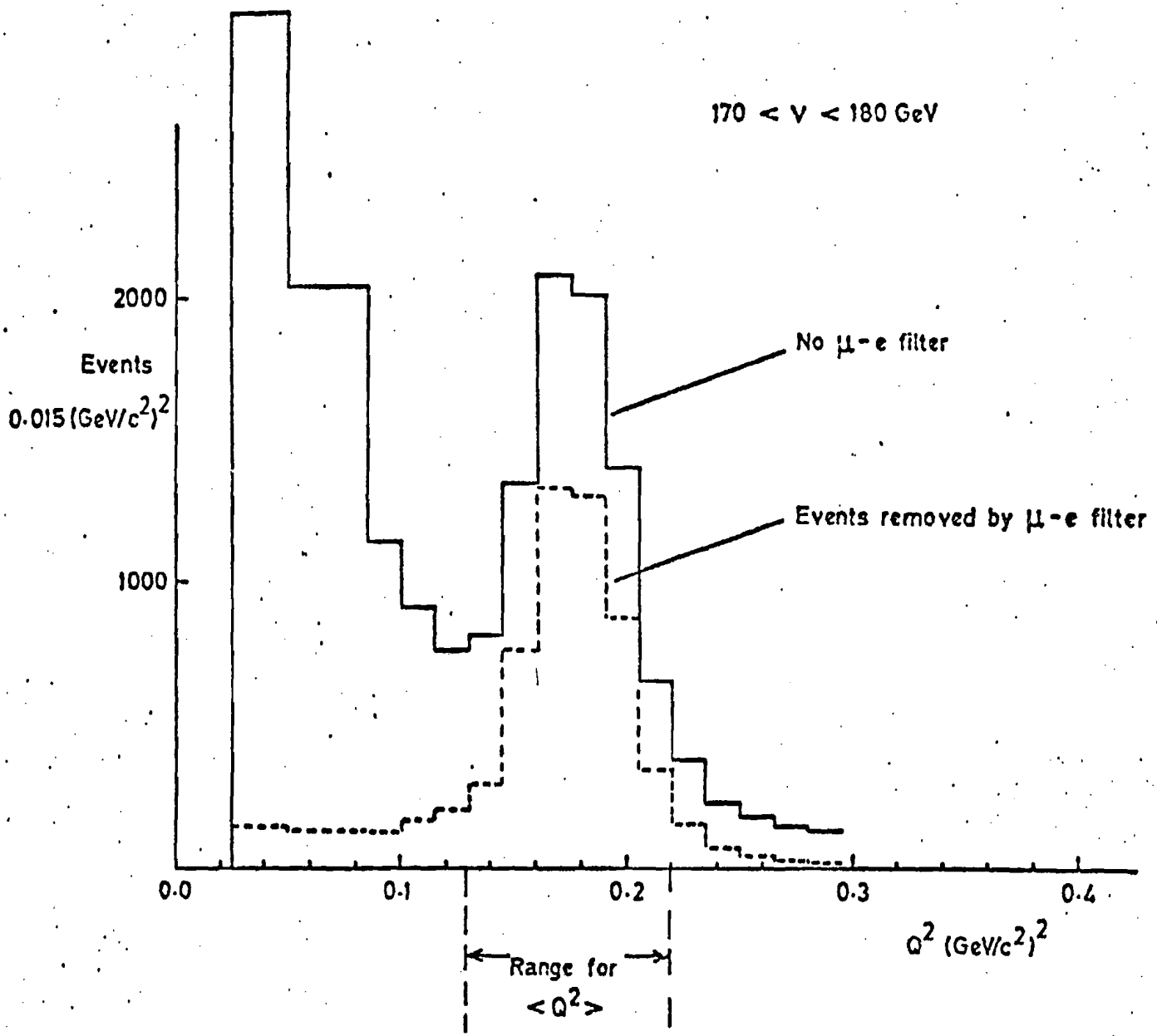
170 < ν < 180 GeV
2000
1000
Events
0·015 (GeV/c²)²
No μ-e filter
Events removed by μ-e filter
0·0
0·1
0·2
0·3
0·4
Q² (GeV/c²)²
Range for
<Q²>

Fig. 8.12

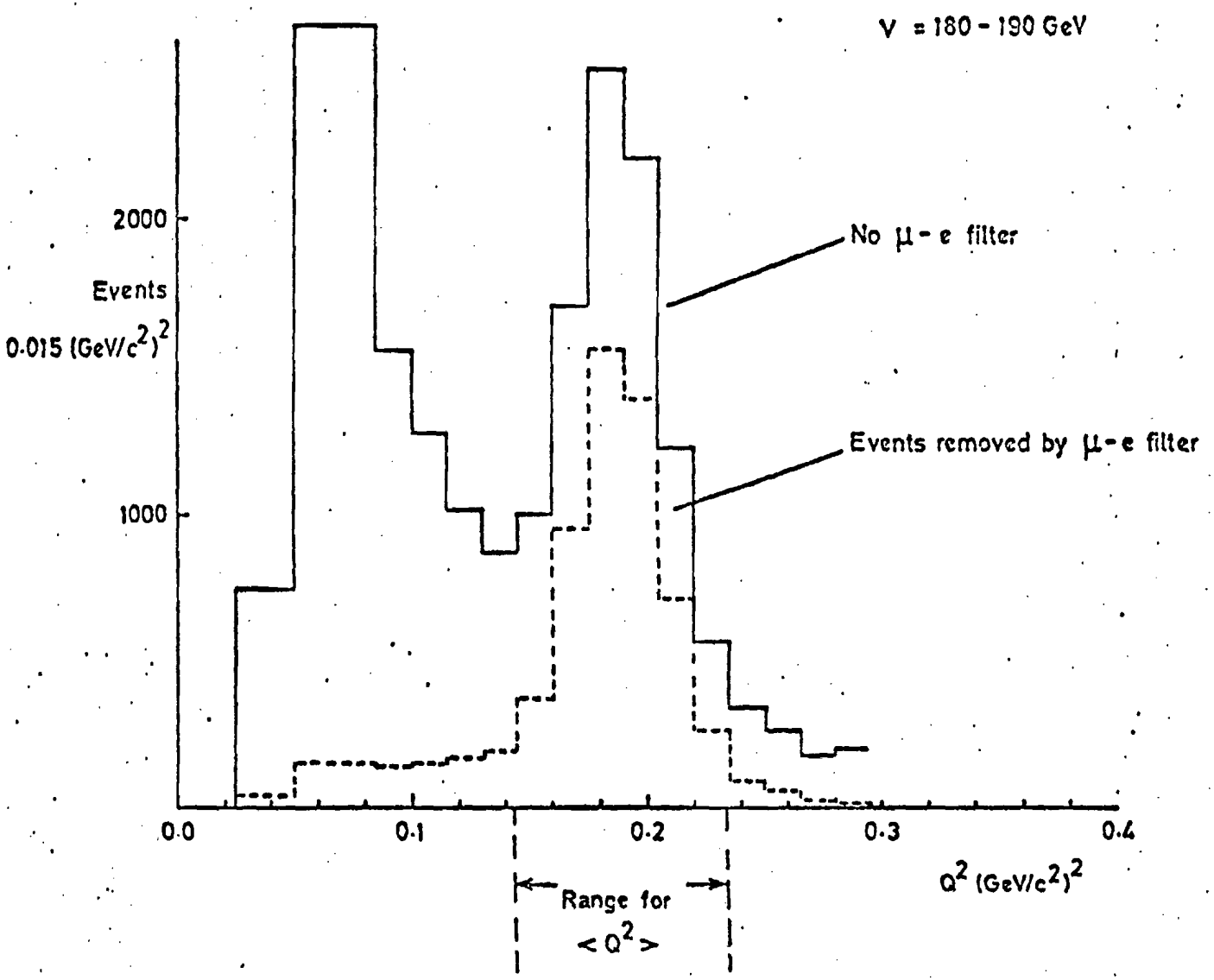
ν = 180 - 190 GeV
2000
Events
0.015 (GeV/c²)²
1000
No μ - e filter
Events removed by μ - e filter
0.0
0.1
0.2
0.3
0.4
Q² (GeV/c²)²
Range for
< Q² >
Fig. 8.13

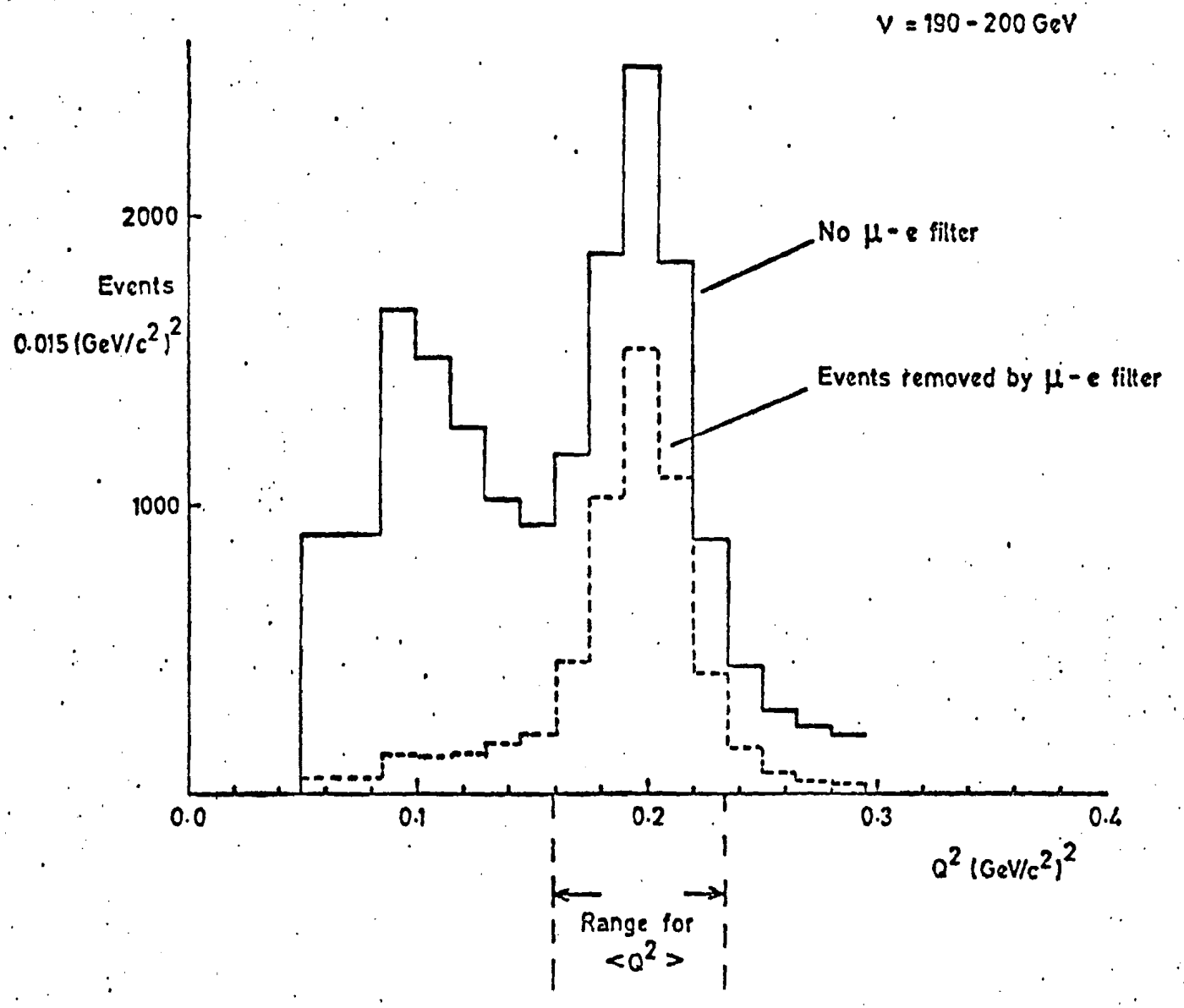
ν = 190 - 200 GeV
2000
1000
Events
0.015 (GeV/c²)²
No μ - e filter
Events removed by μ - e filter
0.0
0.1
0.2
0.3
0.4
Q² (GeV/c²)²
Range for
<Q²>
Fig. 8.14

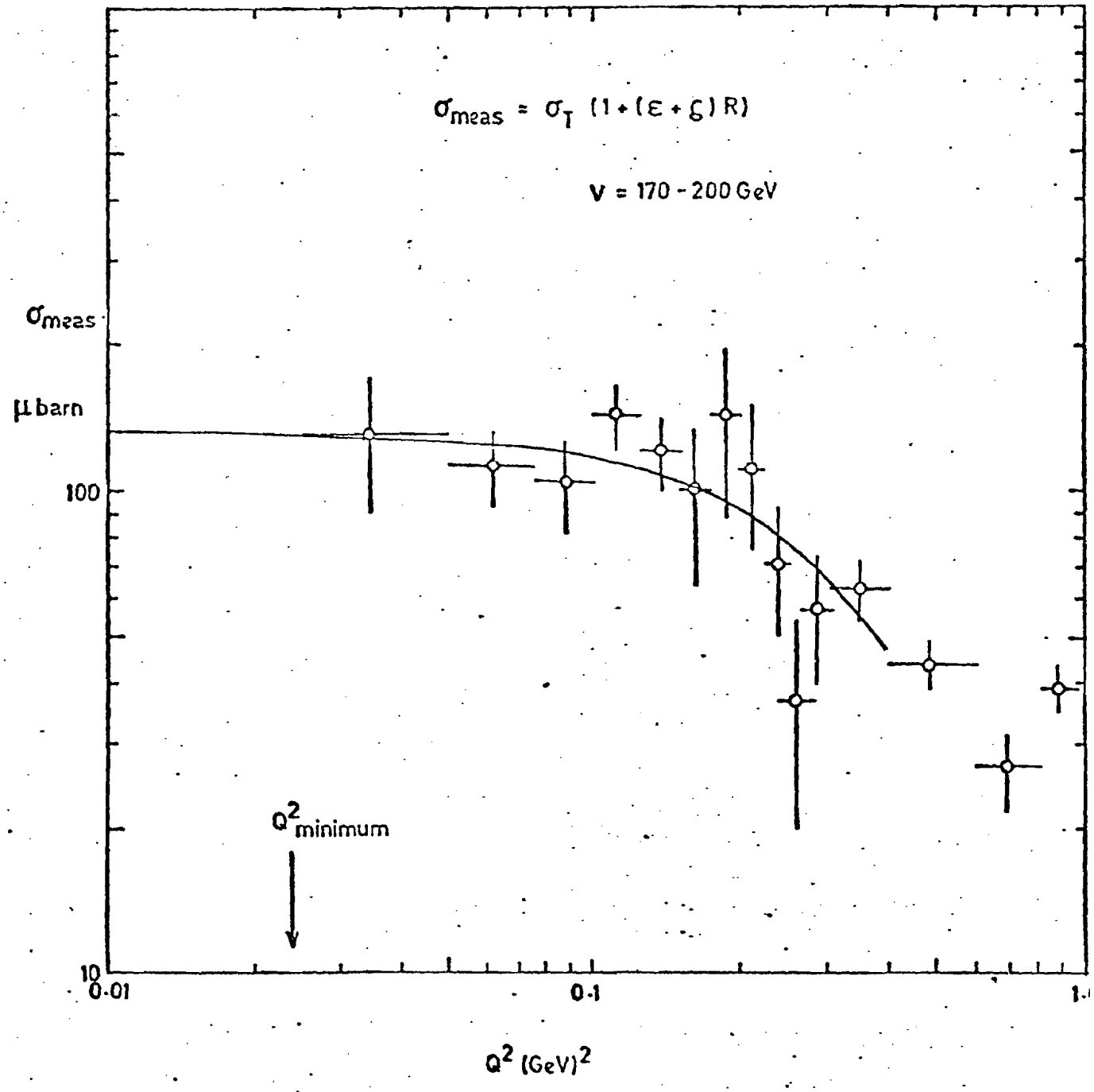
$\sigma_{meas} = \sigma_T (1 + (\varepsilon + \xi) R)$
ν = 170 - 200 GeV
σ_{meas}
μbarn
100
10
0.01
0.1
1
$Q^2_{minimum}$
Q^2 (GeV)^2

Fig. 8.15

WEIGHTED EVENTS AFTER RADIATIVE TAIL SUBTRACTION

[illegible]	50.00	+/-	0 0	5814 293	7106 345	3469 217	2634 151	1874 127	1186 89	2345 195	1593 109	757 78	741 48	595 63	617 60	0 0	0 0	20513 603
0.33-	1.00	+/-	0 0	0 0	0 0	0 0	0 0	0 0	0 0	0 0	234 81	610 82	850 92	797 81	752 90	0 0	0 0	3239 191
0.33-	0.33	+/-	0 0	0 0	0 0	0 0	0 0	0 0	0 0	0 0	0 0	0 0	84 12	26 24	21 30	0 0	0 0	130 40
0.31-	0.32	+/-	0 0	0 0	0 0	0 0	0 0	0 0	0 0	0 0	0 0	0 0	89 18	62 16	54 27	0 0	0 0	224 50
0.30-	0.31	+/-	0 0	0 0	0 0	0 0	0 0	0 0	0 0	0 0	0 0	0 0	33 25	33 20	46 21	0 0	0 0	114 38
0.29-	0.30	+/-	0 0	0 0	0 0	0 0	0 0	0 0	0 0	0 0	0 0	0 0	70 25	36 32	51 28	0 0	0 0	157 47
0.27-	0.29	+/-	0 0	0 0	0 0	0 0	0 0	0 0	0 0	0 0	0 0	0 0	71 20	35 29	29 32	0 0	0 0	135 51
0.25-	0.26	+/-	0 0	0 0	0 0	0 0	0 0	0 0	0 0	0 0	0 0	0 0	124 22	73 31	-31 41	0 0	0 0	165 56
0.24-	0.25	+/-	0 0	0 0	0 0	0 0	0 0	0 0	0 0	0 0	0 0	0 0	87 33	44 34	98 35	0 0	0 0	274 56
0.22-	0.24	+/-	0 0	0 0	0 0	0 0	0 0	0 0	0 0	0 0	0 0	0 0	154 37	151 34	254 40	0 0	0 0	559 64
0.20-	0.22	+/-	0 0	0 0	0 0	0 0	0 0	0 0	0 0	0 0	0 0	0 0	243 40	269 46	459 43	0 0	0 0	971 77
0.19-	0.20	+/-	0 0	0 0	0 0	0 0	0 0	0 0	0 0	0 0	0 0	0 0	516 44	575 48	609 55	0 0	0 0	1700 88
0.17-	0.19	+/-	0 0	0 0	0 0	0 0	0 0	0 0	0 0	0 0	0 0	0 0	674 53	526 53	379 59	0 0	0 0	1679 95
0.16-	0.18	+/-	0 0	0 0	0 0	0 0	0 0	0 0	0 0	0 0	0 0	0 0	595 65	422 51	229 61	0 0	0 0	1246 102
0.14-	0.16	+/-	0 0	0 0	0 0	0 0	0 0	0 0	0 0	0 0	0 0	0 0	449 56	185 57	228 58	0 0	0 0	862 93
0.13-	0.14	+/-	0 0	0 0	0 0	0 0	0 0	0 0	0 0	0 0	0 0	0 0	281 56	137 61	291 60	0 0	0 0	709 104
0.12-	0.13	+/-	0 0	0 0	0 0	0 0	0 0	0 0	0 0	0 0	0 0	0 0	329 56	290 62	236 79	0 0	0 0	855 115
0.11-	0.12	+/-	0 0	0 0	0 0	0 0	0 0	0 0	0 0	0 0	0 0	0 0	401 69	354 73	385 82	0 0	0 0	1140 130
0.09-	0.10	+/-	0 0	0 0	0 0	0 0	0 0	0 0	0 0	0 0	0 0	0 0	290 91	311 87	103 100	0 0	0 0	705 161
0.07-	0.08	+/-	0 0	0 0	0 0	0 0	0 0	0 0	0 0	0 0	0 0	0 0	1609 180	912 191	-152 150	0 0	0 0	2369 302
0.0 -	0.05	+/-	0 0	0 0	0 0	0 0	0 0	0 0	0 0	0 0	0 0	0 0	920 222	43 119	-6 11	0 0	0 0	954 252
		+/-	0 0	5814 293	7106 345	3469 217	2634 151	1874 127	1186 89	2345 195	1892 136	1347 113	8584 362	6131 317	4533 292	0 0	0 0	-19[illegible] [illegible]
[illegible]			-10.0	10.0	30.0	40.0	60.0	80.0	100.0	120.0	140.0	160.0	170.0	180.0	190.0	200.0	210.0	230.0

Fig. 8.16

CALCULATED EVENTS FOR DEEP INELASTIC SCATTERING FOR R = 0.140E+00 USING OMEGA
WITH DEEP INELASTIC RADIATIVE CORRECTION
AND WITH EXPERIMENTAL MOMENTUM RESOLUTION

5.00-	80.00	0	1260	1935	1185	806	588	493	359	295	130	122	115	112	0	0	7361
4.00-	5.00	0	626	699	356	229	164	125	99	81	36	33	32	31	0	0	2510
3.00-	4.00	0	1156	1196	597	383	275	209	165	135	60	56	53	51	0	0	4336
2.00-	3.00	0	2667	2455	1202	772	552	420	331	271	119	111	106	101	0	0	9107
1.00-	2.00	0	0	0	0	0	0	0	1025	836	352	332	312	297	0	0	3155
0.80-	1.00	0	0	0	0	0	0	0	0	392	159	157	145	129	0	0	1001
0.60-	0.80	0	0	0	0	0	0	0	0	0	252	233	218	205	0	0	907
0.40-	0.60	0	0	0	0	0	0	0	0	0	214	359	363	342	0	0	1308
0.30-	0.40	0	0	0	0	0	0	0	0	0	0	317	296	279	0	0	892
0.27-	0.30	0	0	0	0	0	0	0	0	0	0	102	95	90	0	0	288
0.25-	0.27	0	0	0	0	0	0	0	0	0	0	115	107	102	0	0	325
0.23-	0.25	0	0	0	0	0	0	0	0	0	0	131	122	116	0	0	369
0.20-	0.23	0	0	0	0	0	0	0	0	0	0	151	140	134	0	0	425
0.18-	0.20	0	0	0	0	0	0	0	0	0	0	175	163	157	0	0	496
0.15-	0.18	0	0	0	0	0	0	0	0	0	0	208	195	187	0	0	591
0.13-	0.15	0	0	0	0	0	0	0	0	0	0	253	238	230	0	0	720
0.10-	0.13	0	0	0	0	0	0	0	0	0	0	318	299	281	0	0	898
0.07-	0.10	0	0	0	0	0	0	0	0	0	0	416	400	281	0	0	1054
0.05-	0.07	0	0	0	0	0	0	0	0	0	0	596	865	98	0	0	1559
0.02-	0.05	0	0	0	0	0	0	0	0	0	0	517	209	0	0	0	726
0.0 -	0.02	0	0	0	0	0	0	0	0	0	0	0	0	0	0	0	0
		0	5709	6285	3340	2191	1579	1206	1979	2010	1332	4732	4474	3234	0	0	-27464

NU GEV	-10.0	10.0	20.0	40.0	60.0	80.0	100.0	120.0	140.0	160.0	170.0	180.0	190.0	200.0	210.0	230.0

Fig. 8.17

CHAPTER 9

CONCLUSIONS AND COMMENTS

The subject of this thesis is hadron production in deep-inelastic scattering at a laboratory energy of 219 GeV. Two topics have been investigated: charmed particle production; and the production of kaons relative to pions. Both can be described within the same theoretical framework (the quark-parton model, or QCD). A brief summary of the results and conclusions obtained will be given in this chapter.

It has been shown that charm production accounts for less than 20% of the total deep-inelastic cross-section. This result is consistent with other experimental data and theoretical predictions, both of which in fact suggest a smaller contribution (5-10%). It is then apparent that, due to their small hadronic branching ratios, kaons from D-meson decay form only a small fraction of the observed kaon signal. Models which neglect charm should therefore give a reasonable description of kaon production. Indeed, particle ratio distributions showed qualitative agreement with quark parton model predictions. However, discrepancies are observed in the data.

A major problem in discussing these discrepancies is the lack of data in some kinematic regions (large z and high $P_\perp$). Thus, at large z, the ratio K/π appears to be approaching a number of the order 1, contradicting the value of 0.5 which was used as input to the theoretical calculations. However, in this region statistics are very poor and no firm conclusion can be drawn.

The observed discrepancy at low z is more significant as the dataset is larger. It should also be noted that the observed ratios K^+/π^+, K^-/π^- are lower than the predicted values and give an upper limit

to the ratios, since inefficiency in the Cerenkov counter can only lower the true ratios. A difference is observed between the ratios K^+/π^- at low z but this is not statistically significant.

The particle ratio distributions show a rise in K/π with $P_\perp$ at low z. At large z statistics are again poor and the results are inconclusive. Gluon jets may be the 'explanation', but the results are not inconsistent with a quark cascade model.

Finally, it must he noted that charmed particle production has not been observed directly in leptoproduction, but only inferred from dimuon production and scaling violations at low x. In this experiment it was only possible to estimate an upper limit within a reasonable charm production model.

Many questions are therefore left unanswered and more experimental data is required to resolve them.

REFERENCES

1. G. Källen, Elementary Particle Physics, Addison-Wesley (1964).
2. R. Hofstadter, Proc. Int. Symp. on Lepton and Photon Interactions, Stanford (1975), p869 and refernces therein.
3. J.G. Rutherglen, Proc. Int. Symp. on Electron and Photon Interactions at High Energies, Daresbury (1969).
4. L.S. Rochester, et al, Phys. Rev. Lett. 36, 1284 (1976).
5. Y. Watanbe et al, Phys. Rev. Lett., 35, 898 (1975).
   C. Chang et al, Phys. Rev. Lett., 35, 901 (1975).
6. S.D. Drell and J.D. Walecka, Ann. Phys., 28, 18 (1964).
7. L.N. Hand, Phys. Rev., 129, 1834 (1963).
   B. Dombey, Rev. Mod. Phys., 41, 236 (1969).
8. L.N. Hand, Proc. Int. Symp. on Lepton and Photon Interactions, Hamburg (1977) p417.
9. B.A. Gordon et al, Phys. Rev. Lett., 41, 615 (1978).
10. E. Gabathuler, European Conference on Particle Physics, Budapest (1977).
    C.H. Llewellyn-Smith, Lectures presented at the 1977 Cargèse Summer Institute.
    G.B. West, Phys. Reports, 18, 263 (1975).
    R.E. Taylor, Proc. Int. Symp. on Lepton and Photon Interactions, Stanford (1975) p679.
    E. Bloom, Proc. Int. Symp. on Electron-Photon Interactions, Bonn (1973).
11. W.K.H. Panofsky et al, Phys. Rev. 98, 751 (1955).
12. J.D. Bjorken, Phys. Rev. Lett. 16, 408 (1966).
    J.D. Bjorken, Phys. Rev., 179, 1547 (1969).

13. W.K.H. Panofsky, 14th Int. Conf. on High Energy Physics, Vienna (1968) p23.

14. R.P. Feynman, Phys. Rev. Lett., 23, 1415 (1969).
R.P. Feynman, 3rd Int. Conf. on High Energy Collisions, Stony Brook (1969).

15. S. Stein et al, Phys. Rev. D12, 1884 (1975).
P.N. Kirk et al, Phys. Rev. D8, 63 (1973).
J. Friedman and H. Kendall, Ann. Rev. Nuc. Sci. 22, 203, (1972).

16. M. Gell-Mann, Phys. Lett., 8, 214 (1964).

17. H.L. Anderson et al, Phys. Rev. Lett., 37, 4 (1976).
H.L. Anderson et al, Phys. Rev. Lett., 38, 1450 (1977).

18. J.I. Friedman and H.W. Kendall, Ann. Rev. of Nuc. Science, 203 (1972).

19. R.E. Taylor, Proc. Int. Symp. on Lepton and Photon Interactions, Stanford (1975), p679.

20. K.W. Chen, Proc. Int. Symp. on Lepton and Photon Interactions, Hamburg (1977) p467.

21. J.D. Bjorken and E.A. Paschos, Phys. Rev., 185, 1975 (1969), and Phys. Rev. D1, 3151 (1970).

22. J. Kuti and V.F. Weisskopf, Phys. Rev. D4, 3418 (1971).

23. R.P. Feynman, Photon-Hadron Interactions, Benjamin (1972).

24. J. Kogut and L. Susskind, Phys. Rev. D9, 697 (1974) and Phys. Rev. D9, 3391 (1974).

25. R. Dashen, Proc. Int. Symp. on Lepton and Photon Interactions, Stanford (1975) p981.
M. Einhorn, Phys. Rev. D14, 3451 (1976).
D. Gross, Lectures presented at 1977 Cargèse Summer Institure.

26. R.D. Field and R.P. Feynman, Phys. Rev. D15, 2590 (1977).

27. O.W. Greenberg, Phys. Rev. Lett. 13, 598 (1964).

28. R.D. Field and R.P. Feynman, Nuc. Phys. B136, 1 (1978).

29. A. Seiden et al, SLAC-PUB-2107 (1978) (submitted to Phys. Rev. D).

30. A. Seiden, Phys. Lett., 68B, 157 (1977) and SLAC-PUB-1962 (1977).

31. L.M. Sehgal, Proc. Int. Conf. on Lepton and Photon Interactions, Hamburg (1977) p837.

32. J.J. Sakurai, Proc. 1972 McGill University Summer School, p435.

33. H.D. Politzer, Physics Reports 14C, 129 (1924).

34. L. Susskind, Proc. Int. Conf. on Lepton and Photon Interactions, Hamburg (1977) p895 and references therein.

35. S.H.Pordes, Thesis, Harvard (1976), unpublished.

36. R.G. Heisterberg, Thesis, Chicago (1976) unpublished.

37. G.I. Kirkbride, Thesis, Oxford (1976) unpublished.

38. R.G. Hicks, Thesis, Illinois (1978) unpublished.

39. T.A. Numamaker and D.B. Turner, Nucl. Instr. and Meth. 114, 445 (1973).

40. R.M. Fine, Thesis, Chicago (1977) unpublished.

41. H.S. Matis, Thesis, Chicago (1976) unpublished.

42. V.K. Bharadwaj, Thesis, Oxford (1977) unpublished.

43. B.A. Gordon, Thesis, Harvard (1978) unpublished.

44. P.A. Cerenkov, Doklady Acad. of Sci. of the USSR, 2, 451 (1934).

45. I.E. Tamm and I.M. Frank, Doklady Acad. of Sci. of the USSR, 14, 107 (1937).

46. V.P. Zrelov, Cerenkov Radiation in High Energy Physics, Keter Press (1970).

47. R.C.A. Electronic Components, Harrison, N.J. 07029, USA.

48. H. Hinterberger and R. Winston, Rev. of Sci. Instruments, 37, 1094 (1966).

49. Magnetic Shield Division, Perfection Mica Company, Bensenville, Illinois 60106, Catalogue No. MG-4.

50. G.W.C. Kaye and T.H. Laby, Tables of Physical and Chemical Constants (14th Edition).

51. R.C.West (Ed.), Handbook of Chemistry and Physics (1977-78).

52. J.E. Augustin et al, Phys. Rev. Lett. 33, 1406 (1974).

53. J.J. Aubert et al, Phys. Rev. Lett. 33, 1404 (1974).

54. C. Bacci et al, Phys. Rev. Lett. 33, 1408 (1974); Ibid. 1649 (1974).

55. C. Braunschweig et al, Phys. Lett 53 B, 393 (1974).

56. D. Luke, SLAC-PUB-2086 (1978) and references therein.

57. C. Baltay et al, Phys. Rev. Lett. 41, 73 (1978).

58. W.A. Loomis et al, to be published in the Physical Review.

59. C.H. Llewellyn-Smith, Proc. Int. Symp. on Lepton and Photon Interactions at High Energies, Stanford (1975) p709.

60. M. Glück and E, Reya, Florida State Univ. Preprint, HEP 770730.

61. V. Barjer and R.J.N. Phillips, Phys. Rev. Lett. 65B, 167 (1976).

62. J.P. Leveille and T. Weiler, Imperial College London Preprint ICTP/77-78/27.

63. L.S. Osborne et al, Phys. Rev. Lett. 41, 76 (1978)

64. D.G. Aschman et al, Phys. Rev. Lett. 41, 445 (1978)

65. J.F. Martin et al, Phys. Rev. Lett. 40, 283 (1978).

66. A. Seiden, Phys. Lett. 68B, 157 (1977).

67. R.D. Field and R.P. Feynman, Nucl. Phys B136, 1 (1978).

68. R.D. Field and R.P. Feynman, Phys. Rev. D15, 2590 (1977).

69. G.R. Farrar, Nucl. Phys B77, 429 (1974).

70. A. De Rujula et al, CERN Preprint Ref. TH. 2455 (1978).

71. L.W. Mo and Y.S. Tsai, Rev. Mod. Phys 41 205 (1969).

72. F.W. Brasse et al, Nucl. Phys B110, 413 (1976).

73. D.O. Caldwell et al, Phys. Rev. Lett. 40, 1222 (1978).

74. K.E. Eriksson, Nuovo Cimento XIX, 1029 (1961).

75. T. Weiler, Private Communication, via M. Goodman, October 1978.